uOttawa

L'Université canadienne
Canada's university

FACULTÉ DES ÉTUDES SUPÉRIEURES ET POSTOCTORALES

uOttawa

L'Université canadienne
Canada's university

FACULTY OF GRADUATE AND POSDOCTORAL STUDIES

Micheal Hocking
AUTEUR DE LA THÈSE / AUTHOR OF THESIS

M.Sc. (Earth Sciences)
GRADE / DEGREE

Department of Earth Sciences
FACULTÉ, ÉCOLE, DÉPARTEMENT / FACULTY, SCHOOL, DEPARTMENT

The Calypso Hydrothermal Vent Field The Seafloor Expression of an Active Submarine Low-Sulphidation Epithermal System, Bay of Plenty, New Zealand

TITRE DE LA THÈSE / TITLE OF THESIS

Dr. M. Hannington
DIRECTEUR (DIRECTRICE) DE LA THÈSE / THESIS SUPERVISOR

CO-DIRECTEUR (CO-DIRECTRICE) DE LA THÈSE / THESIS CO-SUPERVISOR

EXAMINATEURS (EXAMINATRICES) DE LA THÈSE / THESIS EXAMINERS

Dr. A. Fowler

Dr. B. Cousens

Gary W. Slater
Le Doyen de la Faculté des études supérieures et postdoctorales / Dean of the Faculty of Graduate and Postdoctoral Studies

The Calypso Hydrothermal Vent Field

The Seafloor Expression of an Active Submarine Low-Sulphidation Epithermal System, Bay of Plenty, New Zealand

Michael W. A. Hocking

A thesis submitted to the

Faculty of Graduate and Postdoctoral Studies

In partial fulfillment of the requirements for the

Master of Science Degree in Earth Sciences

Department of Earth Sciences

Faculty of Science

University of Ottawa

Your file Votre référence
ISBN: 978-0-494-49210-9
Our file Notre référence
ISBN: 978-0-494-49210-9

Abstract

The Taupo Volcanic Zone (TVZ) is an area of extensive volcanism and geothermal activity in the North Island of New Zealand. The Calypso Hydrothermal Vent Field (CHVF) is located in an offshore extension of the TVZ on continental shelf, approximately 10 km southwest of the White Island subaerial volcano, at 180-200 m water depth in the Bay of Plenty, New Zealand. Active, moderate temperature (up to 201 °C) hydrothermal venting is contained within the Whakatane Graben, a northeast trending depression that has been partially filled by tephra from regional, subaerial volcanic eruptions.

Venting of hydrothermal fluid through the volcaniclastic material has led to a varied and geographically distinct assemblage of alteration mineral phases in 4 vent fields in an area of approximately 50 km^2. Carbon dioxide is the primary gas phase measured at active vent sites; sulfur is present as reduced H_2S gas.

The North Vent Field (NVF) is the original site of hydrothermal venting reported at Calypso. Weakly lithified volcaniclastic material recovered from this site has been altered primarily to montmorillonite, a dioctahedral smectite clay; minor mixed-layer clays were also detected. Native sulfur is spatially associated with the pervasively clay-altered samples, and is observed cementing volcaniclastic particles and filling primary pore spaces. Anhydrite mounds were also observed in the NVF.

The principal hydrothermal alteration phase at the Southeast Vent Field (SEVF) and the Southwest Vent Field (SWVF) is amorphous silica which has filled the pore spaces between volcaniclastic particles and has overprinted early barite, minor clay, and native sulfur mineral phases. Cinnabar, stibnite, and amorphous arsenic sulfides form crusts on the outer surfaces of the samples as well as filling fractures, and forming inclusions within

pyrite-silica veins. Textural relationships indicate volatile metal As, Sb, and Hg deposition is contemporaneous with silica precipitation. Clay-altered, sulfur-rich samples were also recovered from the Southeast and Southwest Vent Fields (SEVF, SWVF) but are volumetrically subordinate to the silica alteration facies. Several volcaniclastic samples from this site contained liquid hydrocarbon and charcoal fragments.

A similar juxtaposition of alteration phases is observed in active geothermal environments in the subaerial portion of the TVZ (e.g., Waiotapu, Broadlands-Ohaaki). Where fluid conduits intersect the surface, near-neutral pH, chloride water will precipitate silica sinter with elevated volatile metal concentration ± precious metals. Sinter deposits are characterized by a terraced morphology of opal precipitates and define the paleosurface in fossil epithermal systems. Such deposits have not been reported in the submarine environment. However, locations with high silica concentration, "sinter-like" material, and anomalous Hg-Sb-As concentrations have been described. At the Calypso field volcaniclastic material is cemented by amorphous silica similar to the silicified stratigraphy observed below silica sinter in some fossil epithermal deposits.

The CO_2 and H_2S gas present in the hydrothermal fluid rise to areas of elevated topography peripheral to the sinter. Mixing of CO_2 with water creates carbonic acid, and oxidation of H_2S may produce native sulfur and sulfuric acid; the extent of these reactions is limited by the availability of oxygen. In subaerial epithermal systems, the formation of sulfuric acid, and in turn advanced argillic steam-heated alteration, is limited to the vadose zone, where there is sufficient oxygen to produce sulfuric acid. In the absence of atmospheric oxygen, the production of sulfuric acid in submarine environments is similarly limited, and this explains the absence of aluminous clay minerals and alunite in the Calypso

samples. Disproportionation of $SO_{2\,(g)}$ to $H_2SO_{4\,(aq)}$ does, however, create advanced argillic alteration in some higher-temperature submarine volcanic-hydrothermal systems (e.g., Brothers Volcano, de Ronde et al., 2005).

Table of Contents

List of Tables

List of Figures

List of Plates

Acknowledgments

There are many people who provided support and guidance throughout the course of this thesis to whom I am thankful. I would like to express my sincere thanks to Mark Hannington for suggesting and supervising this project. Mark provided numerous opportunities for me over the last two years and his constant encouragement allowed for a timely completion of this thesis. Mark's enthusiasm, good humour, and open door make him an ideal supervisor. This project was funded by a research grant from the National Science and Engineering Research Council (NSERC) to Mark Hannington.

I would like to acknowledge the Society of Economic geologists for a Hugh E. McKinstry Fund student research grant and a travel grant. Travel grants were also provided by the University of Ottawa and the Graduate Students' Association of the University of Ottawa.

I am indebted to Jeanne Percival for her guidance and assistance while conducting X-ray diffraction and SWIR spectroscopy laboratory work at the Geological Survey of Canada (GSC). Numerous clay mineralogy discussions with Jeanne greatly improved this study.

Samples for this study were recovered during research cruise SO-135 aboard the RV *Sonne*. I would like to thank the chief-scientist Peter Stoffers, as well as Cornel de Ronde, the shipboard scientific party, and the captain and crew of the *Sonne* during SO-135. Research cruise SO-135 was principally funded by the German Federal Ministry for Research and Technology (BMFT). Additional funding was provided by the National Institute of Water and Atmospheric Research (NIWA), the Institute of Nuclear and Geological Sciences (IGNS), the University of Auckland, and Natural Resources Canada.

I would also like to thank Ulrich "Uli" Schwarz-Schampera, chief scientist of the research cruise SO-192-2 as well as Thomas Monecke and Sven Petersen, chief scientists of the research cruise P340. Uli, Thomas, and Sven provided a unique opportunity for me study active hydrothermal systems in the marine environment for which I am truly grateful. I am also thankful to the captain and crew of the *Sonne* (SO-192-2*)* and *Poseidon* (P340) as well as the shipboard scientific parties, and the ROPOS crew who all contributed to

successful cruises. These cruises were principally funded by the German Federal Ministry for Research and Technology (BMFT).

Whole-rock geochemical and microprobe analysis was conducted by the Electron Beam Laboratories and Analytical Chemistry Services at the GSC. I would like to thank Pat Hunt who operated the SEM at the GSC as well as the G.G. Hatch isotope laboratory where sulfur isotope analyses were conducted. I am also grateful to the Economic Geology editorial assistants Sandra Sheperd and Bernadette Lancaster for assistance with numerous administrative matters.

Many fellow graduate students provided an enjoyable environment and scientific support during my stay at the university. I would like to particularly thank Vigdís Harðardóttir and Anastasia Vandermost for numerous insightful conversations and for keeping me well fed. To my friends Paul Ferguson, Juraj Farkas, Martin Suchy, Jamil Sader, Benoit Saumur, and Mark Smith, thanks for making my stay in Ottawa a memorable one.

I would like to thank my family for their unwavering support and encouragement, and for providing a number of welcome distractions over the years during visits to Deep River, Calgary, and Vancouver Island. Last but not least, I would like to thank Darla Knight for her cheerful support, companionship, and most importantly her patience.

1.0 Introduction

The Whakatane graben is a NE-trending depression located 10-15 km south of the subaerial White Island volcano in the Bay of Plenty, New Zealand (Figure 1.1; Plate 1.1). Submarine hydrothermal activity was first recognized here by scattering of echo-sounding profiles which are indicative of rising columns of bubbles (Duncan and Pantin, 1969). The first visual inspections of the seafloor in the vicinity of the rising bubbles were made in 1971 during a research cruise aboard Jacque Cousteau's ship the Calypso; for which the vent site was named (Glasby, 1971). Submersible dives confirmed the presence of venting fluid and 6-8 m high anhydrite mounds.

A joint German-New Zealand research program (SO-135), aboard the research vessel (RV) *Sonne*, sailed between Suva, Fiji and Auckland, New Zealand along the Tonga-Kermadec Arc between September 9, 1998 and October 15, 1998 (Stoffers and Wright, 1999). The objectives of the cruise were to characterize tectonic, magmatic, and sedimentary processes along the Kermadec–Havre arc–back arc along the Kermadec subduction margin and its southern extension into the continental TVZ of the North Island of New Zealand. Observation of volcanic fumaroles and sampling of volcanic gases were also conducted on White Island.

The research objectives in the Whakatane graben were to locate, describe, and sample submarine hydrothermal vents with the purpose of: 1) identifying the geological setting of the vent fields; 2) determining the nature and variability of hydrothermal alteration mineralogy; and 3) identifying the fauna proximal to sites of active venting.

Towed camera surveys and dredging were used to observe the seafloor and collect rock samples. The manned submersible JAGO was used to map vent sites, measure the temperature of vent fluids, and collect fluid and biological samples.

Investigation of the Whakatane graben was completed between October 6, 1998 and October 9, 1998 (Stoffers and Wright, 1999). Echo-sounding sonar was used to locate the original Calypso vent, which was renamed the North Vent Field (NVF). Hydrosweep bathymetric mapping was conducted over a 12 x 12 Nm area south of White Island in the vicinity of the Calypso vent (Figure 1.2). Echo sounding was conducted during the mapping operation and led to the discovery of the three new vent fields: the Central Vent Field (CVF), Southeast Vent Field, and Southwest Vent Field (SWVF). These vents along with the NVF comprise the Calypso Hydrothermal Vent Field (CHVF).

Recovered rock samples from CHVF include variably clay-altered lapilli tuff, which commonly contain abundant native sulfur, as well as massive and bedded tuffaceous rocks that are variably silicified and coated with hydrocarbon. Silicified samples contain strong As, Sb, Hg sulfide mineralization and liquid Hg was observed dripping from some recovered samples (Stoffers et al., 1999). Additional hydroweep bathymetry and geological mapping was completed in the Calypso area in April, 2007 during research cruise SO-192-2 aboard the RV *SONNE*. During this cruise rock, fluid, and biological sampling was conducted.

This thesis integrates X-ray diffraction (XRD), shortwave infrared reflectance (SWIR) spectroscopy, microprobe, and scanning electron microscopy mineralogical

techniques with lithogeochemistry and stable isotope geochemistry to describe altered volcaniclastic rocks recovered by ship-based dredge (DR) and television-guided grab (GTVA) sampling from the CHVF during research cruise SO-135, supplemented by observations made during SO-192-2.

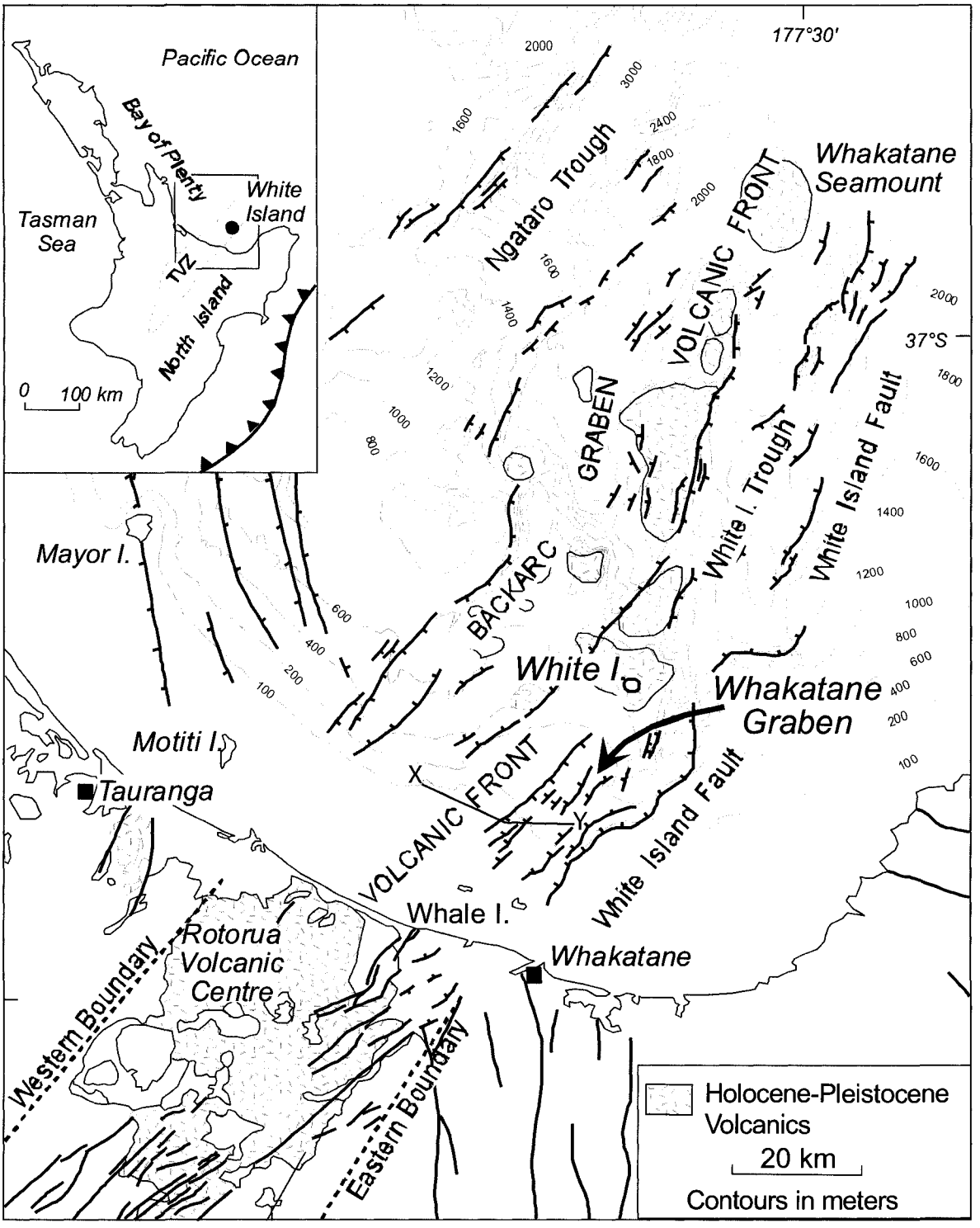

Figure 1.1. Location and basic geological map of the Bay of Plenty, New Zealand (modified from Wright, 1992). The Calypso Hydrothermal Vent Field is contained within the Whakatane Graben, a NE-trending extensional feature located near the eastern margin of the Taupo Volcanic Zone. Calypso is situated between the subaerial White Island andesitic volcano and the silicic volcanic centres on the North Island of New Zealand (e.g., Rotorua). The red XY line is the siesmic transect in Figure 3.2.

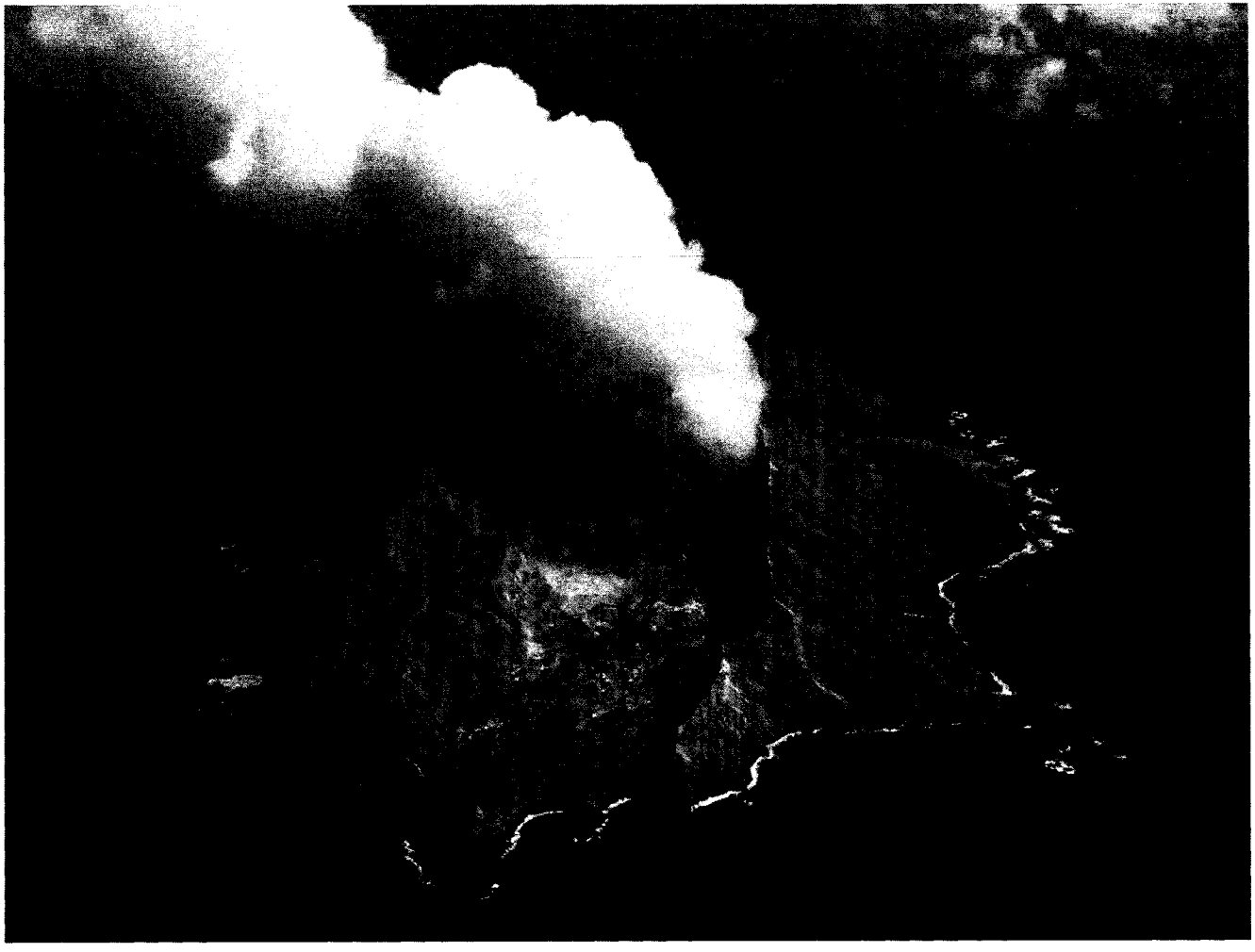

Plate 1.1. An aerial photograph of White Island shows the presence of a central crater lake and a rising, ash-laden, gas-vapour plume. A hydrothermal system has been active on the island for at least 10 000 years. The flux of gas and vapour from the volcano, in tons per year, is 0.13 x 10^6 SO_2, 1.9 x 10^6 H_2O, and 0.44 x 10^6 CO_2. The high temperature (~900°C) rising plume contains base and precious metals with a calculated flux of 110 tons of Cu and >350 kg Au per year (Hedenquist and Lowernsten, 1994).

1.1 Location and Access

The study area was accessed using the research vessel (RV) *Sonne* on cruise SO-135 and SO-192-2. The manned submersible JAGO, dredging, and a towed-camera system, termed the Ocean Floor Observation System (OFOS), were utilized to conduct seafloor research during SO-135. The remotely-operated vehicle ROPOS was used to make seafloor observations, and collect geological, biological, gas, and fluid samples during SO-192-2. Bathymetric mapping and sampling was conducted at four sites of active and fossil hydrothermal activity: the NVF, which covers 1.5 km^2 centered on 37 °36.7' S latitude, 177 ° 0.6.2' E longitude; the CVF, which covers 1 km^2 centered on 37 ° 39.4' S latitude, 177 ° 05.2' E longitude; the SWVF which covers 1 km^2 centered on 37 ° 41.7' S latitude, 177 ° 06.0' E longitude; and the SEVFf which covers 0.5 km^2 centered on 37 ° 41.3' S, 177 ° 07.2' E longitude (Figure 1.2). The NVF is the shallowest vent field surveyed with an average dredge depth of 170.5 m the SEVF and SWVF have average dredge depths of 189.5 m and 181.6 m respectively.

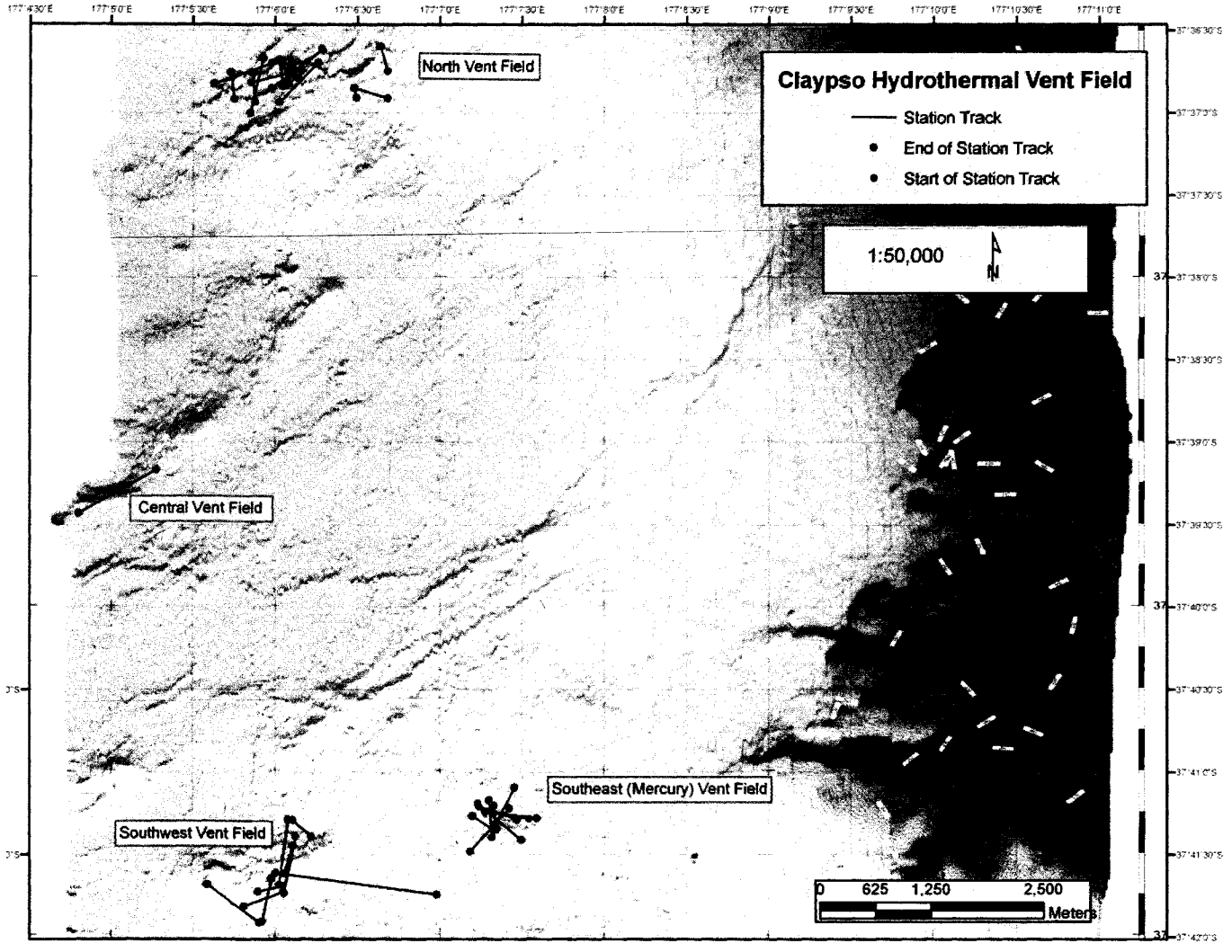

Figure 1.2. Bathymetric map of the Calypso Hydrothermal Vent Field. Station tracks (dredge, Jago, and GTVA) are plotted as solid lines. Hydrothermal activity has been observed in depressions associated with NE trending structures.

1.2 Previous Work

Cruise report *Sonne* 135 (Stoffers and Wright, 1999) is a complete account of work conducted during research cruise SO-135 aboard the RV *Sonne*, including seafloor descriptions, station and sample locations, preliminary rock sample descriptions, and a bathymetric map. Robertson (1999) summarized station data from SO-135 and conducted major and trace element analyses of two rhyolite and nine plutonic samples collected in dredges near the vent sites. Geochemical and petrographic analysis indicates the samples are similar to plutonic and volcanic samples contained within ignimbrite deposits hosted within the TVZ on land. Robertson (1999) also investigated alteration mineralogy of volcaniclastic rocks using transmitted and reflected light microscopy, scanning electron microscopy (SEM), and X-ray diffraction (XRD) analysis. Phyllosilicate alteration minerals were determined to be primarily smectite, illite, and mixed-layer illite-smectite clay minerals replacing glass shards and volcaniclastic fragments. Fine-grained muscovite (sericite) and illite was recognized to be replacing feldspar crystals. Native sulfur and amorphous silica were identified as common phases, which cement volcaniclastic material and line pore spaces. Cristobalite, barite, gypsum, and anhydrite were also identified, along with pyrite, cinnabar, orpiment, realgar, and stibnite. However, the origin of the mineral assemblage was not discussed.

Botz et al. (2002) studied hydrocarbons contained in hydrothermal gas collected during cruise SO-135. Large volumes of CO_2 and gaseous hydrocarbon (CH_4 to C_4H_{10}) were detected in the vent fluids at Calypso, liquid hydrocarbon was also observed on rock samples. Carbon isotopes were used to determine that the liquid hydrocarbon, and much of

the gaseous hydrocarbon, is derived from thermal maturation of buried detrital terrestrial organic matter and drowned coastal vegetation.

The research outlined above provides the framework for this study.

1.3 Purpose and Scope of this Study

1. Contribute to previous alteration studies through a careful paragenetic study and X-ray diffraction analysis to establish the origin of minerals in hydrothermally altered and mineralized rock samples.
2. Use short wave infrared (SWIR) reflectance spectroscopy to (a) further characterize the alteration mineral assemblage and (b) assess the value of the instrument as a new tool for rapid shipboard mineralogical analysis.
3. Use whole-rock geochemical analysis to (a) determine the source of the volcaniclastic material filling the Whakatane graben and (b) identify the chemical changes associated with hydrothermal fluid and rock interaction.
4. Use sulfur isotopes to (a) identify the source of the abundant native sulfur and volatile metal sulfides at Calypso and (b) understand the conditions of sulfur oxidation and sulfur precipitation from hydrothermal fluids.
5. Combine mineralogical and geochemical techniques outlined above to compare the hydrothermal system to subaerial epithermal environments, particularly the subaerial geothermal system on the North Island of New Zealand, and the White Island volcanic-hydrothermal system.
6. Identify potential criteria which may be used to distinguish shallow submarine hydrothermal systems from subaerial systems in the rock record.

2.0 The Epithermal Environment

The term epithermal refers to a range of temperatures and corresponding depths within the shallow Earth's crust in which efficient metal precipitation occurs from hydrothermal fluids, as originally proposed by Lindgren (1922). Fluid inclusion, stable isotope, and geologic data suggest epithermal deposits occur at depths of 50 to 1500 m below the paleo-watertable at temperatures up to 300°C and pressures of less than 100 atmosphere (Simmons et al., 2005 and references therein). This area within the crust is an efficient environment for ore deposition because of the physical and chemical processes that occur during adiabatic boiling of an upwelling hydrothermal fluid (Hedenquist et al., 2000). In subaerial volcanic arcs, epithermal deposits generally occur in intermediate to felsic volcanic rocks. Transitional and submarine ore deposits with epithermal-style alteration and sulfide mineralogy have been observed on the modern ocean floor and in the rock record (e.g., Sillitoe et al., 1996; Hannington et al., 1999; Naden et al., 2005).

The recognition of mineralogical and textural similarities between active hydrothermal systems and fossil epithermal ore deposits has greatly improved the understanding of the ore-forming processes. The classification of epithermal ore deposits broadly reflects the different geothermal and volcanic-hydrothermal volcanic settings associated with arc volcanism (Figure 2.1).

The terminology used to subdivide epithermal deposits that form in geothermal and volcanic-hydrothermal systems has evolved over the last three decades. Classification schemes focus on the alteration mineralogy or the sulfidation state of the hydrothermal fluid and the sulfide minerals which precipitated from the fluid, as summarized by Cooke and Simmons (2000), Hedenquist et al. (2000), and Simmons et al. (2005). Deposits are typically referred to as high- and low- sulfidation (e.g., White and Hedenquist, 1990; White and Hedenquist, 1995; Hedenquist et al., 2000). Sulfidation state refers to the primary equilibrium sulfide assemblage and is related to the oxidation state of the fluid. High sulfidation sulfide assemblages form from fluids that contain abundant oxidized sulfur species (SO_2, HSO_4^-, SO_4^{2-}). Low-sulfidation is used to describe sulfide mineral assemblages that form from fluids in which the sulfur is mainly in a reduced form (e.g., HS^-, H_2S). The oxidation state of magma, from which the sulfur is derived, is a function of the volcanic-tectonic environment where it forms and the pressure conditions under which the fluid evolves (Einaudi et al., 2003; Sillitoe and Hedenquist, 2003). The sulfides that precipitate from the ore forming fluid reflect the redox conditions of the ore forming fluid. High-sulfidation epithermal deposits formed from oxidized sulfur species are characterized by a sulfide assemblage including pyrite-enargite, ± covellite-digenite, famatinite, luzonite, tennantite, and orpiment. Low-sulfidation sulfide assemblages include arsenopyrite-loellingite-pyrrhotite, and Fe-rich sphalerite (Simmons et al., 2005). The oxidation state of the hydrothermal system can also be determined by direct fluid sampling in active environments. The terms acid-sulfate and adularia-sericite are also commonly used to classify deposits. The terms refer to hypogene gangue mineralogy which reflects the formation of a mineral assemblage under acidic (acid-sufate) or neutral pH (adularia-sericite) fluids (Hayba et al., 1985, Heald et al., 1987).

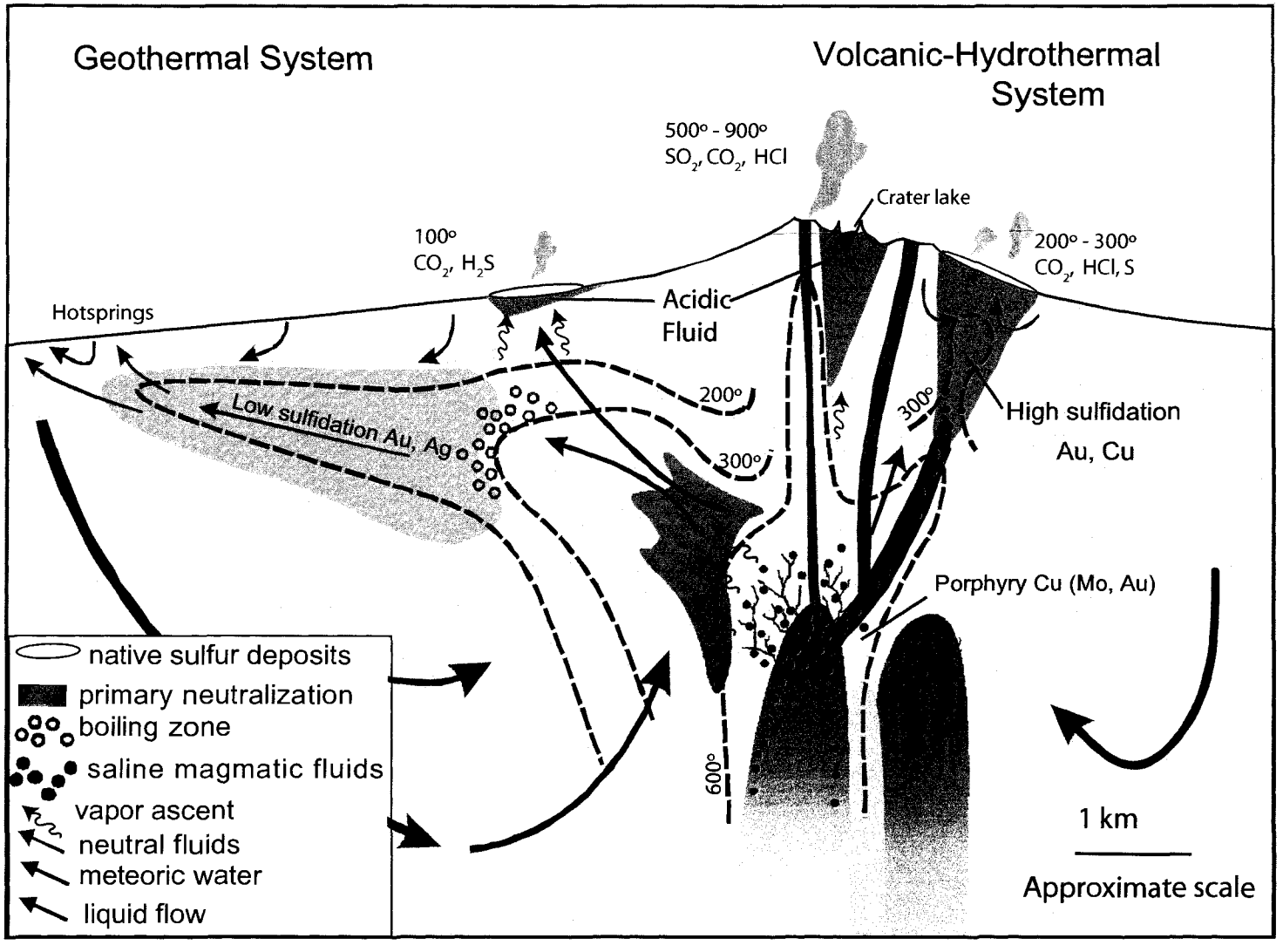

Figure 2.1. Schematic cross-section of geothermal and volcanic-hydrothermal systems and their respective low- and high- sulfidation ore forming environments (after Hedenquist et al., 2000).

2.1 The Volcanic-Hydrothermal Environment

The hydrothermal environment that occurs proximal to active volcanic vents and their subvolcanic, and at times erupting, magma chambers are termed "Volcanic-Hydrothermal" (Hedenquist et al., 2000) or "Magmatic-Hydrothermal" (Simmons et al., 2005). In this environment, high-temperature, acidic, magmatic-derived, and relatively, oxidized fluids ascend to the surface rapidly and consequently do not equilibrate with host volcanic rocks (Giggenbach, 1992). Sulfur present in the fluid occurs primarily in an oxidized form as sulfur dioxide gas ($SO_{2(g)}$), and surface venting occurs at high temperature sulfur fumaroles. The oxidized nature of the sulfur species defines the volcanic-hydrothermal environment and associated ore deposits as high-sulfidation. Sulfur dioxide is the dominate gas in the vapour above temperatures of approximately 400 °C (Rye et al., 1992). Cooling below this temperature will initiate the disproportionation of $SO_{2(g)}$ (Holland, 1965) in water into oxidized and reduced sulfur species, hydrogen sulfide (H_2S), sulfuric acid (H_2SO_4), and native sulfur (S°; reaction 1 and 2).

$$SO_{2(g)} + 4\ H_2O = 3\ H_2SO_{4(aq)} + H_2S_{(g)} \qquad (1)$$

$$3\ SO_{2(g)} + 2\ H_2O = 2\ H_2SO_{4(aq)} + S° \qquad (2)$$

Sulfuric acid, together with magmatic hydrochloric (HCl) and hydrofluoric (HF) acid, will create a solution with a very low pH. These very acid solutions of pH ~ 1 will

leach the volcanic rocks and may lead to the formation low pH acid crater lakes (Hedenquist et al., 2000; Simmons et al., 2005). Acidic leaching of rocks occurs by hydrolysis of minerals, where H^+ ions replace the primary mineral cations (Schoen et al., 1974). Leaching of cations, the conservation of immobile elements, and the introduction of sulfate will create mineral assemblages which are stable at lower pH than the original mineral assemblage of the host rock. Under very acidic conditions most elements will be removed leaving a massive silica residue. Leaching of volcanic phenocrysts and clastic particles of volcaniclastic material will create a porous rock termed vuggy silica (Steven and Ratte, 1960, as cited in Stoffregen, 1987). This is likely a preparatory phase which increases the porosity of the rock and allows for the upward flow of mineralizing fluids (Hedenquist et al., 1998). The acidic solution will become increasingly neutralized during distal migration by reacting with host volcanic rocks. The pH-specific range of alteration minerals commonly leads to a zoned alteration pattern of advanced argillic to argillic alteration assemblages moving away from the volcanic source. Minerals associated with volcanic-hydrothermal advanced argillic alteration, also referred to as hypogene advanced argillic alteration, include quartz, alunite, dickite, pyrophyllite ± diaspore and zunyite and generally form above 200°C (Simmons et al., 2005). An argillic alteration mineral assemblage forms at lower temperatures and mildly acidic pH conditions on the periphery of the deposit and includes illite, smectite, chlorite, mixed-layered clays, pyrite, calcite, and chalcedony (Simmons et al., 2005).

Hydrogen sulfide gas may be only a minor component of the ore-forming fluid in some volcanic-hydrothermal systems (e.g., White Island; Giggenbach et al., 2003). However oxidation of H_2S in the vadose zone can also form H_2SO_4 and contribute to acid-

sulfate, steam-heated advanced argillic alteration as described in the geothermal environment (see below).

White Island is a subaerial andesite-dacite volcano which marks the northern limit of the Taupo Volcanic Zone (TVZ) in the Bay of Plenty. There has been an active hydrothermal system at White Island for at least the last 10 000 years and the calculated metal flux in the ash-laden gas plume rising from the island is 300 tons of copper and greater than 350 kilograms of gold per year (Hedenquist and Lowernsten, 1994) . It is the most active volcano in the TVZ and the site of an active high-sulfidation epithermal system (Hedenquist et al., 1993).

2.2 The Geothermal Environment

Geothermal systems occur distal to the volcanic-hydrothermal environment and to the subvolcanic magma chamber which drives convection of the hydrothermal fluids (Figure 2.1). The lower temperature, dominantly meteoric, low-salinity (1-2 wt %), chloride water equilibrates with the host rocks as it ascends to the surface (Simmons et al., 2005). The fluid is reduced by fluid-rock interaction, primarily with iron-bearing minerals, and therefore sulfur is present in the fluid as reduced H_2S and HS^- (Einaudi et al., 2003). This sulfur may be derived from both magmatic sources and leaching from volcanic rocks. These fluids may have high hydrogen sulfide and carbon dioxide (CO_2) gas concentrations (Simmons et al., 2005). Neutral-pH stable gangue mineralogy includes quartz, chalcedony, carbonate +/- adularia, illite, barite, and fluorite (Hedenquist et al., 2000).

Where fluid conduits intersect the surface, near-neutral pH, chloride water will discharge. Cooling and fluid evaporation will cause the precipitation of opal with a terraced morphology and elevated volatile metal ± precious metals concentrations (Rimstidt and Barnes, 1980; White et al., 1989; Rimstidt, 1997). In fossil epithermal systems, sinters define the paleosurface, designate zones of hydrothermal discharge, and are indicative of low-sulfidation fluids (Hedenquist et al., 2000).

Adiabatic boiling as the fluids ascend to the surface causes a separation between liquid and gas phases; loss of CO_2 will cause the pH of the liquid to increase. The separated CO_2 and H_2S rises to the near surface, commonly to areas of high elevation peripheral to the sinter, where will CO_2 condenses into ground water, and H_2S is oxidized in the vadose zone. These near-surface processes create acid which can lead to the formation of argillic

and advanced argillic alteration assemblages similar to those in the volcanic-hydrothermal environment; this process is termed steam-heated alteration. The distribution of propylitic, argillic, and advanced-argillic alteration phases, along with vein mineralogy and sinter distribution is illustrated in Figure 2.2 from Hedenquist et al. (2000; after Buchanan, 1981 and Sillitoe, 1993).

Condensation of $CO_{2\,(g)}$ in ground water forms carbonic acid (reaction 3; Rimstidt 1997), creating a weak acid solution of pH 4-5 (Simmons and Browne, 2000). The solution percolates downward leaching volcanic rocks and creating an argillic alteration assemblage of illite, illite-smectite, and kaolinite at temperature below 150 °C (Simmons and Browne, 2000).

$$CO_{2(g)} + H_2O \rightarrow H_2CO_{3(aq)} \qquad (3)$$

Oxidation of H_2S gas will produce native sulfur (S°; reaction 4) and sulfuric acid (reaction 5). Mixing of sulfuric acid with meteoric water will create an acid solution with a pH between 2 and 3.

$$H_2S_{(g)} + \tfrac{1}{2}\, O_{2(g)} \rightarrow S^\circ + H_2O \qquad (4)$$

$$H_2S_{(g)} + 2\, O_{2(g)} \rightarrow H_2SO_{4(aq)} \qquad (5)$$

As in the volcanic-hydrothermal environment this acidic solution will leach many of the primary mineral components from the host rock; immobile elements such as aluminum

are conserved. The resulting advanced argillic mineral assemblage is comprised of aluminum sulfates (e.g., alunite) and aluminum-rich clay minerals (e.g., kaolinite). The acid-sulfate, advanced argillic assemblage is typified by a mineral assemblage of alunite, kaolinite, opal, pyrite, and marcasite (Simmons et al., 2005). Silica leached by the acidic solutions will be transported away by the steam-heated water leaving a leached cap on the system (Figure 2.2). The fluids collect at the water table and in topographic depressions; cooling causes precipitation of opal and chalcedony. Iron removed from the host rock by hydrolysis reactions will interact with $H_2S_{(g)}$ proximal to the vent sites to form iron sulfides.

The distribution of steam-heated argillic alteration and advanced-argillic alteration is controlled by the water table. Insufficient dissolved oxygen in meteoric water limits the formation of sulfuric acid to the vadose zone where atmospheric oxygen is abundant (Hedenquist et al., 2000). Descending sulfuric acid will also be neutralized by the water table. Variation in the position of the water table over time may change the distribution of alteration assemblages (e.g., Simmons, 1991).

The active geothermal environments at Waiotapu, Broadlands-Ohaaki, and Wairakei in the TVZ are the best studied active low-sulfidation systems, with associated precious metal deposition, in the world (Browne, 1969; Weissberg, 1969; Weissberg et al., 1979; Brown 1986; Simmons and Browne, 2000). Selected photos of alteration phases and hydrothermal mineral precipitates at the Waiotapu geothermal field are presented in Plate 2.1.

Alteration mineralogy, sulfide mineralization, and the distance from an active volcanic centre suggest that the Calypso Hydrothermal Vent Field is the seafloor expression of a geothermal system. This study will attempt to identify differences between the near surface subaerial geothermal environment and the shallow submarine seafloor geothermal environment.

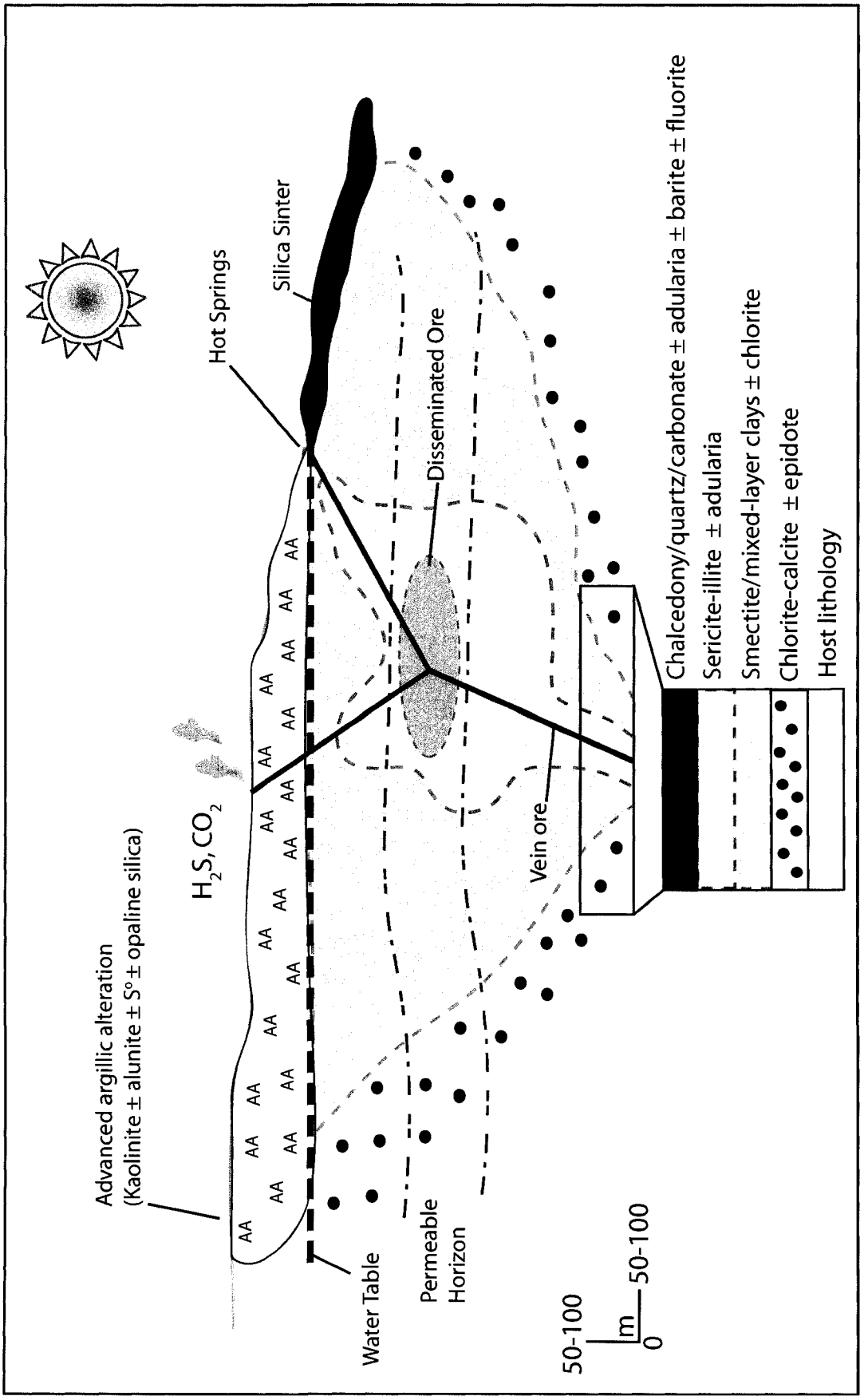

Figure 2.2. Schematic cross-section of alteration mineral assemblage distribution in a subaerial low-sulfidation epithermal system (from Hedenquist et al., 2000, after Buchanan, 1981, and Sillitoe, 1993).

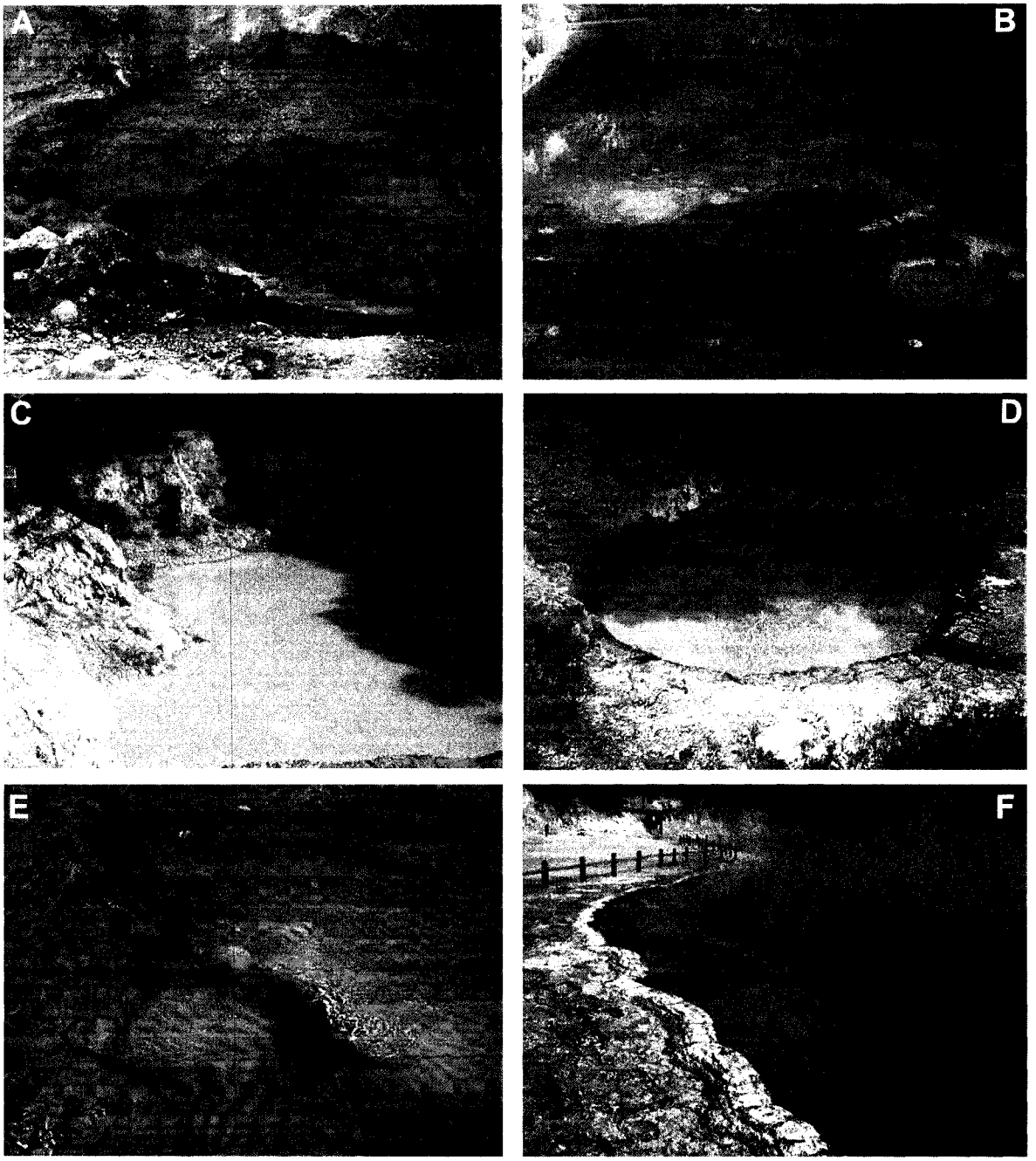

Plate 2.1. Photographs of alteration and mineral precipitation at the Waiotapu geothermal field. A. Sulfur fumaroles hosted by altered volcanic rocks at the Sulfur Cave. B. The yellow coloration at Yellow Pools is caused by arsenic and sulfur precipitation when chloride water mixes with acid-sulfate water. C. Devil's Bath is a hydrothermal eruption crater lake filled with acid-sulfate water with a pH of 3.9. D. High temperature geothermal fluids cause distillation of organic matter and create a mixture of hydrocarbons and acid-sulfate water at Devil's Ink Pots. E. Fluid discharging from Champagne Pool cools to form silica terraces at Primrose Terrace, the largest silica sinter in New Zealand. F. Champagne Pool is an ancient hydrothermal eruption crater which discharges alkali-chloride water. The pool is surrounded by a pale-grey silica sinter with an orange arsenic-antimony sulfide margin.

3.0 Location and Regional Geology of the Calypso Hydrothermal Vent Field

The submarine CHVF is located on the eastern margin of the TVZ on continental shelf, approximately 10-15 km southwest of the subaerial White Island volcano in the Bay of Plenty, New Zealand (Figure 1.1). The TVZ is the southern terminus of the Tonga-Kermadec volcanic arc; a product of westward dipping subduction of the Pacific Plate below the Australian plate (e.g., Bevis et al., 1995, Wallace et al., 2004). Subduction propagates southwards to the Hikurangi Trough where the Hikurangi Plateau, a large, early Cretaceous, ocean island plateau is being subducted below the North Island of New Zealand (Wood and Davy, 1994; Mortimer and Parkinson, 1996). Subduction ceases near 42°S where the Chatham Rise, a continental fragment, collides with the Hikurangi Margin (Wallace et al., 2005). At the terminus of subduction, convergent plate motion is accommodated by the Alpine Fault system on the South Island of New Zealand (Norris and Cooper 1995). Wallace et al. (2005) suggest collision of the Chatham Rise creates an impinging force on the North Island and causes tectonic shortening to shift from the trench to the back-arc region. Collision also causes the downgoing slab to the north of the Chatham Rise to rollback, drawing the eastern edge of the North Island towards the trench. This mechanism has been used to explain clockwise rotation of the eastern side of the North Island relative to the Pacific Plate (Figure 3.1; Wallace et al., 2004; Wallace et al., 2005). This rotation leads to extension of the TVZ at 15 mm yr^{-1} in the Bay of Plenty decreasing to a rate of 5 mm yr^{-1} at 39°S (Wallace et al., 2004).

Hydrothermal venting in the Bay of Plenty is structurally controlled by northeast-trending normal faults developed during Quaternary extension (Pantin and Wright, 1994). This extension has caused the development of NE-trending normal faults and the subsidence of Mesozoic greywacke basement rocks to form the Whakatane graben (Wright, 1990). Seismic data indicate three major volcaniclastic sequences, accounting for 2.5 km of stratigraphy, overly the Mesozoic greywacke basement (Figure 3.2). The sequences are separated by angular unconformities and have been interpreted to represent volcaniclastic material derived from large, caldera-forming rhyolitic eruptions on the subaerial portion of the TVZ (Davey et al., 1995). The basal volcaniclastic sequence was erupted between 0.70 and 1.25 Ma and the middle sequence was deposited between 130 and 400 ka. The upper most stratigraphic sequence is believed to be material derived from post 65-ka eruptions (Davey et al., 1995). Tephrastratigraphy suggests that volcaniclastic material derived from post-18ka subaerial volcanism on the TVZ would have been deposited in the Calypso area (Wright, 1990; Pillans and Wright, 1992; Smith and Shane, 2002).

Fluid venting in the CHVF is contained within the Whakatane Graben at 160 m to 200 m water depth. Hydrothermal venting and marine processes superimposed on this collection of volcanic derived material have created a varied suite of rock types, textures, mineralization, and alteration minerals.

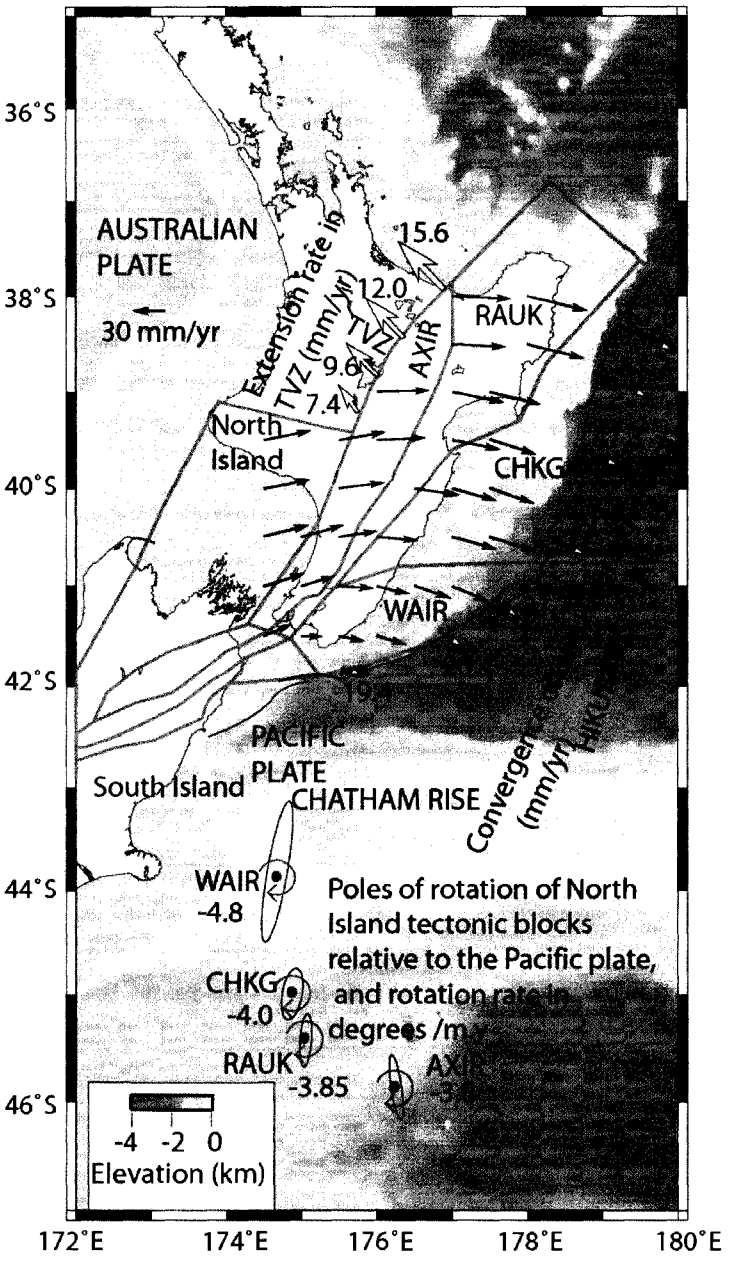

Figure 3.1. Tectonic motion in the North Island region from Wallace et al. (2005). The Pacific plate is subducting below the North Island at the Hikurangi Trough. Sudbuction ceases at the Chatham Rise, a buoyant crustal block, impinging on South Island. This causes roll back of the downgoing slab, drawing the eastern side of the North Island towards the trench. Clockwise rotation of the eastern North Island relative to the Pacific plate creates extension in the back-arc and the formation of the Taupo Volcanic Zone.

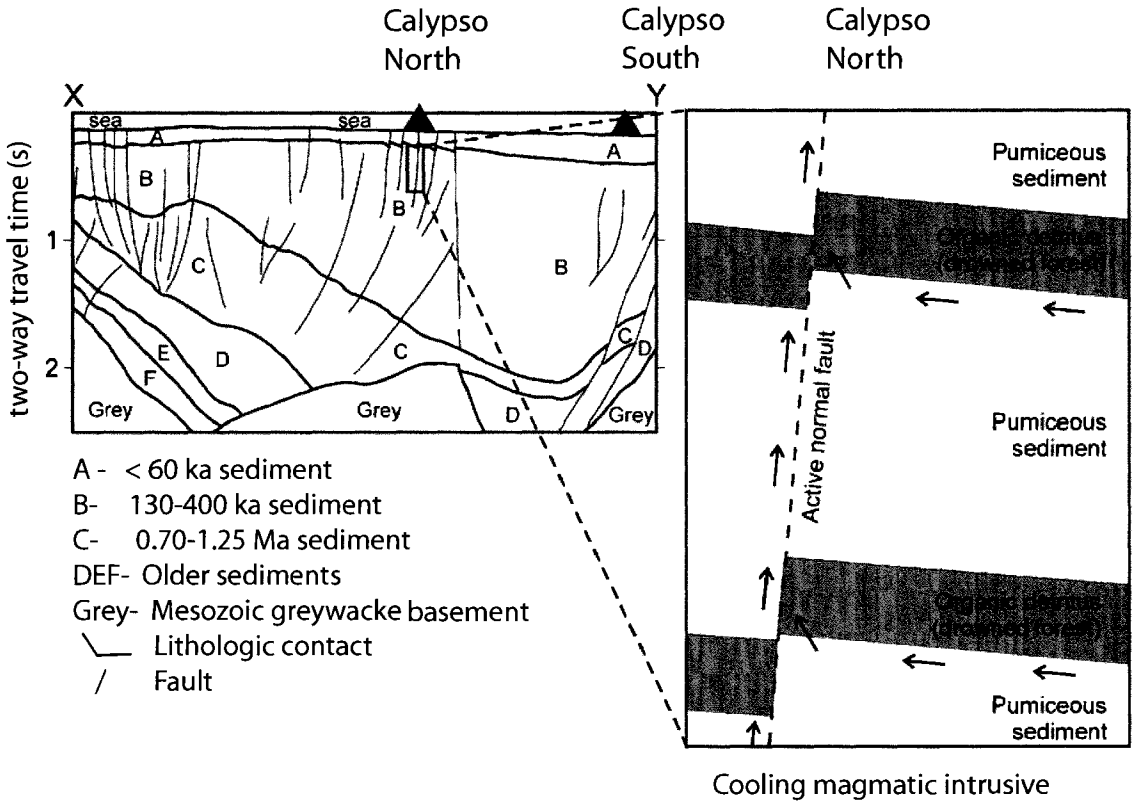

Figure 3.2. Siesmic reflection stratigraphy of the Whakatane Graben (see Figure 1.1 for location of siesmic transect; from Botz et al. 2002, adapted from Davey et al. 1995). The Mesozoic greywacke basement is block faulted and volcaniclastic sediments dip toward the eastern margin of the graben. Recovered rock samples at Calypso were likely derived from stratigraphic unit A. Botz et al. (2002) suggest organic matter is interbedded with volcaniclastic sediments. Hydrothermal fluid flow along primary structures causes thermal maturation of organic matter and normal faults allow mobilization of hydrocarbons to surface.

Investigation of the four main vent locations of the CHVF occurred during two joint German-New Zealand research expeditions: SO-135 aboard the RV *Sonne* (Plate 3.1A) in October, 1998 (Stoffers and Wright, 1999) and SO-192-2 in April, 2007. During SO-135 mapping was conducted at 21 distinct vent sites during 13 stations using the JAGO submersible (79-JAGO, 80-JAGO,108-JAGO; Plate 3.1D) and the towed-camera system OFOS (OFOS- 83, 84, 92, 93, 94, 105, 106, 107; Figure 1.2; Plate 3.1B; Stoffers and Wright, 1999). The OFOS was used to map five areas of the North Vent Field (NVF), one area of the Central Vent Field (CVF), one area of the Southwest Vent Field (SWVF), and two areas of the Southeast (Mercury) Vent Field (SEVF; Figure 1.2). The JAGO submersible was used to sample venting fluids, collect fauna, and measure temperatures on two dives in the NVF (JAGO – 79, 80), and during a single dive on the SEVF (JAGO-108).

The Canadian Scientific Submersible Facilities remotely operated submersible ROPOS (Plate 3.1E, F) was used to collect samples and map the seafloor at Calypso during cruise SO-192-2 on two dives. Dive SO-192-2-R1039 consisted of a transit from the SWVF to the SEVF. Dive SO-192-2-R1040 began in the SWVF where fluid and gas samples were collected from hydrothermal vents located during dive SO-192-2-R1039. The second part of the dive was conducted at the NVF. Selected bottom photographs taken during these dives are presented in Plate 3.2.

Venting of clear hydrothermal fluids was observed to be spatially associated with rocky outcrops along fault scarps which create local depressions subparallel to the regional

NE-trending Whakatane Graben; fluid temperature measurements reached 201°C. Carbon dioxide is the dominant gas in the hydrothermal fluid, accounting for between 45 and 84 % of the gas by volume. Hydrogen sulfide gas accounts for between 0.83 and 1.9 vol % of the gas by volume (Botz et al., 2002). Fluid conduits are represented by small centimeter-scale holes in sandy sediment and along fractures in laminated volcaniclastic material; these vents typically have halos of native sulfur and filamentous bacteria. An increase in the size and abundance of anemone was also noted proximal to the vents. The seafloor in the vicinity of vents was often pockmarked with shrimp burrows and/or gas escape structures. Bioturbation may have provided primary porosity for fluid flow. Anhydrite mounds were also observed at the North and South Vent Fields.

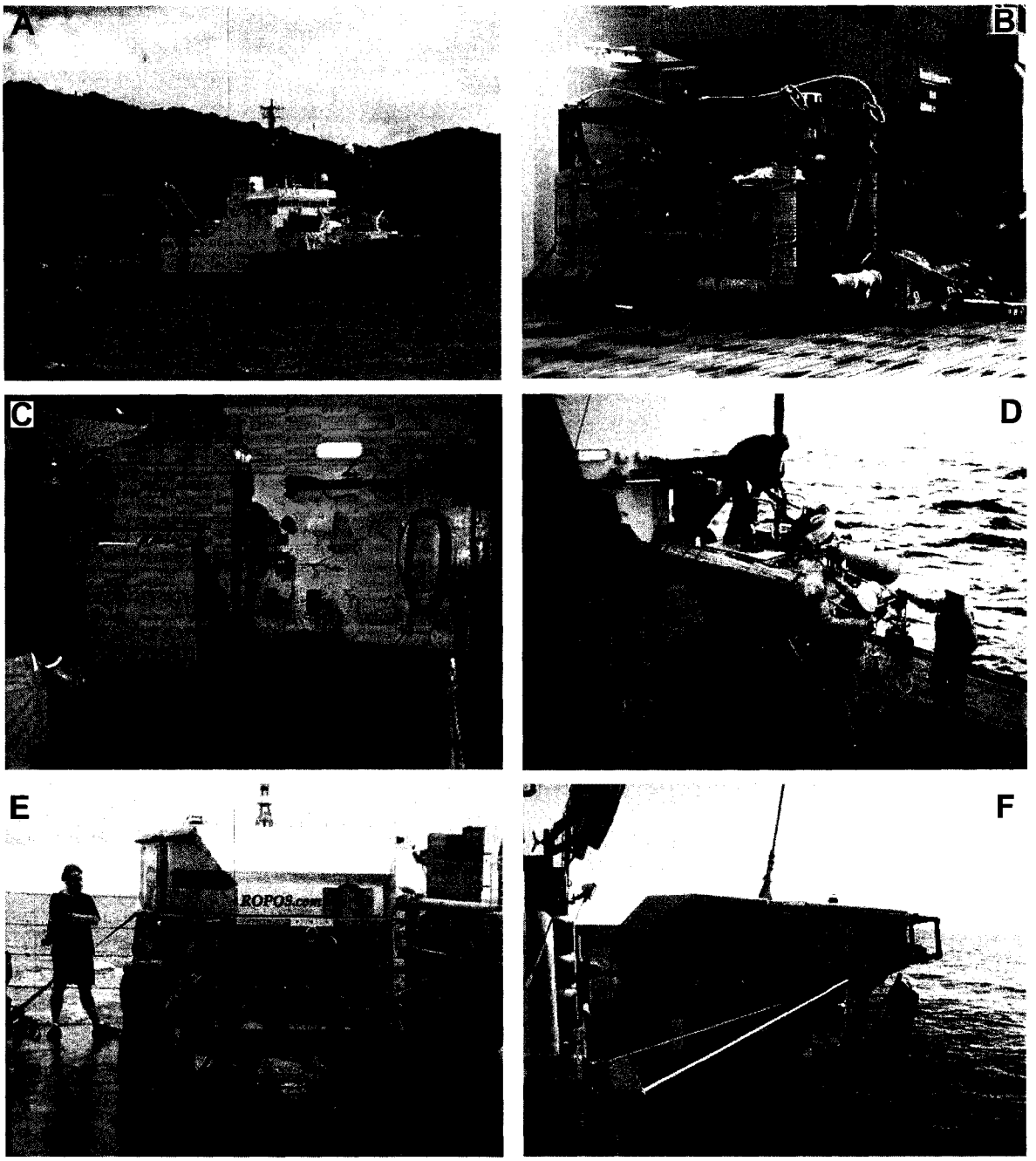

Plate 3.1. A. Research vessel *Sonne*. B. Ocean floor observation system (OFOS) on left, wax piston corer on right. C. Television guided grab sampler (GTVA) depositing a sample on the deck of the *Sonne*. D. JAGO submersible on the deck of the *Sonne*. E. The Canadian Scientific Submersible Facility's remotely operated submersible ROPOS . F. Deployment of ROPOS from the stern of the *Sonne*.

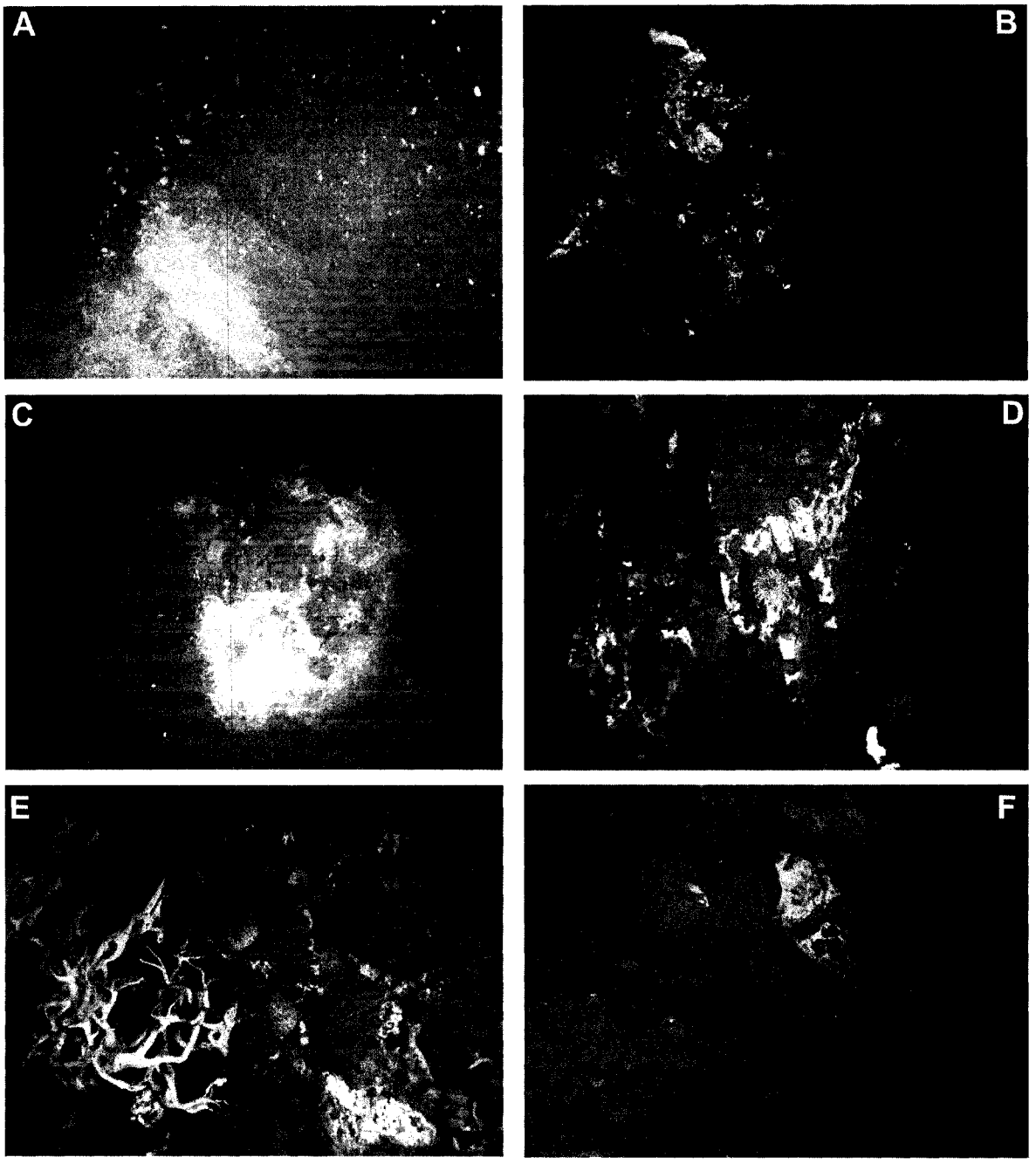

Plate 3.2. Seafloor images of the CHVF from ROPOS dives. Where visible the distance between the two green laser dots is 10 cm. A. Bubbles (dominantly CO_2 and H_2S) venting near angular blocks of altered ash, coated with white bacterial mats. B. Hydrothermally altered blocks of volcaniclastic material covered with white bacteria. C. White bacterial coating on sediment surrounding a hydrothermal vent. D. Red anemones on bacterial coated blocks of layered volcaniclastic material; a sponge and sea perch are also visible. E. The size and abundance of anemones is observed to increase proximal to sites of active hydrothermal fluid venting. F. Sediment near the vent sites is pockmarked with shrimp burrows and/or gas escape features; bioturbation may provided primary porosity for fluid flow.

4.0 Sampling

Rock sampling was conducted from the RV *Sonne* using a ship based dredge, a deep-sea television-controlled grab (GTVA; Plate 3.1C), and by manned submersible (JAGO). Thirty-one dredge samples were collected at both the North and South vent sites at water depths between 150 m and 200 m along dredge tracks up to 300 m in length (Figure 1.2). In total, thirty-one dredge hauls, and three GTVA samples were collected from the Calypso vent fields. This study examined five sample suites from the North Vent Field (GTVA – 81, 82; DR-95, 97, 98, 118), four sample suites from the Southeast (Mercury) Vent Field (DR-85, 88, 89, 110), and five sample suites from the Southwest Vent Field (DR-102, 112, 113, 120, 121).

The recovered samples were grouped into 10 lithofacies based on clast type, clast size, and alteration mineralogy (Table 4.1). These include syneruptive to re-sedimented volcaniclastic rocks of variable grain size and clast type, as well as massive anhydrite, native sulfur mud, and charcoal. Macroscopic alteration mineralogy was broadly subdivided into two end-member types: a clay-rich, silica poor facies and a clay-poor, amorphous silica-rich facies. Clay alteration, and spatially associated native sulfur, is the dominant alteration observed in the NVF; this alteration facies was recovered in smaller quantities from the SEVF and SWVF. X-ray amorphous silica is abundant in the SEVF and SWVF were it cements volcaniclastic material. Sulfide mineralization is associated principally with silicified samples and includes pyrite veins, stibnite needles filling pore spaces, cinnabar crusts, and amorphous arsenic sulfide minerals impregnating the ash matrix. Amorphous arsenic sulfides are also observed in the matrix of clay-rich, silica-

poor, lapilli tuff samples from the SWVF. Amorphous silica precipitation and associated As, Sb, Hg mineralization was not observed in rocks recovered from the NVF

Sixty-two rock samples were analyzed petrographically using both transmitted and reflected light. Bulk and clay mineralogy were determined using X-ray diffraction (XRD), and shortwave infrared reflectance (SWIR) spectroscopy at the Geological Survey of Canada (GSC).

Polished thin sections and grain mounts were analyzed using a Zeiss EVO 50 series scanning electron microscope (SEM) with extended pressure capability (up to 3000 Pa) at the GSC. The instrument is equipped with a backscattered electron (BSE) detector, an Everhart Thornley secondary electron detector, a variable pressure secondary electron detector, a cathodoluminescence detector and an Oxford energy dispersive spectrometry (EDS) system.

	Lithofacies	Samples (vent field)	Characteristics	Primary Minerals	Mineralization	Alteration
	Least altered vitric ash	DR-110wp (SE)	White powdery, non-silicified vitric ash, contained within silicified vitric ash samples	-	-	Least Altered
Silicified, clay poor	Silicified crystal tuff	85 a , b, c, d, -5a, -5b, -5c, 88, 89-02a, 02b (SE),	Crystal ash with vitric shards and pumice	Qtz, Plag, Py, For (minor), Zir (tr), Bar (minor)	Cinn and stb crusts, stb veins, As rich matrix (85a, c, 120, 121).	Amorphous silica cements ash with trace illite; 85a, 120, 121 contains Na-Ca smectite altered ash and amorphous silica
Silicified, clay poor	Silicified crystal tuff with native sulfur	85-06, 89c (SE), 102-05 (SW)	Crystal ash with coarse S°-cemented vitric ash (channel fill)	Qtz, Plag, barite (minor)	-	Amorphous silica cemented ash with illite (tr) and IS (102-05)
Silicified, clay poor	Silicified vitric tuff	110 c , d, e, i, j (SE)	Vitric ash with minor crystal component cemented by amorphous silica	Qtz, Plag	Py veins with sph and cinn inclusions	Amorphous silica cements ash and lines veins. S° in fractures adjacent to veins
Silicified, clay rich	Hydrocarbon rich vitric-crystal tuff	110b (SE) , 113c, d (SW)	Interbedded vitric tuff and crystal ash with liquid hydrocarbon and wood fragments	Qtz, Plag, Py, Zr (tr)	-	Na-Ca smectite and illite (tr) altered glass cemented by amorphous silica
Silicified, clay rich	Barite-rich silicified tuff	112a , 112b, c, 112d, 120, 121 (SW)	Crystal – vitric ash with abundant barite in pore spaces, silicic blocks observed in DR-112 samples	Qtz,	Stb lines fractures , patchy amorphous As sulfide	Na-Ca smectite altered ash and barite laths cemented by amorphous silica

Table 4.1. Calypso lithofacies, alteration mineralogy, and mineralization. Vent fields: N = North Vent Field; SE = Southeast Vent Field; SW = Southwest Vent Field. Qtz = quartz; Plag = plagioclase feldspar; For = forsterite, Zir = zircon, Py =pyrite, Marc = marcasite; Sph = sphalerite; Cinn = Cinnabar; Stb = stibnite; As = Arsenic; Tit = Titanite; S° = native sulfur; IS = interlayer illite-smectite; Msv = massive; tr = trace.

	Lithofacies	Samples (vent field)	Characteristics	Primary Minerals	Mineralization	Alteration
Clay altered	Clay altered lapilli tuff	97-4, 81–82 GTVA (N)	Glassy pumice variably altered to white clay in ash matrix	Qtz, Plag, Py, Marc, Sph (tr)	-	Na-Ca smectite replacing glass
	Clay altered lapilli tuff with native sulfur	95a, 98-02a, -02b , -07a, -07b (N), 110k (SE), 113b, 113-05 (SW)	Glassy pumice variably altered to white clay in cemented ash (clay-sulfur-palgonite matrix); S° lining primary pore spaces	Qtz, Plag, Py	-	Na-Ca smectite replacing glass, with minor illite, mixed-layer clay or vermiculite and talc (110k)
Other	Cherty silicified siltstone	118-04 (N)	Fine-grained silicified siltstone with cherty horizon	Qtz, Plag, Tit.	-	Amorphous silica cemented ash
	Charcoal	113-06 (SW)	Msv charcoal wood fragment	-	Py silica vein	S° in fractures
	Sulfur Mud	89a (SE)	Massive S° mud	-	-	-
	Anhydrite	DR-97 (N)	Msv laminated anhydrite – gypsum	Anh - Gyp	-	-

Table 4.1 (continued). Calypso lithofacies, alteration mineralogy, and mineralization. Vent fields: N = North Vent Field; SE = Southeast Vent Field; SW = Southwest Vent Field. Qtz = quartz; Plag = plagioclase feldspar; For = forsterite, Zir = zircon, Py =pyrite, Marc = marcasite; Sph = sphalerite; Cinn = Cinnabar; Stb = stibnite; As = Arsenic; Tit = Titanite; S° = native sulfur; IS = interlayer illite-smectite; Msv = massive; tr = trace.

4.1 Macroscopic, Petrographic, and SEM Observations of Recovered Samples

4.1.1 Clay-altered lapilli tuff and clay-altered lapilli tuff with native sulfur

Lapilli-sized volcaniclastic material comprises the primary rock type recovered from the NVF (81-82 GTVA, DR-95a, -97-4, -98,) with fewer samples of this type dredged from the SEVF (DR-110k) and the SWVF (DR-113b, -05). Least-altered samples (81-82 GTVA, DR-97-4; Plate 4.1b) are sulfur poor and are comprised of weakly lithified, glassy, juvenile fragments variably altered to soft, pale-grey clay (Plate 4.2 A, B) and cemented by a palagonite/clay ash matrix. Sulfur-impregnated pumice lapilli (DR- 95, Plate 4.1E; DR-98 series, Plate 4.1C, Plate 4.1D; DR-110k, Plate 4.5F; DR-113b, Plate 4.5D; and DR-113-05, Plate 4.5C) are intensely altered to soft hydrated clay; air drying of these samples has caused dessication cracks and contraction of the clay-altered lapilli in some samples (e.g., DR-98, Plate 4.1D.

Scanning electron microscope (SEM) backscatter electron images (BSE) show that the clay has a crenulated appearance (Plate 4.7B). Sulfur is observed rimming the margin and filling void space within clay-altered clasts (Plate 4.7A).

Juvenile pumice volcaniclastic fragments are the primary clast component with lesser quartz-plagioclase porphyry and mudstone lithoclasts. Massive, yellow, native sulfur fills the primary pore spaces of pumice vesicles and rock fractures, causing cementation of clasts in some samples (Plate 4.1C). Clasts are generally matrix supported with rare sedimentary structures (i.e., crossbedding, DR-113b; Plate 4.5D) indicating a volcaniclastic flow or a re-sedimented volcaniclastic origin. Matrix material is a mixture of fine-grained clay-altered ash, palagonite, and native sulfur (Plate 4.2). Primary igneous crystals of quartz and plagioclase, together with pyrite are observed within clasts, and within the ash matrix (Plate 4.6F). Volatile metal mineralization was generally absent from the clay-altered lithofacies; however the orange coloration of sample DR-113b (Plate 4.5C) is likely arsenic sulfide (see Table 6.1). This sample was recovered from the SWVF where As and Sb mineralization was abundant.

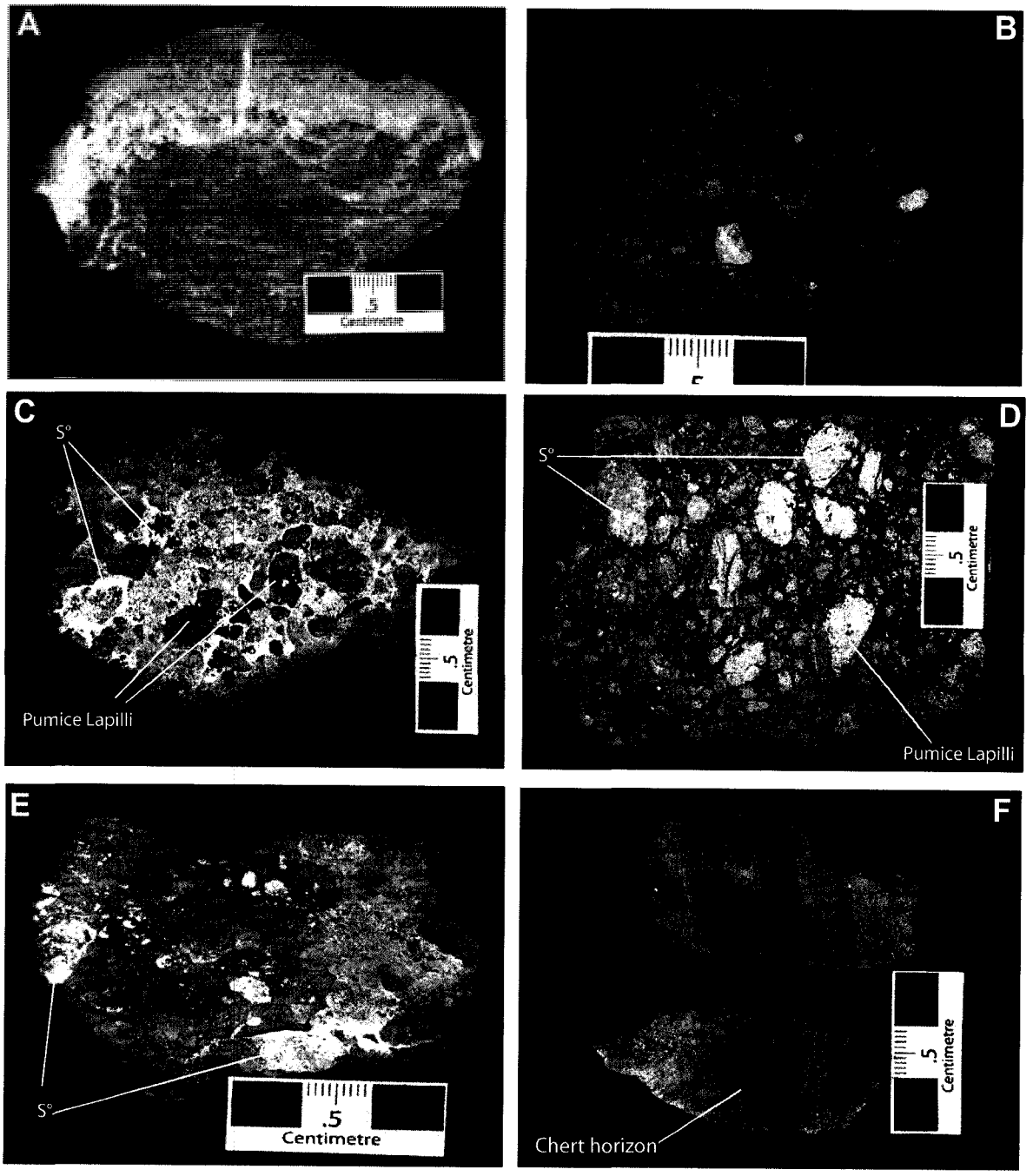

Plate 4.1. Macroscopic features of selected rocks from the North Vent Field. The black scale boxes are 1cm in length. A. Massive laminated anhydrite and gypsum on fine-grained clay altered volcanic substrata (DR-97). B. Weakly lithified, least clay-altered lapilli tuff (DR-97-4). C. Clay-altered pumiceous lapilli cemented by sulfur-clay matrix and massive yellow native sulfur (DR-98-2a). D. Soft, pale-grey, clay-altered pumiceous clasts cemented in fine-grained clay matrix; pumice vesicles are filled with native sulfur. Dessication cracks suggest the presence of smectite (DR-98). E. Dark-grey, clay-altered, pumice clast cemented in pale-grey, clay-altered, matrix and yellow, sulfur-rich, clay-altered matrix; massive native sulfur fills pumice vesicles (DR-95a). F. Silicified tuff with chert bed (DR-118-04).

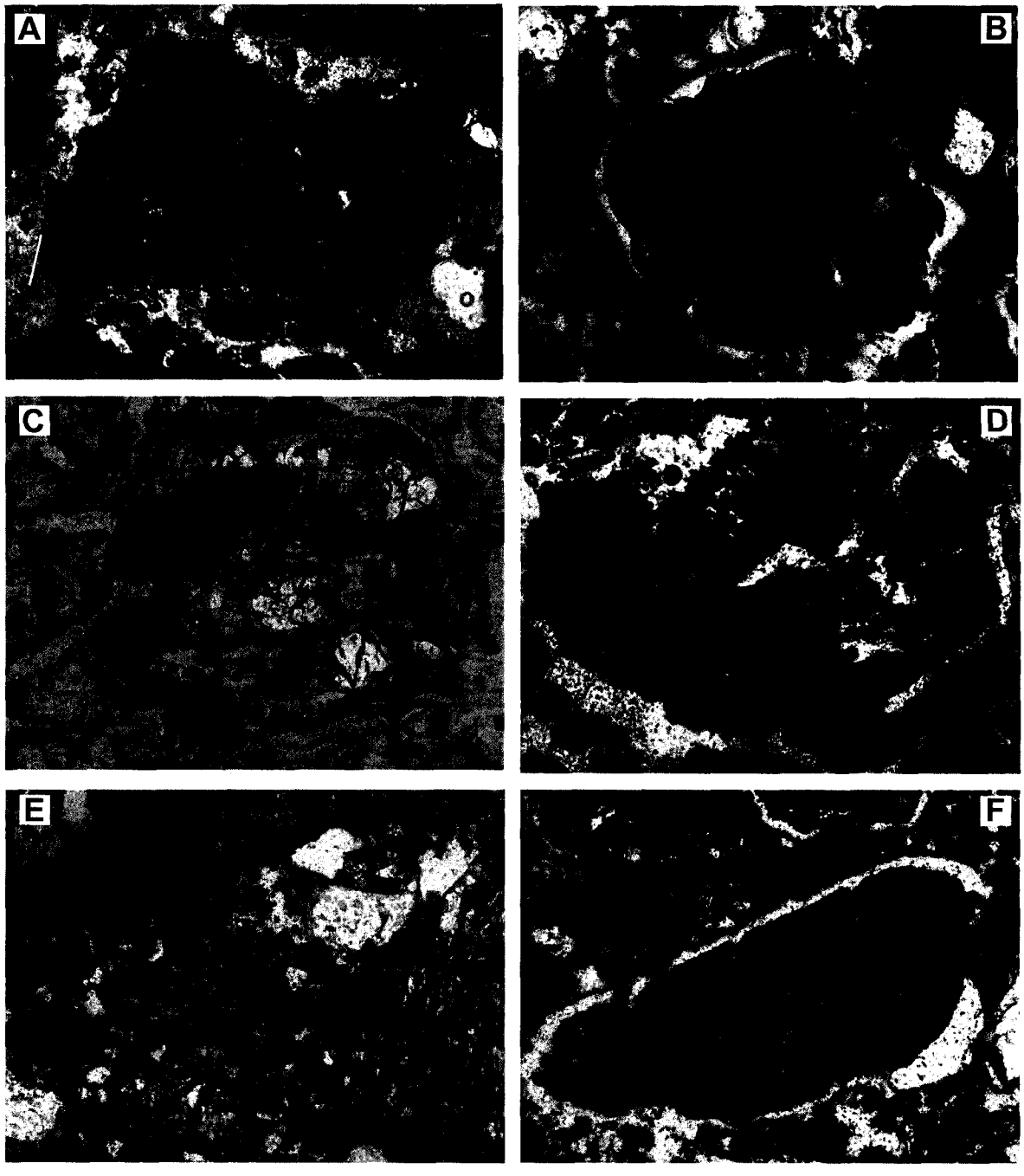

Plate 4.2. Selected photomicrophaphs of variably clay altered lapilli tuff samples from the NVF (field of view = 1.5 mm; transmitted light). Alteration of glass to white smectite clay is observed as a brown felted texture in thin section. Yellow translucent matrix material is believed to be palagonite; a poorly crystalline phase intermediate between volcanic glass and smectite; native sulfur contributes to the yellow coloration in plates D, E, and F. A. Lapilli altered to white clay with felted texture (DR-97-4). B. Clay-altered lapilli in palagonite matrix (DR-97-4). C. Glassy pumice lapilli partialy altered to white felted clay (DR-98-2a). D. Intensely clay-altered lapilli (DR-98). E. Quartz, feldspar, and vesiculated clasts cemented by palagonite-native sulfur matrix (DR-95a). F. Clay-altered volcanic clast (DR-95a).

4.1.2 Silicified tuff

Silicified ash samples were recovered from the SEVF and SWVF, and have been subdivided into a silicified crystal tuff lithofacies (Plate 4.3 A-D) and a silicified vitric tuff lithofacies composed of dominantly juvenile vitric particles (Plate 4.3 E, F; Table 4.1).

Crystal tuff samples (DR-85a, -85b, -85c, -85d, -85-5a, 85-5b, 95-5c, 88, 89-02a, 89-02b) recovered from the SEVF are comprised of quartz and plagioclase grains with subordinate, variably clay-altered, glassy pumice fragments, and minor pyroxene (Plate 4.4 A, B, C). Cinnabar forms crusts on the outer surfaces of two crystal-tuff samples (DR-85a; Plate 4.3B; DR-85c; Plate 4.4D). SEM-BSE images show narrow arcuate cinnabar veins with amorphous silica margins and silica pseudomorphs of barite are observed within the cinnabar vein (Plate 4.7F). Plate 4.7F illustrates the distribution of crystal clasts cemented by dark grey amorphous silica; irregular lines are similar to dessication cracks indicating the presence of swelling clay (i.e., smectite).

In the silicified crystal tuff samples with native sulfur (DR-85-06, -89c, -102-05) the sulfur lines the cavities and fills pore space of coarse volcaniclastic material. Sample DR-89c, composed of fine-grained tuff, contains a tube-like channel structure filled with coarse clastic material cemented by native sulfur (DR-89c; Plate 4.3C).

Silicified vitric tuff samples (DR-110c, -110d, -110e, -110i, -110j) recovered from the SEVF are composed of densely packed glass shards with cuspate shapes, and bubble-wall textures, which likely represent fracturing of bubbles during hydroclastic processes or physical attrition of pumice (Plate 4.4E, Plate 4.7C; Fisher and Schmincke, 1984). Clay alteration of the glass shards is minimal and primary quartz, plagioclase, and pyroxene crystals are rare. Amorphous silica has filled the primary pore spaces between the glass shards making the samples dark grey in colour and well indurated (Plate 4.3E, F; Plate 4.7C). Irregular patches of weakly cohesive, amorphous, white powder (DR-110wp) represent areas of non-silicified vitric ash. Silica conduits form erosion resistant tubes within the non-silicified ash (Plate 4.3E), and erosion of non-silicified ash has created a cast of irregular-shaped silica conduits and silicified fractures (Plate 4.3F). Sulfur is present in fractures (Plate 4.4E) and in silica – pyrite – sulfur veins which are observed in several silicified vitric ash samples (e.g., DR-110D, -110E, Plate 4.3E). Sulfur fills the space between the pyrite and wall rock and is enveloped by amorphous silica (Plate 4.4F). An SEM-BSE image shows a massive amorphous silica halo extending from the vein approximately 2 mm into silicified ash; pyrite inclusions are present in the amorphous silica vein margin (Plate 4.7D). Small inclusions of cinnabar and zoned sphalerite with cinnabar rims occur within the pyrite veins (Plate 4.7E).

Organic rich, crystal tuff samples were recovered from the SEVF and SWVF (DR-110b, -113c, 113d; Plate 4.5E). Wood fragments are observed in coarser beds and liquid hydrocarbon coats the surface of primary crystals and pumice fragments (Plate 4.6E).

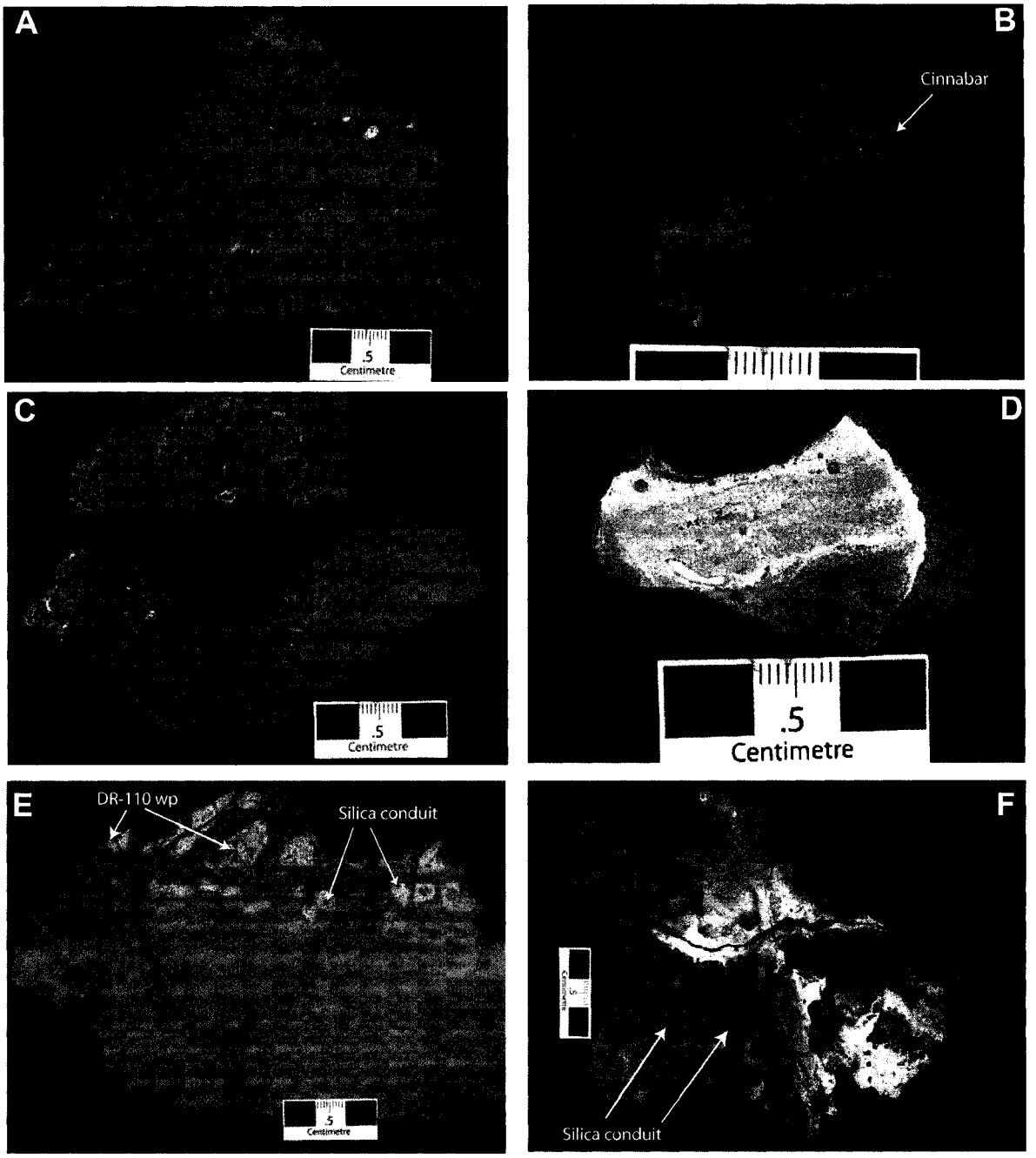

Plate 4.3. Macroscopic features of the rocks recovered from the SEVF. The black boxes are 1 cm in length. A. Quartz-plagioclase crystal tuff with glassy pumice clasts cemented by amorphous silica matrix, minor jarosite staining on sample surface (DR-85-5b). B. Silicified quartz-plagioclase crystal tuff with cinnabar crust (DR-85a). C. Fine-grained crystal ash with channel structure filled with coarser, variably clay-altered, volcanic clasts cemented by native sulfur (DR-89c). D. Channel structure in crystal ash filled with native sulfur mud (DR-89a). E. Silicified vitric tuff with patchy zones of white, non-silicified ash (DR-110 wp) and silica-sulfur-pyrite veins (DR-110) F. Silicified vitric ash. Amorphous silica lined fluid conduits are exposed after weathering of non-silicified ash (DR-110i).

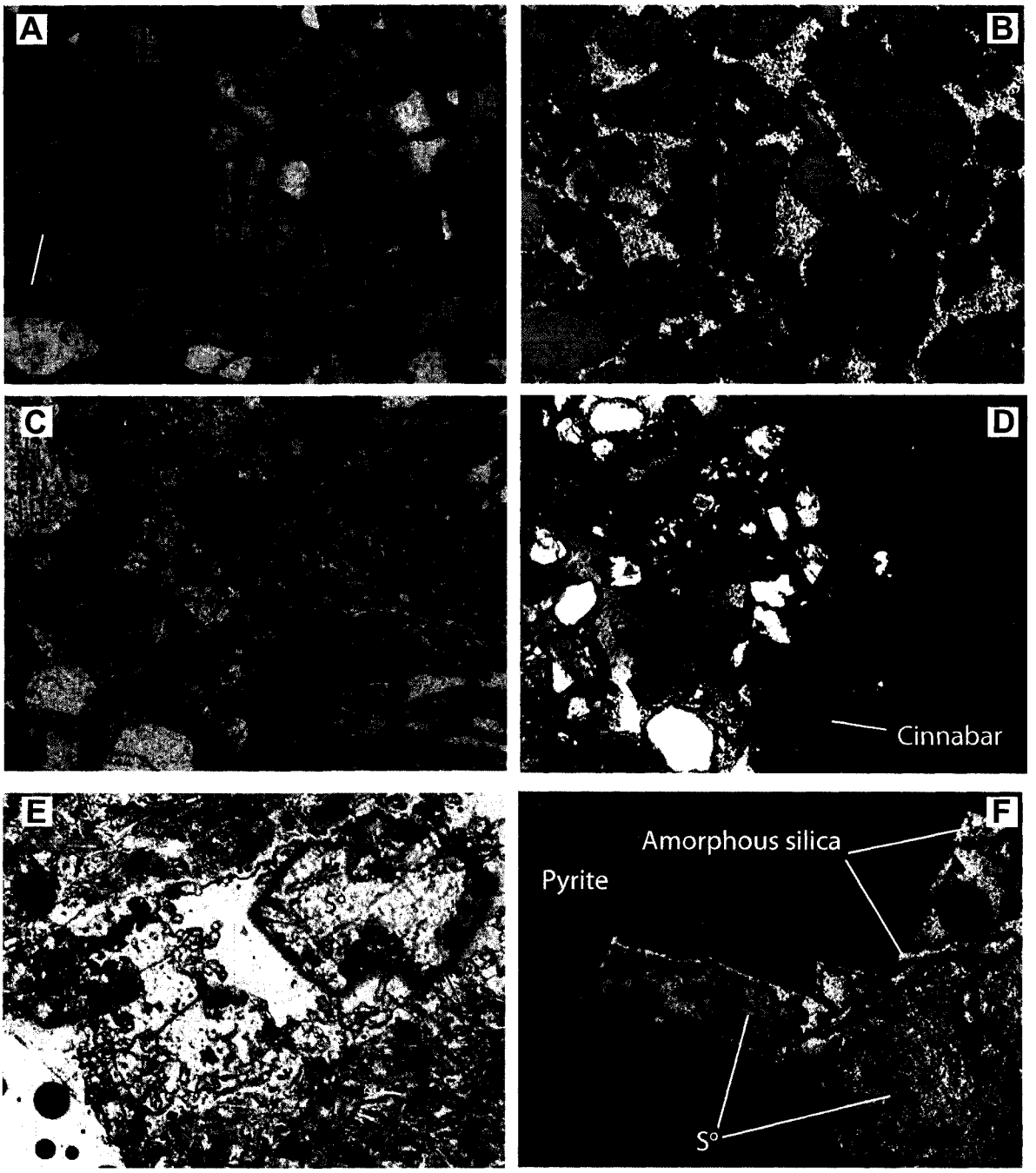

Plate 4.4. Photomicrophaphs of SEVF samples, field of view is 1.5 mm. A. Quartz, plagioclase, crystal ash with rare pumice clasts in felted brown clay-silica matrix viewed with transmitted light (DR- 85-6). B. Photo A viewed with plane polarized reflected light (DR-85-6). C. Quartz-plagioclase crystal ash with glassy pumice clast and clay-altered volcanic clasts (DR-85d; transmitted light). D. Cinnabar crust on margin of quartz and feldspar crystal ash (DR-85c; plane polarized reflected light). E. Native sulfur filling fracture in silicified vitric tuff (DR-110d; field of view = 4mm, transmitted light). F. Sulfur-pyrite-silica vein cutting silicified vitric ash. Silica fills pore space between sulfur and pyrite (DR-110E; transmitted light).

4.1.3 Barite-rich, silicified tuff, with volcanic blocks

Barite-rich, silicified tuffaceous rocks were recovered from the SWVF (DR-112, Plate 4.5A; DR-120, -121, Plate 4.5B). Samples are comprised of variably altered and rounded volcanic clasts, pumice, and quartz crystals. Barite laths are randomly oriented in the primary pore spaces of the volcaniclastic rocks and occur in both pumice-rich samples (Plate 4.5D) and in crystal-rich ash with quartz, plagioclase, and clay-altered juvenile volcanic particles (Plate 4.6A). Barite occurs in both non-silicified (Plate 4.8A) and silicified portions (Plate 4.8B). Large vuggy silica clasts are cemented in the sample by amorphous silica and are believed to be accidental in nature (Plate 4.5A).

Abundant orange arsenic sulfide and black stibnite are observed in the matrix of the barite-rich silicified lithofacies (Plate 4.5A, B). Stibnite radiates from cavities (Plate 4.6B), is observed overgrowing barite laths (Plate 4.6C), and filling fractures in silicified material (Plate 4.8E). Similarly, arsenic sulfides line fractures (Plate 4.6D) and are overgrown by stibnite needles (Plate 4.8D, 4.8E). The arsenic sulfide has a distinctive collomorphous habit (Plate 4.8F).

4.1.4 Other lithofacies

Massive, laminated anhydrite and mounds (Plate 4.1A), cherty siltstone (Plate 4.1F), sulfur mud (Plate 4.3D), and charcoal samples were also recovered from the CHVF.

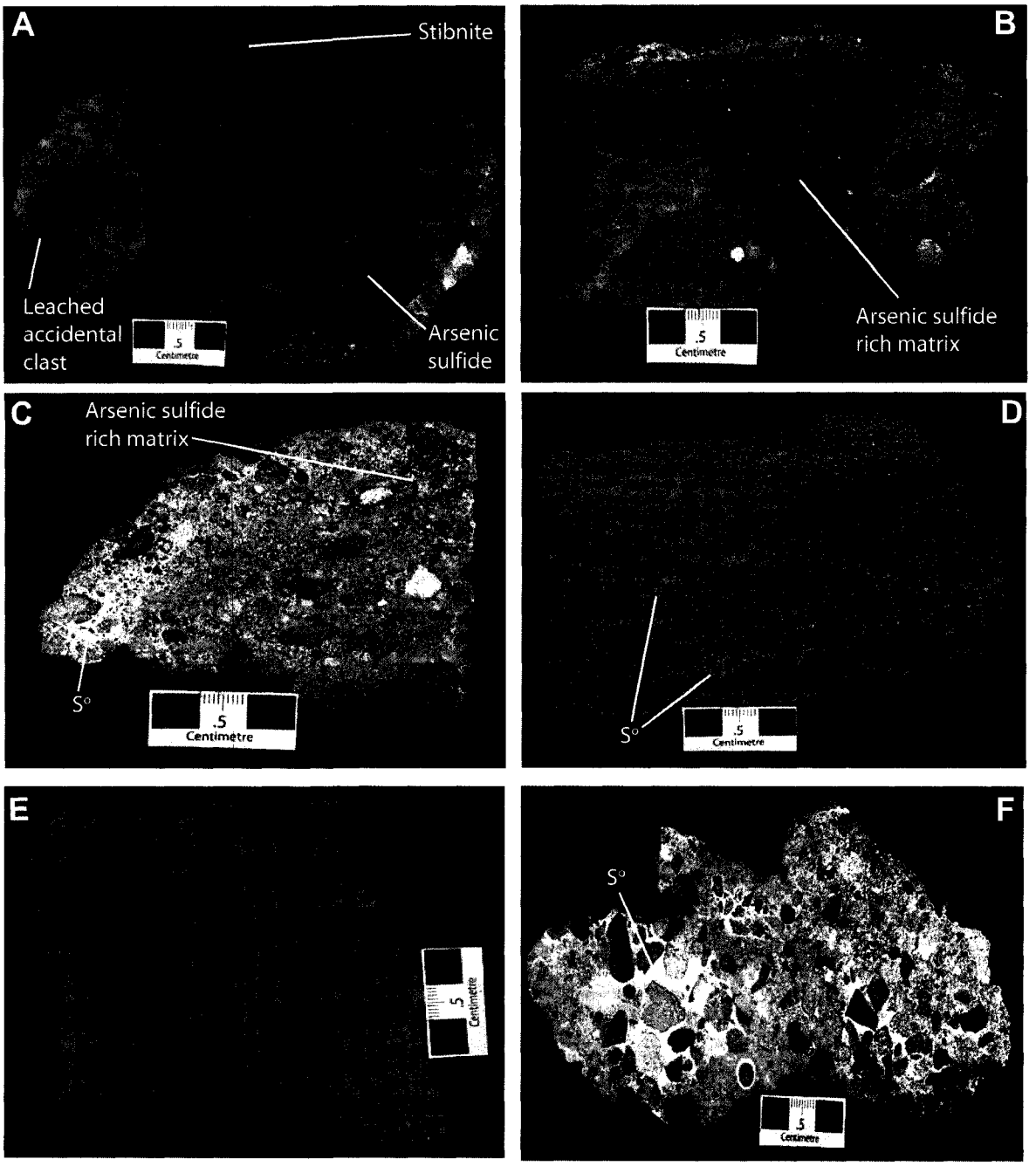

Plate 4.5. Macroscopic features of selected rocks from the Southwest Vent Field (A-E). The black scale boxes are 1cm in length. A. Amorphous arsenic sulfide (yellow orange), stibnite (black) and barite-impregnated silicified ash with few silicic lapilli clasts and rare leached, silicic clasts believed to be accidental in origin (DR-112) B. Amorphous arsenic sulfide and barite-rich silicified ash (DR-121). C. Clay-altered lapilli cemented by amorphous arsenic sulfide (orange)-rich clay and massive native sulfur matrix (DR-113-05). D. Cross-bedded epiclastic sedimentary rock comprised of clay-altered pumice lapilli cemented by a clay-sulfur matrix (DR-113b). E. Hydrocarbon-rich fine-grained tuff inter-bedded with coarser crystal tuff layers; native sulfur is present on some bedding planes (DR-113d). F. Clay-altered lapilli tuff cemented by sulfur-clay matrix and massive yellow native sulfur; sample recovered from the Southeast Vent Field (DR-110k).

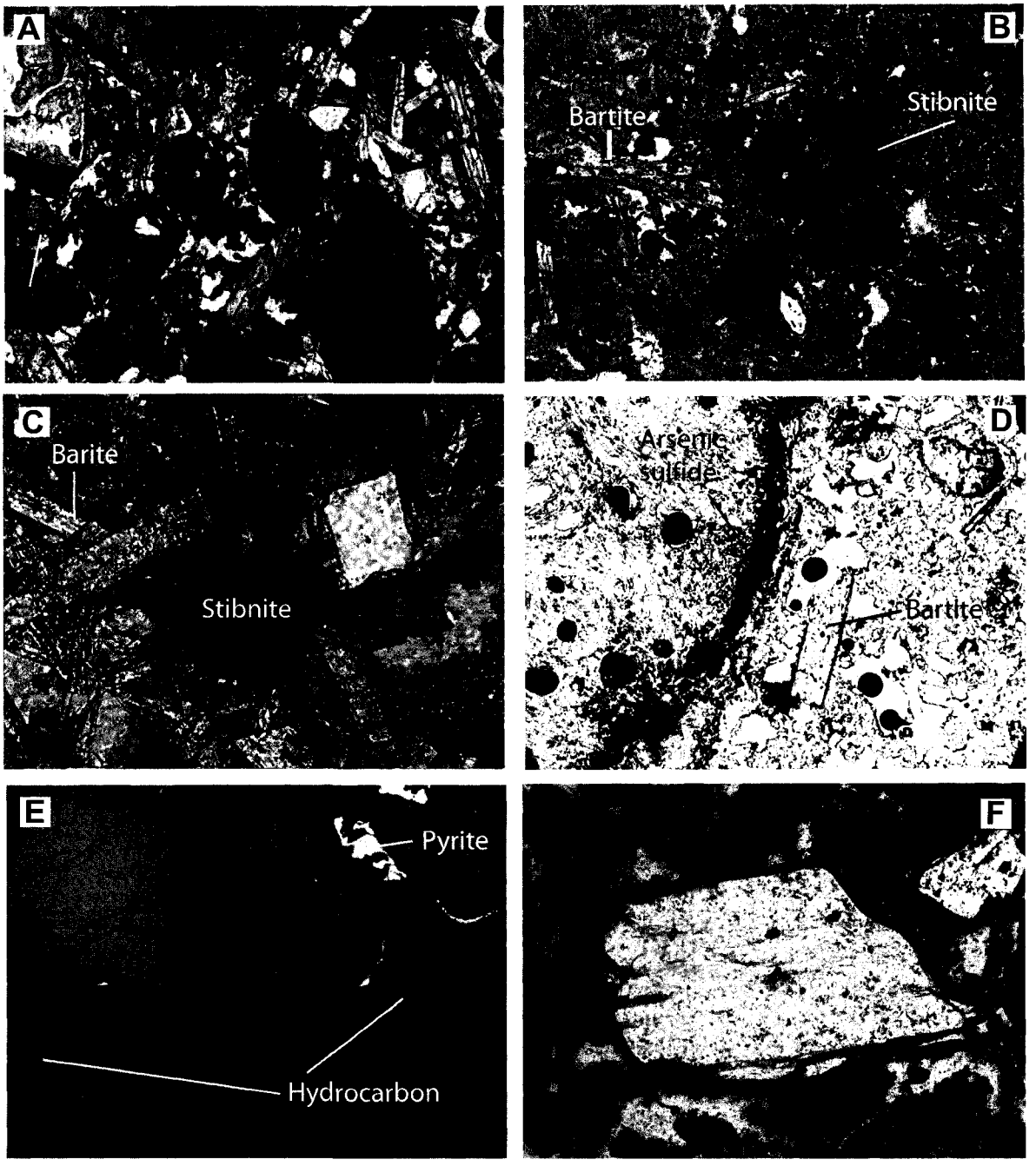

Plate 4.6. Selected photomicrophaphs (field of view = 1.5 mm; transmitted light) of SWVF samples. A. Rounded, quartz-phyric, volcanic clasts altered to brown clay; barite laths fill pore spaces and are overgrown by radiating stibnite needles (DR-120a). B. Black stibnite needles and barite laths filling pore spaces of silicified ash (DR-112e). C. Barite laths in fine grained matrix overgrown by stibnite needles (DR-112d; field of view 2.2 mm). D. Glassy pumice with amorphous arsenic sulfide on fracture surface and barite in primary pore spaces (DR-112e). E. Quartz crystals and pumice clasts rimmed by pyrite and coated with liquid hydrocarbon, in hydrocarbon-rich tuff (DR-113d; plane polarized reflected light). F. Plagioclase crystal and clay-altered glass (brown) cemented by palagonite and native sulfur in lapilli tuff (DR-113-05).

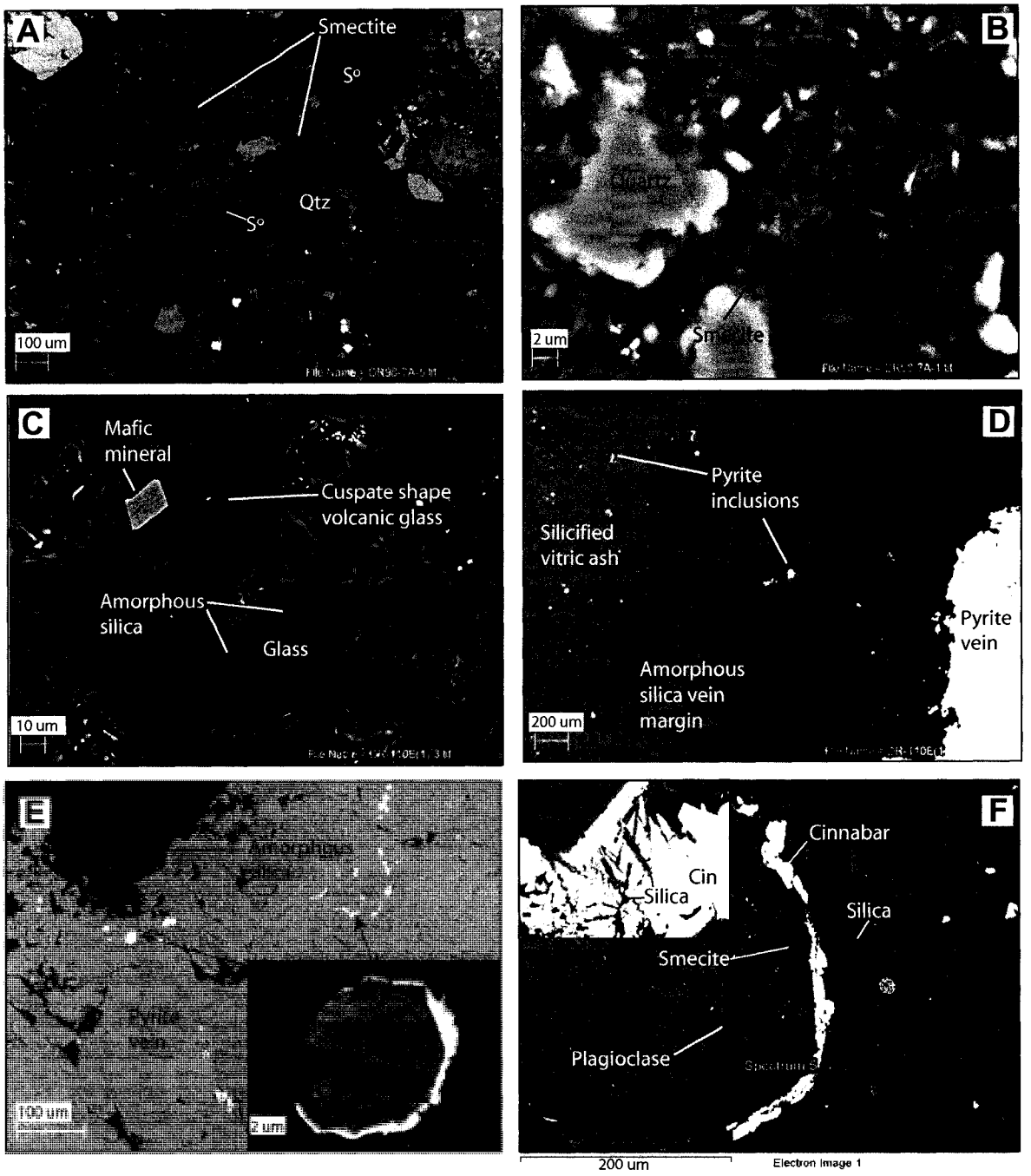

Plate 4.7. SEM-BSE images. A. S° rims the margin and fills pore spaces of smectite-altered pumice lapilli, with few primary igneous phenocrysts (DR-98-7a). B. Crenulated smectite from a clay-altered pumice lapilli (DR-98-7a). C. Silicified vitric tuff (DR-110e). D. Pyrite vein with amorphous silica halo cutting silicified vitric tuff. Pyrite grains contained within amorphous silica indicating the two phases are contemporaneous (DR-110e). E. Cinnabar occurs as inclusions in pyrite vein and rims sphalerite inclusions (DR-110e). F. Clay-rich crystal tuff with clay dessication cracks and irregular amorphous silica banding coating clast rims. Arcuate cinnabar vein is lined with amorphous silica; silica pseudomorphs barite laths within cinnabar vein (top left; DR-85a).

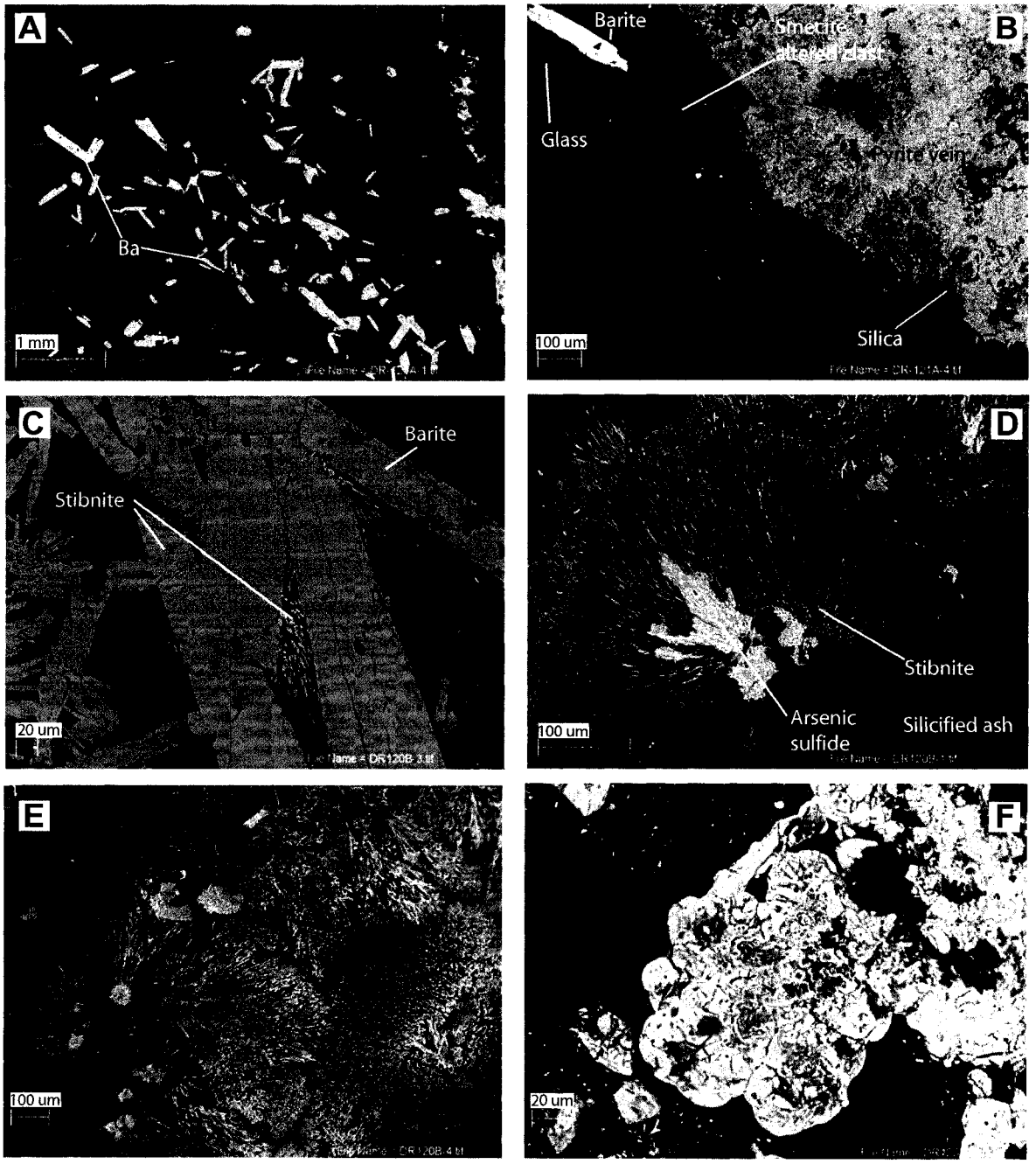

Plate 4.8. SEM-BSE images of selected sulfide and sulfate textures. A. Barite laths appear to be randomly oriented between primary quartz and plagioclase, igneous crystals (DR-121). B. Pyrite vein contact with silicified, crystal and vitric, tuff with barite laths; silica rims pyrite vein (DR-121). C. Barite laths overgrown by stibnite (DR-120). D. Stibnite vein contact with silicified vitric-crystal tuff; stibnite is overgrowing arsenic sulfide mineral (DR-120). E. Radiating stibnite needles fill a fracture, overgrowing primary igneous minerals and arsenic sulfide (DR-120). F. Amorphous As sulfide with colloform banding (DR-120).

4.2 Hydrothermal Mineral Paragenesis

Paragenetic relationships can be established from pyrite-sulfur-silica veining observed in silicified vitric tuff samples (Plate 4.3E, 4.4F, 4.7D, 4.7E). Massive pyrite contains inclusions of cinnabar and sphalerite, and a massive amorphous silica halo extends from the edge of the pyrite vein and grades into silicified vitric tuff. Pyrite is also observed as inclusions within the silica halo. These relationships suggest silicification was both early and contemporaneous with pyrite veining. Sulfur contained in the vein adjacent to the pyrite is enveloped by amorphous silica (Plate 4.4F) but is also observed filling fractures without amorphous silica (Plate 4.4E) suggesting sulfur precipitated prior to silicification. Where silicification was pervasive, it reduced porosity and limited the influx of hydrothermal fluid and gas. Limited clay-alteration in the silicified lithofacies (i.e., samples DR-85a, DR-102-05, DR-110b, DR-112, and DR-113c) suggests that clay alteration occurred prior to silicification. SEM-BSE analysis of barite-rich samples indicates that barite growth occurred between clastic particles prior to silicification (Plate 4.8A); barite is also observed cemented within clastic particles by amorphous silica (Plate 4.8B). Silica with a lath-shaped habit is observed within cinnabar veins; the lath shaped features represent silica pseudomorphs of early barite (Plate 4.7D). Arsenic and antimony sulfide mineralization is observed along fractures (Plate 4.6D) and radiating from pore spaces (Plate 4.6B). SEM-BSE images show arsenic sulfide overgrown by stibnite needles which radiate outward from the margin of silicified tuff into open fractures (Plate 4.8D). Stibnite needles are observed overgrowing barite laths (Plate 4.6C, 4.8C). Cinnabar forms crusts on the outer margins of two samples (DR-85a, Plate 4.3B; DR-85c; Plate 4.4D) and

forms rare veinlets (Plate 4.7F). Arsenic and antimony concentrations show a strong correlation, mercury does not correlate well with other volatile metals. A summary paragenetic mineral sequence is shown in Figure 4.1.

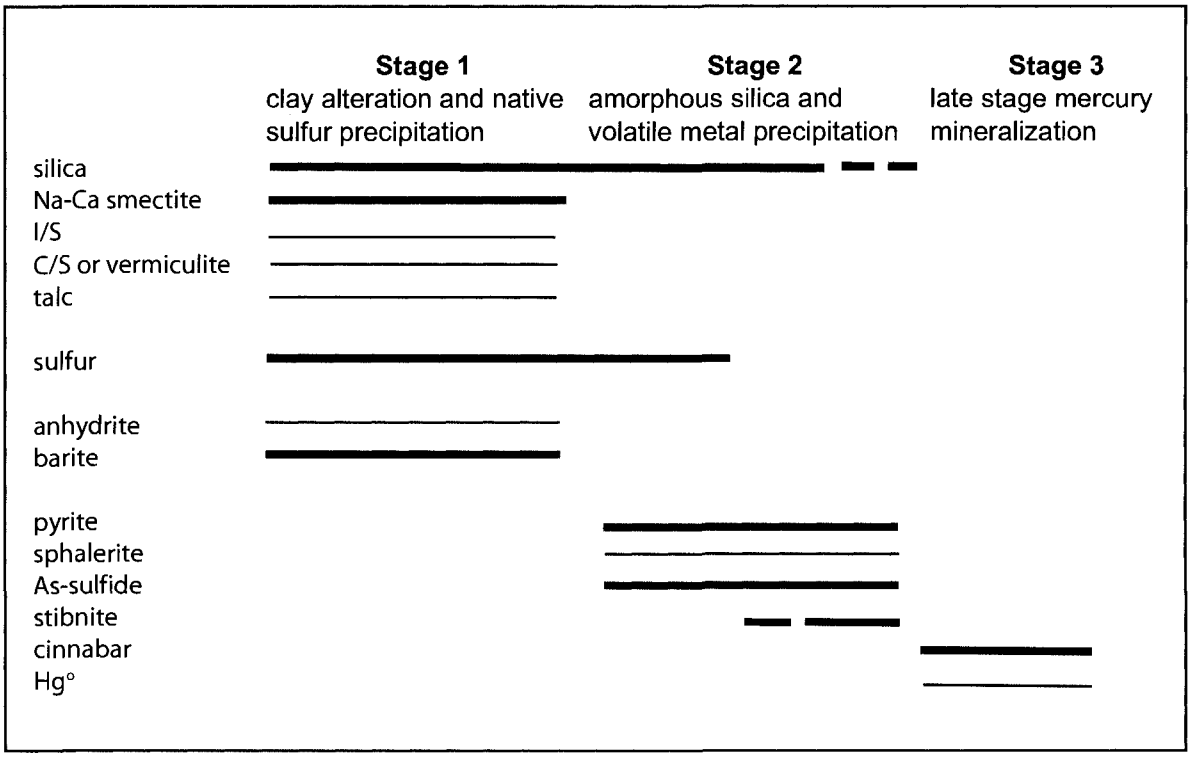

Figure 4.1. Interpreted paragenetic sequence of alteration minerals, metalic sulfides, sulfates, and liquid mercury at Calypso. The width of the black bars indicates the relative abundance of each mineral phase. I/S = mixed-layer illite-smectite; C/S = mixed-layer chlorite-smectite.

5.0 Clay Mineralogy

Macroscopic observations indicate that the recovered sample suite can be broadly subdivided into a clay-poor silicified lithofacies and a clay-altered, silica-poor lithofacies. Clay-altered samples consist primarily of pale grey, weakly-lithified clay which is commonly associated with abundant native sulfur. Dessication cracks have been observed in some of the samples indicating the presence of smectitic clay. X-ray diffraction (XRD) and short wavelength infrared reflectance (SWIR) spectroscopy have been used to identify clay mineral species. Analytical electron microprobe (AEM) analyses have been conducted to determine the composition of the clay minerals.

5.1 X-Ray Diffraction

5.1.1 Methods

The whole-rock and clay mineralogy was determined by oriented X-ray diffraction analysis (XRD) at the Geological Survey of Canada. Whole-rock geochemical pulps were mixed with ethanol and ground to approximately 5 μm using a McCrone model vibratory mill. Forty milligrams of the milled material was then mixed with distilled water and transferred to a glass slide with a pipette and allowed to dry at room temperature. Step-scan XRD data of the oriented slides were collected with a Bruker D8 Advance Powder Diffractometer equipped with a graphite monochromator (5-86° 2θ, 0.04 ° 2θ stepwidth, 4 s/step). A Co tube was used and operated at 40 kV and 40 mA. Samples were then X-rayed after ethylene glycol saturation, and again after a heat treatment at 550 °C for 2.5 hours. The XRD patterns were processed and identified with JADE software in

conjunction with the Powder Diffraction File (PDF) database of the International Centre for Diffraction Data (ICDD).

5.1.2 Results

Mineralogy results are reported in Table 5.1 and representative X-ray patterns are plotted in Figure 5.1. X-ray diffraction analysis of the oriented samples revealed that smectite is the dominant alteration mineral in the clay-rich pumice lapilli lithofacies. Diffraction patterns of the untreated air-dried samples show broad d001 peaks ranging from 13.2Å to 14.48Å (Figure 5.1A). Glycol solvation of the samples caused a shift of this peak to higher spacing, ranging from 16.23 Å to 17Å. Glycol solvation-induced swelling of the interlayer unit is characteristic of smectitic clays (Moore and Reynolds, 1989). Heat treatment collapses the d001 peak to approximately 10Å, which is similar to the d001 peak for illite. The observed discrepancy of the first order, basal reflection, d-spacing between samples is caused by variation of interlayer water molecules (Giorgetti et al., 2006).

Although illite was recorded in only a few clay-altered pumice lapilli samples, it was detected in many of the silicified tuff samples. Illite has an ideal chemical formula of $K_{1.5\text{-}1.0}Al_4[Si_{6.5\text{-}7.0}Al_{1.5\text{-}1.0}O_{20}](OH)_4$ (Deer et al., 1992). Untreated, glycol-treated, and heat-treated samples show low intensity X-ray peaks at ~ 10 Å (Figure 5.1B). The low intensity indicates only trace quantities of illite are present in the samples. Smectite (~13.5 Å) and illite (~10 Å) are detected in eight samples (81-GTVA, DR-85c, 89-2a, 98-2b, 102-05, -110b, 113c, 113d). Glycol solvation of these samples caused the d001 smectite peak to shift to a higher d-spacing (~16.5 Å) with no change of the 10 Å illite X-ray peak (Figure 5.1C). Heat treatment caused a collapse of the d001 smectite peak to 10 Å as noted in the clay-rich pumice lapilli (Figure 5.1A). These samples may represent interlayer illite-

smectite (IS; Figure 5.1D) and/or a mixture of discrete illite and smectite (Figure 5.1C). The poorly crystalline nature of the illite and its low concentration inhibits illite crystallinity measurements.

Untreated diffraction patterns of sample DR-110k (Plate 4.5E) show first order reflections at 13.8 Å and do not show significant variation under glycol solvation (Figure 5.1E). Heating of the samples caused a collapse of the d001 peak. The ~ 9.4 Å peak showed no variation during glycol or heat treatment and was identified as talc. The three treatments indicate this sample contains either mixed-layer smectite-chlorite or vermiculite-chlorite. Additional analysis (e.g., Na, K saturation) are required to distinguish this phase.

Samples with significant volumes of volcanic glass and amorphous silica produced X-ray diffraction patterns with broad humps between approximately 20 and 40 °2θ (Figure 5.1F).

			X-ray Diffraction						SWIR
	Lithofacies	Samples	Smectite	C/S-Verm	I/S	Illite	Talc	Am.	
Clay Rich samples	Clay altered lapilli tuff	97-4 , 81-82 GTVA	X			tr			Mont.
	Clay altered lapilli tuff with native sulfur	95a, 98 series, 113b	X						Mont.
		110k		X			x		Verm.
		113-05			X				Mont.
Silicified, clay poor, samples	Crystal – vitric tuff	85a	x					x	Opal
		85c	tr			tr		X	
		85d						X	
		85b, 88 , 85-5a, 85-5b, 85-5c				tr		X	
	Crystal – vitric tuff	89-02a, 89-02b			x			X	Opal
	Crystal – vitric tuff w/ native sulfur	85-06						X	Opal
		89c				tr		X	
		102-05	X			x			
	Vitric – crystal tuff	110e, 110i, 110j, 110 WP						X	Opal
Silicified clay rich samples	Hydrocrabon rich vitric-crystal tuff	110b	X			x		x	Opal
		113c	x			x		x	
		113d			x			x	
	Barite-rich tuff	112 (a), (b,c), (d,e)	X					x	Opal
		120			x			x	
		121			x			x	
	Anhydrite	DR-97	x						-

Table 5.1. Clay minerals identified by oriented X-ray diffraction and SWIR spectroscopic analysis of CHVF samples. X = major, x = minor, tr = trace, - = not analyzed. Abbreviations: Am. =Amorphous X-ray pattern; I/S = mixed-layer illite-smectite; Mont.=montmorillonite; C/S - Verm = mixed-layer chlorite-smectite or vermiculite.

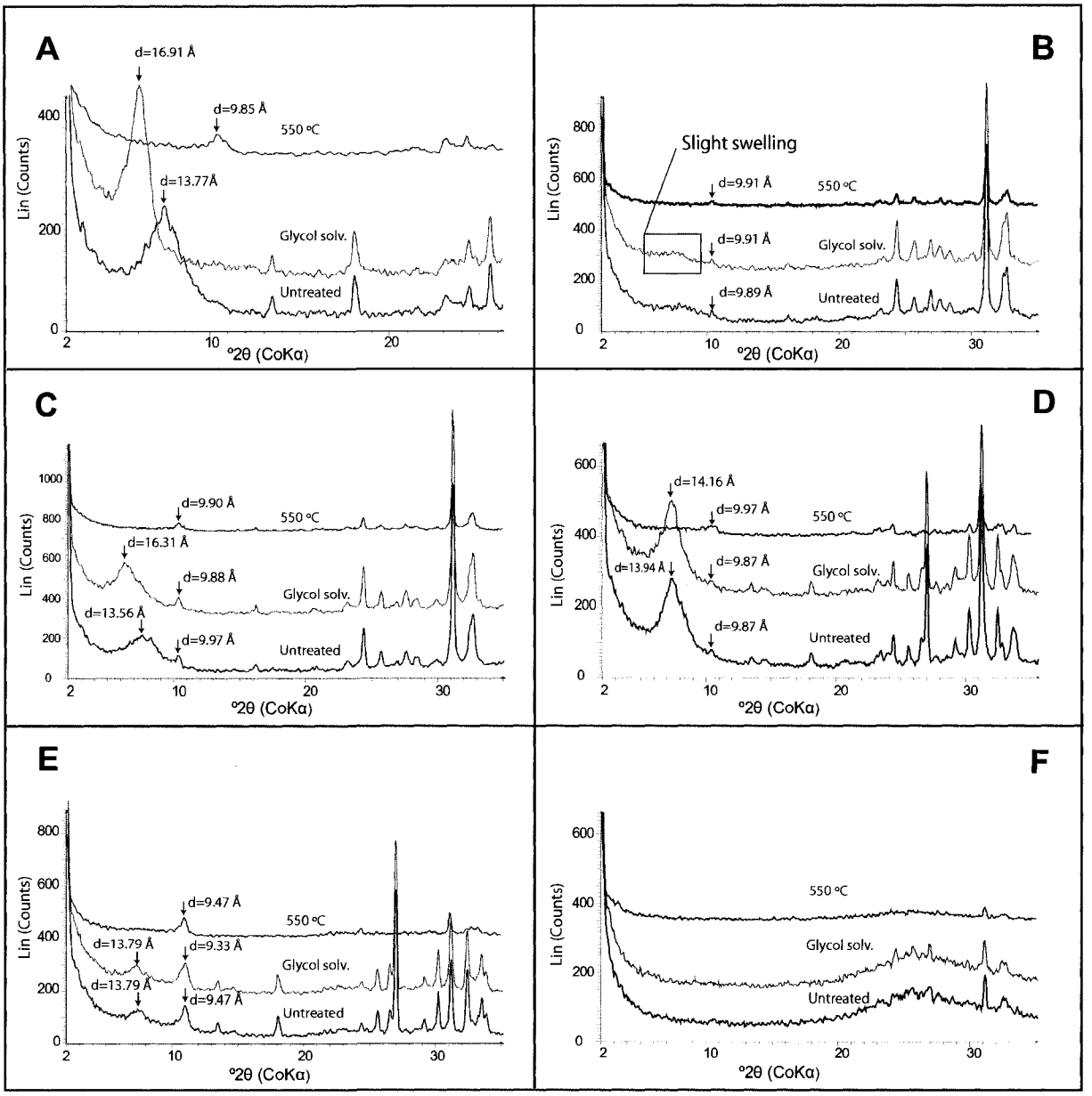

Figure 5.1. XRD patterns (oriented mounts) of six Calypso samples. A. Smectite rich sample (DR-98-7a; basal reflections: untreated = ~14 Å, ethylene glycol solvated = ~17 Å, heated to 550 °C =~10 Å). B. Trace illite (DR-113d; basal reflections: untreated= ~ 9.89 Å, ethylene glycol solvated =9.91 Å, heated to 550 °C = 9.91 Å) Slight swelling under glycol solvation indicates the presence of slight amounts of smectite or a mixed-layer clay. C. Smectite and illite (DR-113c; basal reflections: untreated= 13.56 Å and 9.97 Å, ethylene glycol solvated = 16.31 Å and 9.88 Å, heated to 550 °C = 9.90 Å). D. Mixed-layer smectite-illite (DR-113-05; basal reflections: untreated= 13.94 Å and 9.87 Å, ethylene glycol solvated = 14.16 Å and 9.87 Å, heated to 550 °C = 9.97 Å). E. Vermiculite or mixed-layer chlorite-smectite and talc bearing samples (DR-110k; basal reflections: untreated= 13.79Å and 9.47Å, ethylene glycol solvated = 13.79 Å and 9.33 Å, heated to 550 °C = 9.47 Å). F. Sample with significant amorphous component show broad hump shaped patterns between approximately 20 and 40 ° 2θ (DR-110e).

5.2 Short Wavelength Infrared Reflectance (SWIR) Spectroscopy

Spectral measurements were conducted with an Analytical Spectral Devices (ASD) Inc. Fieldspec® Pro spectroradiometer at the Geological Survey of Canada. Spectra were collected from whole-rock geochemical pulps and from clean, dry, rock slabs at room temperature. Duplicate measurements were made for each spectral reading; white reference and spectra standard measurements were taken every 10^{th} sample. The spectral range of the Fieldspec Pro covers a small portion of the ultraviolet region and extends to the near-infrared region (780 nm to 2500 nm) and has a spectral bandwidth of 3 to 10 nm and a scan time of 100 milliseconds. Spectra were processed using Viewspec® Pro software and the spectra were compared to a library of reference spectra using Specmin® software.

5.2.1 SWIR Principles

Shortwave infrared reflectance (SWIR) spectroscopy has been used extensively for mineral identification in the subaerial environment (e.g., Thompson et al., 1999; Yang et al., 2001; Jones et al., 2005); but has been applied infrequently in seafloor research (e.g., Paulick and Bach, 2006).

Infrared light is subdivided by wavelength into ultraviolet (UV) light (0.002 to 0.4 μm), visible light (0.4 to 0.7 μm), near-infrared (NIR) light (0.7 to 3.0 μm), mid-infrared (MIR) light (3.0 to 30 μm), and far infrared (FIR) light (30 μm to 1 mm) (Clark, 2004; Swayze, 2004). The term visible/near-infrared (VNIR or VIS-NIR) is used to describe the wavelength range from 400 to 2500 μm. The wavelength range from 1000 to 2500 μm, a section of the NIR range, is referred to as the short-wavelength infrared (SWIR) range. Reflected light spectrometers used for mineral identification detect in the SWIR region because of the characteristic absorption of light by different minerals that occurs in the 1.0 to 2.5 μm range (Thompson et al., 1999).

When photons enter a solid they can be reflected from the surface (scattered), absorbed into the surface, or transmitted through the material. Reflected photons are detected by the spectrometer; wavelengths that are absorbed by a mineral, and thus not reflected back to the spectrometer, provided information that helps to identify the mineral. Mineral spectra from a SWIR analysis are often plotted as percentage of reflectance against wavelength, typically in nm or μm, the light that is absorbed by a mineral creates absorption bands that deviate from the spectra "hull". The wavelength position of the absorption band, its depth, and its width, measured as full-width at half maximum, vary with chemical composition for any given mineral (Figure 5.2). The depth of the absorption band is a relative gauge of intensity of absorption; in a given sample, the dominant mineral will thus have a lower reflectance %, or reflectance minimum, than the less dominant mineral phases (Huston et al., 1999; van Ruitenbeek et al., 2005).

Minerals will absorb different wavelengths of light as a function of their crystal structure and chemistry. Absorptions in the SWIR region are caused by combinations and overtones of molecular vibration (bending and stretching) and electrical properties of specific molecules and radicals including: water (H_2O), hydroxyl radicals (OH), ammonia (NH_4), carbonate (CO_3), sulfate (SO_4), and cation-hydroxyl bonds (i.e., Al-OH, Mg-OH, Fe-OH, Si-OH). Light absorption can occur in a mineral by both electronic and vibrational processes. While both electronic and vibrational processes can be used to identify surface materials, molecular vibrations create the most diagnostic absorption bands for minerals and generally occur within the SWIR region (1.0 to 2.5 μm: Thompson et al., 1999).

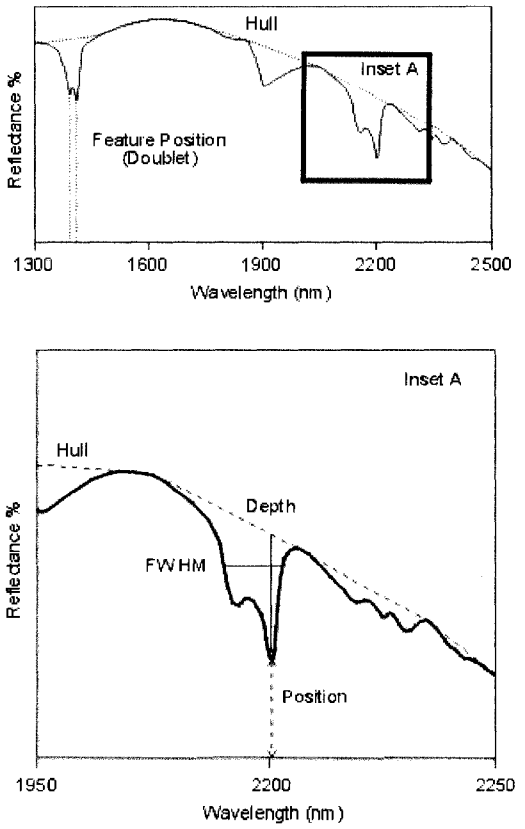

Figure 5.2. Example of a mineral reflectance spectrum (from Thompson et al., 1999) . Wavelengths are plotted against percentage of reflectance. Inset A is an enlarged view of an absorption band at a wavelength position of 2.2 µm. The hull profile is the trace of maximum reflectance from which the absorption features deviate. The full-width half maximum (FWHM) is the width of absorption feature at half of the absorption depth. A doublet is an absorption band that displays two distinct absorption features.

5.2.2 Results

The results of 135 spectral measurements are subdivided by lithofacies and sampling medium and are presented in Table 5.1, and Figures 5.3, 5.4, 5.5, and 5.7. Theoretical spectra mixtures of montmorillonite-opal, montmorillonite-illite, and vermiculite-talc are presented in Figure 5.6. Amorphous silica (opal) and montmorillonite are the spectrally dominant minerals identified in the sample suite; reference spectra of these phases are plotted with Calypso SWIR patterns for comparison. Montmorillonite is a Na-Ca dioctahedral smectite with an ideal chemical formula of (½ Na, Ca)$_{0.7}$ Al$_{3.3}$, Mg$_{0.7}$ Si$_8$O$_{20}$ (OH)$_4$· n (H_2O) (Deer et al., 1992).

Montmorillonite and silica have overlapping absorption features in the 1.4 μm and 1.9 μm wavelength regions caused by vibrations of H_2O + OH and H_2O bonds (e.g., Figure 5.3). A small shoulder occurs on the H_2O + OH absorption feature of montmorillonite at ~1.450 μm – 1.460 μm; this feature is often used to differentiate smectite from other phyllosilicates. Opal can also display this shoulder feature. The depth of the 1.9 μm H_2O absorption feature provides a measure of the mineral's capacity to retain water (Hauff, 2005). Opal has a very wide, trough shaped, asymmetrical, absorption feature that begins near 2.2 μm and extends to higher wavelength (~2.27 μm); this feature has been attributed to vibrations of silica-hydroxyl bonds (SiOH) (Goetz et al., 1983; Rowan et al., 2003). Montmorillonite displays a narrow, medium depth, AlOH absorption feature at ~ 2.21 μm. The overlapping absorption features of montmorillonite and opal in the 1.4 μm, 1.9 μm, and

2.2 μm wavelength regions can complicate the identification of these phases. The width and symmetry of the 2.2 μm AlOH and SiOH absorption feature of montmorillonite and opal can be used to distinguish the two minerals. Mixtures of montmorillonite and opal reference spectra were created with Specmin software and displayed in Figure 5.6A. A pure montmorillonite spectrum is displayed on the bottom of the spectral stack; a spectrum of pure opal is displayed on the top of the spectral stack. Mixing of opal and montmorillonite spectra shows that the narrow, near-symmetrical, 2.2μm absorption feature of 100% montmorillonite progressively widens to the broad, trough-shaped feature of opal.

Spectra taken from geochemical pulps of the silicified lithofacies (including silicified crystal tuff, silicified crystal tuff with sulfur matrix, silicified vitric tuff, and barite-rich silicified tuff) are plotted in Figures 5.3A, 5.3B, 5.4A, and 5.4B. The spectra for each lithofacies are nearly parallel and display very shallow absorption features at ~1.4 μm and ~1.9 μm. The absorption features at ~2.2 μm are shallow, broad, and near symmetrical; the width of these features lies between that of the opal and montmorillonite reference spectra. A single reflectance spectrum of DR-112 in Figure 5.4B shows a narrow 2.2 μm absorption feature and deeper H_2O + OH and H_2O absorption features similar to the reference spectrum of montmorillonite.

SWIR patterns collected from rock samples (cut surfaces) of the equivalent silicified lithofacies are plotted in Figures 5.3C, 5.3D, 5.4C, and 5.4D. These spectra display deeper absorption features at all three wavelength regions; the 2.2 μm absorption feature is a very broad trough-shape that is comparable to the reference spectra of opal.

The spectra of pervasively clay-altered lithofacies (clay-altered lapilli tuff and clay-altered lapilli tuff with native sulfur) collected from geochemical pulps are plotted in Figure 5.5A. The spectra are nearly parallel, with shallow absorption features, and a broad 2.2 μm absorption feature. The spectra are nearly equivalent to the spectra collected from the geochemical pulps of the silicified lithofacies (Figures 5.3A, 5.3B, 5.4A, and 5.4B). Spectra collected from corresponding rocks samples (Figure 5.5C) display much deeper absorption features and a narrow well-defined 2.2 μm absorption feature analogous to the montmorillonite reference spectrum.

Overall, spectra from geochemical pulps appear homogenized with shallower absorption features relative to patterns recovered from rock samples. It has been suggested that heating and grinding during the process of milling rock samples into geochemical pulps may cause the spectral signatures of mineral phases to be degraded (Thompson et al., 1999).

Smectite was identified in the SWIR spectra in the geochemical pulp of a barite-rich, silicified tuff sample (Figure 5.4B). X-ray diffraction also detected smectite in this sample (Table 5.1). However, SWIR spectra collected from equivalent rock samples have very broad 2.2 μm absorption features similar to the opal reference (Figure 5.4D). Amorphous silica coating of the montmorillonite and sample heterogeneities may have caused the opal to be spectrally dominant in the rock samples and spectra of geochemical pulps may reflect a mixture of montmorillonite and amorphous silica.

Illite and mixed-layer illite-smectite were identified by XRD analysis in both silicified and clay-rich samples (Table 5.1). Illite reference SWIR patterns are similar to montmorillonite with the addition of small absorption features at 2.35 μm and 2.45 μm, and a small absorption feature at 2.11 μm in well crystalline samples (Hauff, 2005). These features can be used to identify mixed-layer illite-smectite or mixtures of discrete illite and smectite. Spectral mixtures of illite and montmorillonite are shown in Figure 5.6B. The addition of illite to the montmorillonite spectra creates shallow absorption features at 2.35 μm and 2.45 μm which become more pronounced with increased illite concentration. A shallow inflection was identified at 2.4 μm in the spectra collected from geochemical pulps in both silicified and clay-rich samples (Figures 5.3A, 5.3B, 5.5A, 5.5B). These features were not observed in the corresponding spectra collected from rock samples (Figures 5.3C, 5.3D, 5.5C, 5.5D). The absence of the 2.35 μm and 2.45 μm absorption features indicates the concentration of illite in the Calypso samples is too low to be detected by spectral means.

X-ray diffraction analysis detected mixed-layer chlorite-smectite or vermiculite as well as talc in sample DR-110k. The SWIR patterns from geochemical pulps and corresponding rock samples are plotted in Figures 5.5C and 5.5D. The reference spectra of montmorillonite, vermiculite, chlorite, and talc are plotted for reference. The spectra of DR-110k are very similar to the vermiculite reference spectra, with notable absorption features in the FeOH absorption region at 2.250 μm and in the MgOH wavelength region at 2.3 μm and 2.320 μm. The absorption features of talc and chlorite are not detected in the

DR-110k spectra. Spectral mixing of vermiculite with talc indicates that greater than 30% talc is required to significantly alter the vermiculite SWIR pattern (Figure 5.6C).

The primary alteration lithofacies observed at Calypso (clay-altered lapilli tuff and silicified tuff) are displayed on a single plot (Figure 5.7A) along with the reference spectrum of montmorillonite and opal to demonstrate how the position and symmetry of the 2.2 μm absorption feature can be used to distinguish between the two phases. Variation of the primary cation in the octahedral layer of smectite will alter the mineral SWIR pattern in the ~2.160 μm to 2.360 μm wavelength region where absorptions are caused by bending and stretching of Al-OH, Fe-OH, and Mg-OH bonds. The 2.2 um absorption feature of montmorillonite is caused by bending and stretching of the Al-OH bond, where Al is the primary cation in the octahedral layer of the smectite structure. A spectrum of a clay-altered lapilli tuff from the CHVF and the reference spectrum of montmorillonite, saponite, and nontronite are plotted in Figure 5.7B. Nontronite, a di-octahedral smectite with an ideal formula of $(½Ca, Na)_{0.7}Fe^{3+}{}_4\ Si_{7.3}\ Al_{0.7}O_{20}(OH)_4 \cdot n(H_2O)$ (Deer et al., 1992), displays an absorption feature between 2.285 μm and 2.292 μm caused by vibrations of the Fe-OH bond. Saponite is a tri-octahedral smectite with an ideal formula of $(½Ca, Na)_{0.8}Mg_6Si_{7.2}Al_{0.8}O_{10}(OH)_2 \cdot n(H_2O)$ (Deer et al., 1992). The saponite reference spectrum has a pronounced absorption feature in the MgOH region at ~2.310 μm. The spectrum for Calypso clay-altered lapilli tuff samples parallel the reference spectra of montmorillonite but do not contain the FeOH and MgOH absorption features observed in the nontronite or saponite reference spectra. This demonstrates the ability of SWIR spectroscopy to identify mineral speciation (smectite) and chemical variation with a mineral group.

SWIR spectroscopy was able to rapidly identify smectite in the clay-altered samples and classify the clay as dioctahedral montmorillonite. The minor to trace quantities of illite or mixed-layer illite-smectite were not recognized by this method.

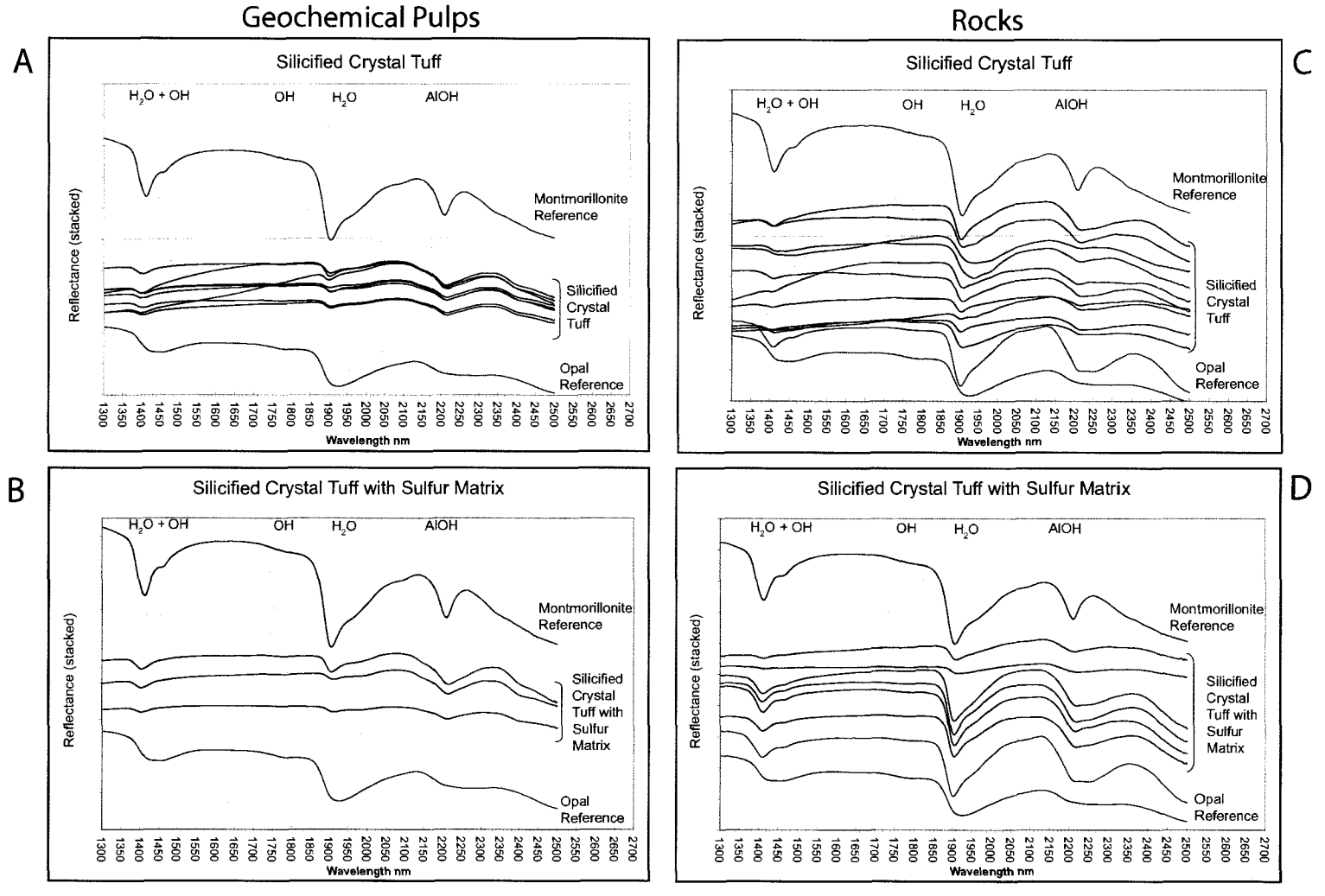

Figure 5.3. SWIR spectra of CHVF silicified crystal tuff and silicified crystal tuff with sulfur matrix samples measured from geochemical pulps (A, B) and rock samples (C, D). Pulp samples appear homogenized; spectral degradation may be caused by the milling process (Thompson et al., 1999). Spectra measured from rock samples are comparable to the reference spectra of opal. The grey bands denote the range of wavelength absorptions caused by vibrations of H_2O + OH, OH, H_2O, and AlOH.

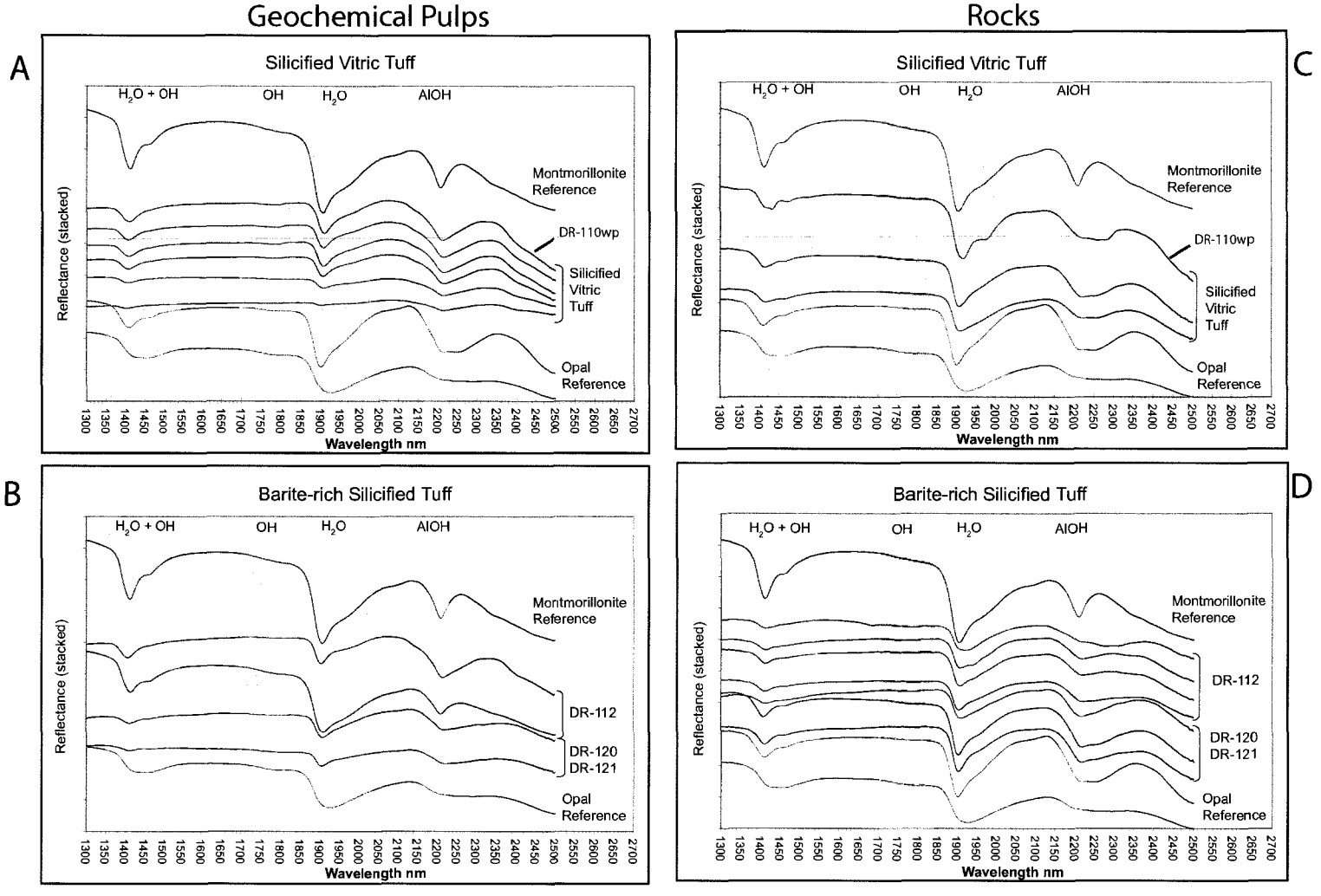

Figure 5.4. SWIR spectra of CHVF silicified vitric ash samples measured from geochemical pulps (A, B) and rock samples (C, D). Pulp samples appear homogenized; spectral degradation may be caused by the milling process (Thompson et al., 1999). Spectra measured from rock samples are comparable to the reference spectra of opal. The grey bands denote the range of wavelength absorptions caused by vibrations of $H_2O + OH$, OH, H_2O, and AlOH.

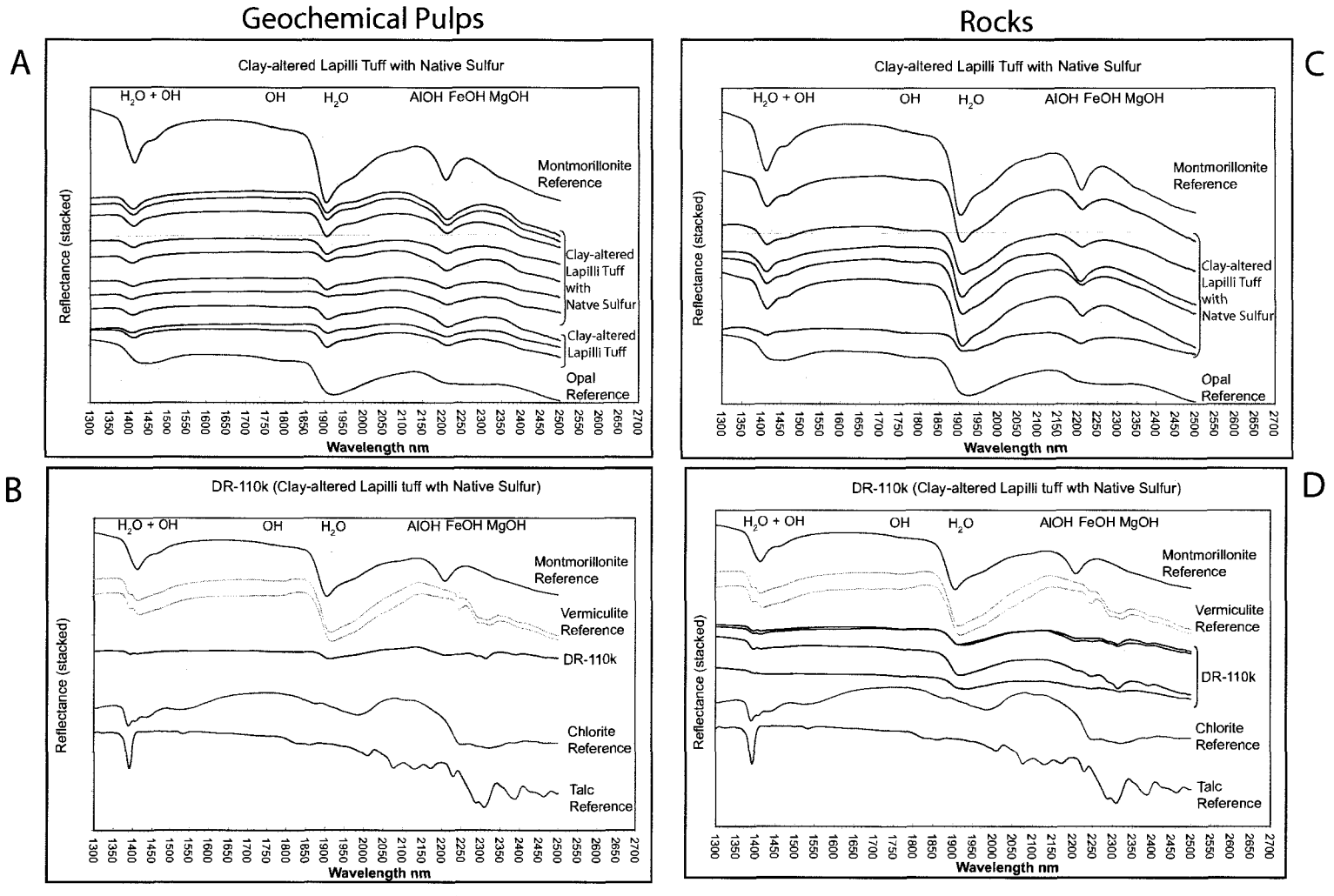

Figure 5.5. SWIR spectra of CHVF clay-altered lapilli tuff samples measured from geochemical pulps (A, B) and rocks samples (C, D). The milling process appears to degrade the spectra from geochemical pulps (Thompson et al., 1999). Spectra measured from rock samples are comparable to the reference spectra of montmorillonite (C); spectra from sample DR-110k is similar to the vermiculite reference spectra (D). The grey bands denote the range of absorptions caused by vibrations of H_2O + OH, OH, H_2O, and AlOH.

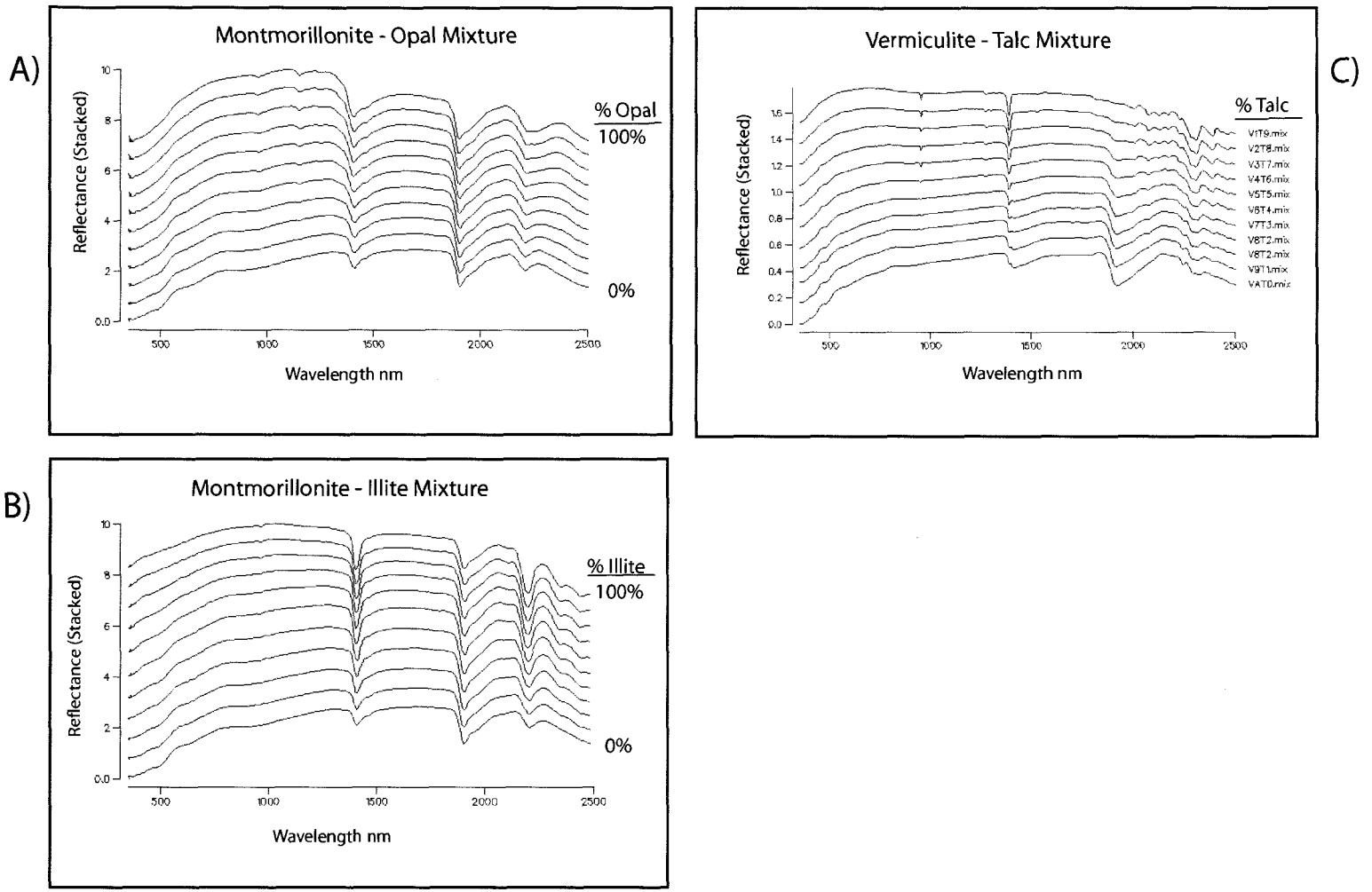

Figure 5.6. Examples of clay and clay-silica spectral mixtures. Montmorillonite - opal mixtures (A) show overlapping H_2O and OH absorption features in the 1400 and 1900 nm wavelength region, the width of the AlOH and SiOH absorption feature near the 2100 nm wavelength region will identify the spectrally dominant mineral. Montmorillonite-illite (B) and vermiculite-talc (C) mixtures of varying proportions are shown for reference.

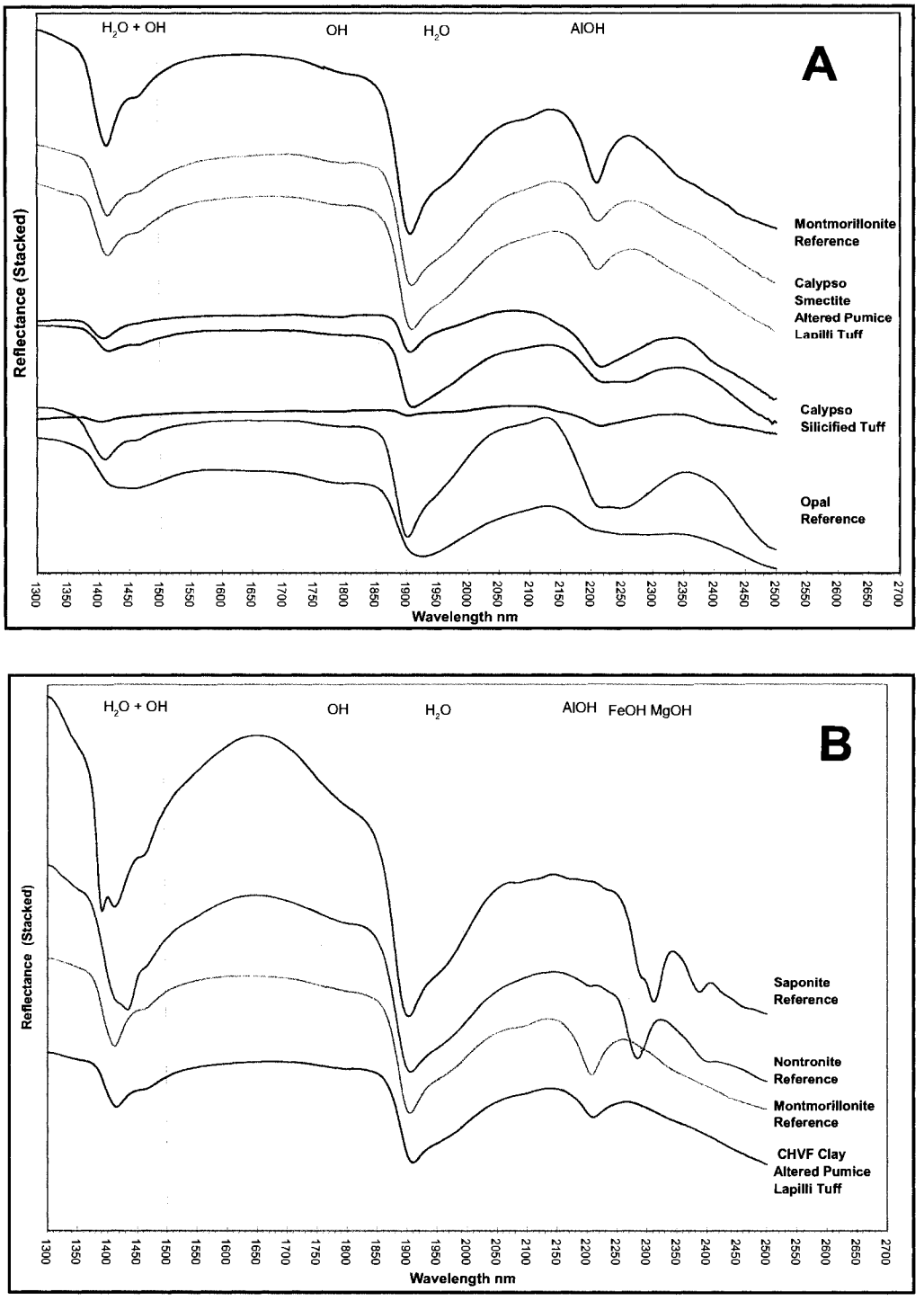

Figure 5.7 A. Spectra taken from Calypso clay-altered pumice lapilli tuff rock samples are comparable to montmorillonite reference, spectra of Calypso silicified tuff is similar to opal reference spectra. B. Plot demonstrates ability of SWIR reflectance spectrometry to distinguish between smectite species. The spectrum for Calypso clay-altered lapilli tuff samples parallel the reference spectra of montmorillonite but do not show the FeOH and MgOH absorption features observed in the nontronite and saponite reference spectra.

5.3 Analytical Electron Microprobe (AEM) Analyses

Thirty-three microprobe analyses of clay minerals were obtained from representative samples of the clay-minerals contained within altered Calypso samples.

5.3.1 Methods

Microprobe analyses of clay minerals were performed on carbon-coated polished thin sections using a Cameca Camebax MBX electron microprobe equipped with WDS (wavelength dispersive) spectrometers at the Geological Survey of Canada. Analytical conditions were typically 15 kV accelerating voltage and 20 to 30 nA beam current, with variable counting times of 10 to 20 seconds and a beam diameter of about 5 μm. Conditions varied with the nature of the samples, depending on grain size and degree of crystallinity of the clays.

5.3.2 Results

Clay-altered lapilli tuff lithofacies

The AEM results of clay minerals contained in the samples from the clay-altered lapilli tuff (DR-97-04) and clay-altered lapilli tuff with native sulfur (DR-98-02, DR-98-07a) are listed in Table 5.2. The data are presented in atoms per $O_{20}(OH)_4$.

X-ray diffraction and SWIR analysis determined that the dominant clay in these samples is dioctahedral montmorillonite. The sum of the octahedral cations ($\sum$VI) in the samples range from 3.660 to 4.654 atoms per formula unit (a.p.f.u) with the exception of analysis DR-97-04 1 which contains 1.630 a.p.f.u. Figure 5.8A illustrates the variation of cations in the octahedral positions in the smectite samples; the average compositions of dioctahedral smectite from the Broadlands-Ohaaki geothermal field are plotted for comparison (Yan et al., 2001). Aluminum and Mg are the primary cations in the octahedral layer and smectite samples from Broadlands-Ohaaki are enriched in ^{VI}Al relative to the Calypso samples. The interlayer cations show considerable variation with end members having high Na and K concentrations and several samples containing relatively equal concentrations of Ca, Na, and K (Figure 5.8B). Most of the analyzed samples have interlayer cation contents ($\sum$VII) of less than 1. Samples DR-98-02 1 and DR-98-07a show notable Na enrichment with $\sum$VII values of 2.64 and 2.22 a.p.f.u. Potassium enrichment in samples DR-98-7a 2 and DR-98-7a 3 may reflect a component of mixed-layer illite from K^+ addition.

Clay Altered Samples

Sample	DR-97-04						DR98-02			DR98-07a		
Clay Habit	Rimming pyrite	Replacing ash			Matrix	Replacing pumice	Replacing pumice			Replacing pumice		
XRD	Smectite						Smectite			Smectite		
	1	2	3	4	5	6	1	2	3	1	2	3
Si	9.901	7.651	7.993	7.627	7.146	7.954	7.369	7.998	7.465	7.416	7.500	8.166
Al IV	0.000	0.349	0.007	0.373	0.854	0.046	0.631	0.002	0.535	0.584	0.500	0.000
Al VI	0.874	2.826	2.846	2.853	2.884	2.758	2.577	3.008	3.256	2.140	2.819	2.770
Ti	0.005	0.010	0.090	0.014	0.018	0.022	0.008	0.013	0.004	0.016	0.050	0.020
Cr	0.005	0.001	0.002	0.000	0.000	0.000	0.002	0.001	0.003	0.006	0.002	0.002
Fe	0.106	0.180	0.206	0.131	0.115	0.126	0.061	0.079	0.028	0.088	0.482	0.211
Mn	0.012	0.003	0.003	0.001	0.001	0.000	0.001	0.001	0.000	0.006	0.000	0.000
Mg	0.645	1.456	1.133	1.460	1.637	1.474	1.166	1.159	0.920	1.665	1.008	0.659
Ca	0.024	0.106	0.094	0.139	0.151	0.126	0.096	0.141	0.167	0.123	0.065	0.026
Na	0.101	0.130	0.147	0.189	0.216	0.130	2.156	0.112	0.460	2.280	0.108	0.082
K	0.063	0.100	0.081	0.106	0.103	0.105	0.057	0.046	0.054	0.040	0.617	1.065
ΣVI	1.630	4.472	4.275	4.458	4.654	4.380	3.812	4.259	4.208	3.909	4.359	3.660
ΣXII	0.188	0.336	0.322	0.434	0.470	0.361	2.309	0.299	0.681	2.443	0.790	1.173
VI Al + Fe	0.980	3.006	3.052	2.984	2.999	2.884	2.638	3.087	3.284	2.228	3.301	2.981
Fe+Mg	0.751	1.636	1.339	1.591	1.752	1.600	1.227	1.238	0.948	1.753	1.490	0.870

Table 5.2. AEM analyses of white clay minerals in clay-altered lapilli tuff samples. Wholerock XRD clay analysis indicates the presence of smecite in all samples. Compositions are given in atoms per $O_{20}(OH)_4$. All Fe was treated as Fe^{3+}. $\sum$ VI = sum of octahedral cations, $\sum$ XII = sum of interlayer cations.

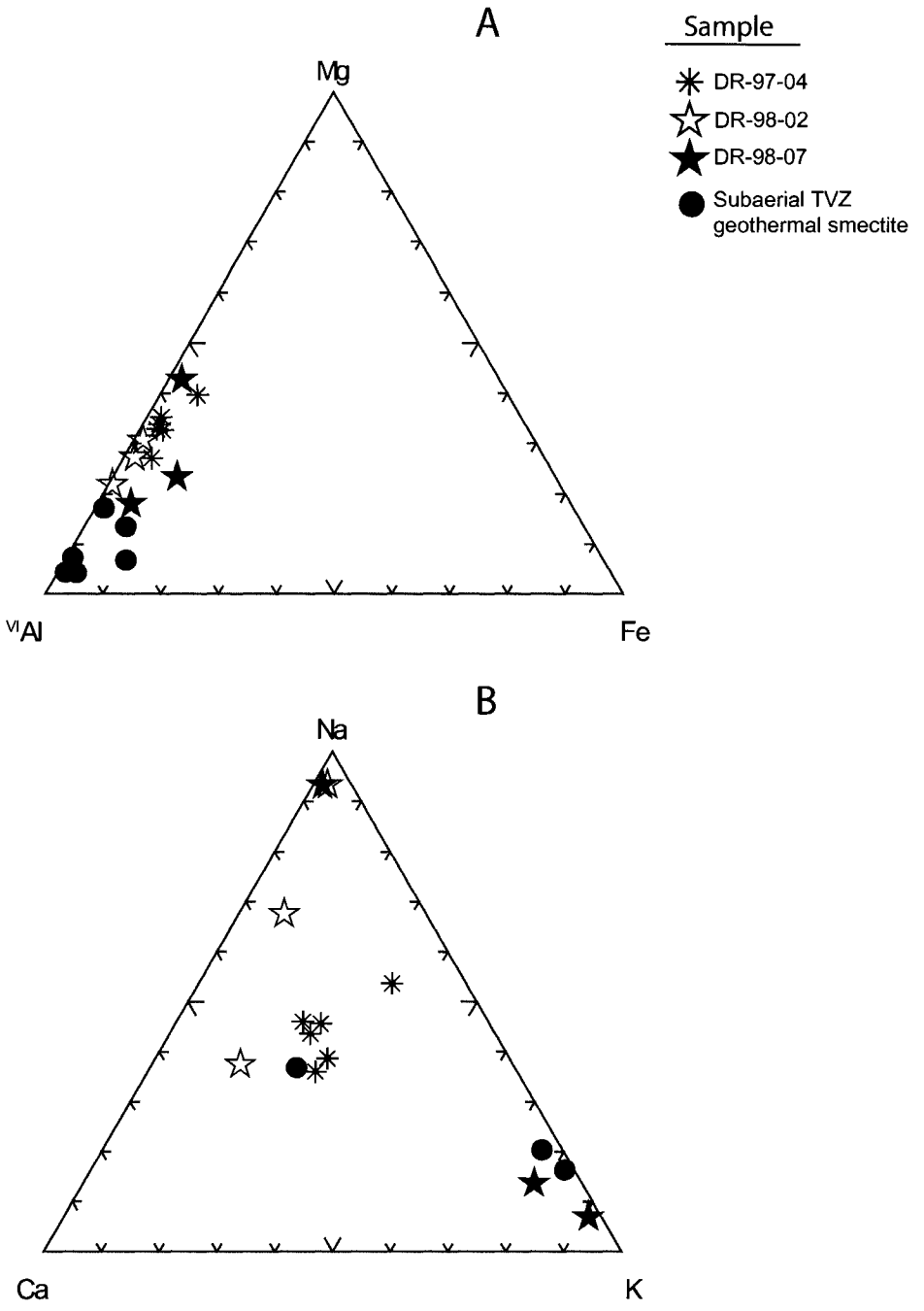

Figure 5.8. Compositional variations of clay in clay-altered lapilli tuff samples. Whole-rock XRD analysis indicates smectite is the clay mineral phase. A. The ^{VI}Al-Mg-Fe plot demonstrates the variation of different cations contained in the octahedral positions in the smectite. B. The Na-Ca-K plot shows the relative proportions of interlayer cations. Average dioctahedral smectite compositions from the Broadlands-Ohaaki subaerial TVZ geothermal field are plotted for reference (Yan et al., 2001). All Fe was treated as Fe^{3+}. Formulae were calculated on the basis of $O_{20}(OH)_4$.

Silicified tuff lithofacies

The AEM results of clay minerals contained in the samples from the hydrocarbon-rich silicified tuff (DR-113c) and barite-rich silicified tuff (DR-120f) lithofacies are listed in Table 5.3. AEM analysis of clay minerals contained in the samples from the silicified crystal-tuff (DR-85-5a, DR-85-6, DR-88, and DR-89-2a) and silicified vitric tuff (DR-110e, DR-110i) lithofacies are listed in Table 5.4. The data are presented in atoms per $O_{20}(OH)_4$.

X-ray diffraction analysis identified minor smectite and illite in sample DR-113c, mixed-layer illite-smectite in samples DR-120f and DR-89-2a, and trace amounts of illite in samples DR-85-5a and DR-88. Clay minerals were not detected by XRD of SWIR analysis in samples DR-85-6, DR-89, DR-110e, or DR-110i. The SWIR spectra indicate opal is the spectrally dominant phase in these samples.

Figure 5.9A illustrates the variation of cations in the octahedral positions in the clay minerals. Aluminum is the dominant cation, but Mg enrichment is apparent in samples in which illite-smectite and smectite were identified by XRD (DR-89-2a, DR-120f, and DR-113c). The interlayer cations are primarily Na and K; samples DR-113c 4, DR-113c 5, and DR-120f 4 have the highest K concentrations (Figure 5.9B). The interlayer cation content ($\sum$VII) of the samples show considerable variation, with many more values > 1 when compared with the clay-altered lithofacies.

AEM analyses confirmed that Al is the principal elements in the dioctahedral layer of the clays which is consistent with the chemical composition of montmorillonite and illite (Figure 5.9 A). Elevated Mg and Fe concentrations may reflect a smectitic composition. Interlayer cations display a range of Na-Ca-K values. The K enrichment reflects the chemical composition of illite or mixed-layer illite-smectite (e.g., Huggett and Cuadros, 2005; Bauluz et al., 2002).

Silicified Ash with Minor Clay

Sample	DR-113c							DR-120f			
Colour	Green				White			White			
Clay Habit	Rimming ash			Matrix	Matrix			In altered clast		Between glass shards	
XRD	Smectite-illite							IS			
	1	2	3	4	5	6	7	1	2	3	5
Si	9.691	9.382	7.866	7.770	7.673	8.422	8.636	7.366	7.779	9.141	7.813
Al IV	0.000	0.000	0.134	0.230	0.327	0.000	0.000	0.634	0.221	0.000	0.187
Al VI	1.298	1.745	2.359	2.087	2.208	2.550	2.003	2.747	2.532	1.963	3.088
Ti	0.002	0.003	0.181	0.021	0.042	0.003	0.024	0.010	0.054	0.009	0.017
Cr	0.004	0.005	0.005	0.005	0.004	0.001	0.002	0.001	0.001	0.004	0.003
Fe	0.104	0.094	0.721	1.109	1.129	0.074	0.154	0.138	0.860	0.143	0.227
Mn	0.008	0.006	0.005	0.005	0.009	0.000	0.005	0.013	0.018	0.006	0.008
Mg	0.016	0.013	0.881	1.142	0.868	0.192	0.351	1.778	0.938	0.029	0.367
Ca	0.068	0.095	0.045	0.019	0.034	0.163	0.135	0.073	0.112	0.157	0.048
Na	0.415	0.301	0.103	0.118	0.058	1.020	1.480	0.149	0.158	0.202	0.626
K	0.513	0.492	0.910	1.202	1.384	0.768	0.577	0.196	0.388	0.629	0.918
ΣVI	1.420	1.855	4.142	4.359	4.247	2.819	2.532	4.673	4.384	2.144	3.699
ΣXII	0.996	0.888	1.058	1.339	1.476	1.951	2.192	0.418	0.658	0.988	1.592
VI Al + Fe	1.402	1.839	3.080	3.196	3.337	2.624	2.157	2.885	3.392	2.106	3.315
Fe+Mg	0.120	0.107	1.602	2.251	1.997	0.266	0.505	1.916	1.798	0.172	0.594

Table 5.3. AEM analyses of white and green coloured, fine-grained, clay minerals in clay-poor, silicified tuff samples. Wholerock XRD clay analysis indicates the presence of smectite, illite, and mixed layer illite-smectite (IS) in the samples. Compositions are given in atoms per $O_{20}(OH)_4$. All Fe was treated as Fe^{3+}. $\sum$ VI = sum of octahedral cations, $\sum$ XII = sum of interlayer cations.

Silicified Samples with Minor Clay

Sample	DR-85-5a		DR-85-6	DR-88		DR-89-2a		DR-110e		DR-110i
Clay Habit	Replacing ash		Replacing ash	Matrix		Replacing clast		Between glass shards	Matrix	In cavity
XRD	Tr. Illite		n.d	Tr. Illite		IS		n.d		n.d
	1	2	1	1	2	1	2	1	2	1
Si	8.380	7.126	9.179	9.578	10.046	9.313	9.711	7.620	9.357	9.020
Al IV	0.000	0.874	0.000	0.000	0.000	0.000	0.000	0.380	0.000	0.000
Al VI	2.587	2.581	1.883	0.949	0.946	1.433	1.353	3.096	1.612	2.076
Ti	0.015	0.231	0.016	0.029	0.019	0.022	0.001	0.091	0.016	0.016
Cr	0.001	0.005	0.004	0.000	0.005	0.002	0.001	0.005	0.003	0.001
Fe	0.209	0.695	0.086	0.208	0.070	0.163	0.039	0.402	0.114	0.116
Mn	0.004	0.000	0.005	0.006	0.000	0.000	0.004	0.003	0.009	0.010
Mg	0.184	0.534	0.020	0.226	0.101	0.659	0.028	0.529	0.045	0.059
Ca	0.027	0.418	0.125	0.023	0.032	0.082	0.152	0.100	0.139	0.222
Na	1.256	0.263	0.554	1.114	0.326	0.223	0.396	0.049	0.555	0.381
K	0.548	0.634	0.532	0.690	0.156	0.325	0.250	0.599	0.492	0.428
ΣVI	2.995	4.041	2.005	1.412	1.136	2.277	1.421	4.118	1.787	2.267
ΣXII	1.831	1.315	1.211	1.827	0.514	0.630	0.798	0.748	1.186	1.031
VI Al + Fe	2.796	3.276	1.969	1.157	1.016	1.596	1.392	3.498	1.726	2.192
Fe+Mg	0.393	1.229	0.106	0.434	0.171	0.822	0.067	0.931	0.159	0.175

Table 5.4. AEM analyses of white, fine-grained, clay minerals in clay-poor, silicified tuff samples. Wholerock XRD clay analysis indicates the presence of mixed layer illite smectite (IS) and trace illite (Tr. illite) in the samples; clay was not detected (n.d) by XRD in samples DR-85-6, DR-110e, and DR-110i. Compositions are given in atoms per $O_{20}(OH)_4$. All Fe was treated as Fe^{3+}. $\sum$ VI = sum of octahedral cations, $\sum$ XII = sum of interlayer cations.

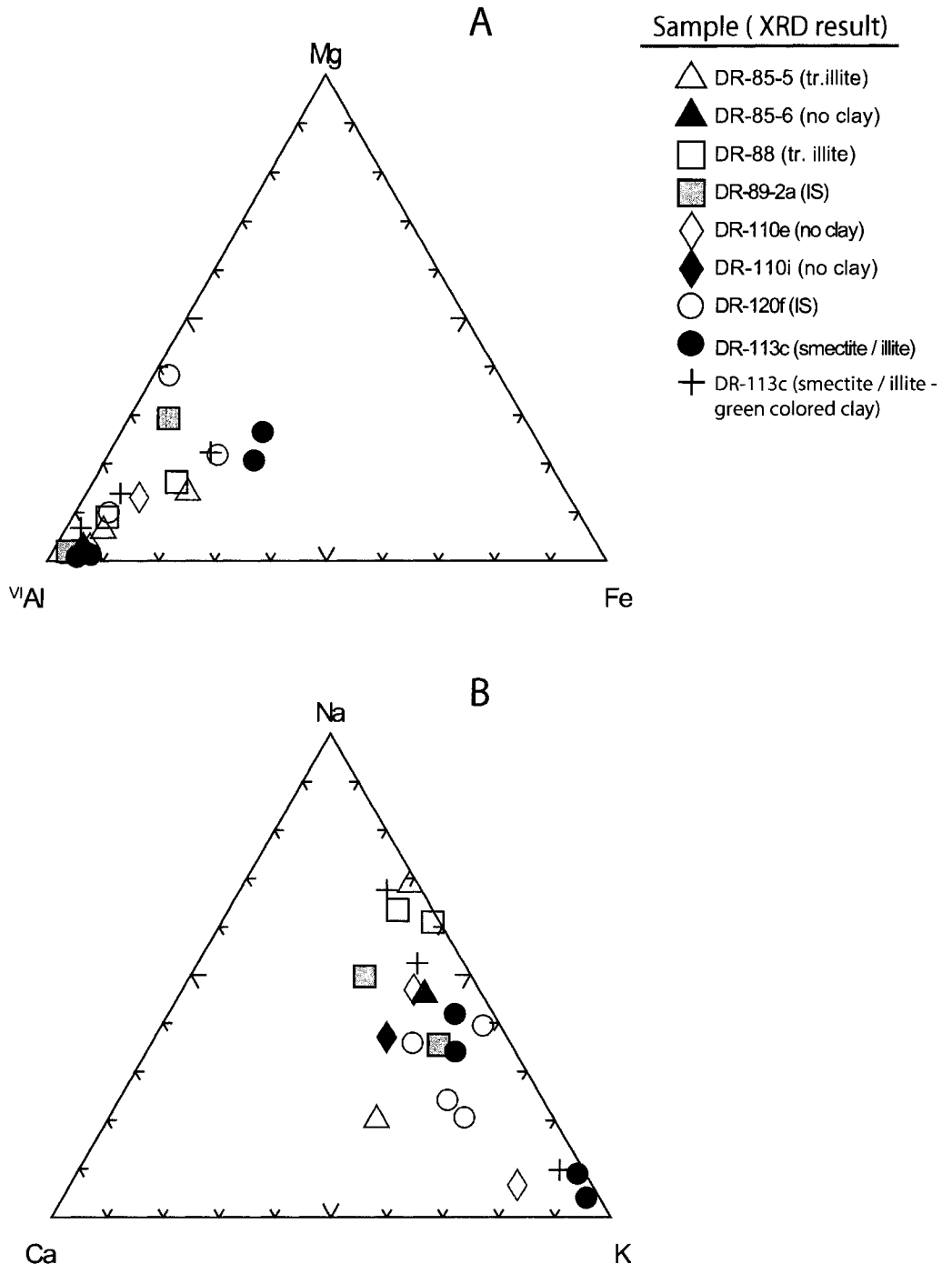

Figure 5.9. Compositional variations of clay samples in silicified samples. Whole-rock XRD clay mineral identification is provided in the sample legend bracket. A) The ^{VI}Al-Mg-Fe plot demonstrates the variation of different cations contained in the octahedral positions in the smectite-illite structure. B) The Na-Ca-K plot shows the relative proportions of interlayer cations. All Fe was treated as Fe^{3+}. Formulae were calculated on the basis of $O_{20}(OH)_4$. with interlayer illite.

6.0 Lithogeochemistry

Table 6.1 contains the whole-rock geochemical analyses of 40 altered rock samples and 4 pyrite veins from the Calypso Hydrothermal Vent Field (CHVF). Gold, As, Sb, Hg, W, Se, and Br were analyzed by instrumental neutron activation analysis (INAA); F and Cl were analyzed by specific ion electrode; S and C were analyzed by Dionex (pyrohydrolysis method followed by ion chromatography); all others elements were analyzed by ICP-ES and ICP-MS at the Geological Survey of Canada in Ottawa. Standard GSC procedures were used to ensure that the data is precise and accurate.

Seafloor sampling procedures coupled with the limitations of seafloor observations restricted the capacity for a systematic sampling program in which least altered samples could be selected peripheral to the hydrothermal system or within discrete geological units. Sample DR-110wp was selected to represent the least-altered felsic vitric ash. The sample was hand-picked from non-silicified portions of sample DR-110, Plate 4.3E) and provides a least altered equivalent to the silicified vitric tuff lithofacies. Samples DR-97-04 and 81-82 GTVA were selected to represent least-altered lapilli tuff; these samples do not contain the abundant native sulfur observed in other clay-altered samples and have a lower overall clay mineral content (see Figure 6.19).

Samples were collected at three hydrothermal vent sites over an area of approximately 30 km^2 (Figure 1.2). Accordingly, the samples display variation in primary igneous

material and alteration minerals, which is reflected by sample chemistry. Lithogeochemical techniques have been employed to (a) elucidate the source of volcanic detritus, (b) subdivide the samples by alteration facies, and (c) estimate the chemical variation caused by hydrothermal alteration and the addition of hydrothermal precipitates.

Table 6.1 Whole-rock geochemistry of recovered rock samples from the Calypso Hydrothermal Vent Field, sorted by lithofacies

	Cherty Tuff	Barite Rich Silicified Tuff w/ Volcanic Blocks					Silicified Crystal tuff									
DR-	118-04	112a	112b,c	112d,e	120.0	121.0	85d	85c	85b	85a	88.0	89-02a	02b	85-05a	-05b	-05c
SiO2 (wt%)	83.90	69.20	57.40	61.40	56.50	77.50	78.70	81.50	75.50	69.10	74.20	81.10	74.80	70.70	69.50	78.80
TiO2	0.13	0.13	0.08	0.09	0.22	0.20	0.47	0.19	0.79	0.33	0.39	0.22	0.31	1.09	1.07	0.58
Al2O3	6.50	3.60	2.70	3.10	5.90	6.70	10.30	5.80	9.20	5.20	11.10	6.50	9.40	10.50	9.50	8.40
Fe2O3	1.95	0.56	0.24	0.28	1.00	2.30	2.43	1.29	3.22	1.41	2.28	1.26	1.74	4.00	4.06	2.51
MnO	<0.01	0.01	0.01	0.01	0.04	0.06	0.06	0.02	0.08	0.03	0.04	0.02	0.03	0.12	0.13	0.06
MgO	0.12	0.47	0.32	0.37	1.31	0.40	0.81	0.48	0.95	0.53	0.59	0.49	0.65	1.46	1.47	0.75
CaO	0.23	0.25	0.18	0.20	0.70	0.83	1.96	0.50	1.45	0.45	1.31	0.56	0.81	2.07	1.95	1.26
Na2O	0.20	0.87	0.63	0.51	1.20	1.79	2.67	1.81	2.15	0.95	3.08	1.98	2.75	2.82	2.58	2.36
K2O	5.06	0.75	0.51	0.62	1.07	1.39	1.45	1.14	1.34	0.61	2.25	1.30	1.82	1.52	1.34	1.47
CO2	0.20	0.05	0.05	0.05	0.05	0.05	0.05	0.05	0.05	0.05	0.05	0.05	0.05	0.05	0.10	0.05
C	0.10	0.10	0.10	0.10	0.80	0.30	0.10	1.10	0.30	0.80	0.40	0.70	0.80	0.10	0.10	0.10
P2O5	0.01	0.04	0.01	0.01	0.03	0.02	0.05	0.04	0.03	0.02	0.05	0.03	0.05	0.07	0.06	0.05
S	1.4	3.29	5.52	4.33	6.26	2.40	0.56	0.79	2.54	3.68	2.17	0.59	0.97	4.85	6.29	1.94
Total	99.9	86.90	83.40	83.60	81.00	96.60	99.70	95.20	97.90	85.40	98.00	95.30	94.30	99.50	98.30	98.60
LOI	1.40	3.60	4.20	3.60	11.80	5.20	3.00	6.60	6.20	20.10	6.50	5.80	6.70	6.60	8.40	4.30
Ba (ppm)	770	70300	150000	119000	56300	25200	460	4140	2750	21800	550	5000	840	410	530	1820
Sr	43	4780	5840	5820	3300	980	170	390	200	710	150	430	150	220	190	180
Rb	160	33	25	28	56	71	46	46	43	20	75	50	68	48	42	48
Cs	4.1	8.6	7.5	7.7	31	32	7.1	8.2	8.1	4.6	14	11	9.9	11	9.1	10
Be	1.2	0.5	0.5	0.6	1.1	0.9	1	0.9	1.0	0.5	1.5	0.9	1.2	1.1	0.9	1.1
F	99	365	400	431	510	295	204	220	--	--	286	271	280	296	304	195
Cl	588	2690	1753	876	2997	2884	2071	4865	--	--	3953	4898	4132	1415	1660	562
Br	1.7	17.8	<7.0	6.9	<4.5	14.6	12.2	25.5	<0.5	<0.5	18.4	22.8	25.6	6	7.8	1.8
Cr	<10	13	10	10	12	34	18	16	43	23	22	19	19	52	40	32
V	9	59	35	46	44	28	54	27	58	30	40	29	41	63	55	55
Sc	3.6	2.6	1.9	2	4.7	3.5	7.7	3.8	9.3	3.9	6.7	3.8	5.9	13	12	7.5
Sn	0.8	0.9	0.3	0.6	1.2	1.2	1.1	1.4	1.2	1.3	1.3	1.4	1.9	1.0	1.5	1.1
U	1.3	4.9	3.3	4.3	6	7	16	5.9	4.2	7.4	2.8	2.4	3.3	2.4	2.2	2
Th	4.1	1.4	0.6	0.8	1	3.1	4.0	3.5	4.4	2.4	6.4	3.4	5.3	4.9	4.7	4.7
Nb	4.9	2.4	1.6	2.1	3.1	4.2	6.1	4.1	10	4.4	6.6	4	6	12	11	7.4
Zr	85	53	39	40	80	74	160	79	460	190	120	80	110	550	460	290
Y	9.5	3.1	2.2	2	6.8	8.1	10	7.8	11	5.4	14	8.6	12	13	13	11
Hf	2.2	1.3	1	1	1.9	1.9	3.6	2	9.7	4	2.9	2	2.7	12	10	6.7
Ta	3.6	1.3	0.5	1.2	0.5	1.5	2.2	1.0	3.1	1.2	1	0.6	2	1.4	0.9	1.1
W	688	291	<10	295	127	237	373	149	479	216	96	56	498	129	44	147
As	232	981	2630	4960	1600	1870	23	2180	42	<9.6	4.8	614	7730	10	7.1	17
Sb	29	694	14100	1960	5160	483	2	505	3	<0.8	0.6	49	305	0.5	0.5	2

Table 6.1 Whole-rock geochemistry of recovered rock samples from the Calypso Hydrothermal Vent Field, sorted by lithofacies

	Cherty Tuff	Barite Rich Silicified Tuff w/ Volcanic Blocks					Silicified Crystal tuff									
DR-	118-04	112a	112b,c	112d,e	120.0	121.0	85d	85c	85b	85a	88.0	89-02a	02b	85-05a	-05b	-05c
Hg	8	30	29	7	190	78	1	5000	15000	95000	50	860	4000	4	0.5	3300
Cu	18	29	48	47	16	5	5	13	5	5	5	5	5	5	12	5
Zn	10	440	940	710	260	78	36	21	68	110	36	29	46	47	51	41
Pb	28	100	180	170	10	19	13	10	17	11	47	7	12	150	260	110
Ag	13	47	190	150	6.6	0.4	<0.1	0.4	<0.1	0.2	0.6	<0.1	0.9	0.4	<0.1	0.4
Au (ppb)	421	<2	<60	<10	628	<2	<2	<20	<20	<20	5	<2	34	<2	11	<2
Bi	0.1	0.1	0.1	0.1	0.1	0.1	0.1	0.1	0.1	0.1	0.1	0.1	0.1	0.1	0.1	0.1
Cd	0.1	0.4	0.8	0.6	0.1	0.4	0.1	0.2	0.1	0.6	0.1	0.1	0.3	0.1	0.1	0.1
Ga	6.1	24	29	19	17	8	10	9.4	10	7.3	12	8.8	11	11	11	9.7
Tl	6.4	71	330	420	1600	390	0.4	140	12	13	0.7	30	35	0.7	0.5	6.8
In	<0.1	<0.1	<0.1	<0.1	<0.1	<0.1	<0.1	<0.1	<0.1	<0.1	<0.1	<0.1	<0.1	<0.1	<0.1	<0.1
Co	80	31	8	25	6.0	29	50	23	55	24	14	15	--	21	11	27
Se	<3	<3	<5	<3	<3	5	<3	<3	<3	<5	<3	<3	28.0	-3.0	<3	15.0
Te	<0.1	<0.1	<0.1	<0.1	<0.1	<0.1	<0.1	<0.1	<0.1	<0.1	<0.1	<0.1	<0.1	<0.1	<0.1	<0.1
Mo	3	1.6	3.2	1.3	0.9	34	55	6.8	7.9	10	3.2	4	8.3	2.8	1.3	1.3
Ni	5	5	5	5	5.0	22	5	5	5	5	5	5	13	5	5	5
La	8.8	2.7	2.4	1.7	2.5	7.2	11	8	12	5.2	15	8.7	13	15	14	13
Ce	19	5.6	2.8	3.3	6.9	16	22	18	25	12	30.0	19	27	30	28	26
Pr	2	0.7	0.4	0.4	1.0	1.8	2.5	2.1	3.1	1.4	3.5	2.2	3.3	3.5	3.3	3.1
Nd	8	2.7	1.6	1.7	4.9	6.9	9.9	7.7	11	5.2	13	8.2	12	13	12	11
Sm	1.4	0.5	0.4	0.4	1.2	1.4	2.2	1.5	2	1	2.8	1.6	2	2.6	2.3	2.1
Eu	0.4	0.1	0.2	0.1	0.9	0.5	0.6	0.3	0.6	0.3	0.6	0.3	0.5	0.8	0.7	0.5
Gd	1.3	0.5	0.4	0.3	1.1	1.2	1.8	1.3	1.7	0.9	2.4	1.4	1.9	2.3	2	1.7
Tb	0.2	0.1	0.1	0.1	0.2	0.2	0.3	0.2	0.3	0.2	0.4	0.2	0.3	0.4	0.4	0.3
Dy	1.4	0.5	0.4	0.3	1.1	1.2	1.7	1.2	1.7	0.9	2.3	1.3	1.9	2.3	2.2	1.7
Ho	0.3	0.1	0.1	0.1	0.3	0.3	0.4	0.3	0.4	0.2	0.5	0.3	0.4	0.5	0.5	0.4
Er	1	0.3	0.2	0.2	0.7	0.8	1.1	0.8	1.1	0.6	1.4	0.8	1.1	1.4	1.3	1
Tm	0.2	0.1	<0.1	<0.1	0.1	0.1	0.2	0.1	0.2	0.1	0.2	0.1	0.2	0.2	0.2	0.2
Yb	1.1	0.4	0.3	0.3	0.8	0.9	1.2	0.9	1.4	0.7	1.5	0.9	1.3	1.7	1.6	1.3
Lu	0.2	0.1	0.1	<0.1	0.1	0.1	0.2	0.1	0.2	0.1	0.2	0.1	0.2	0.3	0.3	0.2
Al2O3/ TiO2	50.0	27.7	33.8	34.4	26.8	33.5	21.9	30.5	11.6	15.8	28.5	29.5	30.3	9.6	8.9	14.5
Al2O3/ Na2O	32.5	4.1	4.3	6.1	4.9	3.7	3.9	3.2	4.3	5.5	3.6	3.3	3.4	3.7	3.7	3.6
Al2O3/Na2O+CaO	15.1	3.2	3.3	4.4	3.1	2.6	2.2	2.5	2.6	3.7	2.5	2.6	2.6	2.1	2.1	I
Na/K	0.1	1.8	1.9	1.3	1.7	2.0	2.8	2.4	2.4	2.4	2.1	2.3	2.3	2.8	2.9	2.4
Si/Al	21.9	32.6	36.1	33.6	16.2	19.6	13.0	23.8	13.9	22.5	11.3	21.2	13.5	11.4	12.4	15.9
A/CNK[1]	1.0	1.3	1.4	1.7	1.3	1.1	1.1	1.1	1.2	1.7	1.1	1.1	1.2	1.0	1.0	1.1
A/NK[2]	1.1	1.6	1.7	2.1	1.9	1.5	1.7	1.4	1.8	2.3	1.5	1.4	1.4	1.7	1.7	1.5
CIA[3]	51.1	57.2	58.5	62.3	57.2	52.9	51.9	53.1	54.7	63.1	52.9	53.3	54.1	51.1	50.7	52.0

Table 6.1 Whole-rock geochemistry of recovered rock samples from the Calypso Hydrothermal Vent Field, sorted by lithofacies

	Cherty Tuff	Barite Rich Silicified Tuff w/ Volcanic Blocks					Silicified Crystal tuff									
DR-	118-04	112a	112b,c	112d,e	120.0	121.0	85d	85c	85b	85a	88.0	89-02a	02b	85-05a	-05b	-05c
HASHI-AI[4]	92.3	52.1	50.6	58.2	55.6	40.6	32.8	41.2	38.9	44.9	39.3	41.3	41.0	37.9	38.3	38.0
SERI[5]	1.2	1.9	1.6	1.5	2.2	2.8	3.7	2.8	3.2	2.0	4.1	3.0	3.8	3.8	3.6	3.4
CCPI[6]	28.2	38.9	32.9	36.5	50.4	45.9	44.0	37.5	54.4	55.4	35.0	34.8	34.3	55.7	58.5	46.0
AAAI[7]	93.8	81.3	83.6	85.0	63.8	72.0	59.1	74.5	62.4	78.2	59.8	72.8	64.0	52.7	53.7	64.3
SI[8]	92.8	95.1	95.5	95.2	90.5	92.0	88.4	93.4	89.1	93.0	87.0	92.6	88.8	87.1	88.0	90.4
S°I[9]	17.7	47.8	67.2	58.3	51.5	26.4	5.2	12.0	21.6	41.4	16.4	8.3	9.4	31.6	39.8	18.8
LOI-(S+C)[10]	-0.1	0.2	-1.4	-0.8	4.7	2.5	2.3	4.7	3.4	15.6	3.9	4.5	4.9	1.7	2.0	2.3
Zr/Y	8.9	17.1	17.7	20.0	11.8	9.1	16.0	10.1	41.8	35.2	8.6	9.3	9.2	42.3	35.4	26.4
Zr/Sc	23.6	20.4	20.5	20.0	17.0	21.1	20.8	20.8	49.5	48.7	17.9	21.1	18.6	42.3	38.3	38.7
Zr/Nb	17.3	22.1	24.4	19.0	25.8	17.6	26.2	19.3	46.0	43.2	18.2	20.0	18.3	45.8	41.8	39.2
Zr/Ti(ppm)	5.2	3.3	3.9	3.6	2.9	3.0	2.7	3.3	4.7	4.6	2.5	2.9	2.8	4.0	3.4	4.0
Zr/Hf	38.6	40.8	39.0	40.0	42.1	38.9	44.4	39.5	47.4	47.5	41.4	40.0	40.7	45.8	46.0	43.3
Y/Ti(ppm)	0.6	0.2	0.2	0.2	0.2	0.3	0.2	0.3	0.1	0.1	0.3	0.3	0.3	0.1	0.1	0.2
Nb/Y	0.5	0.8	0.7	1.1	0.5	0.5	0.6	0.5	0.9	0.8	0.5	0.5	0.5	0.9	0.8	0.7
Nb/Ta	1.4	1.8	3.6	1.8	6.6	2.8	2.8	4.1	3.2	3.7	6.6	6.5	3.0	8.6	12.6	6.7
Nb/U	3.8	0.5	0.5	0.5	0.5	0.6	0.4	0.7	2.4	0.6	2.4	1.7	1.8	5.0	5.0	3.7
Th/Nb	0.8	0.6	0.4	0.4	0.3	0.7	0.7	0.9	0.4	0.5	1.0	0.9	0.9	0.4	0.4	0.6
Nb/La	0.6	0.9	0.7	1.2	1.2	0.6	0.6	0.5	0.8	0.8	0.4	0.5	0.5	0.8	0.8	0.6
Nb/Hf	2.2	1.8	1.6	2.1	1.6	2.2	1.7	2.1	1.0	1.1	2.3	2.0	2.2	1.0	1.1	1.1

Table 6.1 (continued)

	Silicified Crystal tuff with Sulfur Matrix			Sulfur Mud	Char-coal	Clay-Altered Lapilli Tuff			Clay-Altered Lapilli Tuff with Native Sulfur								Organic-rich Silicifed Tuff		
DR-	85-06	89c	102-05	89a	113-06	81-GA	82-GA	97-04	95a	98-02a	02b	07a	07b	113b	113-05	110k	110b	113c	113d
SiO2 (wt%)	71.20	41.00	46.90	11.00	2.90	66.40	62.90	55.30	45.80	42.90	40.90	39.40	36.80	39.40	34.70	31.90	67.70	67.40	69.70
TiO2	0.75	0.28	3.16	0.10	0.03	0.34	0.39	0.57	0.38	0.36	0.38	0.32	0.30	0.59	0.58	0.31	0.34	0.43	0.49
Al2O3	8.20	8.50	10.80	2.50	0.90	16.90	19.10	17.30	13.50	12.10	12.90	11.20	11.80	12.10	11.20	7.30	9.70	14.40	10.20
Fe2O3	3.31	2.41	11.10	0.72	6.37	2.72	3.26	6.30	2.57	2.55	4.82	2.26	3.34	3.06	3.78	1.83	1.92	2.51	2.19
MnO	0.09	0.03	0.02	0.01	0.01	0.04	0.02	0.02	0.02	0.04	0.01	0.03	0.01	0.01	0.02	0.01	0.01	0.02	0.02
MgO	0.92	0.64	1.22	0.25	0.30	1.23	1.24	3.47	1.24	2.29	2.88	2.28	3.46	2.38	3.58	7.80	0.51	1.26	0.57
CaO	1.34	0.75	0.31	0.24	0.09	4.10	2.45	2.82	2.21	1.54	0.97	1.21	0.27	0.21	0.47	0.47	0.96	1.07	0.96
Na2O	2.33	2.16	1.82	0.70	0.78	3.81	3.36	3.40	2.67	2.29	2.03	1.93	1.67	1.43	1.55	1.39	2.67	3.54	2.72
K2O	1.44	1.63	2.51	0.44	0.03	1.24	0.77	0.78	0.99	1.01	1.03	0.82	0.48	0.32	0.83	0.44	1.52	2.05	1.64
CO2	0.05	0.05	0.10	--	0.05	0.05	0.05	--	0.05	0.10	0.05	0.10	0.05	0.05	0.05	0.05	0.05	0.05	0.10
C	0.30	0.60	0.10	2.00	40.10	0.10	0.10	0.20	0.10	0.30	0.10	0.10	0.10	0.60	0.60	0.30	0.50	0.40	0.90
P2O5	0.05	0.05	0.06	0.02	0.01	0.02	0.03	0.12	0.08	0.06	0.07	0.06	0.07	0.05	0.03	0.03	0.01	0.03	0.02
S	8.25	37.70	18.30	81.60	33.50	0.96	2.05	4.87	25.60	25.80	23.20	34.60	29.40	27.90	28.70	43.10	10.40	4.20	8.71
Total	98.30	96.00	97.20	99.70	88.00	98.10	95.90	95.40	95.50	91.40	89.50	94.60	87.80	88.70	89.10	94.90	96.40	97.40	98.40
LOI	11.20	42.80	18.80	83.80	81.60	4.20	6.30	11.00	30.90	33.80	32.70	41.40	41.50	39.00	36.80	48.60	13.10	8.50	12.10
Ba (ppm)	420	2490	5650	1120	29200	960	970	1510	2030	710	1730	1400	28	5980	28800	140	690	810	1620
Sr	110	180	160	61	450	260	230	230	190	140	150	120	30	310	780	50	150	200	170
Rb	48	63	100	18	1.5	42	25	22	31	36	29	28	14	12	37	14	63	96	70
Cs	6.5	5.6	14	1.7	1	2.1	1.9	1.4	2.1	1.9	1.2	1.7	0.9	3.2	6.7	1.0	25	40	30
Be	1	1.1	1.4	0.3	0.3	1.3	1.0	1.1	0.9	0.8	0.3	0.6	0.3	0.3	0.8	0.6	1.2	1.7	1.2
F	347	282	570	--	25	350	580	965	837	708	918	872	1319	1492	988	557	434	818	433
Cl	1925	3540	3728	--	6090	6186	8436	8130	4098	3887	4336	4347	5210	3546	4244	3848	2786	4473	2475
Br	10.9	16.3	20.9	10.7	55.2	37.4	27.6	33.7	23.8	25.2	24.6	21.8	26.7	24.3	28.4	29.3	16.2	19.5	15.4
Cr	29	18	43	<10	<10	18	31	10	14	24	10	21	<10	<10	24	18	12	26	15
V	35	35	270	14	16	46	61	97	65	62	65	59	50	44	64	44	24	58	36
Sc	8.4	5.5	17	2	1.2	8.5	11	15	8.6	8.8	8.6	7.7	7.9	7	7.3	4	4.8	8.8	6.2
Sn	1.2	0.8	3.6	0.3	11	1.2	1.3	1.4	1.1	0.9	1.4	1	0.6	1.3	1	0.6	1.9	2	1.5
U	7.9	2.2	4.7	5.2	2.4	14	22	7.4	25	17	9.8	18	1.8	2	25	25	1.6	2	1.6
Th	5.1	4.6	3.3	1.9	0.3	5	6.7	6.5	5.3	4.9	4.5	3.9	4.4	6.2	4.3	3.7	5.2	7.5	5.2
Nb	11	5	31	1.6	19	5.3	6.4	5.6	5.3	5.1	4	4.4	3.8	8.4	7.7	4.2	5.3	7.3	6.5
Zr	450	99	890	30	43	110	150	140	100	96	82	85	80	130	160	99	130	160	190
Y	14	11	19	3.1	9.1	12	9.3	17	11	14	10	12	14	11	14	7.4	8.1	13	8.9
Hf	9.7	2.6	18	0.8	0.4	2.9	3.7	3.3	2.9	2.6	2.2	2.3	2.1	3.1	3.7	2.5	3	3.8	4.2
Ta	2	0.7	1.7	0.1	0.2	1.1	0.8	0.6	0.9	0.5	0.4	0.5	0.4	0.6	0.2	0.5	0.7	0.9	0.7
W	254	48	111	3	<5	26	125	49	96	27	13	34	18	26	31	27	103	81	76
As	18	105	3590	39	4730	182	15	19	141	68	424	71	86	725	551	150	380	207	475
Sb	1.1	5.2	960	6.5	4130	2.5	1.6	1.9	17	9.4	23	13	10	587	184	12	1100	308	1870

Table 6.1 (continued)

	Silicified Crystal tuff with Sulfur Matrix			Sulfur Mud	Char-coal	Clay-Altered Lapilli Tuff			Clay-Altered Lapilli Tuff with Native Sulfur							Organic-rich Silicifed Tuff		
DR-	85-06	89c	102-05	89a	113-06	81-GA	82-GA	97-04	95a	98-02a	02b	07a	07b	113b	113-05	110k	110b	113c	113d
Hg	0.5	230	15	250	12000	2	41	84	12	12	9	14	900	45	56	21	23	21	21
Cu	5	5	12	5	5	10	11	15	15	11	12	5	5	5	12	5	12	15	13
Zn	39	33	200	29	20	29	240	67	28	34	53	30	23	14	26	25	53	53	34
Pb	9	8	14	3	3	10	33	11	9	10	8	9	8	10	7	13	13	14	9
Ag	<0.1	<0.1	0.4	<0.1	<0.1	0.1	0.4	0.2	0.4	0.4	0.3	<0.1	<0.1	<0.1	2.3	0.1	1	<0.1	<0.1
Au (ppb)	<2	<2	39	<2	<30	3	<2	<2	<2	<2	<2	<2	<2	<2	124	<2	<2	<2	<5
Bi	0.1	0.1	0.1	0.1	0.1	0.1	0.1	0.1	0.1	0.1	0.1	0.1	0.1	0.1	0.1	0.1	0.1	0.1	0.1
Cd	0.1	0.1	0.2	0.1	0.3	0.1	0.7	0.1	0.3	0.4	0.2	0.5	0.1	0.1	0.3	0.4	0.1	0.1	0.1
Ga	8.9	9.4	15	3.2	4.3	17	18	17	13	13	12	11	11	13	14	7.6	11	16	11
Tl	0.6	0.8	180	8.8	130	2.3	1.6	1.3	11	5.2	7.8	6.6	6.5	63	48	2.9	61	56	45
In	<0.1	<0.1	0.1	<0.1	0.1	<0.1	<0.1	0.1	<0.1	<0.1	0.1	<0.1	<0.1	<0.1	<0.1	<0.1	<0.1	<0.1	<0.1
Co	32	7	19	3	46	14	19	10	16	12	14	9	11	9	9	6	17	18	16
Se	<3	<3	18	5	<3	<3	<3	<3	<3	<3	<3	<3	<3	<3	<3	<3	<3	<3	<3
Te	<0.1	<0.1	<0.1	<0.1	<0.1	<0.1	<0.1	<0.1	<0.1	<0.1	<0.1	<0.1	<0.1	<0.1	<0.1	<0.1	<0.1	<0.1	<0.1
Mo	22	7.4	13	6.7	89	27	43	20	65	92	55	100	5	2.5	55	85	2.4	2.1	2.9
Ni	5	5	5	5	5	5	11	5	5	10	10	10	5	5	11	5	5	11	5
La	13	12	13	3.5	1.8	13	15	17	12	12	12	12	11	19	5.8	9.1	11	20	14
Ce	25	24	30	8	3.8	26	30	34	25	25	22	24	22	40	21	20	23	44	27
Pr	3.0	2.8	3.9	0.9	0.5	2.9	3	3.8	2.8	2.9	2.5	2.7	2.5	4.7	2.9	2.2	2.4	4.9	3
Nd	12	11	16	3.4	2.1	11	10	15	11	11	9.9	11	9.6	18	11	8.3	9	18	11
Sm	2.2	2.3	3	0.6	0.4	2.4	1.7	3.4	2.2	2.2	2.1	2	2	3	2.3	1.7	1.5	3.1	1.8
Eu	0.5	0.5	0.9	0.1	0.1	0.8	0.6	0.9	0.6	0.7	0.6	0.6	0.5	0.9	0.7	0.5	0.5	0.8	0.5
Gd	2.1	2	2.6	0.6	0.7	2.2	1.1	3.2	1.9	2.1	1.7	1.8	1.9	2.1	1.9	1.3	1.3	2.4	1.4
Tb	0.3	0.3	0.4	0.1	0.2	0.4	0.2	0.5	0.3	0.4	0.3	0.3	0.3	0.3	0.3	0.2	0.2	0.4	0.2
Dy	2.1	1.8	2.7	0.6	1.1	2.1	1.4	2.9	1.9	2.2	1.7	1.8	2	1.7	2.1	1.2	1.3	2.3	1.4
Ho	0.5	0.4	0.6	0.1	0.3	0.4	0.3	0.6	0.4	0.5	0.4	0.4	0.5	0.4	0.5	0.3	0.3	0.5	0.3
Er	1.5	1.1	2	0.3	1	1.2	1	1.6	1.2	1.4	1	1.1	1.3	1	1.4	0.7	0.8	1.3	0.9
Tm	0.2	0.2	0.4	0.1	0.2	0.2	0.2	0.3	0.2	0.2	0.2	0.2	0.2	0.2	0.2	0.1	0.1	0.2	0.2
Yb	1.7	1.2	2.6	0.4	1.5	1.4	1.3	1.6	1.3	1.5	1.1	1.3	1.5	1.2	1.6	0.9	1.0	1.4	1.1
Lu	0.3	0.2	0.5	0.1	0.2	0.2	0.2	0.3	0.2	0.3	0.2	0.2	0.2	0.2	0.3	0.1	0.2	0.2	0.2
Al2O3/ TiO2	10.9	30.4	3.4	25.0	30.0	49.7	49.0	30.4	35.5	33.6	33.9	35.0	39.3	20.5	19.3	23.5	28.5	33.5	20.8
Al2O3/ Na2O	3.5	3.9	5.9	3.6	1.2	4.4	5.7	5.1	5.1	5.3	6.4	5.8	7.1	8.5	7.2	5.3	3.6	4.1	3.8
Al2O3/Na2O+CaO	2.2	2.9	5.1	2.7	1.0	2.1	3.3	2.8	2.8	3.2	4.3	3.6	6.1	7.4	5.5	3.9	2.7	3.1	2.8
Na/K	2.5	2.0	1.1	2.4	47.4	4.7	6.6	6.6	4.1	3.4	3.0	3.6	5.3	6.8	2.8	4.8	2.7	2.6	2.5
Si/Al	14.7	8.2	7.4	7.5	5.5	6.7	5.6	5.4	5.8	6.0	5.4	6.0	5.3	5.5	5.3	7.4	11.8	7.9	11.6
A/CNK[1]	1.0	1.3	1.7	1.2	0.6	1.1	1.8	1.5	1.4	1.6	2.1	1.8	3.1	3.9	2.6	2.0	1.2	1.4	1.3
A/NK[2]	1.5	1.6	1.9	1.5	0.7	2.2	3.0	2.7	2.5	2.5	2.9	2.8	3.6	4.5	3.2	2.6	1.6	1.8	1.6
CIA[3]	51.2	56.0	63.2	54.8	37.9	52.9	63.8	59.9	58.7	61.2	67.5	64.1	75.8	79.7	72.2	66.9	55.5	59.0	56.1

Table 6.1 (continued)

	Silicified Crystal tuff with Sulfur Matrix			Sulfur Mud	Char-coal	Clay-Altered Lapilli Tuff			Clay-Altered Lapilli Tuff with Native Sulfur								Organic-rich Silicifed Tuff		
DR-	85-06	89c	102-05	89a	113-06	81-GA	82-GA	97-04	95a	98-02a	02b	07a	07b	113b	113-05	110k	110b	113c	113d
HASHI-AI[a]	39.1	43.8	63.7	42.3	27.2	23.8	25.7	40.6	31.4	46.3	56.6	49.7	67.0	62.2	68.6	81.6	35.9	41.8	37.5
SERI[b]	3.3	3.2	2.8	1.7	1.8	4.8	4.4	4.4	3.7	3.3	3.0	2.9	2.7	2.4	2.6	2.4	3.7	4.5	3.7
CCPI[c]	52.9	44.6	74.0	46.0	89.2	43.9	52.1	70.0	51.0	59.5	71.6	62.3	76.0	75.7	75.6	84.0	36.7	40.3	38.8
AAAI[d]	60.8	53.6	58.3	48.0	19.9	42.1	47.2	36.3	42.8	41.2	41.0	42.1	40.5	49.5	38.3	24.8	62.1	53.4	62.1
SI[e]	89.7	82.8	81.3	81.5	76.3	79.7	76.7	76.2	77.2	78.0	76.0	77.9	75.7	76.5	75.6	81.4	87.5	82.4	87.2
SºI[g]	50.2	81.6	62.9	97.0	97.4	5.4	9.7	22.0	65.5	68.1	64.3	75.5	71.4	69.8	71.9	85.5	51.7	22.6	46.1
LOI-(S+C)[10]	2.7	4.5	0.4	0.2	8.0	3.1	4.2	5.9	5.2	7.7	9.4	6.7	12.0	10.5	7.5	5.2	2.2	3.9	2.5
Zr/Y	32.1	9.0	46.8	9.7	4.7	9.2	16.1	8.2	9.1	6.9	8.2	7.1	5.7	11.8	11.4	13.4	16.0	12.3	21.3
Zr/Sc	53.6	18.0	52.4	15.0	35.8	12.9	13.6	9.3	11.6	10.9	9.5	11.0	10.1	18.6	21.9	24.8	27.1	18.2	30.6
Zr/Nb	40.9	19.8	28.7	18.8	2.3	20.8	23.4	25.0	18.9	18.8	20.5	19.3	21.1	15.5	20.8	23.6	24.5	21.9	29.2
Zr/Ti(ppm)	4.8	2.8	2.2	2.4	11.4	2.6	3.1	2.0	2.1	2.1	1.7	2.1	2.1	1.8	2.2	2.6	3.1	3.0	3.1
Zr/Hf	46.4	38.1	49.4	35.7	97.7	37.9	40.5	42.4	34.5	36.9	37.3	37.0	38.1	41.9	43.2	39.6	43.3	42.1	45.2
Y/Ti(ppm)	0.1	0.3	<0.1	0.2	2.4	0.3	0.2	0.2	0.2	0.3	0.2	0.3	0.4	0.1	0.2	0.2	0.2	0.2	0.1
Nb/Y	0.8	0.5	1.6	0.5	2.1	0.4	0.7	0.3	0.5	0.4	0.4	0.4	0.3	0.8	0.6	0.6	0.7	0.6	0.7
Nb/Ta	5.5	7.7	18.2	12.3	90.5	4.8	7.8	9.2	5.7	9.4	10.0	9.0	10.3	13.8	36.7	8.9	7.4	7.9	9.6
Nb/U	1.4	2.3	6.6	0.3	7.9	0.4	0.3	0.8	0.2	0.3	0.4	0.2	2.1	4.2	0.3	0.2	3.3	3.7	4.1
Th/Nb	0.5	0.9	0.1	1.2	0.0	0.9	1.0	1.2	1.0	1.0	1.1	0.9	1.2	0.7	0.6	0.9	1.0	1.0	0.8
Nb/La	0.8	0.4	2.4	0.5	10.6	0.4	0.4	0.3	0.4	0.4	0.3	0.4	0.3	0.4	1.3	0.5	0.5	0.4	0.5
Nb/Hf	1.1	1.9	1.7	1.9	43.2	1.8	1.7	1.7	1.8	2.0	1.8	1.9	1.8	2.7	2.1	1.7	1.8	1.9	1.5

Table 6.1 (continued)

	Silicified Vitric Tuff					Quartz-Pyrite Veins			
DR-	110c	110e	110i	110j	110wp	110d	110e	d2	d1
SiO2 (wt%)	75.30	80.40	80.40	79.70	70.50	55.30	36.30	--	--
TiO2	0.12	0.11	0.14	0.13	0.26	0.04	0.01	--	--
Al2O3	6.10	6.10	7.50	7.50	13.70	1.60	0.60	--	--
Fe2O3	8.02	2.06	1.35	1.71	1.88	22.10	37.00	1.1	0.3
MnO	0.03	0.03	0.04	0.04	0.06	0.01	0.01	--	--
MgO	0.19	0.14	0.23	0.18	0.29	0.08	0.04	--	--
CaO	0.63	0.64	0.71	0.72	1.14	0.22	0.10	--	--
Na2O	1.72	1.80	2.41	2.25	3.37	0.49	0.21	0.1	0.1
K2O	1.39	1.44	1.77	1.93	2.82	0.37	0.14	--	--
CO2	0.10	0.05	0.05	0.05	0.05	0.10	0.05	--	--
C	0.10	0.10	0.10	0.10	0.10	0.40	0.40	--	--
P2O5	0.15	0.02	0.04	0.02	0.09	0.01	0.01	--	--
S	4.90	3.61	0.98	3.18	0.97	22.60	36.00	--	--
Total	98.90	96.70	95.80	97.60	95.50	103.30	110.90	--	--
LOI	7.10	7.00	5.20	7.20	7.10	19.20	26.90	--	--
Ba (ppm)	600	1860	500	560	1700	180	50	25	25
Sr	68	64	64	72	110	21	20	--	--
Rb	48	49	56	58	84	14	5	7.5	7.5
Cs	9.4	7.1	9.4	9.1	15	2.8	1.1	0.5	0.5
Be	0.9	1	1.1	1.2	1.7	0.3	0.3	--	--
F	299	217	254	236	--	25	--	--	--
Cl	1876	2015	4501	3390	--	<100	--	--	--
Br	10	7.2	19.5	13.3	19.7	4.4	<0.5	4	3.3
Cr	<10	<10	<10	<10	<10	12	17	31	<5
V	18	5	8	9	16	<5	<5	--	--
Sc	2.7	2.8	3.5	3.2	6.4	1.2	0.6	0.3	0.2
Sn	2	1.2	2	1.5	2.5	1.3	0.3	--	--
U	2.9	1.3	6.2	1.7	11	1.2	0.6	0.3	0.3
Th	4.2	4.2	4.7	5.3	9.7	1.2	0.5	0.1	0.1
Nb	4.4	4.3	5.5	5.1	8.7	1.4	0.5	--	--
Zr	71	81	90	88	170	24	9.1	--	--
Y	12	12	15	14	24	3.4	1.3	--	--
Hf	1.9	2.2	2.5	2.6	4.6	0.7	0.2	<1	<1
Ta	1.3	1.7	2.2	1.8	0.7	0.7	<0.1	--	--
W	190	252	297	245	<1	260	<1	<1	<1
As	1300	214	30.1	107	51	1480	2130	269	40
Sb	31	1.2	1	0.8	1.6	1.2	7.2	15	6.5

Table 6.1 (continued)

	Silicified Vitric Tuff					Quartz-Pyrite Veins			
DR-	110c	110e	110i	110j	110wp	110d	110e	d2	d1
Hg	130	26	0.5	0.5	0.5	520	800	24	72
Cu	5	5	5	5	5	5	5	--	--
Zn	38	32	32	24	46	230	310	100	204
Pb	37	15	16	29	80	4	1	--	--
Ag	1.2	0.4	0.6	0.2	<0.1	0.6	0.7	<5	<5
Au (ppb)	<2	<2	<2	<2	<2	<2	<2	<2	5.0
Bi	0.1	0.1	0.1	0.1	0.2	0.1	0.1	--	--
Cd	0.1	0.1	0.2	0.1	0.1	0.1	0.1	--	--
Ga	6.6	6.6	8.5	7.9	15	2.5	1.3	--	--
Tl	59	7.8	0.7	0.4	0.7	110	190	--	--
In	<0.1	<0.1	<0.1	0.1	<0.1	<0.1	<0.1	--	--
Co	34	36	43	53	3	26	1	7	5
Se	<3	<3	<3	<3	<3	<3	4	<3	4
Te	<0.1	<0.1	<0.1	<0.1	<0.1	<0.1	<0.1	--	--
Mo	9.4	2.3	27	3.9	64	11	15	--	--
Ni	5	5	5	5	5	5	5	--	--
La	12	12	13	13	20	3	0.9	--	--
Ce	23	23	26	26	43	6.4	2.1	--	--
Pr	2.6	2.6	3.2	3	5.1	0.7	0.3	--	--
Nd	10	10	12	12	20	3	1.1	--	--
Sm	1.9	2	2.3	2.6	4.2	0.6	0.2	--	--
Eu	0.3	0.4	0.4	0.4	0.8	0.1	<0.1	--	--
Gd	1.7	1.9	2.1	2.2	3.8	0.5	0.2	--	--
Tb	0.3	0.3	0.3	0.4	0.6	0.1	<0.1	--	--
Dy	1.8	1.9	2.2	2.3	3.7	0.5	0.2	--	--
Ho	0.4	0.4	0.5	0.5	0.8	0.1	<0.1	--	--
Er	1.1	1.2	1.4	1.4	2.4	0.3	0.1	--	--
Tm	0.2	0.2	0.2	0.2	0.4	0.1	<0.1	--	--
Yb	1.2	1.4	1.5	1.6	2.6	0.4	0.1	--	--
Lu	0.2	0.2	0.2	0.3	0.4	0.1	<0.1	--	--
Al2O3/ TiO2	50.8	55.5	53.6	57.7	52.7	40.0	60.0	--	--
Al2O3/ Na2O	3.5	3.4	3.1	3.3	4.1	3.3	2.9	--	--
Al2O3/Na2O+CaO	2.6	2.5	2.4	2.5	3.0	2.3	1.9	--	--
Na/K	1.9	1.9	2.1	1.8	1.8	2.0	2.3	--	--
Si/Al	20.9	22.4	18.2	18.0	8.7	58.6	102.7	--	--
A/CNK[1]	1.1	1.1	1.0	1.1	1.3	1.0	0.9	--	--
A/NK[2]	1.4	1.3	1.3	1.3	1.6	1.3	1.2	--	--
CIA[3]	52.7	51.8	51.1	51.4	56.2	49.9	46.9	--	--

Table 6.1 (continued)

	Silicified Vitric Tuff					Quartz-Pyrite Veins			
DR-	110c	110e	110i	110j	110wp	110d	110e	d2	d1
HASHI-AI[4]	40.2	39.3	39.1	41.5	40.8	38.8	36.7	--	--
SERI[5]	2.7	2.8	3.4	3.3	4.4	1.5	1.2	--	--
CCPI[6]	72.5	40.4	27.4	31.1	26.0	96.3	99.1	--	--
AAAI[7]	74.8	75.7	70.6	71.7	59.5	87.5	91.2	--	--
SI[8]	92.5	92.9	91.5	91.4	83.7	97.2	98.4	--	--
S°I[9]	44.5	37.2	11.6	29.8	6.6	93.4	98.4	--	--
LOI-(S+C)[10]	2.1	3.3	4.1	3.9	6.0	-3.8	-9.5	--	--
Zr/Y	5.9	6.8	6.0	6.3	7.1	7.1	7.0	--	--
Zr/Sc	26.3	28.9	25.7	27.5	26.6	20.0	15.2	--	--
Zr/Nb	16.1	18.8	16.4	17.3	19.5	17.1	17.8	--	--
Zr/Ti(ppm)	4.7	5.9	5.1	5.4	5.2	4.8	7.3	--	--
Zr/Hf	37.4	36.8	36.0	33.8	37.0	36.4	37.9	--	--
Y/Ti(ppm)	0.8	0.9	0.9	0.9	0.7	0.7	1.0	--	--
Nb/Y	0.4	0.4	0.4	0.4	0.4	0.4	0.4	--	--
Nb/Ta	3.4	2.5	2.5	2.8	12.8	2.0	20.4	--	--
Nb/U	1.5	3.3	0.9	3.0	0.8	1.2	0.8	--	--
Th/Nb	1.0	1.0	0.9	1.0	1.1	0.9	0.9	--	--
Nb/La	0.4	0.4	0.4	0.4	0.4	0.5	0.6	--	--
Nb/Hf	2.3	2.0	2.2	2.0	1.9	2.1	2.1	--	--

1 A/CNK = molar Al2O3/(CaO + Na2O +K2O) (Maniar and Poccoli, 1989)
2 A/NK = molar Al2O3/(Na2O +K2O) (Maniar and Poccoli, 1989)
3 CIA = Chemical index of alteration = molar ratio of Al2O3/(Al2O3 + Na2O + CaO + K2O) (Fedo et al. 1995)
4 HASHI-AI= Hashimoto-alteration index = 100 x [(K2O +MgO)/(K2O +MgO + Na2O + CaO)] (Ishikawa et al., 1979)
5 SERI = Sericite index = K2O /(K2O + Na2O) (Sakai and Date, 1983)
6 CCPI = chlorite-carbonate-pyrite index = 100 x [(MgO + FeO*)/(MgO + FeO*+K2O + Na2O)] (Large et al., 2001)
7 AAAI = Advanced argillic alteration - index = 100 x [SiO2/(SiO2 + (10 x MgO) + (10 x CaO) + (10 x Na2O)] (Williams and Davidson, 2004)
8 SI = Silicification Index = 100 x (SiO2 / (SiO2 + Al2O3)) (van Ruitenbeek et al. 2005)
9 S°I = Native sulfur index = (100 * S)/(S + Al2O3)
10 LOI-S=Loss on ignition - sulfur

6.1 Results

Previous workers have suggested that the volcaniclastic material contained in the Whakatane graben, and recovered from the Calypso hydrothermal vents, is an accumulation of felsic volcanic tephra, akin to subaerial ignimbrite deposits on the North Island of New Zealand. These deposits are formed during caldera building eruptive events on the subaerial portion of the TVZ (Davey et al., 1995). The close proximity of White Island suggests this volcano also may have contributed andesitic material to the sediments of the CHVF. Geochemical analysis of felsic ignimbrites from the TVZ (Sutton et al., 1995; Bignall et al., 1996) and andesite samples from White Island (Cole et al., 2000) along with alkali rhyolites from Mayor Island (Figure 1.1; Ewart et al., 1968) were compared with the Calypso rock samples in an attempt to identify the magmatic affinity and possible sources of the volcaniclastic material recovered from the CHVF.

6.1.2 Preliminary Assessment of Major Element Data

The bulk rock geochemistry of the recovered volcaniclastic material in the CHVF has been strongly affected by hydrothermal alteration. Visual observation and mineralogical analysis of the Calypso sample suite indicate that the clay-altered with native sulfur lithofacies have been altered to montmorillonite with trace quantities of illite and large quantities of native sulfur have been precipitated in the pore spaces of these rocks.

Smectite forms by the hydration of primary igneous material; this process is believed to cause only slight variation in the major element chemistry of rock (cf. Gifkins et al., 2000, as cited in Gifkins and Allen, 2001). However, significant quantities of silica, volatile metals, and pyrite (veins) have been added to the volcaniclastic protolith of the various silicified lithofacies. Significant barite mineralization in the barite-rich silicified tuff also has diluted the major and minor element concentrations.

A plot of SiO_2 vs. $Na_2O + K_2O$ (after Le Bas et al., 1986) shows large variations in SiO_2 (35 – 84 wt %) and alkali concentrations of the Calypso suite (~1 to 6 wt% $Na_2O + K_2O$; Figure 6.1). The least-altered vitric ash sample DR-110wp plots within the compositional field of the TVZ ignimbrites. The least clay-altered lapilli tuff samples without sulfur (DR-97-04 and 81-82 GTVA) plot within the compositional field of the White Island andesite samples. Clay-altered laplli tuff with native sulfur samples (DR-98, -95, -113) and silicified crystal tuff with native sulfur samples (DR-89c and DR-102-05) contain low concentrations of silica (~35 – 48%). Silicified samples show low concentrations of alkali metals and plot within or above the SiO_2 range of TVZ ignimbrites. If it is assumed that no Si, S, or Ba has been added or removed in the least-altered samples the most likely protoliths of the volcaniclastic material are TVZ rhyolite and White Island andesite.

Calypso samples display similar geochemical distributions when plotted on the AFM [(Na2O + K2O) – FeO – MgO] plot of Irvine and Baragar (1971) and on a Al-Fe-Ti ternary plot of Rickwood (1989) (Figure 6.2). The least-altered felsic ash (DR-110wp) plots within the compositional fields of the TVZ ignimbrite. The least altered lapilli tuff

(DR-97-04) and clay-altered lapilli with native sulfur samples (DR-95, -98, - 113b, 113-05) plot within, or very near, to the compositional field of the White Island andesite samples. Sample DR-110k shows a strong Mg enrichment reflecting the presence vermiculite or mixed layer chlorite-smectite and talc in the sample. Sample DR-102-05 contains elevated Fe.

A plot of Al_2O_3/Na_2O vs. Na_2O shows that the majority of the Calypso samples lie within the normal Na_2O range for volcanic rocks of between 2 and 5 wt % (Figure 6.3A). Low Na_2O values may be a reflection of dilution by native sulfur (e.g., clay-altered lapilli tuff with sulfur; DR-98, -113b, -113-05), silica, and barite. However, Na-depletion is typical during breakdown of volcanic glass and feldspars during the formation of phyllosilicate minerals in the submarine settings (e.g., Ishikawa et al., 1976; Munha and Kerrich, 1980; Gifkins and Allen, 2001). Andesite flows collected from the submarine environment at White Island display a loss of Na_2O relative to subaerial andesite samples (Cole et al., 2000); this trend may reflect Na loss during the hydration of primary volcanic material and the formation of secondary clays. A plot of Al_2O_3/Na_2O vs. $K_2O/(K_2O + Na_2O)$ is used to remove the effect of element dilution by addition of silica, sulfur, and barite (Figure 6.3B). Calypso samples cluster closer together than plot A with a clear separation between clay-altered samples with higher Na values and silicified samples with lower Na values. Submerged White Island andesite samples show Na loss relative as observed in plot A.

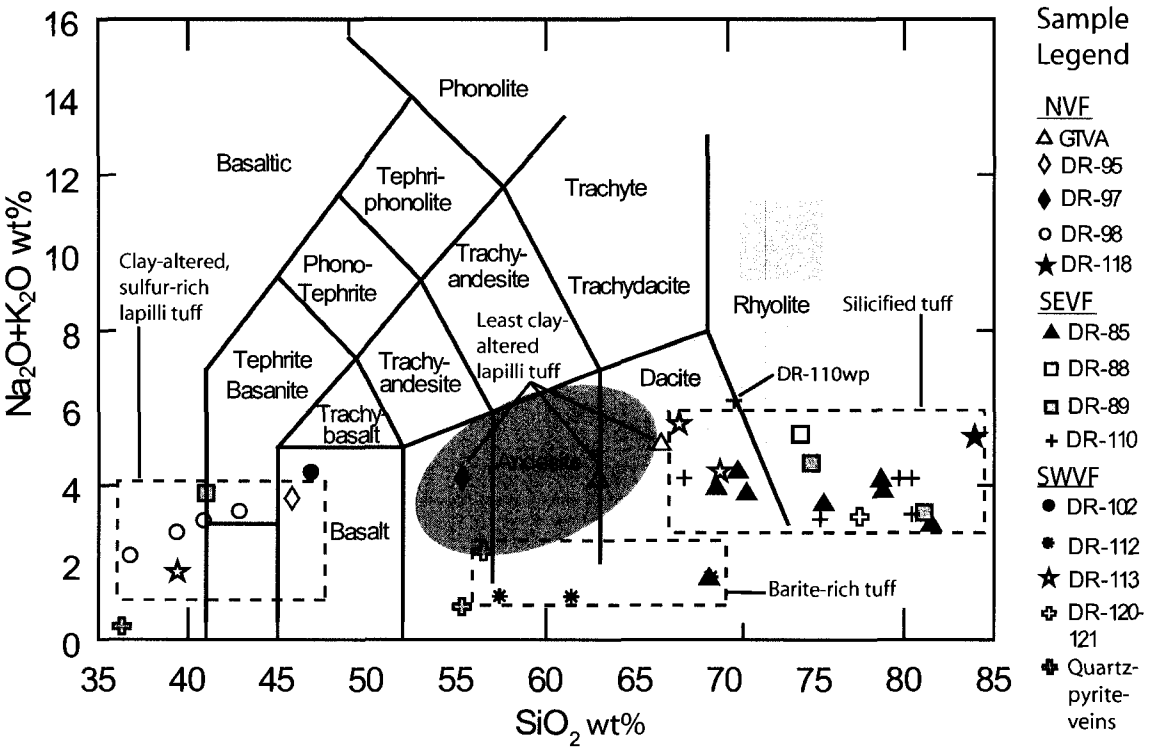

Figure 6.1. Total alkalis versus silica plot of Le Bas et al. (1986). The shaded blue oval denotes the compositional space of the White Island andesite sample suite (Cole et al., 2000), the shaded orange box represents the compositional space of ignimbrites from the Taupo Volcanic Zone (TVZ; Bignall et al., 1996, Sutton et al., 1995), and the red box represents the composition space of Mayor Island rhyolite samples (Ewart et al., 1968). Calypso samples show considerable variation in chemical composition. Initial major element compositions have been altered by the addition of silica and native sulfur. Although normally used for unaltered samples, this diagram illustrates the effects of hydrothermal alteration in the Calypso sample suite.

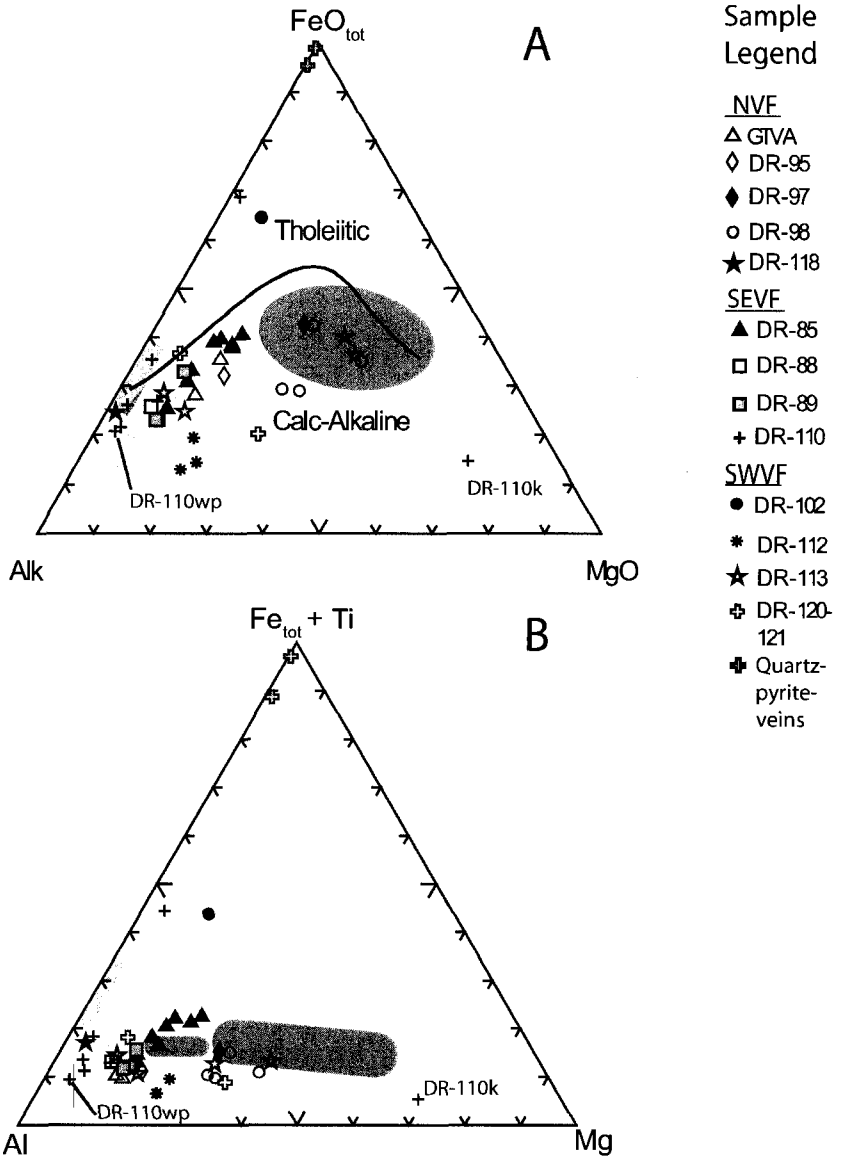

Figure 6.2. Major element plots of the Calypso samples subdivided by samples series. A. AFM [($Na_2O + K_2O$) - FeO_{tot} - MgO] plot of Irvine and Baragar (1971). B. Al - Fe+Ti - Mg plot after Rickwood (1989). The shaded blue ovals denote the compositional space of the White Island Andesite sample suite (Cole et al., 2000), the shaded orange box represents the compositional space of ignimbrites from the Taupo Volcanic Zone (TVZ; Sutton et al., 1995; Bignall et al., 1996), and the red box represents the composition space of Mayor Island rhyolite samples (Ewart et al., 1968). Clay-altered lapilli tuff samples from the NVF (DR-97-04, DR-95, DR-98) and SWVF (DR-113b, DR-113-05) have higher Fe, Mg, and Ti values and lower Si values relative to other Calypso samples and plot in the field of White Island andesite samples. Silicified tuff samples plot primarily within the compositional field of the TVZ ignimbrite samples; DR-85 series plots between the TVZ ignimbrite and the White Island andesite field. Barite-rich samples DR-112 and DR-120-121 from the SWVF plot outside of the defined compositional fields. Although normally used for unaltered samples, these diagrams illustrate the effects of hydrothermal alteration in the Calypso sample suite.

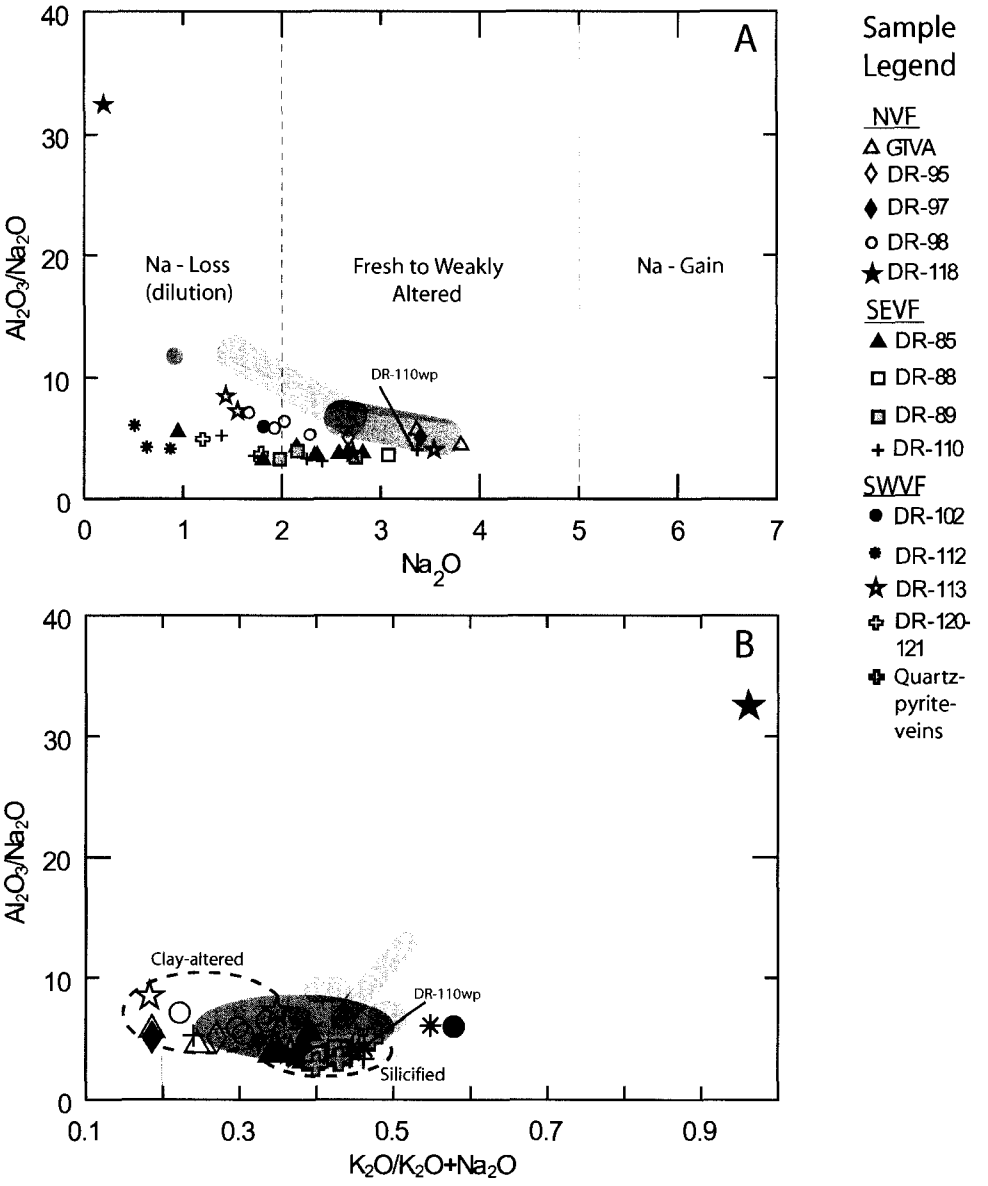

Figure 6.3. A. Plot of Al_2O_3/Na_2O vs. Na_2O values; samples are subdivided by series number. Shaded blue boxes represent the compositional range of subaerial White Island andesite samples, shaded green boxes represent the compositional range of submarine White Island andesite samples (Cole et al., 2000), and the shaded orange box represents the compositional space of ignimbrites from the Taupo Volcanic Zone (TVZ; Sutton et al., 1995; Bignall et al., 1996). Submerged White Island andesite samples and several of the Calypso samples including samples from the DR-113, DR-98, DR-120, DR-112, and DR-85 series show Na-loss relative to subaerial White Island andesite samples. The TVZ ignimbrites have a large range of Na_2O values. B. Plot of Al_2O_3/Na_2O vs. $K_2O/(K_2O + Na_2O)$ is used to remove the effect of element dilution by addition of silica, sulfur, and barite. Calypso samples cluster closer together than plot A with a clear separation between clay-altered samples with higher Na values and and silicified samples with lower Na values. Submerged White Island andesite samples show Na loss as observed in plot A.

6.2 Immobile-element Geochemistry

Major element analyses of the least-altered rock samples indicate that the silicified-vitric tuff lithofacies has a chemical composition equivalent to the TVZ ignimbrites. In comparison, the least clay-altered lapilli tuff has a chemical composition that approximates the White Island andesite samples. The majority of the Calypso rocks are altered and many samples have no obvious least altered equivalent sample. The most clay-altered samples are predominantly from the NVF, the most proximal vent field to White Island. Immobile-element geochemistry utilizes elements that are not affected by hydrothermal alteration and diagenetic processes to help identify the initial composition, to aid in determining the source of the volcaniclastic material, and to asses the gains and losses due to hydrothermal alteration.

The preliminary assessment of major element data suggests many major elements were likely mobile during hydrothermal alteration and/or diluted by addition of hydrothermal precipitates. The alteration of primary igneous materials to secondary minerals and the associated mass changes are well documented during submarine diagenesis (e.g., Fisher and Schmincke 1984; Gifkins and Allen 2001); in seafloor hydrothermal systems (e.g., Munha and Kerrich, 1980; Large et al., 2001), and in the subaerial epithermal environment (e.g., Hedenquist et al., 2000; Callaghan 2001; Simmons et al., 2005). Mineralogical changes are usually accompanied by mobility of major elements with the exception of Al and Ti, which can be shown to be immobile (MacLean,

1990; Barrett and Maclean, 1999), except during the most intense hydrothermal alteration (Finlow-Bates and Stumpfl, 1981). Similarly, the high field strength elements (HFSE; i.e., Y, Zr, Nb, Hf, Ta, Ga, and P) are highly immobile (e.g., Maclean, 1990) with minor exceptions (Finlow-Bates and Stumpfl, 1981), making them very useful for characterizing source regions or relative mass gains and losses of other elements, as they are largely unaffected by hydrothermal alteration or metamorphism.

Plots of TiO_2 vs. Al_2O_3, Zr, Nb, Y, and Hf and Zr vs. Al_2O_3, TiO_2 Nb, Y, and Hf were examined to test the mobility of these elements at Calypso (Figures 6.4, 6.5, 6.6, 6.7, 6.8; cf. MacLean and Barrett, 1993). Bi-variant plots of any two immobile elements will create linear arrays if the samples are cogenetic. The linear array forms an alteration line; mass gains of other elements (e.g., Si, Ba, S) will dilute the immobile element concentration of the altered samples, whereas mass loss of mobile elements (e.g., leaching of major cations) will increase the relative concentration of the remaining immobile elements.

This is demonstrated in the silicified vitric ash samples (Figure 6.4 A-D). Each immobile element pair forms a linear array suggesting that the samples are cogenetic. The linear arrays also indicate that the HFSEs and Al_2O_3 are immobile relative to TiO_2, and that the Y, Nb, Hf, TiO_2, and Al_2O_3 are immobile relative Zr. The least-altered sample (DR-110wp) has the highest concentrations of immobile elements of all the samples. The concentrations of immobile elements in the silicified samples are considerably lower because of dilution by silica addition. The immobile elements of the silicified crystal tuff lithofacies display similar trends (Figure 6.5, 6.6). However, there is more scatter of Al_2O_3 and Y indicating mobility relative to TiO_2 and Zr. Alternatively, differential alteration can cause these elements to be fractionated from one another (Young and Nesbitt, 1998). For

example titanium occurs primarily in mafic minerals, and Al_2O_3 is contained principally in feldspars which alter more readily.

Clay-altered lapilli samples from each vent field show a similar pattern with HFSE, TiO_2, and Zr forming linear arrays, and Al_2O_3 and Y showing some scatter (Figure 6.7). Samples DR-97-04, DR-113b, and DR-113-05 have somewhat different immobile element ratios than the other clay-altered samples indicating possible differences in the composition of the protolith. Immobile element ratios of clay-altered lapilli tuff with native sulfur (DR-98, DR-95) from the NVF alone also form coherent arrays, with Al_2O_3 and Y displaying the most scatter (Figure 6.8).

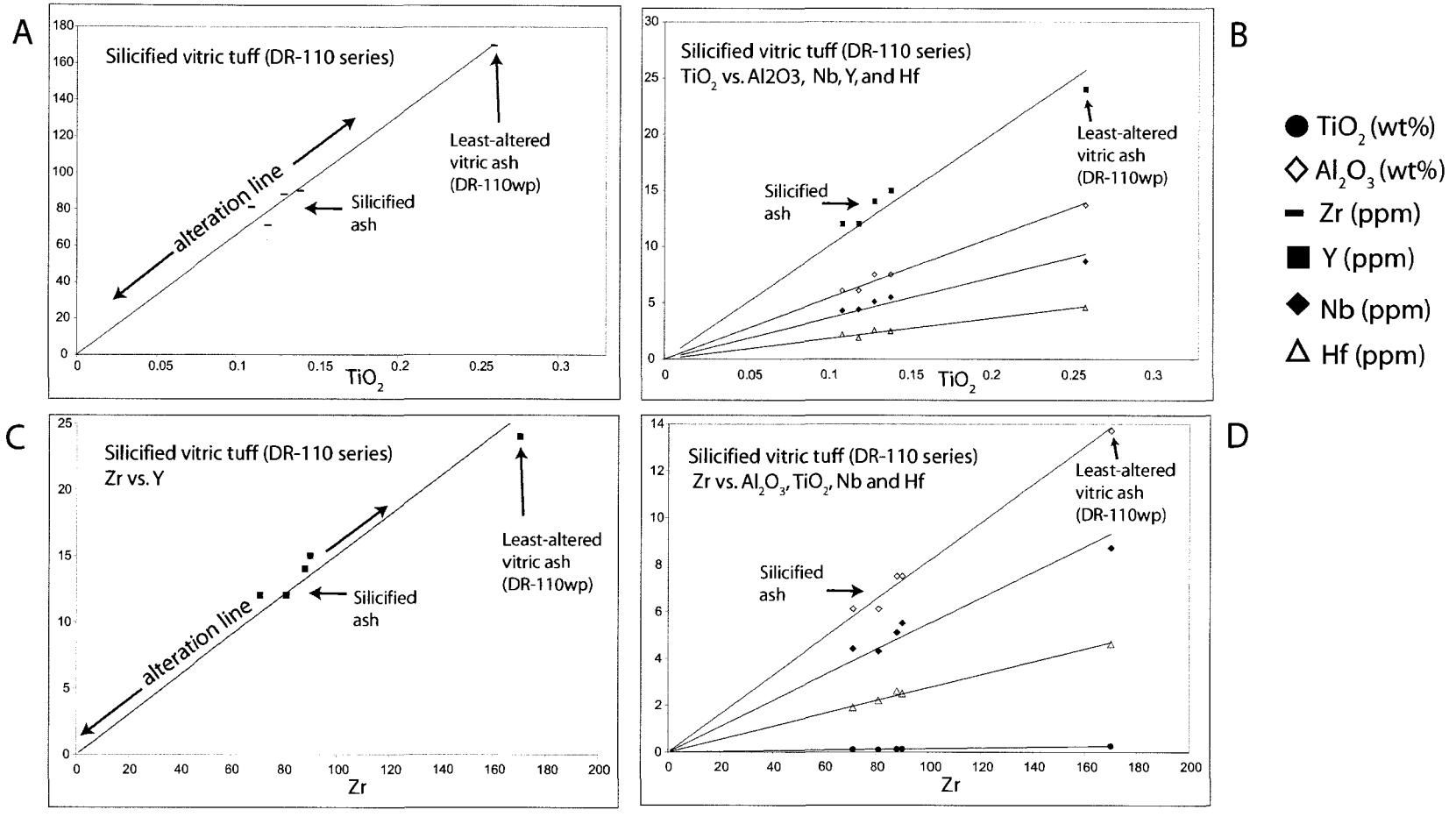

Figure 6.4. Immobile element ratios of silicified vitric tuff from the SEVF. A. TiO_2 vs. Zr. B. TiO_2 vs. Al_2O_3, Nb, Y, and Hf. Least altered (non-silicified, weakly lithified ash) sample DR-110wp has the highest ratio values, silicified tuff sample form a linear array on the alteration line at lower ratio values (MacLean and Barrett, 1993). Dilution of immobile elements is caused by silica addition; linear arrays suggest Al_2O_3, Y, Nb, Zr, and Hf were immobile relative to TiO_2. C. Zr vs. Y. D. Zr vs. Al_2O_3, Nb, Hf, and TiO_2. Linear arrays suggest Al_2O_3, TiO_2, Y, Nb, and Hf are immobile relative to Zr.

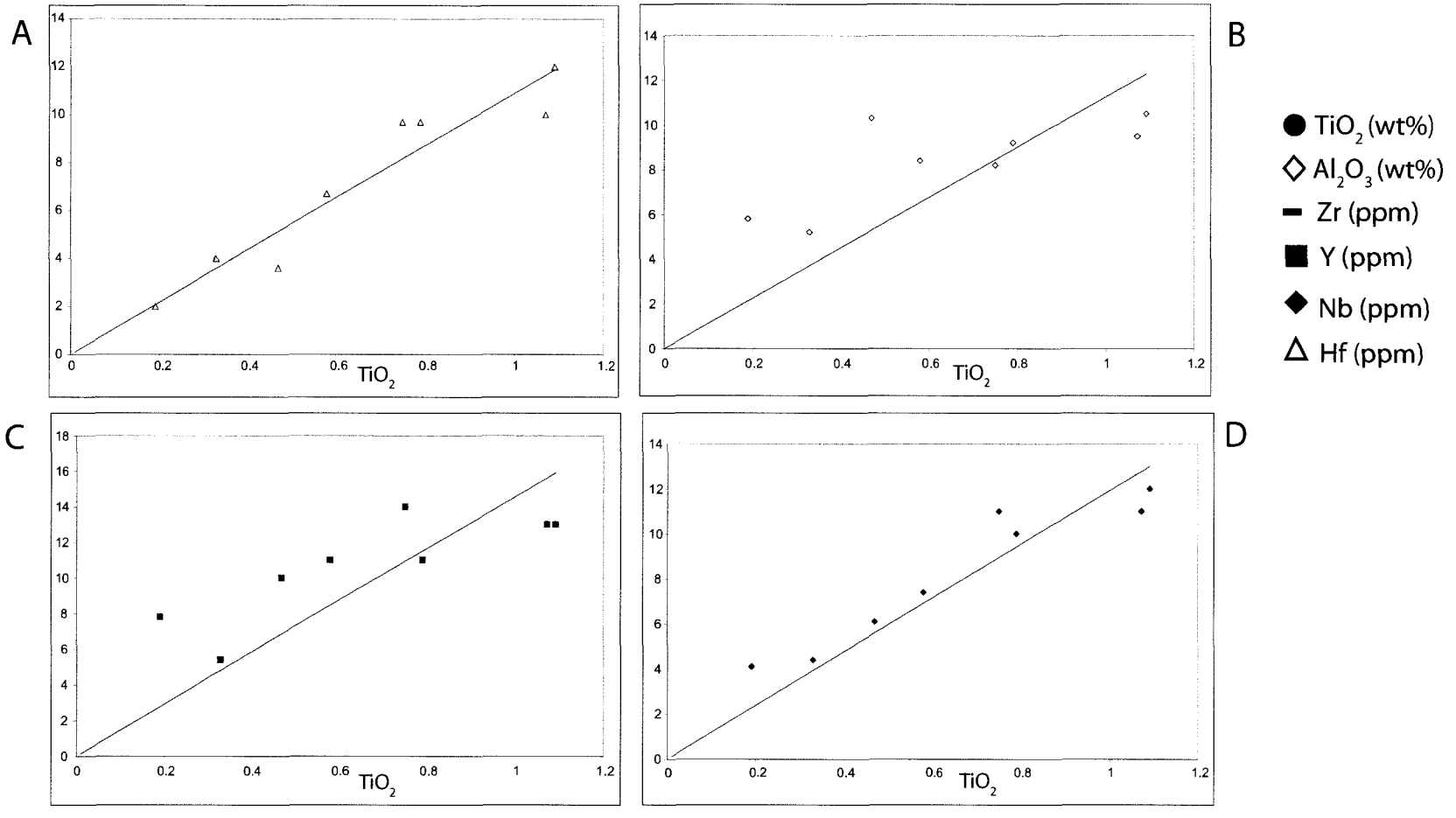

Figure 6.5 Immobile element ratios of silicified crystal tuff (DR-85 series) from the SEVF. A. TiO_2 vs. Hf. B. TiO_2 vs. Al_2O_3. C. TiO_2 vs. Y. D. TiO_2 vs. Nb. Linear arrays of Nb and Hf suggest these elements are immobile relative to TiO_2 (MacLean and Barrett, 1993). Al_2O_3 and Y show more scatter indicating element variation during alteration or differential alteration (see text), TiO_2 vs. Zr is shown in Figure 6.6.

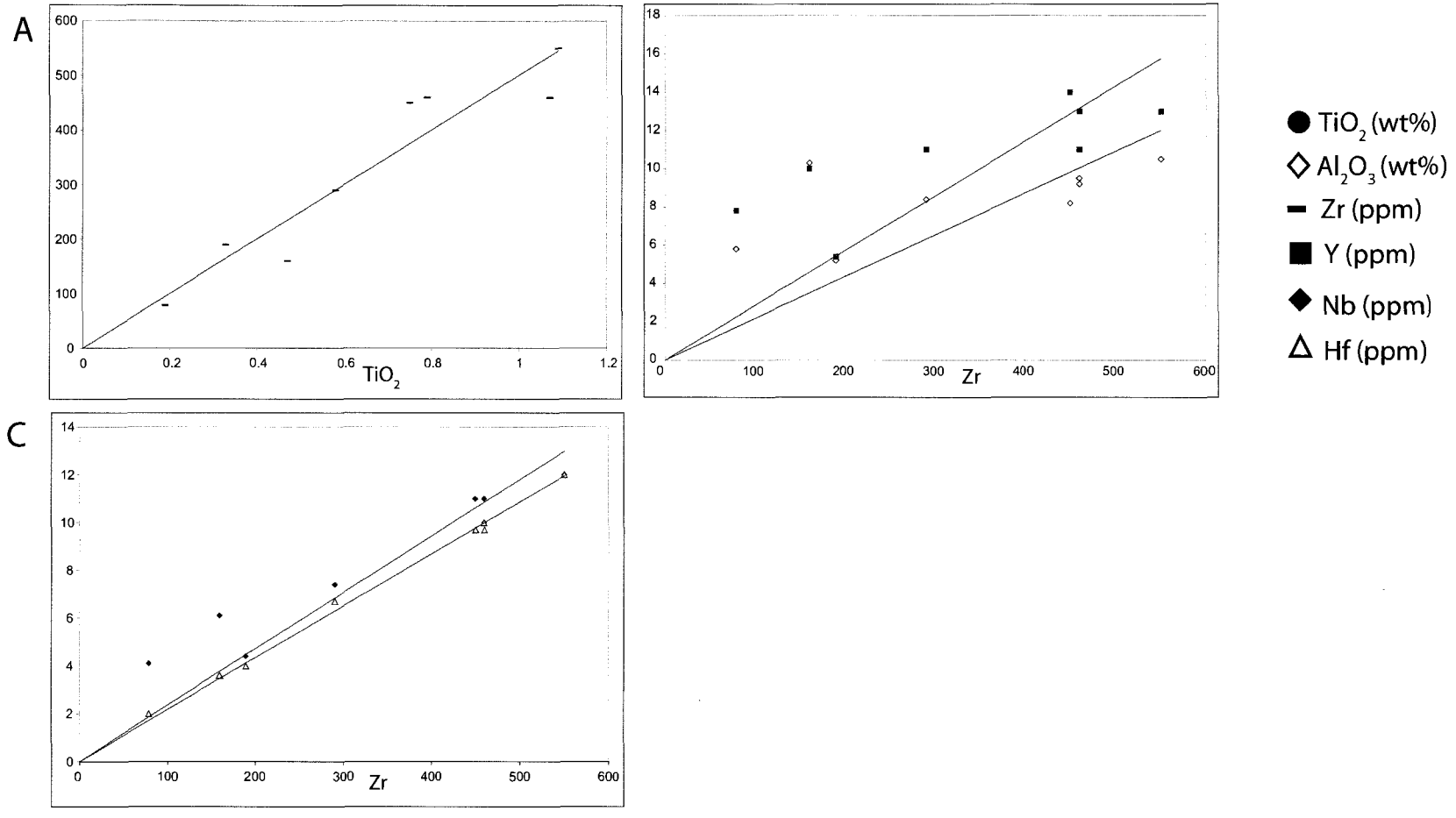

Figure 6.6. Immobile element ratios of silicified crystal tuff (DR-85 series) from the SEVF. A. TiO_2 vs. Zr. B. Zr vs. Al_2O_3 and Y. C. Zr vs. Nb and Hf. Linear arrays suggest that Zr is immobile relative to TiO_2 and Nb and Hf are immobile relative to Zr (MacLean and Barrett, 1993). Al_2O_3 and Y show more scatter indicating element variation during alteration or differential alteration (see text).

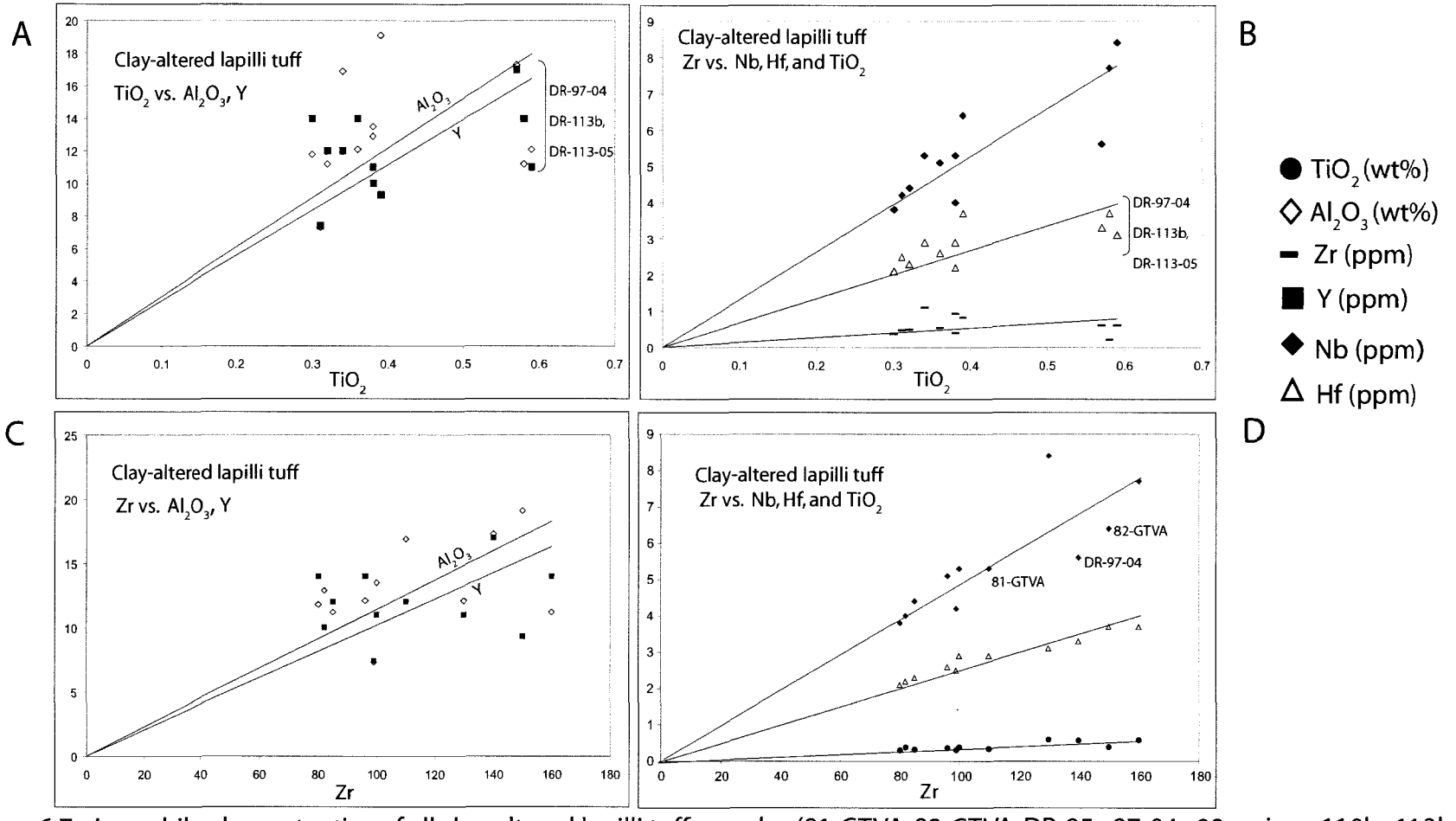

Figure 6.7. Immobile element ratios of all clay-altered lapilli tuff samples (81-GTVA, 82-GTVA, DR-95, -97-04, -98 series, - 110k, -113b, -113-05) recovered from the NVF, SEVF, and SWVF. A. TiO_2 vs. Al_2O_3 and Y. B. TiO_2 vs. Nb, Hf, and Zr. C. Zr vs. Al_2O_3 and Y. D. Zr vs. TiO_2, Nb, and Hf. Separation between DR-97-04, DR-113b, and DR-113-05 and all other samples indicates possible differences in initial composition. Al_2O_3 and Y arrays show considerable scatter indicating mobility relative to TiO_2 and Zr or differential alteration (see text). Linear arrays suggest Nb and Hf, and are immobile relative to TiO_2 and Zr. The linear arrays of TiO_2 vs. Zr suggest these elements were immobile during alteration.

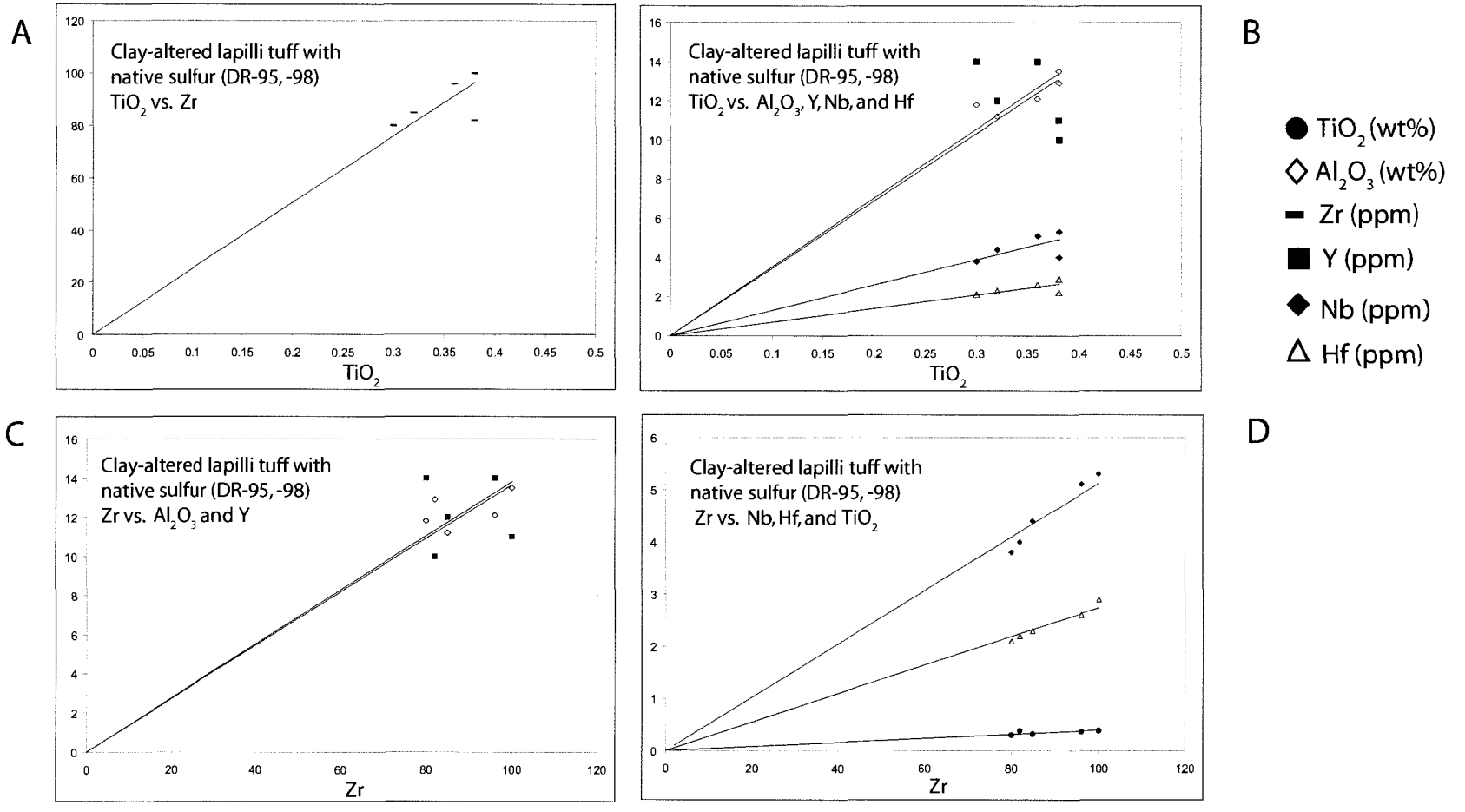

Figure 6.8. Immobile element ratios of clay-altered lapilli tuff with native sulfur samples (DR-95, -98) recovered from the NVF. A. TiO_2 vs. Zr. B. TiO_2 vs. Al_2O_3, Y, Nb, and Hf. C. Zr vs. Al_2O_3 and Y. D. Zr vs. Nb, Hf, and TiO_2. The linear arrays of TiO_2 vs. Zr suggest these elements were immobile during hydrothermal alteration (Maclean and Barrett, 1993). The linear arrays formed on plots of Nb and Hf vs. TiO_2 and Zr suggest these were also immobile during alteration. Al_2O_3 and Y arrays show some scatter indicating mobility of elements or differential alteration (see text).

6.2.1 Magma Affinity

On a Zr/TiO_2 vs. Nb/Y discrimination diagram (Winchester and Floyd, 1977) the Calypso samples are dominantly subalkaline (Nb/Y<0.7) and plot in the rhyodacite/dacite compositional field along with TVZ ignimbrite (Figure 6.9). The White Island andesite samples straddle the andesite and andesite/basalt fields and the least altered sample DR-110wp and all vitric tuff samples lie in the centre of the TVZ ignimbrite field. The clay-altered samples DR-98 and DR-97-04 plot proximal to the White Island andesite compositional field whereas silicified crystal tuff (DR-85 and DR-102-05), barite-rich silicified tuff samples (DR-112), and clay-altered lapilli tuff with native sulfur (DR-113b) plot outside these fields.

Immobile rare earth elements (REE) La and Yb, together with low field strength element (LFSE) Th, HFSE Zr and TiO_2 may be used to discriminate magmatic affinity in volcanic rocks (Barrett and MacLean, 1994; Barrett and Maclean, 1999). The La/Yb, Th/Yb and Zr/TiO_2 plots show that all of the Calypso samples are dominantly calc-alkaline (Figure 6.10). TVZ ignimbrites also plot within the calc-alkaline field, whereas White Island andesite plots in the calc-alkaline and transitional fields. These plots reveal a notable Zr enrichment in the DR-85 series (silicified-crystal tuff).

Immobile elements plots of all Calypso samples, TVZ ignimbrite, and White Island

andesite are shown in Figure 6.11. Least altered vitric tuff (DR-110wp) plots consistently within the compositional range of TVZ ignimbrite, and least clay-altered (DR-97-04, 81-82 GTVA) samples plot in or near the compositional field of White Island andesite. Silicified crystal tuff samples (DR-85 and DR-102-05) show elevated TiO_2, Nb, and Zr relative to Al_2O_3 and Y, and clay-altered samples (81-82 GTVA, DR-95, 97-04, 98) have elevated Al_2O_3 values. Figure 6.11B is a plot of TiO_2 vs. Zr with compositional fields defined by MacLean and Barrett (1993). The defined fields correspond to the compositional range of White Island andesite, TVZ ignimbrite, and Mayor Island rhyolite. The bulk of the Calypso samples plot as a linear array within the dacite compositional field overlapping the TVZ ignimbrite field. The clay-altered lithofacies samples DR-97-04, DR-113, and DR-113b plot within the White Island compositional range on the margin of the basalt-andesite and dacite fields as do sample DR-95, and -98. Sample DR-102-05 plots within the basalt-andesite field and has elevated Zr and TiO_2 concentration relative to the Calypso sample suite. A plot of TiO_2 vs. Nb displays a similar linear trend of the Calypso samples (Figure 6.11E).

Multi-element diagrams normalized to the Primitive Mantle (Extended PM # 2; McDonough and Sun, 1995) are provided in Figure 6.12 and 6.13. The compositional range of White Island andesite samples and TVZ ignimbrites are plotted for comparison. The PM-normalized signatures of the Calypso samples are comparable to the White Island andesite and TVZ ignimbrite signatures. White Island andesite and TVZ ignimbrite show near parallel PM-normalized signatures and display the distinctive negative Nb (relative to Th) and La "arc signature" (Swinden et al., 1997). The TVZ ignimbrite samples have slightly elevated Th and light rare earth element (LREE) concentrations, and are depleted in

Ti, V, and Sc relative to the White Island andesite samples. Sample DR-102-05 is a notable exception; it does not display the negative Nb arc-signature and has notable enrichments of Ti, Zr, Hf, and Eu relative to the TVZ rocks (Figure 6.12). The silicified crystal-tuff (DR-85 series) has a similar Zr and Hf enrichment but contains the arc signature. Barite-rich silicified-tuff samples DR-112, DR-120, and DR-121 are nearly parallel to the TVZ rocks but have lower concentrations of all plotted elements, most likely caused by barite-silica dilution.

Chondrite-normalized REE diagrams show similar relationships (Figure 6.14 and 6.15). White Island andesite and TVZ ignimbrites have LREE-enriched chondrite-normalized signatures typical of calc-alkaline arc volcanic rocks (Stolz et al., 1990), and the Calypso samples fall within the general compositional range of these rocks. Negative Eu anomalies are visible in the silicified crystal tuff with native sulfur (DR-89 and DR-88) as well as in the silicified vitric ash (DR-110). Mineralized sample DR-120 has a less pronounced LREE enrichment but a positive Eu anomaly typical of hydrothermal precipitation (e.g., Whitford et al., 1988). Other barite-rich silicified-tuff samples (series DR-112) are near parallel to the TVZ rocks but have a lower concentration of all plotted elements and variable Eu.

A comparison of the least clay-altered lapilli tuff (sample 81-GTVA) and the least-altered vitric ash sample (DR-110wp) indicate similar Primitive Mantle- (Figure 6.16A) and chondrite- (Figure 6.16B) normalized multi-element profiles.

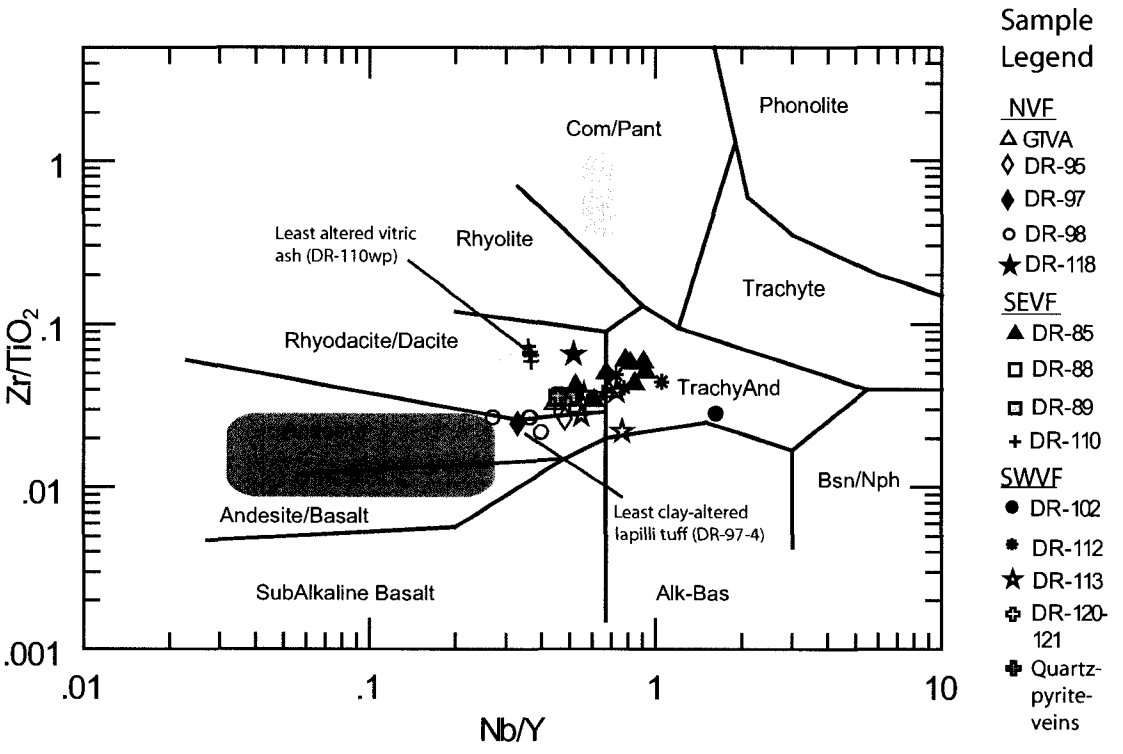

Figure 6.9. Modified Zr/TiO_2 - Nb/Y plot from Winchester and Floyd (1977). a) Calypso samples are plotted by sample number. The shaded blue box represents the compositional space of White Island andesite samples (Cole et al., 2000); the shaded orange box represents the compositional space of ignimbrites from the Taupo Volcanic Zone (Sutton et al., 1995; Bignall et al., 1996); the shaded red box represents the compositional range of alkaline rholites from Mayor Island (Ewart et al., 1968). Calypso sample plot within the compositional field of subalkaline (Nb/Y <0.7) and alkaline (Nb/Y>0.7) andesite to rhyolite/dacite.

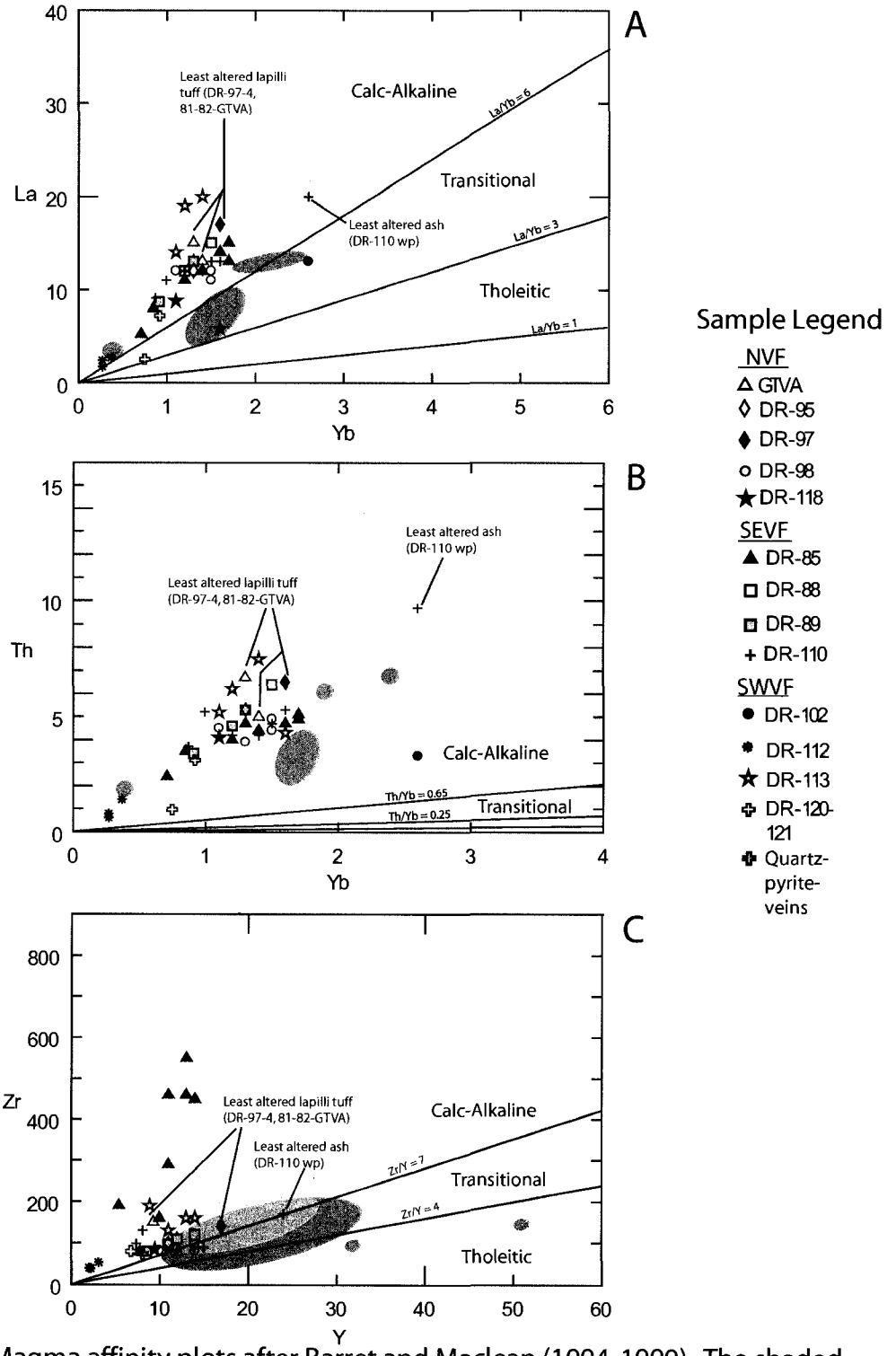

Figure 6.10. Magma affinity plots after Barret and Maclean (1994, 1999). The shaded blue ovals denotes the compositional space of the White Island andesite sample suite (Cole et al., 2000), the shaded orange ovals represents the compositional space of subaerial ignimbrites from the TVZ (Bignall et al., 1996, Sutton et al., 1995). A. La-Yb; B. Th/Yb; and C. Zr/Y plot indicate Calypso samples have a calc-alkaline to transitional magmatic affinity.

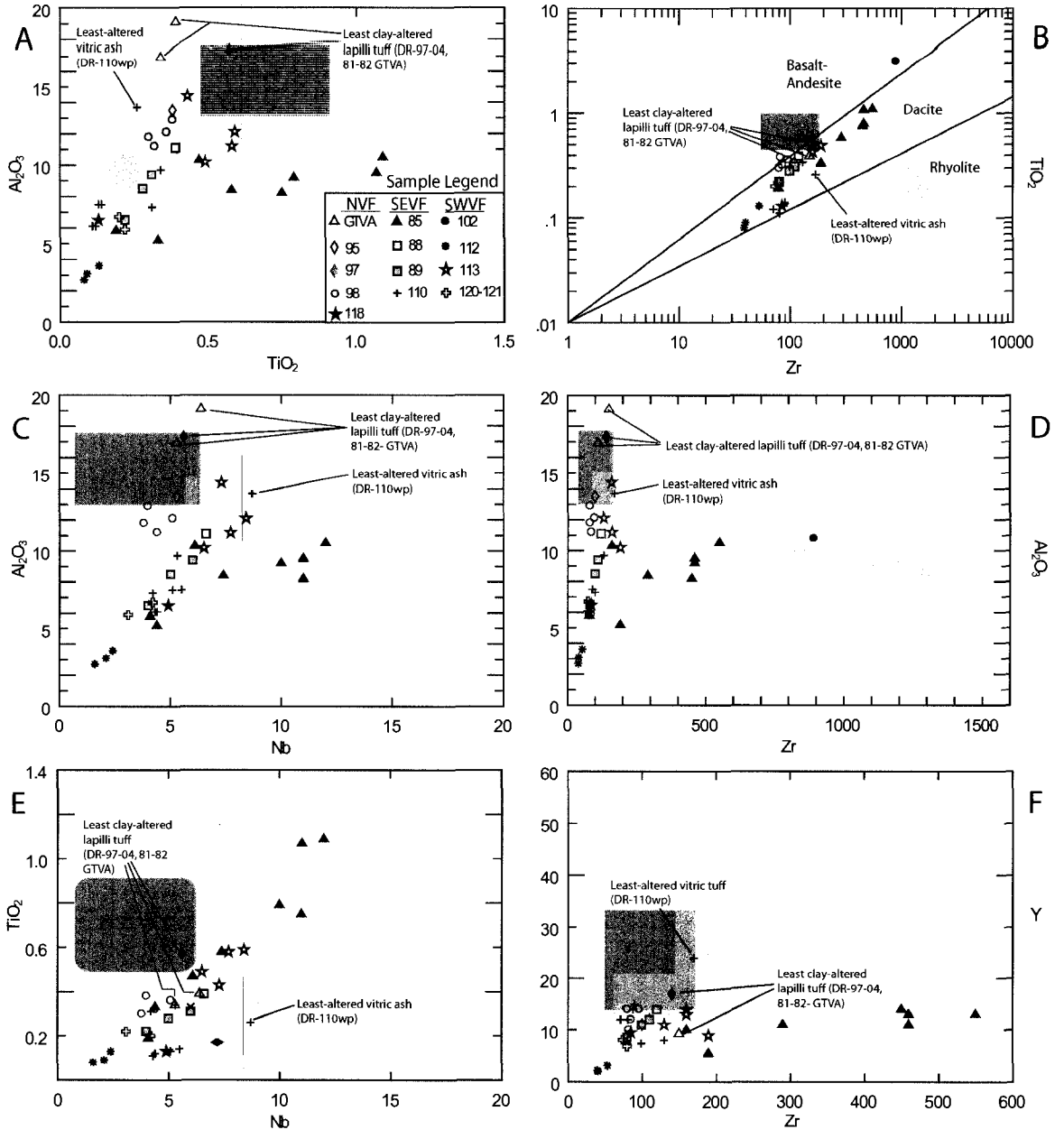

Figure 6.11. Discrimination diagrams of Calypso samples. A. Immobile incompatible pair Al_2O_3 vs. TiO_2. B. Log TiO_2 vs. Log Zr, basalt-andesite/dacite/rhyolite compositional fields from Gifkins et al., (2005) after Maclean and Barret (1993). C. Al_2O_3 vs. Nb D. Al_2O_3 vs. Zr. E. TiO2 vs. Nb. F. Y vs. Zr. The compositional space of White Island andesite (shaded blue boxes; Cole et al., 2000), TVZ felsic ignimbrites (shaded orange boxes; Sutton et al., 1995; Bignall et al., 1996;), and Mayor Island rhyolite (shaded red boxes in plots A, B, D; Ewart et al., 1968) are plotted for comparison.

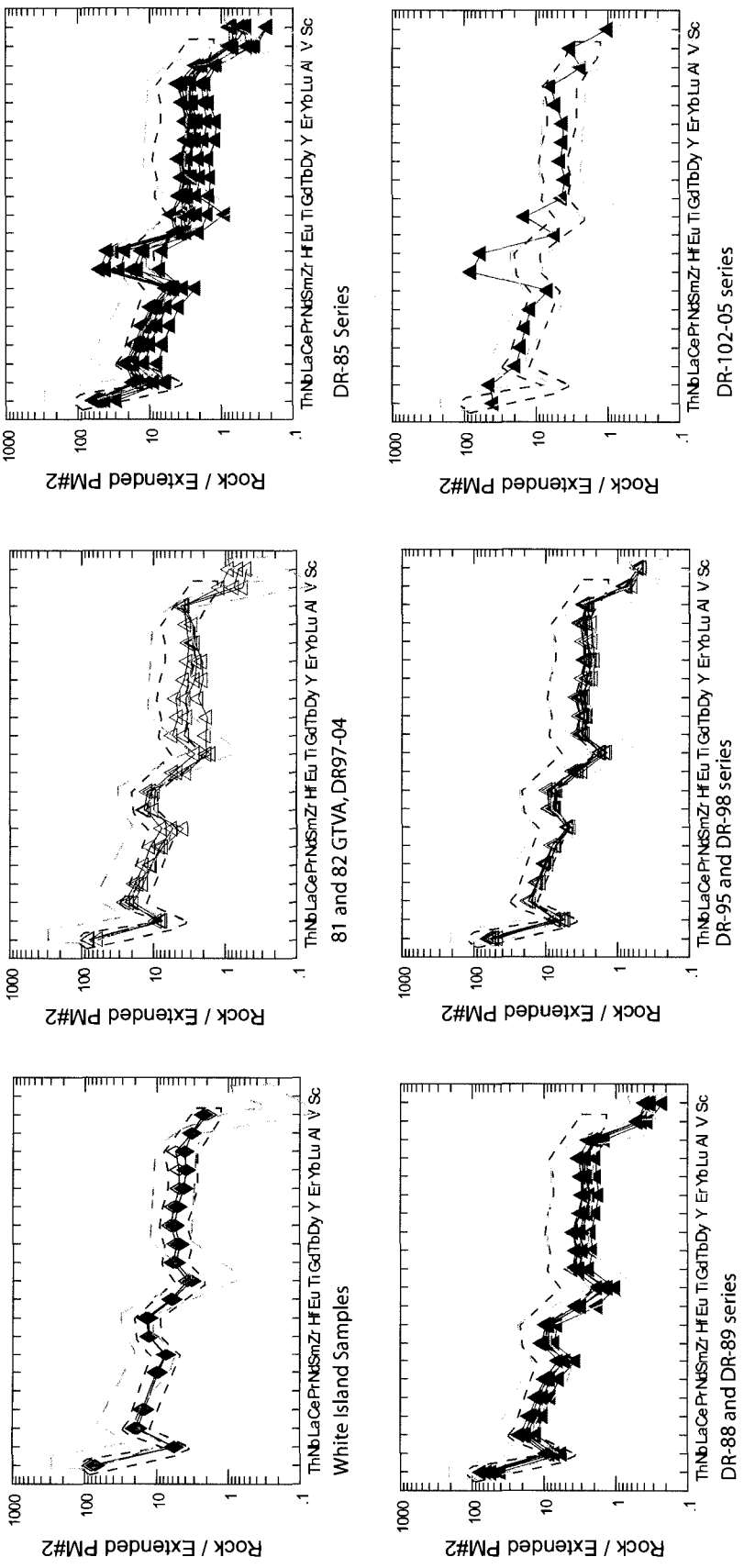

Figure 6.12. Multi-element diagrams of the Calypso samples suite normalized to the Primitive Mantle (Extended PM #2; Sun and McDonough 1995). White Island andesite samples plotted in the top left (Cole et al., 2000), the dashed blue polygon (- - - - -) denotes the range of elements from the White Island Andesite suite, the dashed orange polygon (– · – · –) denotes the element range from Taupo Volcanic Zone (TVZ) ignimbrites (Sutton et al., 1995; Bignall et al., 1996).

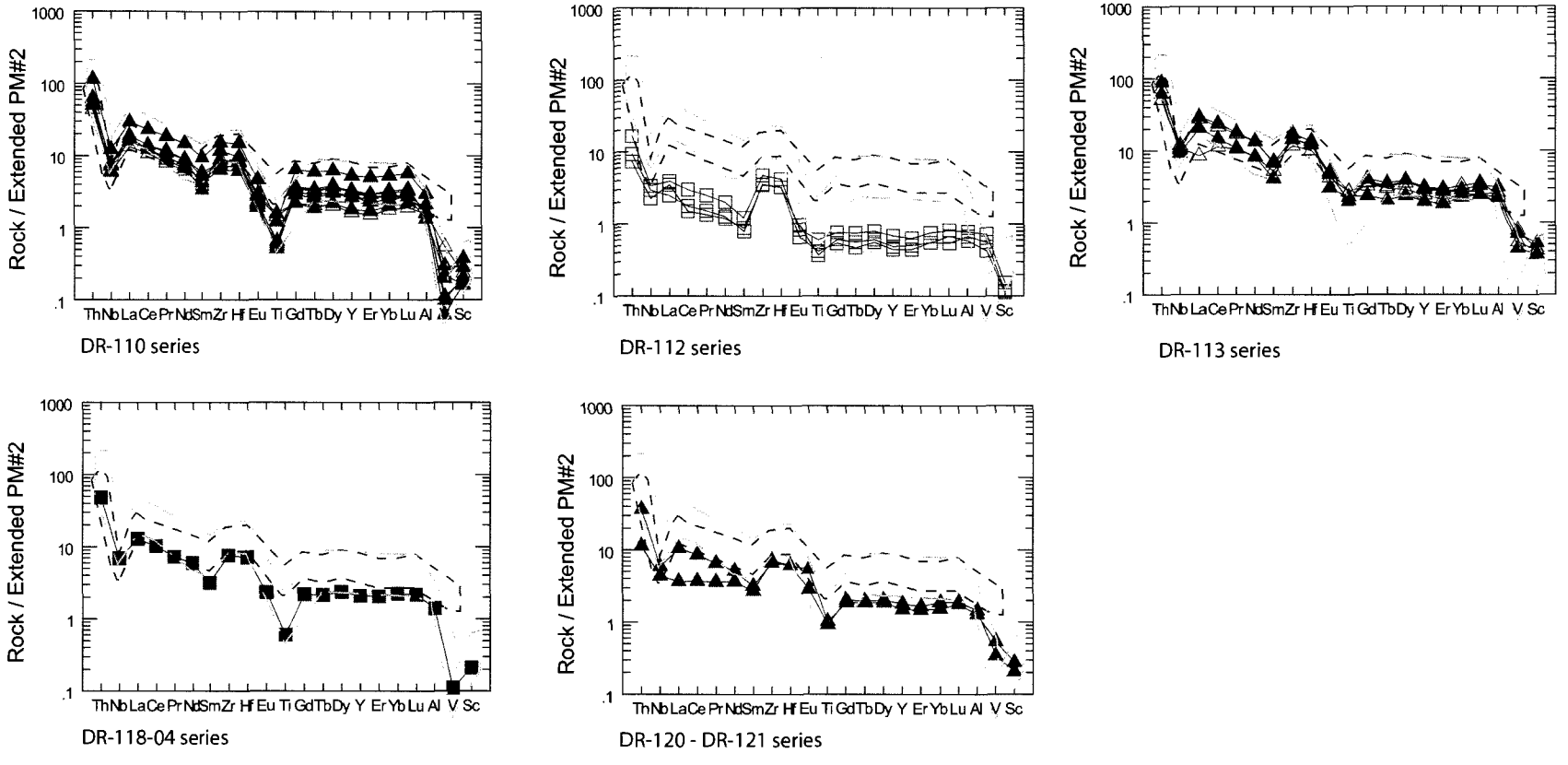

Figure 6.13. Multi-element normalized diagrams of the Calypso sample suite normalized to the Primitive Mantle (Extended PM #2; Sun and McDonough 1995). The dashed blue polygon (- - - - -) denotes the range of elements from the White Island andesite suite (Cole et al., 2000), the dashed orange polygon (– —) denotes the element range from Taupo Volcanic Zone (TVZ) ignimbrites (Sutton et al., 1995; Bignall et al., 1996).

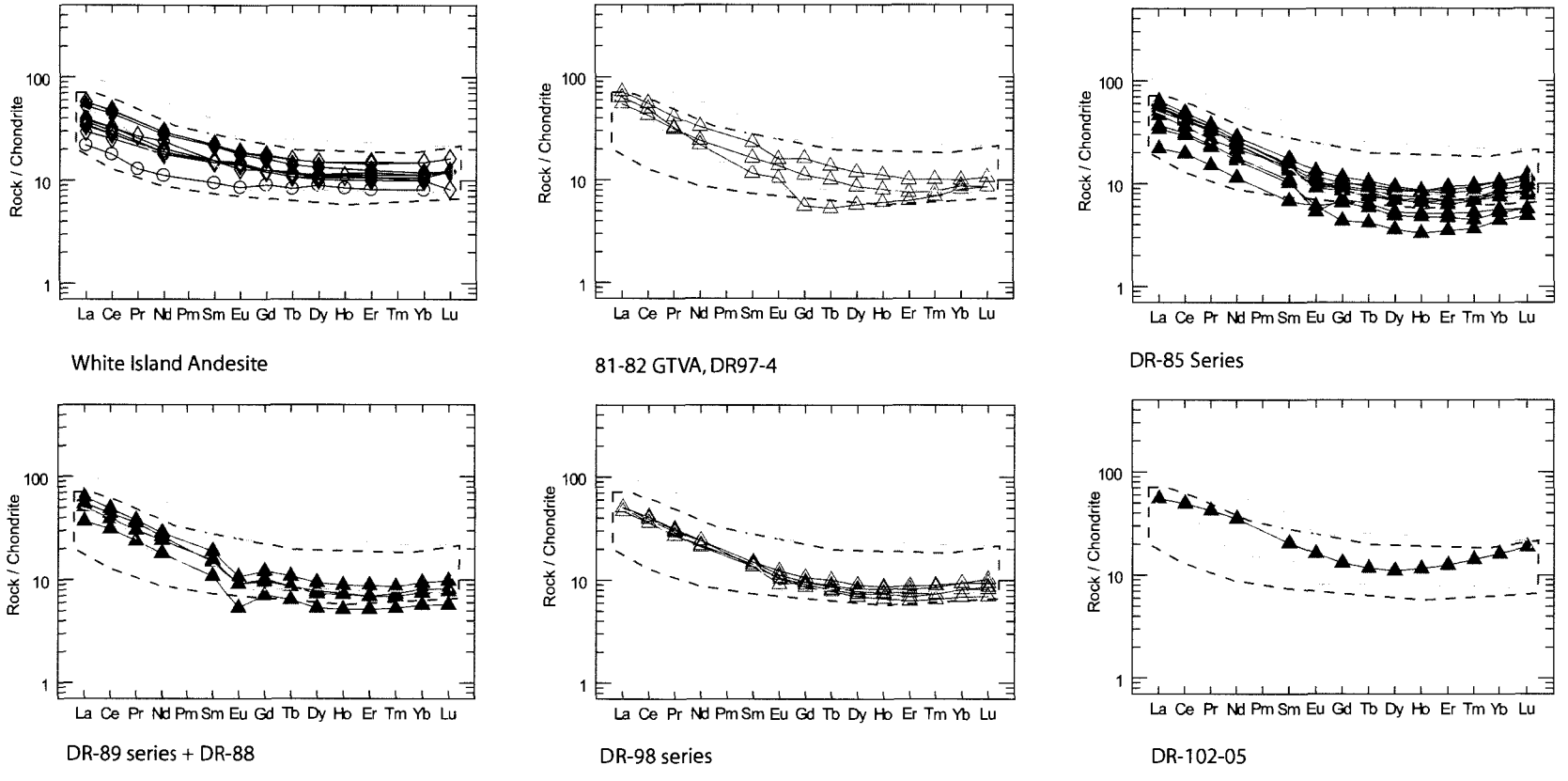

Figure 6.14. Rare earth element (REE) multi-element diagrams of the Calypso sample suite normalized to chondrite (REES-Chondrite; Sun and McDonough, 1995). White Island andesite samples are plotted in the top left (Cole et al., 2000), the dashed blue polygon (- - - -) denotes the range of REE values from the White Island Andesite suite. The dashed orange polygon ( ) denotes the REE profile range of subaerial felsic ignimbrites from the Taupo Volcanic Zone (Sutton et al., 1995; Bignall et al., 1996).

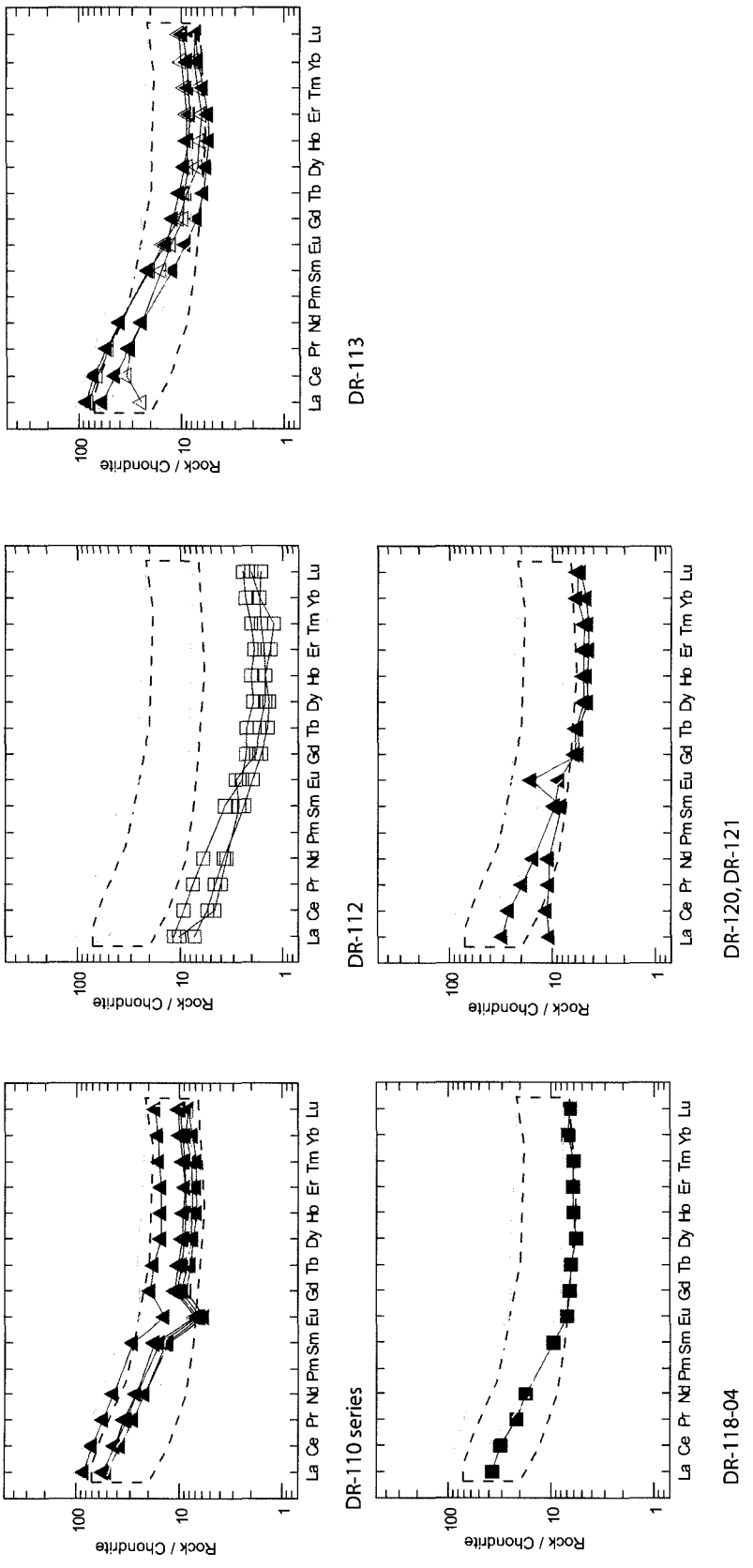

Figure 6.15. Rare earth element (REE) multi-element diagrams of the Calypso sample suite normalized to chondrite (REES-Chondrite; Sun and McDonough 1995). The dashed blue polygon (- - - -) denotes the range of REE values from the White Island andesite suite (Cole et al., 2000). The dashed orange polygon (— — —) denotes the REE profile range of subaerial felsic ignimbrites from the Taupo Volcanic Zone (Bignall et al., 1996, Sutton et al., 1995).

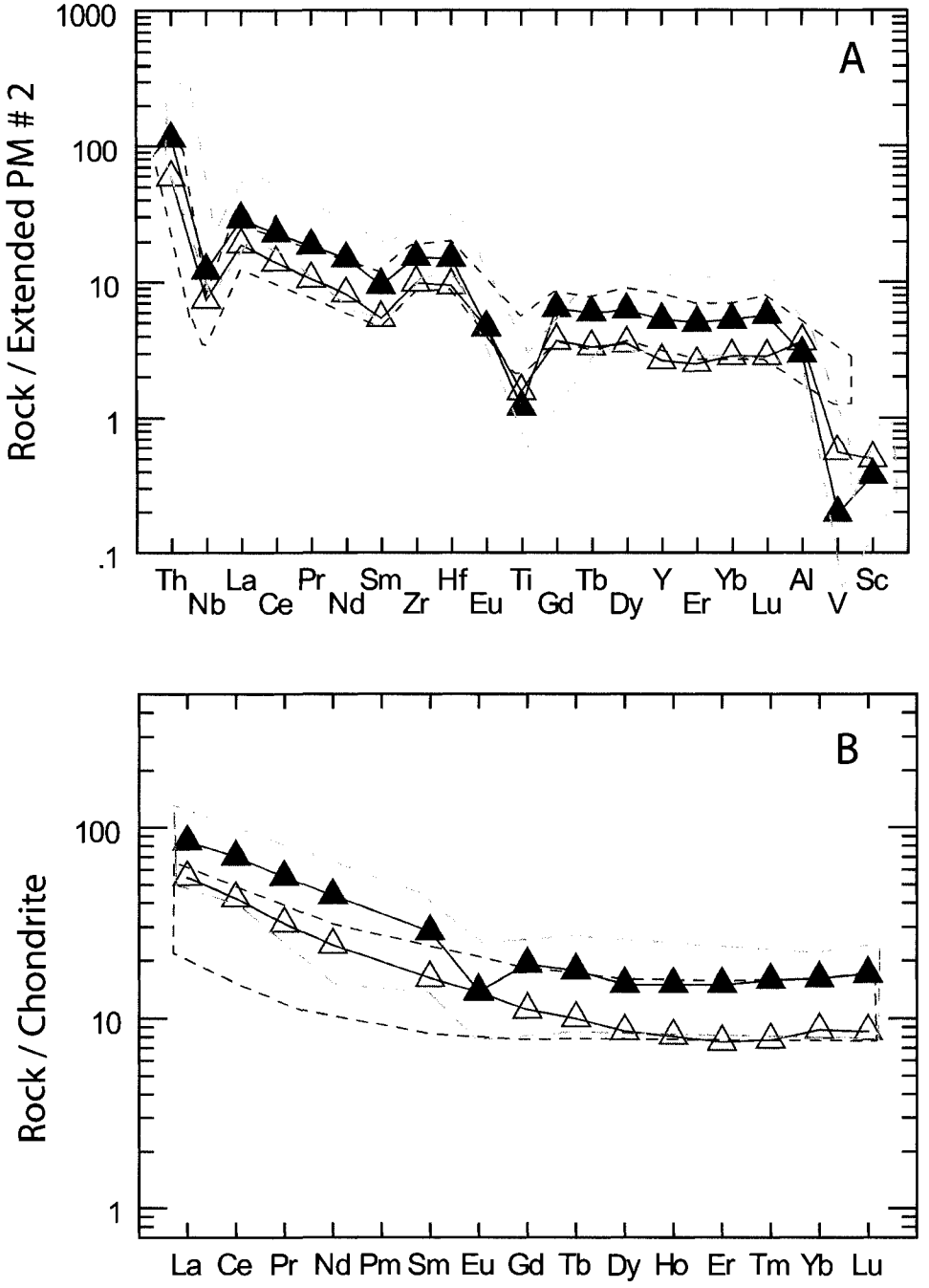

Figure 6.16. Multi-element diagrams of least altered rock samples from the CHVF normalized to A, the Primitive Mantle (Extended PM #2; Sun and McDonough 1995); and B, Chondritic meteorite (REEs-Chondrite; Sun and McDonough, 1995). The compositional space of White Island andesite samples (Cole et al., 2000) is contained by the dashed blue line (- - -). The dashed orange line (– –) denotes the compositional profile of subaerial ignimbrites from the Taupo Volcanic Zone (Sutton et al., 1995; Bignall et al., 1996). △least altered felsic ash recovered from the SEVF (DR-110 wp); ▲ least altered clay-altered lapilli tuff recovered from the NVF (81-GTVA).

6.2.2 Volcaniclastic Provenance

During sedimentary processes Al, Fe, Ti, Mn, Zr, Hf, Nb, Sn, Cr, Ni, V, Co, and some REEs may be concentrated residually in particulate matter. These elements can be used to infer the provenance of the sedimentary or volcaniclastic material (cf. McLennan, 1989; McLennan et al., 2003). Multi-element normalized diagrams and discrimination diagrams show that White Island andesite and the TVZ ignimbrite samples have similar concentrations of HFSE, LFSE, REE, and immobile major elements (i.e., Ti and Al). Their chemical similarity makes it difficult to distinguish the source of volcaniclastic material at Calypso. The TVZ ignimbrites are more evolved rocks relative to the White Island andesite samples, and immobile and compatible transition metals Cr, V, Sc, and Ni can be used to identify material derived from the more primitive volcanic source (cf. McLennan et al., 1993). Vanadium and Cr are redox sensitive trace metals and may show strong enrichment in reduced environments (i.e., organic shales; McLennan et al., 2003). However, hydrocarbon-rich lithofacies (DR-110b, -113c, -113d) do not exhibit any V enrichment relative to the Calypso suite (Table 6.1), probably reflecting the immature nature of the organic matter (Botz et al., 2002). The bulk of the Calypso samples have Sc concentrations similar to TVZ ignimbrites (Figure 6.17 A, C, D, E, F). The least clay-altered lapilli tuff sample (DR-94-07) has elevated Sc (15 ppm) and V (97 ppm) which approach the concentration of these elements in White Island andesite samples (Figure 6.17C). Silicified crystal-tuff samples (DR-85) show elevated Sc, Nb, and TiO_2 but are not enriched in V, relative to the other Calypso samples. Sample DR-102-05 has very high Sc (17 ppm), Nb (31ppm), V (270 ppm), and TiO_2 (3.2 wt %).

Incompatible elements Th, Nb, Zr, Al, and the LREE will concentrate in the melt during igneous fractionation; these elements partition strongly into felsic volcanic rocks and upper continental crust. A ratio of Th, Nb, Al, Zr, or a LREE against a highly compatible element (e.g., Sc) will increase with continuing igneous differentiation (Mclennan et al., 1993). Zirconium values may increase independently of Th, Nb, Al, and LREE where samples contain a component of accumulated heavy minerals (i.e. zircons). Figure 6.17E is a plot of Nb/Sc vs. Zr/Sc (similar to the Th/Sc vs. Zr/Sc plot of McLennan et al., 1990 and McLennan et al., 2003). Felsic TVZ ignimbrites have higher Zr/Sc and Nb/Sc values than White Island andesite. Clay-altered lithofacies (81-82 GTVA, DR-97-04, DR-95, and DR-98) have low ratio values similar to White Island andesite samples; DR-97-04 has the lowest Zr/Sc and Nb/Sc values of all Calypso samples. The majority of the Calypso samples have plot within the compositional field of TVZ ignimbrite. The silicified crystal tuff samples DR-85 and sample DR-102-05 have very high Zr/Sc values suggesting possible zircon accumulation. A plot of Al_2O_3/Sc vs. Zr/Sc shows similar relationships (Figure 6.17F) with the majority of the Calypso samples plotting within the compositional range of the TVZ ignimbrites. Clay-altered lapilli tuff (81-81 GTVA, DR-95, and DR-98) has Al_2O_3/Sc ratios similar to or slightly lower than TVZ ignimbrite and lower Zr/Sc ratios. Sample DR-97-04 has the lowest Al_2O_3/Sc and Zr/Sc ratios of all Calypso samples and plots near the White Island andesite field. The silicified crystal tuff (DR-85 series) and sample DR-102-05 have very high Zr/Sc values.

Ternary plots of Sc-Th-Zr/10 and Sc-Al_2O_3-Th (after Bhatia and Crook, 1986) show similar relationships, with most samples falling within the compositional field of TVZ

ignimbrites (Figure 6.18). White Island andesite samples have elevated Sc and lower Zr, Al, and Th relative to TVZ ignimbrite. Silicified crystal tuff samples (DR-85 series) and sample DR-102-05 show strong Zr enrichment. Barite-rich silicified tuff (DR-112, DR-120) and samples DR-113-05 and DR-113d have slightly elevated Zr and lower Th than the TVZ ignimbrites. Clay-altered lapilli samples (81-82 GTVA, DR-95, -97-04, -98) have elevated Sc values and Al_2O_3 concentrations.

Silicified crystal-tuff samples DR-85 and 102-05 show strongly elevated Zr, Hf, and TiO_2 values. The increase in concentration of these elements independent of other highly incompatible elements (i.e. Th, LREE, Al), as would be expected during igneous fractionation, strongly suggest the samples contain a component of accumulated heavy minerals (after McLennan et al., 1990, 2003). Trace amounts if zircon were detected by XRD which supports the geochemical data. Volcaniclastic material descending through the water column will be sorted in to a dense, crystal-rich, fraction and a more buoyant pumice and pumiceous ash fraction (Cas et al., 1990; Cas, 1992). Marine processes superimposed on the sorted ash may have further concentrated the heavy mineral phases. Mayor Island (Figure 1.1) pantellerite/rhyolite has very high Zr concentration and a similar Nb/Y values to the Calypso suite. However, Zr/TiO_2 of these samples are much higher than DR-85 and DR-12-05 samples (Figure 6.9) suggesting, although proximal to the Whakatane Graben, it does not appear to be the source of Zr.

Geochemical data of the recovered Calypso samples shows that the silicified lithofacies, with the exception of the DR-85 series and sample DR-102-05, are composed primarily of dacitic vitric and crystal tuff material, most likely derived from caldera-building eruptions on the North Island of New Zealand (Davey et al., 1995).

Discrimination diagrams (Figures 6.9, 6.17E, 6.17F) show the that clay-altered, and clay-altered with native sulfur, lapilli tuff samples (81-82 GTVA, DR-95, - 97-04, - 98) from the North Vent Field (NVF) have less evolved chemical compositions approaching that of White Island andesite samples. This is the most proximal vent field to the subaerial White Island volcano.

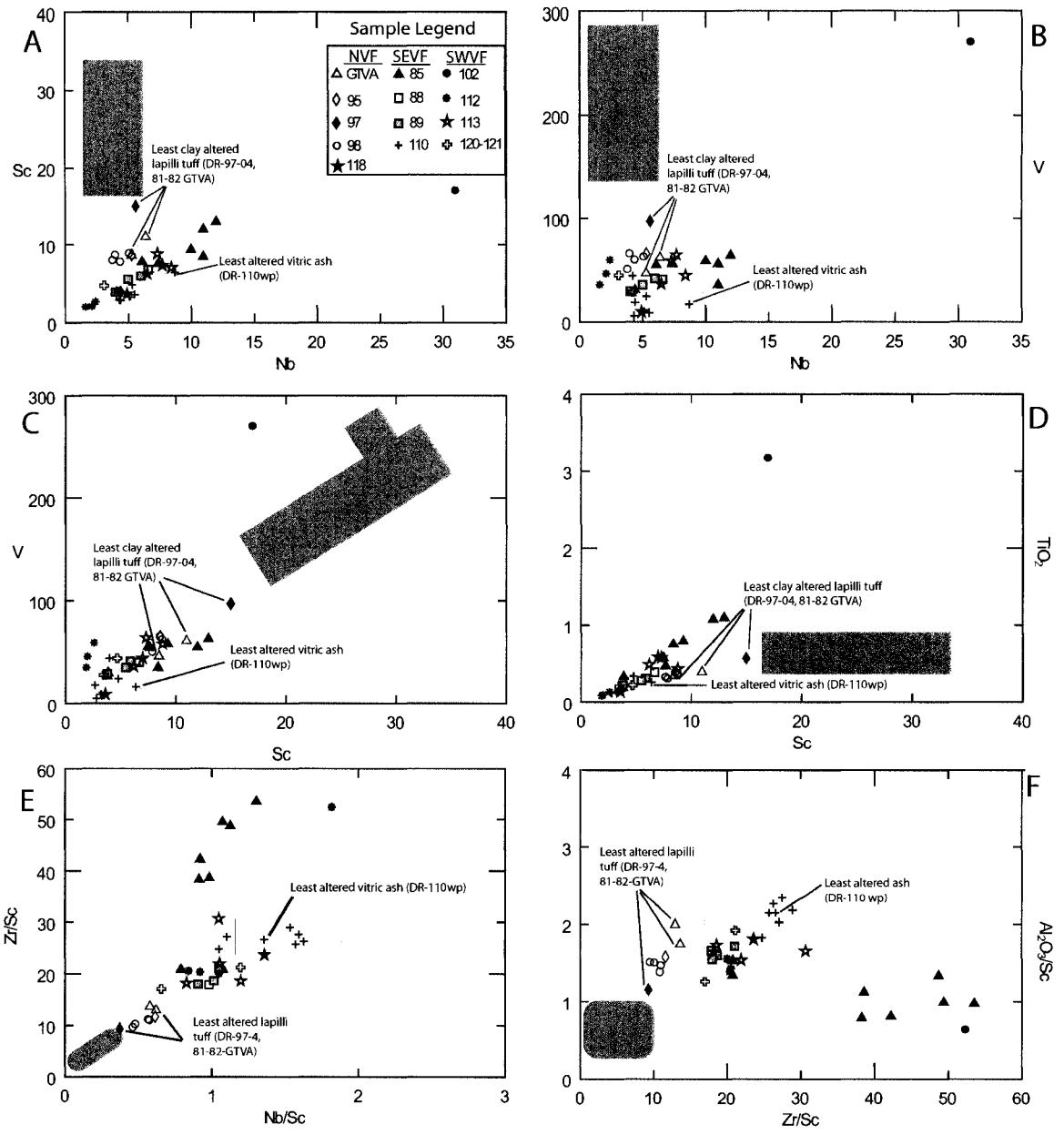

Figure 6.17. Sedimentary provenance discrimination diagrams of Calypso samples. A. Immobile transitional metal and high field strength element pair Sc vs. Nb. B. V vs. Nb. C. V vs. Sc. D. TiO_2 vs. Sc. E. Plot of Zr/Sc vs. Nb/Sc. F. Plot of Al_2O_3/Sc vs. Zr/Sc (adapted from McLennan et al., 2003), both ratios generally increase with increasing igneous differentiation, Zr/Sc ratios increase independent of Al_2O_3/Sc and Nb/Sc where samples contain a component of accumulated heavy minerals (i.e., zircon). The compositional space of White Island andesite (shaded blue boxes; Cole et al., 2000), TVZ felsic ignimbrites (shaded orange boxes; Sutton et al., 1995; Bignall et al., 1996) are plotted for comparison.

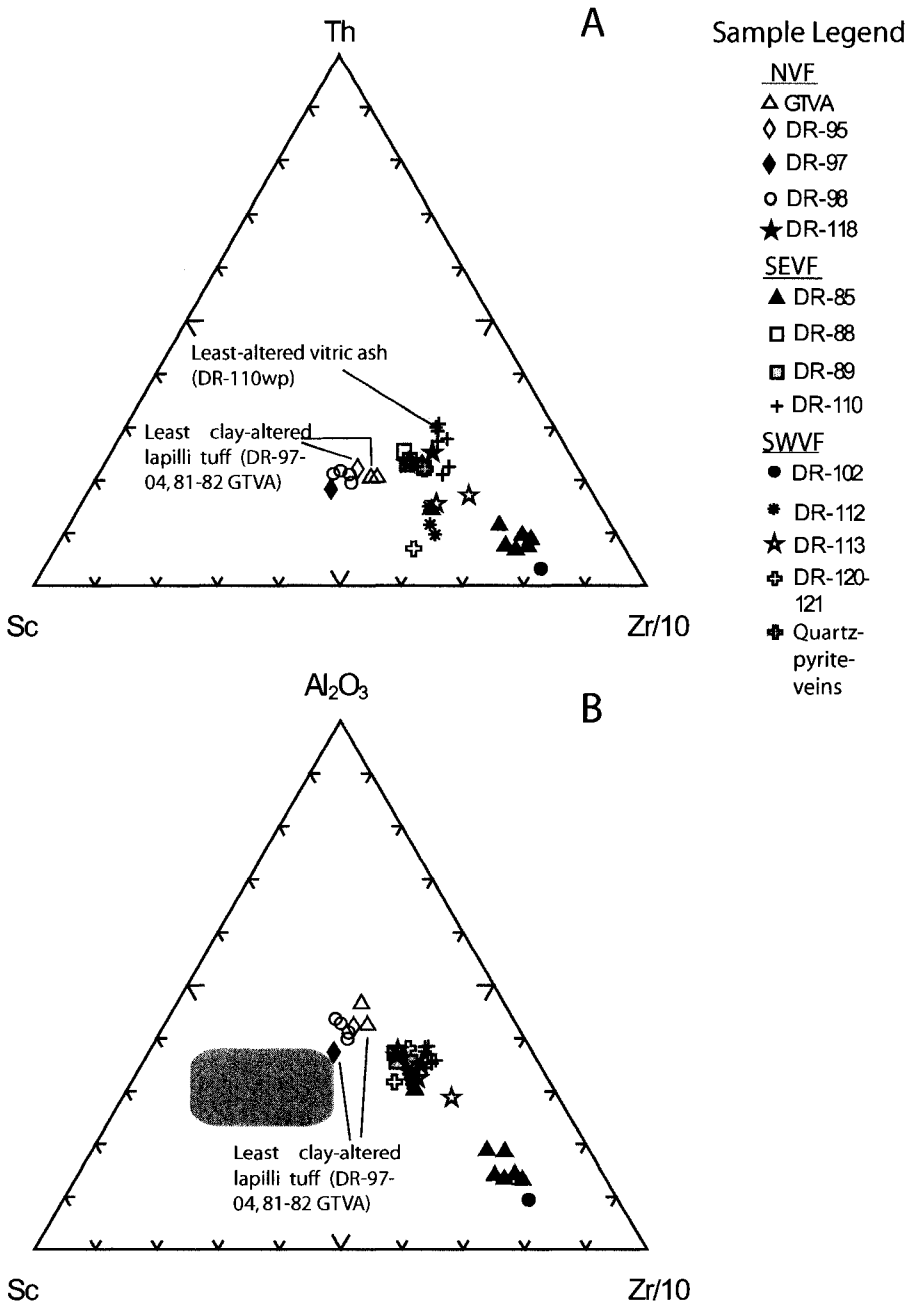

Figure 6.18. Sedimentary provenance discrimination diagrams of CHVF samples. The shaded blue box represents the compositional space of White Island andesite samples (Cole et al., 2000), and the shaded orange boxes represents the compositional space of ignimbrites from the TVZ (Sutton et al., 1995; Bignall et al., 1996). A. Sc-Th-Zr/10 diagram (after Bhatia and Crook, 1986). B. Sc-Al_2O_3-Zr/10 diagram. White Island andesite samples have elevated Sc and lower Zr, Al, and Th relative to TVZ ignimbrite. Clay altered pumice lapilli GTVA-81-82, DR-95, -97-04, -98 plot near the White Island andesite field suggeting the samples contain a component of less fractionated material. DR-85 series and DR-102-05 contain high Zr values indicating potentail heavy mineral accumulation.

6.2.3 Alteration Geochemistry

The progressive leaching of alkali metals and silica during alteration of volcanic glass to clays decreases the Si/Al and Al/(Na + Ca + K) ratios of the rocks. Chemical indexes of alteration provide a measure of clay alteration intensity. The Alteration Index [AI = 100 x (K_2O +MgO)/(K_2O +MgO + Na_2O + CaO)] is a measure of K and Mg mass gain coupled with a mass loss of Na and Ca during the replacement of plagioclase and volcanic glass by chlorite or sericite (Ishikawa et al., 1976). The Chemical Index of Alteration (CIA) is a ratio of Al/(Al +Na + Ca +K) and provides an assessment of alkali element loss relative to constant Al concentration during hydrothermal alteration or weathering of igneous minerals to aluminum rich clays (Fedo et al., 1995; Nesbitt, 2003). Chemical Index of Alteration values of ≤ 50 represent unaltered samples; pure secondary clay minerals have values > 75. The silicification index [SI = 100x SiO_2 / (SiO_2 + Al_2O_3)] is a measure of Si enrichment relative to aluminum (van Ruitenbeek et al., 2005).

A plot of SI vs. CIA subdivides the Calypso sample suite into four subpopulations: 1) quartz-pyrite veins (DR-110d, -110e); 2) dominantly silicified samples (DR- 85b, -85c, -85d, -85-05a, -85-05b, -85-05c, -85-06, -88, -89-02a, -89-02b, -110b, -110c, -110e, -110i, -110j, -113d, -118-04, -120, -121); 3) silicified + clay altered samples (DR- 85a, -112a, -112bc, -112de); and 4) dominantly clay altered samples (81-82 GTVA, DR-89c, -95a, -97-04, -98-02a, -98-02b, -98-07a, -98-07b, -102-05, -110k, -113b, -113c, -113-05).

The silicified and silica-clay lithofacies are most closely associated with volatile-metal mineralization. As noted previously, the least-altered vitric ash (DR-110wp) plots in the compositional range of TVZ ignimbrites. Least clay-altered lapilli tuff sample 81-

GTVA plots within the compositional range of White Island andesite; samples 82- GTVA and DR-97-04 have higher CIA values.

The Feldspar Diagram after Nesbitt (2003) is used to quantify the mineralogical changes during hydrothermal alteration or weathering (Figure 6.20). Whole-rock geochemical analyses are plotted in A-CN- K space, which represents the molar values of Al-(Ca + Na)-K. In this plot, the CIA (chemical index of alteration) corresponds to the percentage of Al_2O_3. Silicified samples preserve the ratios of the unaltered rock and plot primarily within the compositional space of subaerial TVZ ignimbrite, indicating preserved A-CN-K ratios. The clay-altered samples, and submerged White Island andesite samples show a trend toward the compositional field of smectite.

The Mafic Diagram, also after Nesbitt (2003), plots molar Fe + Mg to illustrate the destruction of mafic minerals (Figure 6.21). As in the Feldspar Diagram, silicified crystal tuff (sample series DR-85) falls in the andesite field, whereas most of the silicified samples plot within the compositional range of the TVZ ignimbrites. In this diagram, silica-pyrite veins and pyritic silicified tuff (i.e., DR-110c) plot toward the FM apex. The clay-altered lapilli tuff and clay-altered lapilli tuff with native sulfur samples plot in the compositional range of smectite. Submerged White Island andesite samples display a similar trend of elevated Al relative to the subaerial andesite samples.

The clay altered lapilli tuff and clay-altered lapilli with native sulfur lithofacies have been primarily altered to montmorillonite [$(½Na, Ca)_{0.7}Al_{3.3}Mg_{0.7}Si_8O_{20}(OH)_4 \cdot n(H_2O)$] with minor to trace illite [$K_{1.5\text{-}1.0}Al_4(Si_{6.5\text{-}7.0}Al_{1.5\text{-}1.0}O_{20})(OH)_4$] (Deer et al., 1992) and mixed-layer illite-smectite. Vermiculite [$(Mg, Ca)_{0.6\text{-}0.9}(Mg, Fe^{3+}, Al)_{6.0}$ (Al,

$Si)_8O_{20}(OH)_4 \cdot n(H_2O)]$ and/or mixed-layer chlorite [(Mg, Fe^{2+}, Fe^{3+}, Mn, $Al)_{12}$ ((Si, $Al)_8O_{20}(OH)_{16}$]-smectite and minor talc [$Mg_6Si_8O_{20}(OH)_4$] were detected in a single clay-altered lapilli tuff sample (DR-110k) from the SEVF (Deer et al., 1992). Smectitic clays generally form at low temperatures at the periphery of hydrothermal systems in alkaline conditions where Mg, Ca, and Na are available (e.g., Simmons and Browne, 2000). Diagenetic smectite may also form by the hydration of volcanic material at ambient temperatures in the submarine environment (Gifkins et al., 2005). However, alteration geochemistry (see Figure 6.19) indicates the sulfur-rich lapilli tuff samples are more intensely altered to clay than is typical under diagenetic conditions, and a correlation between native sulfur and the intensity of clay alteration confirms a hydrothermal origin for the clay minerals (e.g., see Figure 6.22C below).

The clay altered lapilli tuff samples have low Si concentrations (36.8 to 55.3 wt %) and low Si/Al ratios (5.3 to 7.4) typical of clay minerals, and high loss on ignition (LOI; 4.20 to 41.50 wt %), corrected for sulfur and carbon, values [LOI-(S+C) = 3.1 to 12 wt %] reflecting molecular water and OH. Elevated sulfur concentrations (0.96 to 34.6 wt %) reflect the presence of massive native sulfur in primary pore spaces, sulfur mixed within the matrix, and sulfide. The clay-altered samples are also strongly enriched in fluorine (350 – 1492 ppm) relative to other CHVF samples (Table 6.1).

In a plot of Al/Si vs. LOI-(C+S), clay-altered samples (DR-95, -97-04, 98, -113b, 113-05) have elevated Al/Si and LOI – (C+S), clearly distinguishing clay-rich and clay-poor samples (Figure 6.22A). Strongly clay-altered samples also have elevated sulfur concentrations which positively correlate with LOI – (S+C) and Al/Si (Figure 6.22B, C).

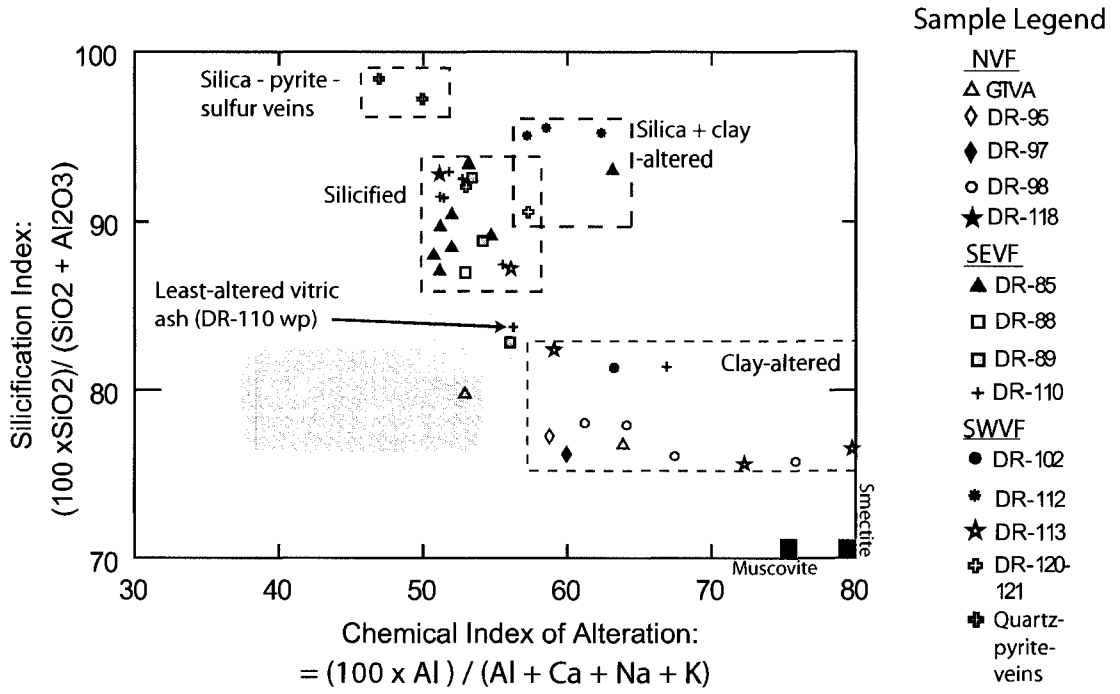

Figure 6.19. An alteration box plot which utilizes the Silicification Index (SI; Van Ruitenbeek et al., 2005) and the Chemical Index of Alteration (CIA; Fedo et al., 1995; Nesbitt, 2003) to subdivide the Calypso sample suite by alteration facies. The SI is a measure of Si concentration relative to Al, which is considered immobile. The CIA is the percentage of Al_2O_3 in a sample and a measure of increasing Al concentration relative to Na, Ca, and K loss during alteration or weathering. Unaltered samples have CIA values of approximately ≤ 50, and secondary clay mineral have values of > 75. The shaded blue box represents the compositional space of subaerial White Island andesite samples (Cole et al., 2000), and the shaded orange box represents the compositional space of subaerial TVZ ignimbrites (TVZ; Sutton et al., 1995; Bignall et al., 1996).

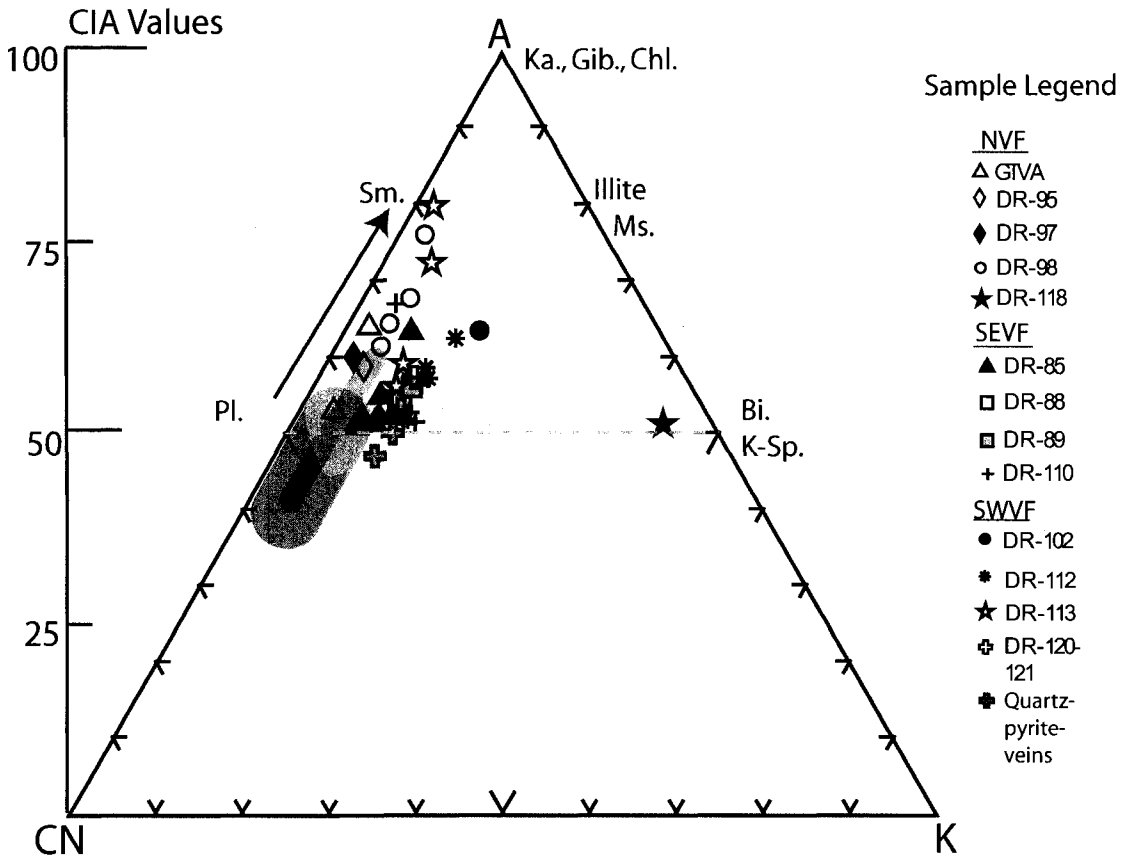

Figure 6.20. The Feldspar Diagram after Nesbitt (2003). The shaded blue box represents the compositional space of White Island andesite samples, the narrow shaded green box represents the compositional space of submerged White Island andesite lava flows (Cole et al., 2000), and the shaded orange boxes represents the compositional space of ignimbrites from the Taupo Volcanic Zone (TVZ; Sutton et al., 1995; Bignall et al., 1996). Calypso sample wholerock geochemical analysis are plotted in A-CN- K [Al-(Ca+Na)-K] space, the CIA (chemical index of alteration) values represent the percentage of Al_2O_3. Silicified samples plot primarily in the compositional space of TVZ ignimbrite samples indicating preserved A-CN-K ratios. The clay altered samples, and submerged White Island andesite samples display a trend toward the compositional field of smectite. Abbreviations: Ka, Kaolinite; Gib, gibbsite; Cht, chlorite; Sm, smectite; Ms, muscovite; Pl, plagioclase; Bi, biotite; K-sp, K-feldspar.

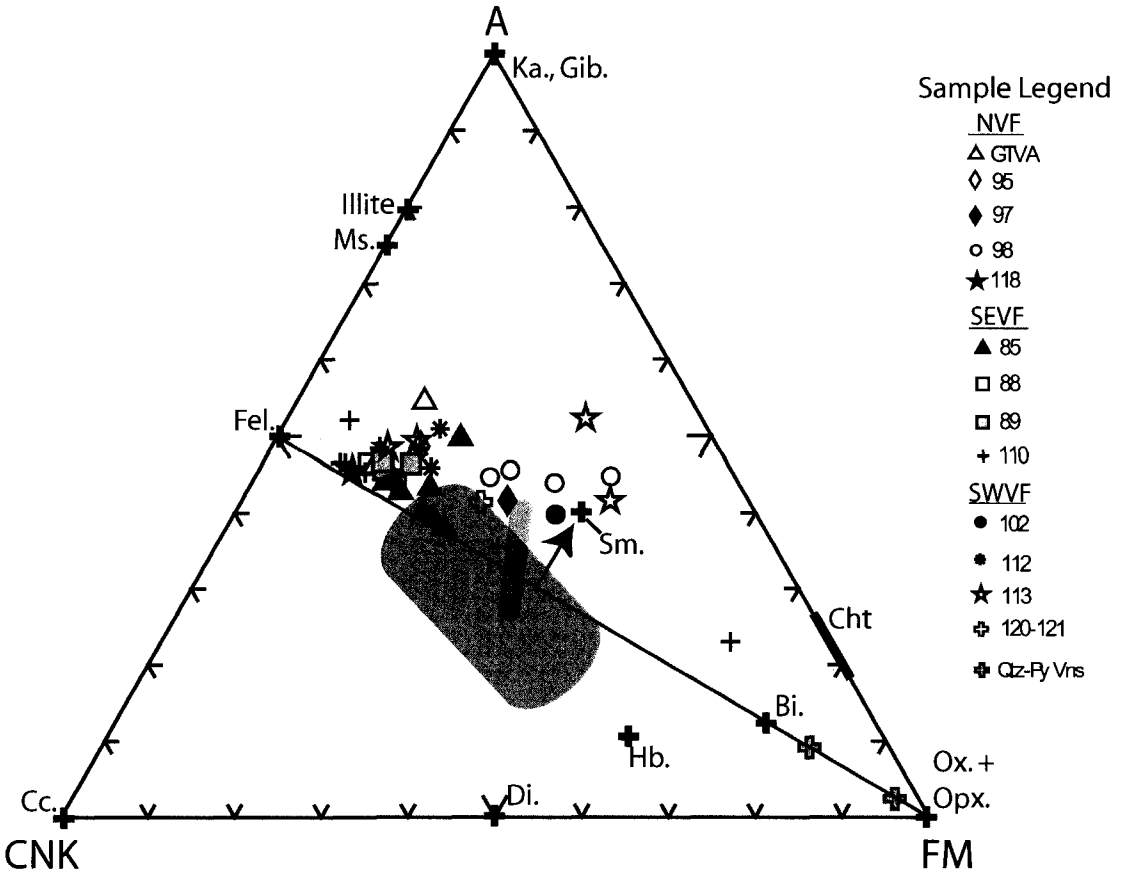

Figure 6.21. The Mafic Diagram after Nesbitt (2003). The shaded blue box represents the compositional space of White Island andesite samples, the narrow shaded green box represents the compositional space of submerged White Island andesite lava flows (Cole et al., 2000), and the shaded orange boxes represents the compositional space of ignimbrites from the Taupo Volcanic Zone (TVZ; Sutton et al., 1995; Bignall et al., 1996). Calypso sample wholerock geochemical analysis are plotted in A-CNK-FM [Al-(Ca + Na + K) – (Fe + Mg)] space. Silicified samples plot primarily in the TVZ ignimbrite compositional field and on the margins of the White Island andesite compositional field. The clay altered samples, and submerged White Island andesite samples display a trend toward the compositional field of smectite.

Abbreviations: Ka, Kaolinite; Gib, gibbsite; Cht, chlorite; Sm, smectite; Ms, muscovite; Pl, plagioclase; Bi, biotite; K-sp, K-feldspar.

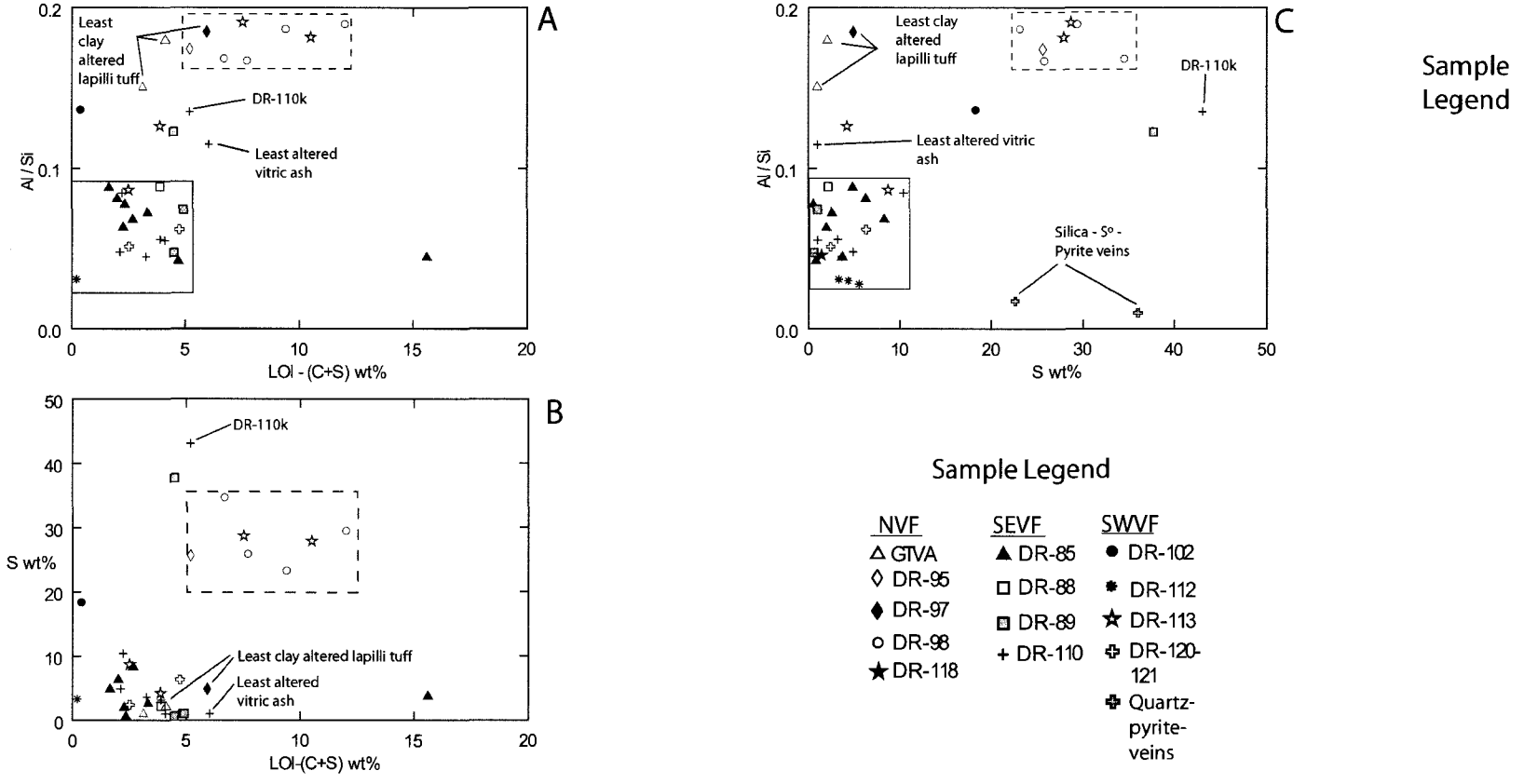

Figure 6.22. Discrimination plots utilizing loss on ignition (LOI), S, Al/Si values to subdivide clay altered and silicified samples. Samples 81-82 GTVA, and DR-97-04 represent the least clay-altered, sulfur poor, lapilli tuff samples from the NVF. Series 110 consists primarily of silicified vitric ash, DR-110wp is non-silicified, weakly consolidated ash representing the least altered sample. DR-110k is a clay altered sulfur rich lapilli tuff sample. LOI values have been corrected for sulfur and carbon [LOI-(C+S)]; dashed boxes represent the compositional space of pervasively clay altered and sulfur rich samples from the NVF (DR-98 series, DR-95) as well as samples DR-113b and DR-113-05 from the SWVF. Solid line boxes identify silicified tuff samples; clay + silica samples plot between the two regions. Clay minerals have elevated Al/Si and LOI values relative to silicate minerals, silicate glass, and amorphous silica (plot A). Elevated Al/Si and LOI values associated with clay altered samples show a positive correlation with elevated S values (plot B and C).

6.2.4 Metal Concentrations

The amorphous silica and abundant volatile metal concentrations observed in samples recovered from the SE and SW vent fields are reflected in the whole-rock geochemistry. Silicified samples, with high total Si content, high Si/Al ratios, and low LOI, have the highest total volatile metal concentrations (up to 9.5 wt% Hg, 0.5 wt% As, and 1.41 wt% Sb; Table 6.1). Arsenic, Sb, and Tl show a strong association (Figure 6.23 A, B, G), but correlate poorly with Hg (Figure 6.23C, H, I). Silver and Au concentrations display no obvious trends with the volatile metals (Figure 6.23 D, E). Silver concentrations are generally less than 20 ppm with the exception of the DR-112 series with values ranging up to 190 ppm. Gold values are generally below detection, with a concentration of 626 ppb detected in a single sample (DR-120; Figure 6.23E). Barite-rich tuff samples contain between 2.52 and 15 wt % Ba, but barite does not correlate well with volatile metals (Figure 6.23F).

The NVF rocks do not contain high concentrations of volatile metals as observed at the SE and SW vent fields. The cherty siltstone sample (DR-118-04) in the CHVF contains elevated As, Sb, Ag, and the second highest Au value (421 ppb) observed at the CHVF (Table 6.1).

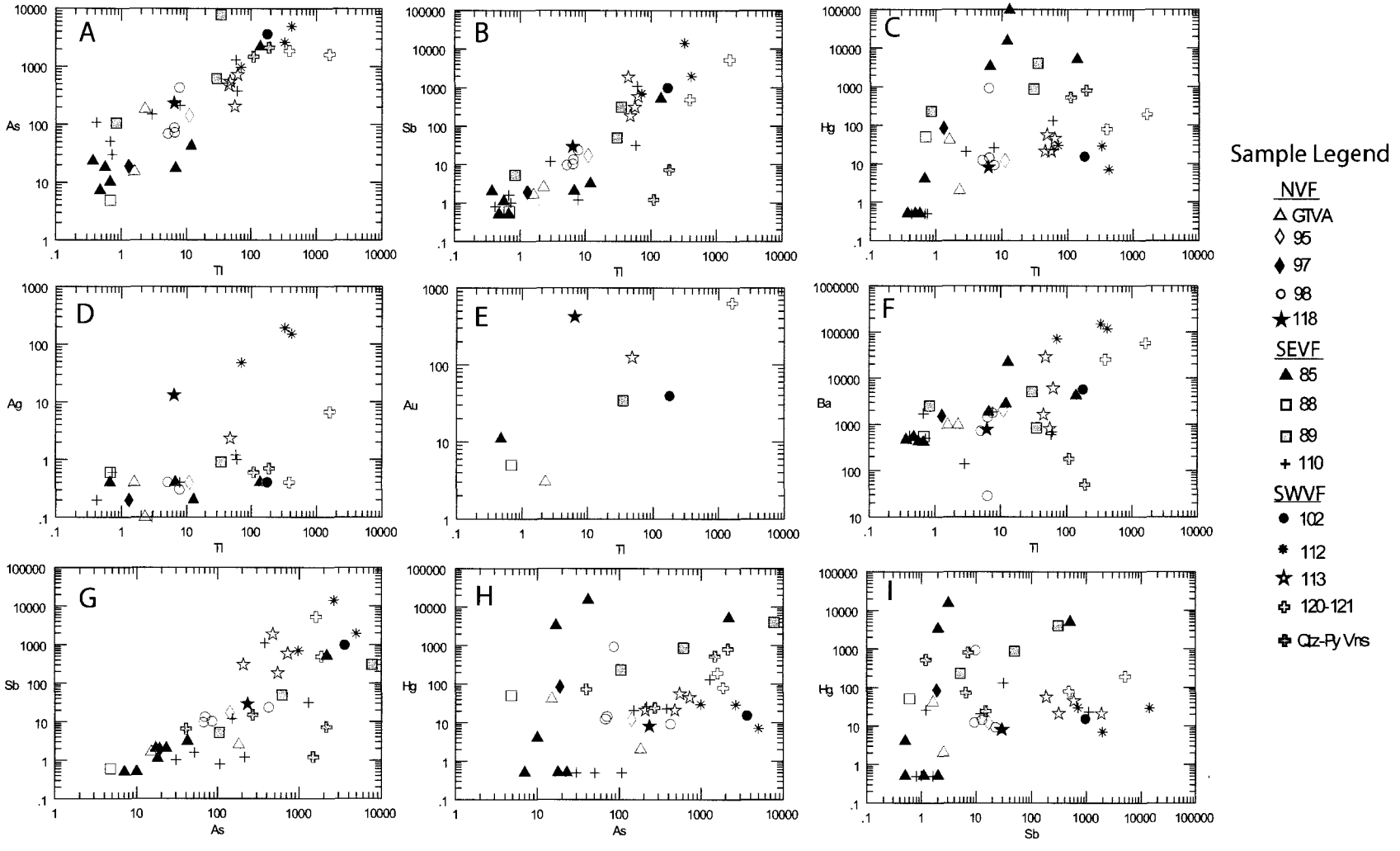

Figure 6.23. Log/log bivariant plots of selected elements in samples from the Calypso vent fields; sorted by sample series number: As, Sb, and Tl concentrations display a strong correlation (plots A, B, G). Hg, Ag, and Au values show considerable scatter relative to other volatile metals.

6.3 Mass Changes

Mass gains and losses during alteration were determined using the single precursor method of Maclean (1990). An enrichment factor (EF) is calculated using an element determined to be immobile; Ti was used for Calypso samples. The EF is calculated by dividing the concentration of Ti in the least-altered, precursor sample by the concentration of Ti in the altered sample. A reconstituted composition (RC) of the altered rock can be calculated by multiplying the EF by the concentration of each element in the altered rock. The mass change (MC) is then determined by subtracting the concentrations of each element in the precursor sample from the RC. The use of this method has been demonstrated in numerous ancient volcanic successions (MacLean and Barrett, 1993; Barrett and MacLean, 1994; Gifkins and Allen, 2001).

6.3.1 Clay-alteration

The least clay-altered sample was selected by a combination of visual inspection and chemical characteristics (e.g., CIA-SI box plot, Figure 6.19). The least clay-altered, lapilli tuff sample (81-GTVA) has high Si/Al ratios, low sulfur and LOI-S (Figure 6.22), and low AI and CIA index (Figure 6.19) values relative to the other clay-altered samples. This sample plots within the compositional space of White Island andesite on the CIA-SI box plot (Figure 6.19). Sample 82-GTVA was selected as the altered equivalent. It has a higher concentration of immobile elements relative to 81-GTVA, indicating an overall

mass loss of other elements. The calculated mass changes of major elements indicate an 11% mass loss of SiO_2, with minor losses of CaO, Na_2O, and K_2O during clay alteration (Figure 6.24A). Significant mass gains of Fl, Cl, W, Hg, Zn, and Pb, and losses of Ba, Sr, Rb were also observed (Figure 6.24B).

Similar criteria were used to select two sulfur-rich lapilli tuff samples, one intensely clay-altered, and a least-altered equivalent. Sample DR-98-7a was selected as the least-alerted equivalent of DR-98-7b (i.e., CIA values; Table 6.1). Calculated mass changes are similar to those of the sulfur-poor clay-altered lapilli tuff samples. Slight mass losses were observed for SiO_2, CaO, Na_2O, K_2O, Ba, Sr, Rb. Mass gains were observed for Fe_2O_3, MgO, Fl, Cl, and Hg (Figure 6.24C, 6.24D).

7.3.2 Silicification

Sample DR-110wp was previously identified as the least-altered vitric tuff. Sample DR-110wp has similar aluminum/alkali metal ratios (e.g., A/NK, A/CNK, CIA), alteration index values, and immobile element ratios (e.g., Zr/Ti, Nb/Y) to the silicified vitric ash samples (Table 6.1). The silicified vitric ash samples have higher silicification index and Si/Al values and contain lower concentrations of immobile elements, indicating dilution from the large mass gains of silica. Calculated mass changes between DR-110i and DR-110i wp indicate an 80% mass addition of SiO_2 with very minor increases of Fe_2O_3, MgO and alkali elements (Figure 6.25A). An increase in volatile and base metals (except Pb) is also observed during silicification.

Volatile metals mineralization is concentrated in the SEVF and SWVF. Arsenic and antimony mineralization is most abundant in the silicified barite-rich tuff (DR-112, DR-120, DR-121), and the highest concentrations of mercury sulfide and native mercury are in the silicified crystal-tuff (DR-85, DR-89). Pyrite veins which cut the silicified vitric tuff also have high concentrations of volatile metals. Arsenic, Sb, Hg sulfide and amorphous silica precipitate from near-neutral pH fluid discharge in the subaerial system (e.g., Simmons et al., 2005); this mechanism likely persists at Calypso although with seawater rather dominantly meteoric fluids.

Clay alteration and native sulfur is most readily observed in the NVF with fewer samples recovered from the SEVF (DR-110K) and the SWVF (DR-113b – 113-05). The spatial and geochemical association between pervasive clay alteration and native sulfur suggest that alteration and sulfur precipitation are associated with discharge of hydrothermal gases (dominantly CO_2 and H_2S).

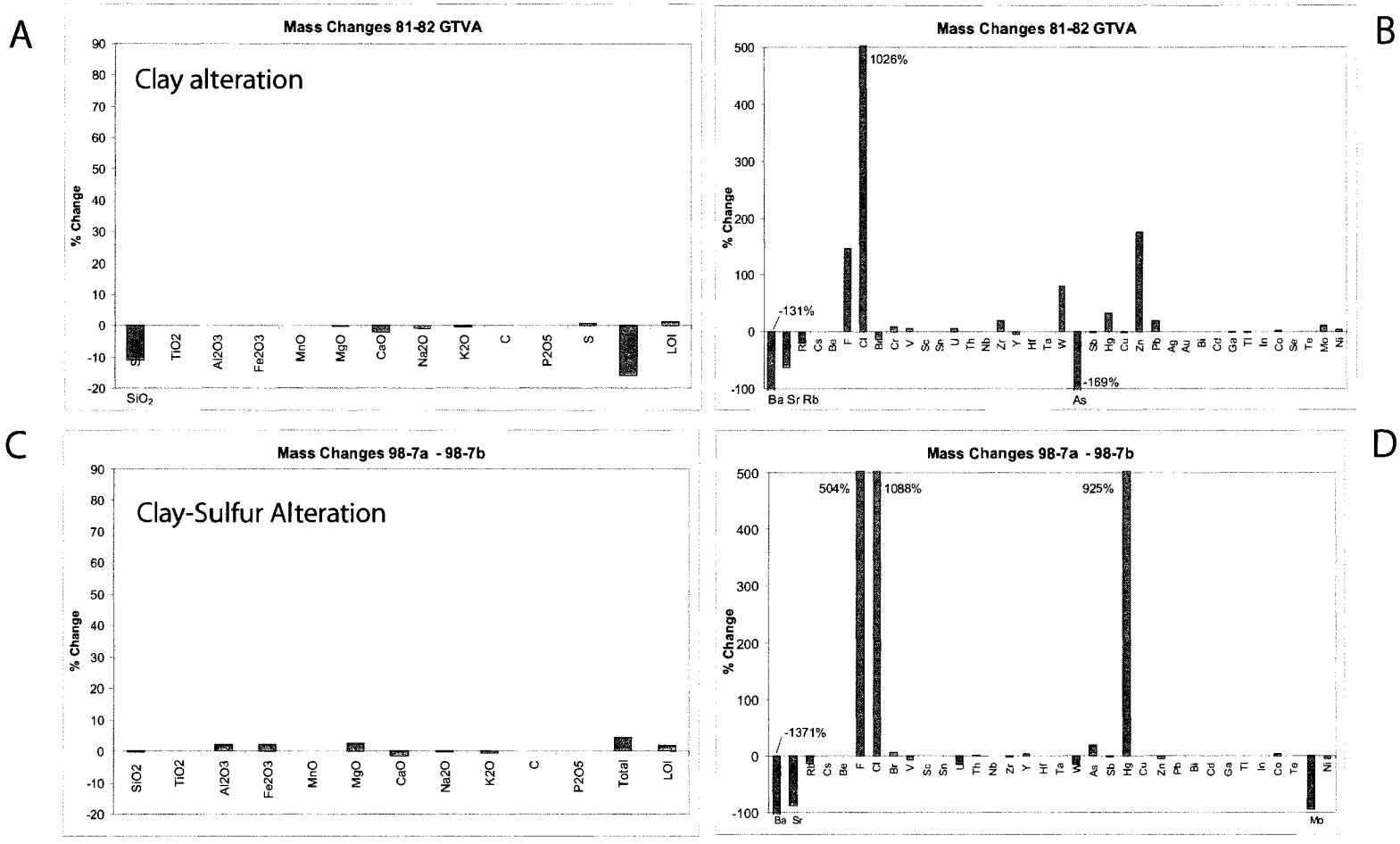

Figure 6.24. Mass changes incurred during hydrothermal alteration of primary igneous material and precipitation of elements from hydrothermal fluid. Changes calculated using the single precursor method by Barrett and MacLean (1990); TiO_2 was used to determine the enrichment factor. Major (A) and trace element (B) variation during progressive alteration from least clay-altered glassy lapilli tuff (81-GTVA) to montmorillonite altered lapilli tuff (82-GTVA). Major (C) and trace (D) element variation during between montmorillonite altered and sulfur rich lapilli tuff (DR-98-7a) to more intensely altered clay-sulfur altered lapilli tuff (DR-98-7b).

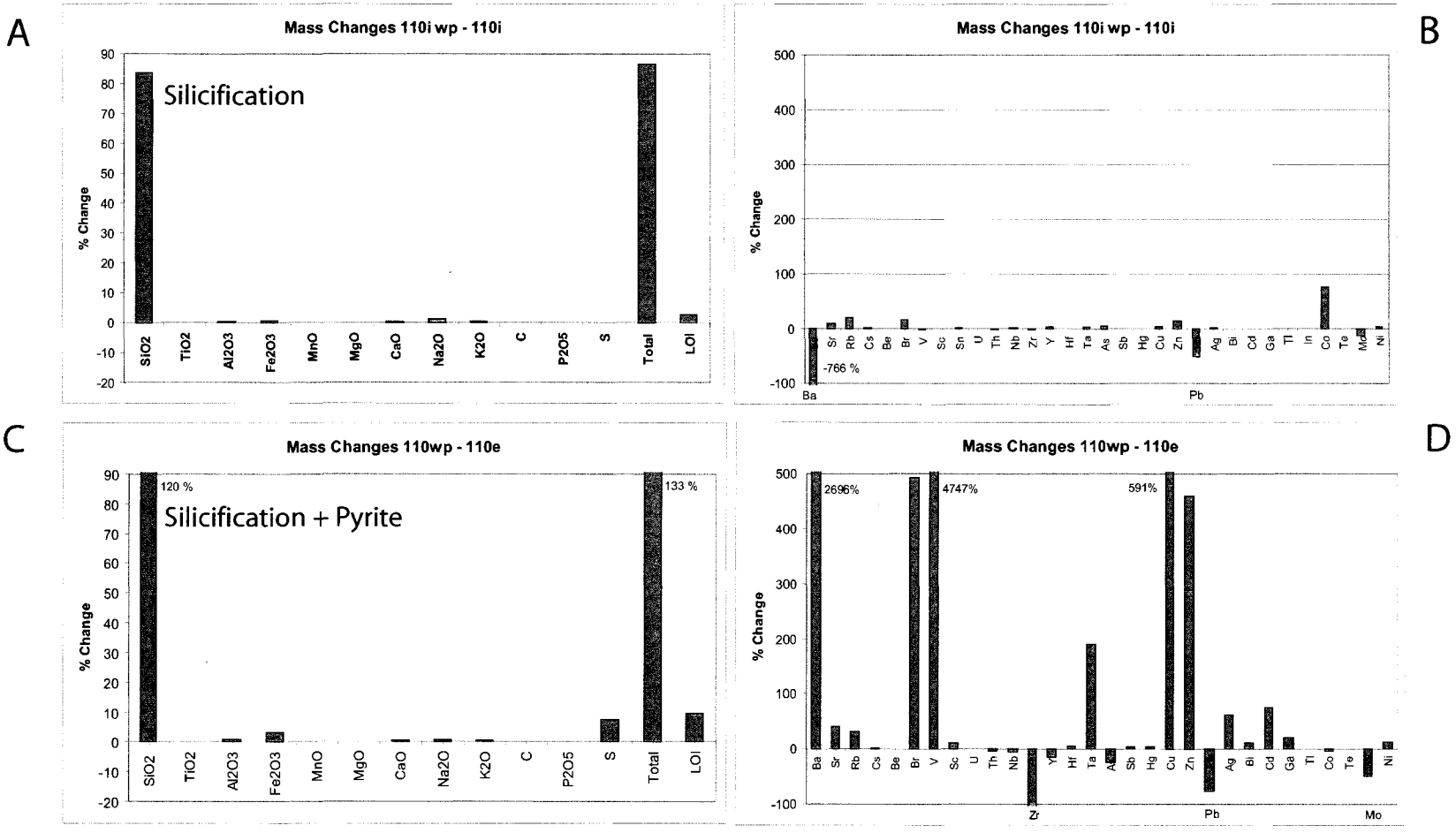

Figure 6.25. Mass changes incurred during hydrothermal alteration of primary igneous material and precipitation of elements from hydrothermal fluid. Changes calculated using the single precursor method by Barrett and MacLean (1990); TiO_2 was used to determine the enrichment factor. Major (A) and trace element (B) variation during alteration from least altered, weakly consolidated, vitric ash (DR-110i wp) to silicified tuff (DR-110i). Major (C) and trace element (D) variation during alteration from least altered, weakly consolidated, ash (DR-110i wp) to silicified tuff with cross cutting silica-sulfur-pyrite veining (DR-110e).

7.0 Sulfur Isotope Geochemistry

Native sulfur, sulfur mud, pyrite, and volatile metal sulfides are present in abundance at the CHVF. Massive native sulfur is observed on the seafloor in the vicinity of active fluid venting at the CHVF (Stoffers and Wright, 1999). Native sulfur lines fractures and fills void spaces in recovered volcaniclastic material. Pumiceous clasts have been cemented by native sulfur and mixtures of sulfur and clay, and pumice vesicles commonly contain massive native sulfur. Pyrite is disseminated, primarily throughout the pumiceous lapilli tuff samples, and pyrite-silica veins with clots of native sulfur fill fractures within the silicified tuff samples. Arsenic, Sb and Hg sulfides are observed filling fractures and coating the exteriors of samples. Sulfur isotope analysis of these phases has been conducted to a) identify the source of the sulfur, and b) determine the conditions which allowed for submarine precipitation of native sulfur and metallic sulfides.

Sulfur has four stable isotopes with ^{32}S and ^{34}S being the most abundant. Mass-dependant fractionation is caused because the mass of ^{34}S is 6.2% greater than that of ^{32}S (Faure and Mensing, 2005). The $^{34}S/^{32}S$ ratio of sulfur found in nature is expressed as $\delta^{34}S$, which is defined as:

$$\delta^{34}S = [(\,^{34}S/^{32}S)_{sample} - (^{34}S/^{32}S)_{standard}) / (^{34}S/^{32}S)_{standard}]$$

The Canyon Diablo meteorite is used as the international sulfur isotopic standard. The sulfur contained within the troilite (FeS) meteorite has a $^{34}S/^{32}S$ ratio of 0.0450. This

value approximates the $^{34}S/^{32}S$ ratio of mafic igneous rocks (Smitheringale and Jensen, 1963; Schneider, 1970). Due to mass differences of the sulfur isotopes, they react at different rates in various chemical reactions. If a given reaction does not go to completion, the isotopic value of the products will differ from that of the residual reactants. The enrichment or depletion of the $^{34}S/^{32}S$ can be used to reveal the origin of a sulfur compound (Schoen and Rye, 1970).

The speciation of sulfur in a hydrothermal fluid is dictated by the oxidation-reduction conditions of the system. Hydrogen sulfide gas contains sulfur in a reduced state with a valence state of -2 and native sulfur has a valence state of 0. Oxidized species in the form of $SO_{2\,(g)}$ and sulfate (SO_4^{2-}, H_2SO_4) have valence states of + 4 and + 6, respectively (Faure, 1998). Thus, sulfur isotopic ratios of native sulfur, sulfate, and sulfide allows inferences to be made about the redox conditions under which these sulfur compounds formed.

Sulfur contained within primitive magmas or sulfur gases derived from the magmas will have $\delta^{34}S$ values near zero [e.g., Mid-Ocean Ridge Basalt (MORB), $\delta^{34}S \pm 0$ ‰; Sakai et al., 1984]. Andesites in island arc environments have $\delta^{34}S$ values of 5-7 ‰ (Ueda and Sakai, 1984; Woodhead et al., 1987). The assimilation of isotopically heavy (+20 ‰) seawater SO_4^- bearing marine sediments into arc magmas creates the ^{34}S enrichment relative to MORB (Woodhead et al., 1987). The sulfur contained within the gas samples collected from geothermal wells, in the subaerial portion of the TVZ, consists primarily of $H_2S_{\,(g)}$. Gas samples collected from fumaroles at the subaerial volcano of White Island consist primarily of oxidized $SO_{2\,(g)}$. These two environments, with distinctly different

oxidation-reduction conditions, are two possible sources of sulfur at Calypso. The $\delta^{34}S$ values of sulfur gas in samples from White Island fumaroles (Giggenbach et al., 2003) and subaerial TVZ geothermal wells (Giggenbach, 1995), along with the values of sulfur compounds collected at Calypso are illustrated in Figure 7.1.

Fluid sampling of active vents conducted during SO-135 indicate that reduced sulfur, present as $H_2S_{(g)}$, is the dominant sulfur species in the hydrothermal fluid at Calypso (Botz et al., 2002). The $\delta^{34}S$ of the $H_2S_{(g)}$ was not measured. Sulfur isotopes have been used to determine if the sulfur compounds at Calypso precipitated from $H_2S_{(g)}$ with an isotopic composition analogous to that at White Island or similar to $H_2S_{(g)}$ sampled in geothermal wells on the subaerial portion of the TVZ.

Fluid sampling was also conducted at the Calypso vents during research cruise SO-192-2 in May, 2007. Sulfur isotope analyses of $H_2S_{(g)}$ in the fluid will yield a better understanding of the sources of sulfur at Calypso and the redox conditions that allowed for precipitation of native sulfur and sulfides (R. Botz Pers. Comm. 2007).

7.1 Methods

Analytical work was conducted at the G.G. Hatch stable isotope facility at the University of Ottawa on hand-picked mineral separates. Analyses were conducted by elemental analyzer (EA) combustion and continuous flow-isotope ratio mass spectrometry (CF-IRMS) as outlined by (Grassineau et al., 2001). Analyses are reported in standard δ notation relative to Canyon Diablo Troilite (CDT).

7.2 Results

The sulfur isotope ratios obtained from native sulfur, sulfur mud, and sulfide minerals recovered from the North Vent Field, Southeast Vent Field, and Southwest Vent Field are summarized in Table 7.1.

The $\delta^{34}S$ values at Calypso range from -5.3‰ to +6.9‰ with an average of + 2.6‰ (n = 52). Native sulfur samples from the NVF have a wide range of $\delta^{34}S$ values from -4.4 to 6.6‰ with an average value of 3.4 ‰ (n = 9), native sulfur from the SEVF has $\delta^{34}S$ values of between + 3.3‰ and + 6.7‰ with an average value of + 4.5‰ (n = 11). The $\delta^{34}S$ values of native sulfur from the SWVF are slightly lower, ranging from -1.0‰ to + 4.4‰ with an average of + 2.2‰ (n = 6). The average of all native sulfur recovered from Calypso is + 3.4 ‰ (n = 26).

Sulfur mud at Calypso has a slightly lower of $\delta^{34}S$ values ranging from - 3.6‰ to 5.1‰ with an average value of + 2.7‰ (n = 12).

Pyrite (average $\delta^{34}S$= + 0.3‰: n = 9), stibnite (average $\delta^{34}S$= + 0.4‰: n = 2), and cinnabar ($\delta^{34}S$= + 1.1‰: n = 1) samples are isotopically lighter than native sulfur (average $\delta^{34}S$= + 3.4‰: n = 26) and sulfur mud (average $\delta^{34}S$= + 2.7‰: n = 12).

The $\delta^{34}S$ values of $H_2S_{(g)}$ measured from selected geothermal wells on the subaerial portion of the TVZ (i.e., Kawerau, Ti Tikitere, Ro Rotorua, Waiotapu, MK Mokai, Broadlands, Rotakawa, Wairakei) range from + 3.2‰ to + 8.2‰ with an average value of +

5.14‰ (n = 32: Giggenbach, 1995). These systems are typified by near neutral-pH, chloride water fluids with sulfur occurring primarily as $H_2S_{(g)}$.

In contrast, fumarolic discharge from the subaerial portion of White Island contains $SO_{2\,(g)}$, $H_2S_{(g)}$, and S° (elemental sulfur in the vapour). Sulfur occurs primarily in the oxidized state as $SO_{2\,(g)}$, with a SO_2:H_2S ratio of 4:1 (Giggenbach et al., 2003). The $SO_{2\,(g)}$ values range from -6.3‰ to + 7.2‰ with an average values of 3.8‰ (n = 14: Giggenbach et al., 2003). The $H_2S_{(g)}$ and S° contained within the fumurolic vapour is formed when $SO_{2\,(g)}$ disproportionates in water into reduced and oxidized sulfur species (reactions 6 and 7: cf. de Ronde et al., 2005 and references therein).

$$SO_{2\,(g)} + 4\,H_2O = 3\,H_2SO_{4\,(aq)} + H_2S_{(g)} \qquad (6)$$

$$3\,SO_{2\,(g)} + 2\,H_2O = 2\,H_2SO_{4\,(aq)} + S° \qquad (7)$$

These reactions are accompanied by a kinetic isotope effect where the sulfide is enriched in ^{32}S and the sulfate is enriched in ^{34}S (Ohmoto and Rye, 1979); and (Ohmoto and Lasaga, 1982). The $\delta^{34}S$ values of $H_2S_{(g)}$ from the White Island fumaroles range from -4.3‰ to 4‰ with an average value of -1.34‰ (n = 12). Elemental sulfur in the vapour has $\delta^{34}S$ values that range from -8.9‰ to -0.3‰, with an average value of -4.71‰ (n = 13). The isotopic values of the reduced species are considerably lighter than the oxidized $SO_{2\,(g)}$, consistent with the disproportionation reactions (Giggenbach et al., 2003).

7.3 Sources of Sulfur

The $\delta^{34}S$ of Calypso samples ranges from approximately -5‰ to + 7‰ (Figure 7.2). The wide range likely reflects the formation of sulfur compounds under non-equilibrium conditions. Hydrogen sulfide gas at Calypso may be derived from several sources including 1) bacterial reduction of seawater sulfate; 2) leaching of sulfur from underlying rocks, 3) inorganic reduction of seawater sulfate; 4) disproportionation of magmatic SO_2 into H_2S; and 5) reduction of magmatic SO_2 to H_2S.

Reduction of seawater sulfate to sulfide by anaerobic bacteria is a common process in the marine sedimentary setting (Canfield, 2001; Faure and Mensing, 2005). Bacteria consume sulfate ions and through metabolic processes and excrete $H_2S_{(g)}$ enriched in ^{32}S by up to 50% (Faure and Mensing, 2005). The maximum temperature for the production of organically-reduced seawater sulfate is < 120°C (Canfield, 2001). Sulfide produced by this process will have a light ($\delta^{34}S < 0$ ‰) isotopic signature.

Sulfur may be mobilized from the underlying stratigraphy by ascending hydrothermal fluid. Leached sulfur ($H_2S_{(aq)}$) will inherit the isotopic composition of the sulfur in the rocks (e.g., Island Arc andesite $\delta^{34}S = \sim 3$ - 7.5‰; Figure 7.1: Ueda and Sakai 1984). Hydrogen sulfide derived from bacterially reduced sulfide in underlying marine sediments will be enriched in ^{32}S. This mechanism has also been show to contribute isotopically light sulfur to some seafloor hydrothermal systems (e.g., Shanks et al., 1995 as cited in Herzig et al., 1998). This pattern is also observed in sulfides from volcanogenic

massive sulfide deposits that formed in sedimented environments (e.g., Guaymas Basin, Figure 7.3; Peter and Shanks, 1992; Hannington et al., 2005).

The reduction of seawater sulfate in seafloor hydrothermal systems at temperatures between 200°C and 300°C would have $\delta^{34}S$ values between -4‰ and + 21‰ depending on the extent of equilibrium (Ohmoto and Rye, 1979). The sulfur isotopic composition of anhydrite at Calypso is 21.6 ‰ which is comparable to the sulfur isotopic values of modern seawater sulfate ($\delta^{34}S$ + 20.9 ‰: Rees et al., 1978).

Disproportionation of $SO_{2\ (g)}$ to $H_2SO_{4\ (aq)}$, $H_2S_{\ (g)}$, and native sulfur has been described at several submarine volcanic-hydrothermal environments (e.g., Figure 7.2; Hine Hina, Lau back-arc: Herzig et al., 1998; Brothers Volcano, Kermadec Arc: de Ronde et al., 2005). Sulfuric acid produced by this reaction has created advanced argillic alteration in these environments. Native sulfur formed by this reaction is strongly enriched in ^{32}S (e.g., White Island SO_2-S°; Figure 7.1). The considerably heavier isotopic value of native sulfur at Calypso (+ 3.4‰; n = 26) and the absence of an advanced argillic mineral assemblage indicates this processes did not occur at Calypso.

The isotopic composition of most native sulfur and sulfur mud samples overlap the sulfur isotopic range of $H_2S_{(g)}$ in geothermal wells on the subaerial TVZ and White Island $SO_{2(g)}$ (Figure 7.1). The narrow range of $\delta^{34}S$ values of $H_2S_{\ (g)}$ reported from geothermal wells situated over a large area suggest a uniform source and has been attributed to a degassing magma chamber (Steiner and Rafter, 1966). This suggests a contribution of reduced magmatic sulfur or sulfur leached from underlying igneous rocks with this

composition has been added to the Calypso hydrothermal system. Average sulfur isotopic values of pyrite (+ 0.3‰), stibnite (+ 0.4‰), and cinnabar (+ 1.1‰) samples are isotopically lighter than native sulfur (+ 3.4‰: n = 26) and sulfur mud (+ 2.7‰: n = 12). This range likely reflects a combination of higher temperature fluids with a magmatic sulfur composition and a contribution of light reduced sulfur (bacterial reduction) from the basement rocks from where the metals were leached.

7.4 Sulfur Oxidation-Reduction Reactions in Hydrothermal systems

At a salinity of 35‰ NaCl and an ambient temperature of 4°C at Calypso the seawater will have an average oxygen solubility of 315.7 μmol kg^{-1} (Kester, 1975 as cited in Chester, 1990) and an average sulfate concentration of 2.712 g/kg at a (Chester, 1990). Abiotic oxidation of $H_2S_{(g)}$ to native sulfur (reaction 8) does not cause any appreciable isotopic fractionation (Sakai, 1957; Rafter et al., 1960). $H_2S_{(g)}$ may also react with sulfate to form native sulfur (reaction 9; Faure and Mensing, 2005). The oxidation of H_2S to native sulfur by sulfate is a proposed mechanism for precipitation of native sulfur in salt domes (Jones et al., 1956; Feely and Kulp, 1957). Other workers doubt the thermodynamic validity of this mechanism and indicate dissolved oxygen is the oxidant (Davis and Kirkland, 1970; Davis and Kirkland, 1979). A shift to a heavier isotopic sulfur composition would be expected when H_2S is oxidized by isotopically heavy marine sulfate ($\delta^{34}S$ of 20.5‰).

$$H_2S_{(g)} + \tfrac{1}{2} O_{2(g)} \rightarrow S^\circ + H_2O \qquad (8)$$

$$SO_4^{2-}{}_{(aq)} + 3\ H_2S_{(g)} \rightarrow 4\ S^\circ + 2\ H_2O + 2OH^-_{(aq)} \qquad (9)$$

Oxidation of $H_2S_{(g)}$ to $H_2SO_{4\ (aq)}$ (sulfuric acid) by a variety of reactions (e.g., reaction 10) is accompanied by a large positive shift in the isotopic value of the sulfate (Sakai, 1957).

$$H_2S_{(g)} + 2\ O_{2\ (g)} \rightarrow H_2SO_{4\ (aq)} \qquad (10)$$

The extent of this reaction (10) is limited by the availability of oxygen; insufficient dissolved oxygen in seawater may preclude this process (cf. Rye et al., 1992; Hedenquist et al., 2000). However, this reaction has previously been suggested to explain native sulfur deposits and advanced argillic alteration assemblages associated with sulfuric acid production at the submarine Jade Hydrothermal Field (Marumo and Hattori, 1999).

The distribution of bacteria and sulfuric acid at subaerial solfataras (Ehrlich and Schoen, 1967) and experimental data for bacterial mediated oxidation of $H_2S_{(g)}$ to sulfuric acid (Schoen, 1969) suggest inorganic oxidation of $H_2S_{(g)}$ to $H_2SO_{4\ (aq)}$ is not possible without bacteria to catalyze the process. Isotopic analysis of sulfur and sulfate minerals in acid-sulfate steam-heated alteration suggests that the $H_2S_{(g)}$ is primarily oxidized by atmospheric oxygen to native sulfur; sulfur is then oxidized by sulfur-oxidizing bacteria of the genus *Sulfolobus* (Mosser et al., 1973) to $H_2SO_{4\ (aq)}$. Bacterial oxidation of $H_2S_{(g)}$

directly to $H_2SO_{4\,(aq)}$ has been observed at low temperature (< 70° C) geothermal vents with low gas emission rates suggesting bacterial oxidation is temperature sensitive (Schoen and Rye, 1970) and may be restricted to a narrow temperature range (Mosser et al., 1973). Experimental data indicate bacterial oxidation of $H_2S_{(g)}$ show a shift of -6‰ in native sulfur derived from $H_2S_{(g)}$ (Kaplan and Rafter, 1958) and a -18‰ in sulfate derived from $H_2S_{(g)}$ (Kaplan and Rittenberg, 1962). Bacterial mediated oxidation of native sulfur to sulfate shows no fractionation or slight positive fractionation of +2‰ (Kaplan and Rittenberg, 1962).

Aerobic and anerobic S-oxidizing bacteria have been recognized in acidic and near-neutral pH conditions in both marine and terrestrial environments, including the genus members of *Thiobacillus, Acidianus, Aquifex, Metalosphaera, Sulfolobus, Sulfobacillus, Beggiatoa, Thiovolum , and Thiomicrospira.* The bacteria oxidize S° or H_2S using O_2 as the oxidant in the biologically mediated process (Amend et al., 2004).

Hydrogen sulfide at Calypso has a wide range of sulfur isotopic compositions but does not display strong positive isotopic shifts that would be expected with oxidation by marine sulfate. The majority of native sulfur and sulfur mud samples do not have a strong enrichment of ^{32}S as would be expected by bacterial oxidation. Dissolved oxygen is the likely mechanism for oxidation of $H_2S_{(g)}$ at Calypso. Evidence of further oxidation of the $H_2S_{(g)}$ or native sulfur to sulfuric acid was not observed. Insufficient dissolved oxygen may have inhibited this reaction and prevented the development of an advanced-argillic acid-sulfate alteration mineral assemblage.

Analyzed Phase	Host Lithology	^{34}S ‰ CDT Average	Range	(n)
	North Vent Field			
Native sulfur	Clay-altered lapilii tuff	3.4	-4.4 to 6.6	(9)
Sulfur-rich mud	Clay-altered lapilii tuff	-1.9	-3.6 to -0.1	(2)
Pyrite	Clay-altered lapilii tuff	1	-5.3 to 4.3	(3)
Anhydrite	Massive anhydrite	21.6	--	(1)
	Southeast Vent Field			
Native sulfur	Silicified crystal and vitric tuff	4.5	3.3 to 6.7	(11)
Native sulfur	Clay-altered lapilii tuff	-0.5	--	(1)
Sulfur-rich mud	Silicified crystal and vitric tuff	3.1	0.2 to 4.5	(7)
Pyrite	Silicified vitric tuff	-0.5	-2.0 to 0.2	(4)
Cinnabar	Silicified crystal tuff	1.1	--	(1)
	Southwest Vent Field			
Native sulfur	Silicified crystal tuff	2.2	-1.0 to 4.4	(6)
Sulfur-rich mud	Clay-altered lapilii tuff	4.3	--	(1)
Sulfur-rich mud	Charcoal	5.1	3.2 to 6.9	(2)
Pyrite	Silicified tuff	1	-2.2 to 4.1	(2)
Stibnite	Barite-rich silicified tuff with volcanic blocks	0.4	-1.1 to 4.1	(2)
Amorphous arsenic sulfide	Barite-rich silicified tuff with volcanic blocks	3.4	3.3 to 3.5	(2)
Amorphous arsenic sulfide	Clay-altered lapilli tuff	2.2	-1.0 to 5.4	(2)
Amorphous arsenic sulfide	Silicified crystal tuff	1.3	--	(1)

Table 7.1. Sulfur isotope composition of native sulfur, sulfur-rich mud, anhydrite, and metal sulfides recovered from Calypso.

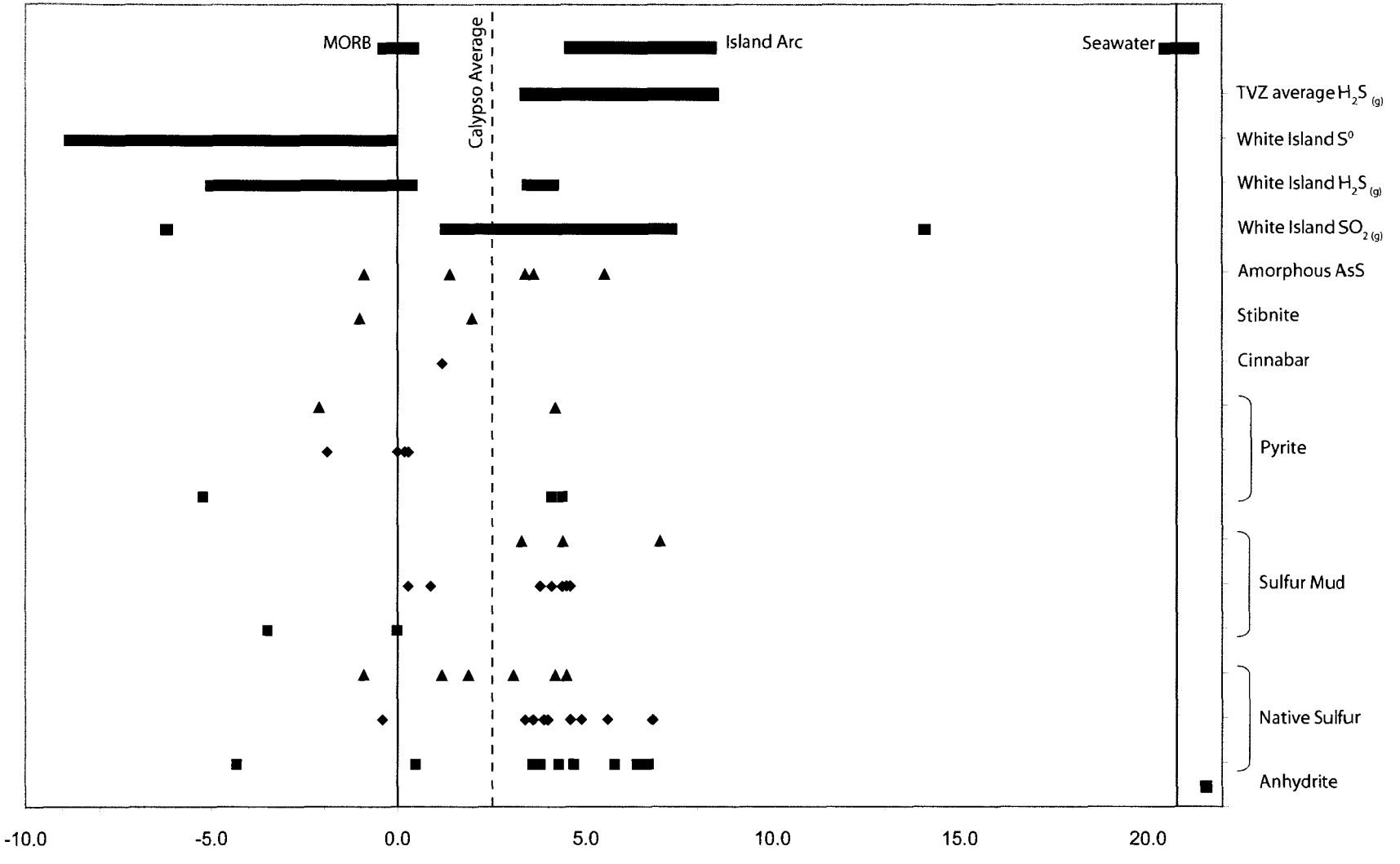

Figure 7.1. Compilation of sulfur isotopic data (‰ $\delta^{34}S$) for native sulfur, sulfur mud, and sulfide samples from the North (■), South-east (◆), and Southwest (▲) Vent Fields at Calypso. References: White Island fumarolic $SO_{2(g)}$, $H_2S_{(g)}$, S^0, Giggenbach et al. (2003); TVZ average $H_2S_{(g)}$, Giggenbach (1995); MORB, Sakai et al. (1984); Island Arc, Ueda and Sakai (1984); Seawater, Rees et al. (1978).

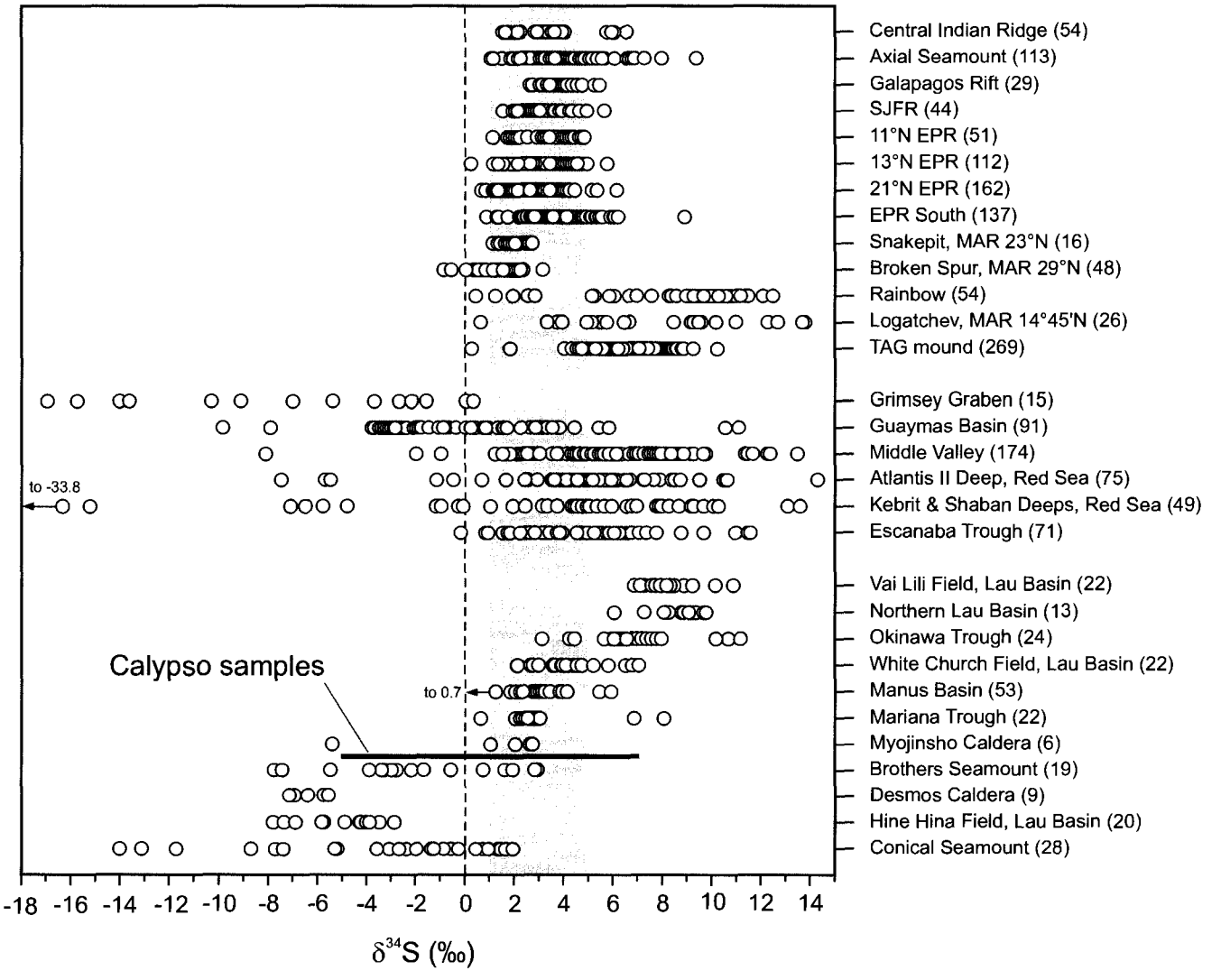

e 7.2. Sulfur isotope compositions of representative sea-floor polymetallic sulfides from Hannington et al., (2005). The da vided into mid-ocean ridges, sedimented environments, and arc and back-arc basin settings. The red bar represents the ran alues in samples recovered from Calypso.

8.0 Discussion and Conclusions

8.1 Host Rock

The sample suite recovered from Calypso is composed primarily of dacitic volcaniclastic material derived from intermediate to felsic caldera-building eruptions on the North Island of New Zealand. A smaller quantity of scoriaceous volcaniclastic material recovered largely from the North Vent Field is andesitic in composition and was likely the product of eruptions and associated volcaniclastic processes on White Island. The Zr enrichment of samples DR-85 and DR-102-05 is likely caused by accumulation of heavy minerals.

8.2 Alteration and Mineralization

The Calypso sample suite can be broadly subdivided into a clay-poor, silicified, lithofacies that is associated with As, Sb, Hg volatile metal mineralization and a pervasively clay-altered lithofacies that is associated with abundant native sulfur.

X-ray diffraction of the clay-altered samples indicates smectite is the principal clay-mineral present. Mixed-layer illite-smectite and minor illite is also present in the samples; distinguished by very low intensity X-ray peaks (i.e., 10Å). A single sample (DR-110k) displayed an X-ray pattern consistent with talc and either mixed-layer smectite-chlorite or vermiculite. Short wavelength infrared reflectance spectroscopy was able to rapidly identify smectite in the clay-altered samples and classify the clay as a dioctahedral

montmorillonite. The minor to trace quantities of illite or mixed-layer illite-smectite were not detected by this method. The SWIR analysis of sample DR-110k indicates vermiculite is present in the sample; this method did not detect talc. Samples display better spectral patterns when the spectra are collected from rock samples as the milling processes appears to degrade the spectral pattern and possibly homogenize the spectrum of multiple phases.

Analytical electron microprobe analyses confirm that Al is the principal cation in the dioctahedral layer of the clay minerals, with minor Mg (Figure 5.8). This is consistent with the chemical composition of montmorillonite. Interlayer includes Na, Ca, and K and samples with elevated K concentrations reflect the metasomatic addition of K^+ and the illitization of smectite (e.g., Bauluz et al., 2002; Huggett and Cuadros, 2005). Dioctahedral clay minerals from drill core in the Broadlands-Ohaaki geothermal system have a lower concentration of Mg in the dioctahedral layer and a lower interlayer Na-content relative to the Calypso samples (Figure 5.8; Yan et al., 2001). Smectite forms under alkaline conditions where Mg, Ca, and Na are abundant (Deer et al., 1993), and the submarine environment may provide a higher concentration of dissolved Mg and Na than in subaerial systems; the composition of the volcanic rocks is also a factor.

Smectite can be the product of both diagenetic alteration of volcanic glass and hydrothermal alteration (Gifkins and Allen, 2001; Gifkins et al., 2005). The clay-altered samples can be chemically distinguished from the least-altered and silicified samples using Al-alkali element ratios and silica concentrations. The high LOI of clay-altered samples and elevated Al/Si ratios of clays also distinguishes clay-altered samples from least-altered and silicified samples. The strong association between samples with an elevated clay-

component and a high concentration of native sulfur suggests that gases (e.g., CO_2, which together with H_2S, accounts for most of the gas) are responsible for the clay alteration. Mass change calculations between increasingly clay-altered samples show very minor losses of alkali elements and minor to moderate silica loss. Barium, Rb, and Sr also show mass loss reflecting the destruction of feldspar. Fluorine also shows large mass gains and may be related to the presence of magmatic gases (e.g., Manus Basin: Douville et al., 1999). The presence of illite and mixed-layer clays, which are stable at higher temperatures, further suggest a hydrothermal, rather than diagenetic origin of the clay minerals at Calypso.

The juxtaposition of clay, silica and associated As, Sb, Hg sulfide at Calypso is similar to alteration and mineralization observed in active geothermal environments in the subaerial portion of the TVZ (e.g., Waiotapu, New Zealand). Notable differences are observed between the subaerial (Figure 2.1) and shallow submarine geothermal environments (Figure 8.1). Figure 8.2 is an interpreted cross-section of the distribution of alteration mineral assemblages at Calypso. The $CO_{2\ (g)}$ and $H_2S_{\ (g)}$ present in the hydrothermal fluid rise to areas of elevated topography. Mixing of $CO_{2\ (g)}$ with water creates carbonic acid which alters the volcaniclastic material to smectite. The presence of minor illite and illite-smectite mixed layer clays indicates K^+ metasomatism and formation at higher temperatures than pure smectite, consistent with measured temperatures in the vents. The H_2S is oxidized by dissolved oxygen to form native sulfur which fills the pore spaces that provided conduits for gas flow. Insufficient dissolved oxygen or the absence of appropriate bacteria prevent further oxidation of native sulfur or $H_2S_{\ (g)}$ to form sulfuric acid. A submarine solfatara and smectite altered volcanic rocks form in place of a typical

acid-sulfate-type advanced argillic alteration assemblage seen in the subaerial environment (e.g., Figure 2.2).

In the submarine environment silica deposits with a sinter morphology have not been reported; however locations with high silica concentration, "sinter-like" material, and anomalous Hg-Sb-As concentrations have been described (e.g., Hannington et al., 1986; Binns et al., 1993). Mixing of hydrothermal fluids with seawater, and the absence of a mechanism to concentrate silica, may inhibit sinter formation in the submarine environment. Instead silicification of permeable horizons may occur, as has been described stratigraphically below surface sinter deposits in fossil epithermal systems (e.g., Ivanhoe Mining District, Nevada; Wallace, 2003), and in modern geothermal systems (e.g., Broadlands-Ohaaki; Simmons and Browne, 2000). At Calypso, vitric and crystal-rich tuff samples have been cemented by abundant amorphous silica; clay alteration is minor within these lithofacies. Silicification is associated with high temperature fluids, which also carried metals. While clay alteration and sulfur precipitation associated with gas-rich vents is widespread, with samples recovered from each vent field, venting of SiO_2-rich and metal-rich fluids appears to have been more localized. Silica and volatile-metal mineralization is limited to the SWVF and SEVF which have average depths of 181.6 m and 189.5 m, the average water depth at the NVF is shallower at 170.5 m. Gas discharge and associated steam-heated alteration typically occurs peripheral to the silica sinters at areas of elevated topography in the subaerial environment. The morphology of the seafloor appears to exhibit a similar control with gas discharge occurring primarily at shallower levels and high temperature fluid discharge (silica + As, Sb, Hg) at deeper depth.

Boiling fluid was observed at active vents on the seafloor at Calypso, suggesting that boiling initiated in the sub-seafloor environment; this may explain the absence of significant quantities of precious metals at the seafloor at Calypso. Silica sinter in the subaerial environment is often barren of precious metals because of similar subsurface deposition in the boiling zone (Brown, 1986).

8.3 Sulfur Sources

The isotopic composition of most native sulfur and sulfur mud samples overlap the sulfur isotopic range of $H_2S_{(g)}$ in geothermal wells on the subaerial TVZ and White Island SO_2 (Figure 7.1). The narrow range of $\delta^{34}S$ values of $H_2S_{(g)}$ reported from geothermal wells situated over a large area suggest a uniform source and has been attributed to a degassing magma chamber (Steiner and Rafter, 1966). This suggests a contribution of reduced magmatic sulfur or sulfur leached from underlying igneous rocks with this composition has been added to the Calypso hydrothermal system. Average sulfur isotopic values of pyrite (+ 0.3 ‰), stibnite (+ 0.4 ‰), and cinnabar (+ 1.1 ‰) samples are isotopically lighter than native sulfur (+ 3.4 ‰: n = 26) and sulfur mud (+ 2.7 ‰: n = 12). This range likely reflects a combination of higher temperature fluids with a magmatic sulfur composition and a contribution of light reduced sulfur (bacterial reduction) from the basement rocks from where the metals were leached.

Dissolved oxygen in seawater oxidized $H_2S_{(g)}$ to native sulfur; evidence of further oxidation of the $H_2S_{(g)}$ to sulfuric acid was not observed. Insufficient dissolved oxygen

and/or neutralization by seawater prevented the development of an advanced argillic, acid-sulfate-type alteration mineral assemblage. The origin of the sulfur in the anhydrite mounds in the NVF and most likely barite at the SWVF is seawater sulfate.

8.4 Shallow Submarine Epithermal Systems in the Rock Record

The Calypso Hydrothermal Vent Field is the seafloor expression of a shallow-submarine low-sulfidation epithermal deposit. This study suggests that recognition of submarine stratigraphy and the alteration facies associated with submarine hydrothermal systems are important criteria for distinguishing fossil submarine epithermal mineralization in the geological record. Bioturbated pelagic sediment covers the CHVF area and rock exposure is limited to fault scarps. Pelagic limestone in the stratigraphy of fossil hydrothermal systems would indicate a marine environment. However, the epigenetic nature of epithermal systems makes it difficult to make a clear association between stratigraphy and the environment where the hydrothermal system formed.

The paleo-surface of subaerial fossil hydrothermal systems is recognized by the presence of silica sinter and steam-heated acid-sulfate alteration. At Calypso, silica discharge is recorded by silicification of volcaniclastic material, and intense clay-alteration associated with abundant native sulfur occurs in place of an acid-sulfate mineral assemblage. The clay minerals are predominantly smectite and contain elevated Mg and Na relative to smectite in geothermal wells on the subaerial portion of the TVZ. However,

differences in the initial composition of the volcanic protolith may cause some of the observed chemical variation between submarine and subaerial smectite samples.

Barite deposition in the subaerial low-sulfidation epithermal environment is rare (Sillitoe and Hedenquist, 2003) because of the absence of large volumes of sulfate. At Calypso the availability of seawater sulfate has allowed for precipitation of large quantities of barite which is present in samples that also contain amorphous silica and As and Sb mineralization.

The sulfur isotopic composition of anhydrite at Calypso indicates that it formed from seawater sulfate. Anhydrite has a retrograde solubility and will dissolve in ambient temperature seawater, consequently anhydrite has a low preservation potential. Sulfur isotope analysis of anhydrite veins typical of subaerial deposits (e.g., Hedenquist et al., 1998) may help distinguish deposits that did not form in a submarine environment. Barite has a higher preservation potential and, although not done for this study, sulfur isotope analyses would likely indicate that the sulfate is derived from seawater.

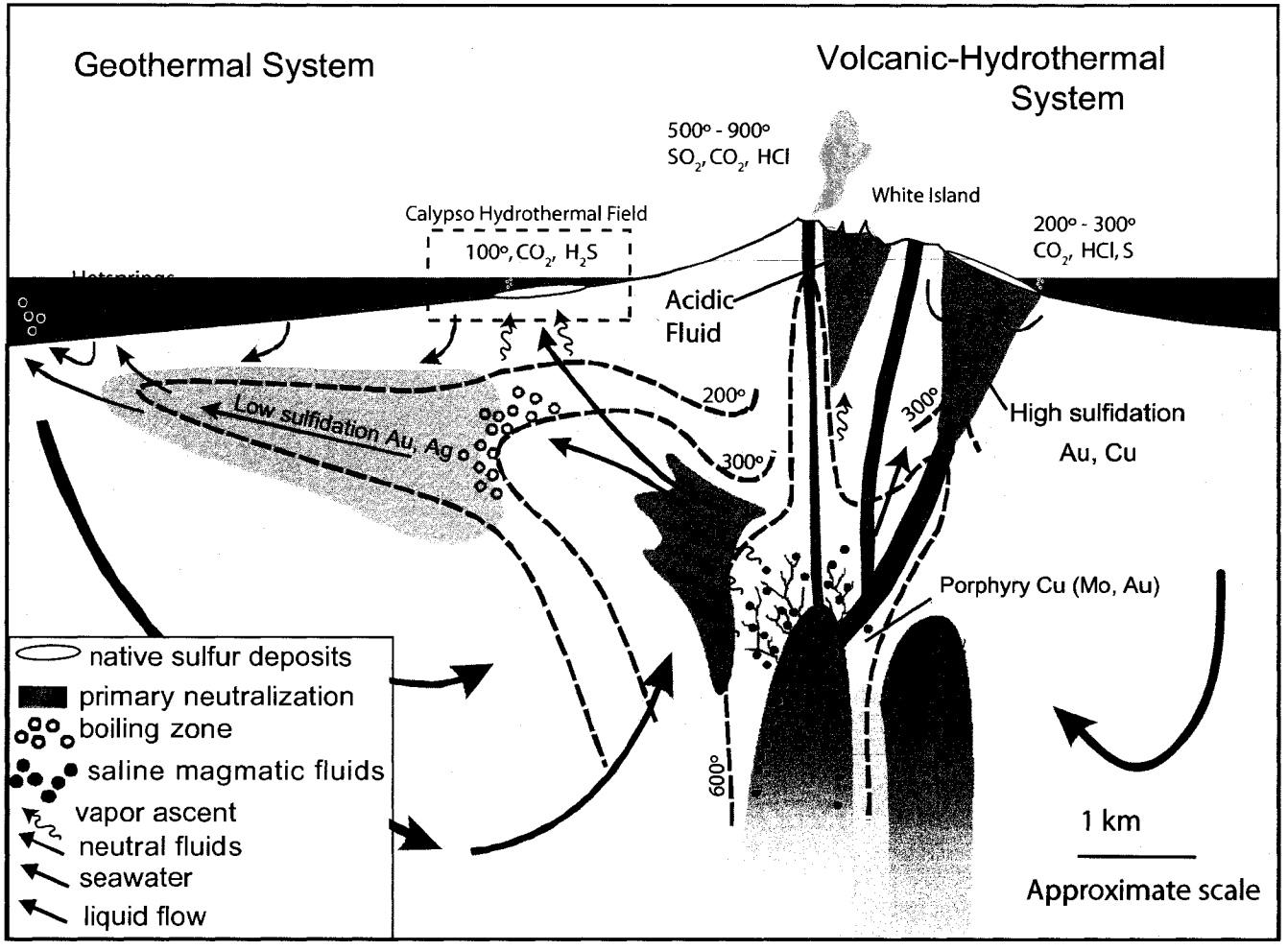

Figure 8.1. The submarine epithermal environment modified from Hedenquist et al., (2000) and Schwarz-Schampera (Pers. Comm. 2007) In the absence of atmospheric oxygen hydrogen sulfide gas cannot be oxidized to sulfuric acid in the submarine environment. This explains the absence of a low-pH stable aluminous, advanced-argillic, mineral assemblage at Calypso. Disproportionation of sulfur dioxide to sulfuric acid does, however, create advanced argillic alteration in some higher-temperature submarine volcanic-hydrothermal systems (e.g., Brothers Volcano, de Ronde et al., 2005).

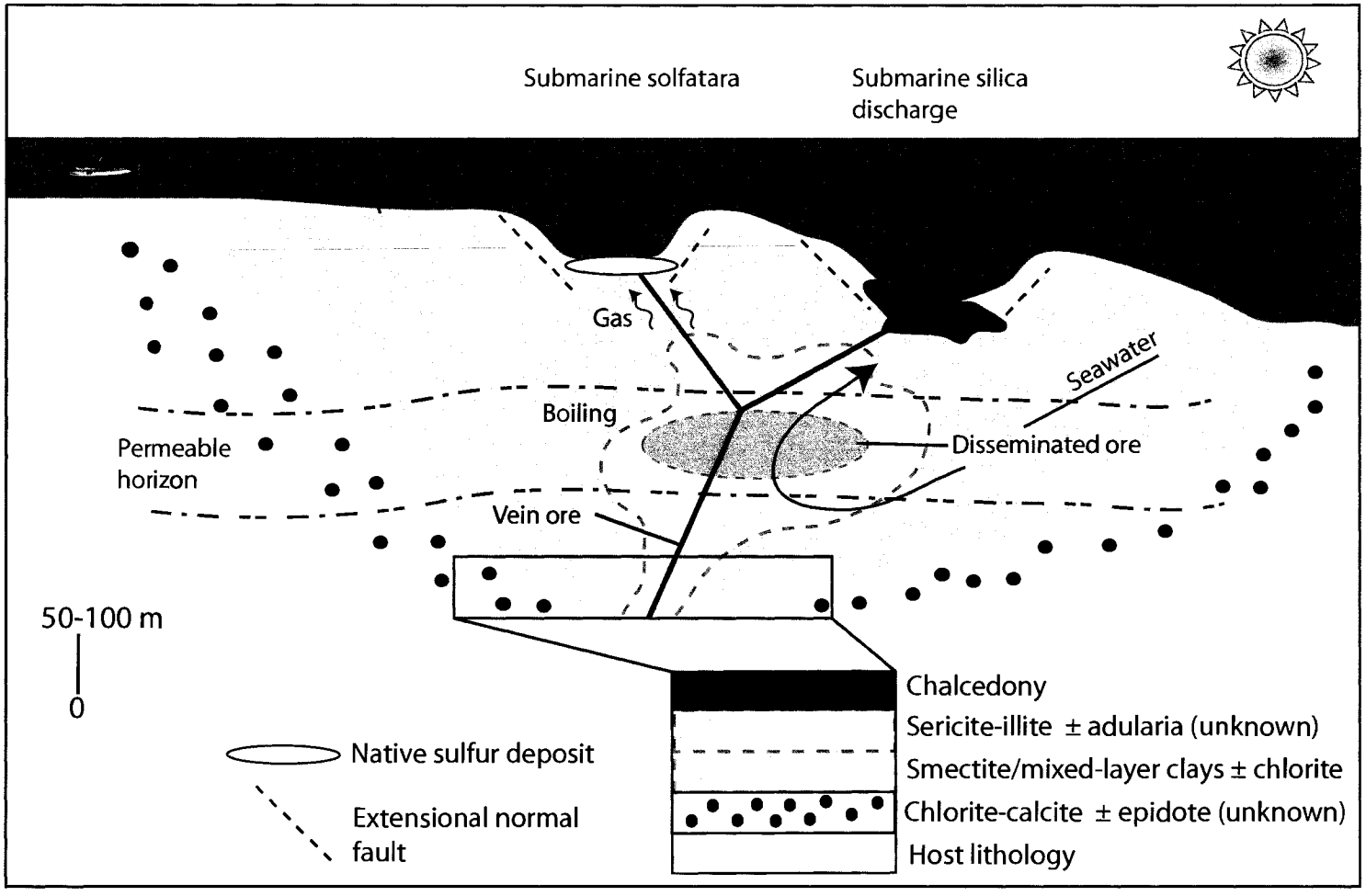

Figure 8.2. Interpreted cross-section of alteration mineral assemblage distribution at Calypso. The distribution of the ore zones as well as the sericite-illite and chlorite-calcite alteration assemblages is inferred from Hedenquist et al. (2000, after Buchanan, 1981 and Sillitoe, 1993) but is not recognized at Calypso. Where fluid conduits intersect the seafloor amorphous silica and volatile metals discharge into unconsolidated tephra and cement the volcaniclastic particles. $H_2S_{(g)}$ is oxidized at the seafloor to native sulfur; smectite and mixed layer smectite minerals are associated with sulfur precipitation. An advanced-argillic mineral assemblage is not observed at Calypso indicating sulfuric acid formation did not occur or the acid was neutralized at the seafloor.

9.0 References

Amend, J.P., Rogers, K.L., and Meyer-Dombard, D.R, 2004, Microbially mediated sulfur-redox; energetics in marine hydrothermal vent systems, *in* Amend, J. P., Edwards, K. J., and Lyons, T.W., eds., Sulfur Biogeochemistry; Past and Present: Geological Society of America Special Paper, v. 379: p.17-34.

Barrett, T.J. and MacLean, W.H, 1994, Mass changes in hydrothermal alteration zones associated with VMS deposits of the Noranda area: Exploration and Mining Geology, v. 3, p. 131-160.

Barrett, T.J., and MacLean, W.H., 1999, Volcanic sequences, lithogeochemistry, and hydrothermal alteration in some bimodal volcanic-associated massive sulfide systems; *in* Barrie, C.T. and Hannington, M.D., eds., Volcanic-associated Massive Sulfide Deposits; Processes and Examples in Modern and Ancient Settings, Reviews in Economic Geology, v. 8, p. 101-131.

Bauluz, B., Peacor, D.R., and Ylagan, R.F., 2002, Transmission electron microscopy study of smectite illitization during hydrothermal alteration of a rhyolitic hyaloclastite from Ponza, Italy: Clays and Clay Minerals, v. 50, p. 157-173.

Bevis, M., Taylor, F.W., Schutz, B.E., Recy, J., Isacks, B.L., Helu, S., Singh, R., Kendrick, E., Stowell, J., Taylor, B., and Calmant, S., 1995, Geodetic observations of very rapid convergence and back-arc extension at the Tonga Arc: Nature, v. 374, p. 249-251.

Bhatia, M.R. and Crook, K.A.W., 1986, Trace element characteristics of graywackes and tectonic setting discrimination of sedimentary basins: Contributions to Mineralogy and Petrology, v. 92, p. 181-193.

Bignall, G., Browne, P.R.L., and Kyle, P.R., 1996, Geochemical characterisation of hydrothermally altered ignimbrites in active geothermal fields from the central Taupo Volcanic Zone, New Zealand: Journal of Volcanology and Geothermal Research, v. 73, p. 79-97.

Binns, R.A., Scott, S.D., Bogdanov, Y.A., Lisitzin, A.P., Gordeev, V V (Gordeyev,V.V.), Gurvich, E.G., Finlayson, E.J., Boyd, T., Dotter, L.E., Wheller, G.E., and Muravyev, K.G., 1993, Hydrothermal oxide and gold-rich sulfate deposits of Franklin Seamount, western Woodlark Basin, Papua New Guinea: Economic Geology, v. 88, p. 2118-2149.

Botz, R., Wehner, H., Schmitt, M., Worthington, T.J., Schmidt, M., and Stoffers, P., 2002, Thermogenic hydrocarbons from the offshore Calypso hydrothermal field, Bay of Plenty, New Zealand, Chemical Geology, v.186, p. 235-248.

Brown, K.L., 1986, Gold deposition from geothermal discharges in New Zealand: Economic Geology, v. 81, p. 997-983.

Browne, P.R.L., 1969, Sulfide mineralization in a Broadlands geothermal drill hole, Taupo Volcanic Zone, New Zealand: Economic Geology, v. 64, p. 156-159.

Buchanan, L.J., 1981, Precious metal deposits associated with volcanic environments in the Southwest; Relations of tectonics to ore deposits in the southern Cordillera: Arizona Geological Society Digest, v. 14, p. 237-262.

Callaghan, T., 2001, Geology and host-rock alteration of the Henty and Mount Julia gold deposits, western Tasmania: Economic Geology, v. 96, p. 1073-1088.

Canfield, D.E., 2001, Biogeochemistry of sulfur isotopes; *in* Valley, J.W., and Cole, D.R., eds., Stable Isotope Geochemistry: Reviews in Mineralogy and Geochemistry, v.43, p. 609-636.

Cas, R.A.F. and Large, R.R., 1992, Submarine volcanism; eruption styles, products, and relevance to understanding the host-rock successions to volcanic-hosted massive sulfide deposits: Economic Geology, v. 87, p. 511-541.

Cas, R.A.F., Allen, R.L., Bull, S.W., Clifford, B.A., and Wright, J.V., 1990, Subaqueous, rhyolitic dome-tome tuff cones; a model based on the Devonian Bunga Beds, southeastern Australia and a modern analogue: Bulletin of Volcanology, v.52, 159-174.

Chester, R., 1990, Marine geochemistry. London, United Kingdom Unwin Hyman, 690p.

Clark, R.N., 2004, Chapter 2: Spectroscopy of rocks and minerals, and principles of spectroscopy, *in* King P.L. and Ramsey, M.S. and Swayze, G.A., eds., Infrared Spectroscopy in Geochemistry, Exploration Geochemistry, and Remote Sensing, Short Course Series Volume 33: Mineralogical Association of Canada, Canada, pp. 17-35.

Cole, J.W., Thordarson, T., and Burt, R.M., 2000, Magma origin and evolution of White Island (Whakaari) volcano, Bay of Plenty, New Zealand: Journal of Petrology, v. 41, p. 867-895.

Cooke, D.R. and Simmons, S.F., 2000, Characteristics and genesis of epithermal gold deposits, *in* Hagemann, S.G., and Brown, P.E., eds., Gold in 2000: Reviews in Economic Geology, v. 13, p. 221-244.

Davey, F.J., Henrys, S.A., and Lodolo, E., 1995, Asymmetric rifting in a continental back-arc environment, North Island, New Zealand; Taupo Volcanic Zone, New Zealand: Journal of Volcanology and Geothermal Research, v. 68, p. 209-238.

Davis, J.B. and Kirkland, D.W., 1979, Bioepigenetic sulfur deposits: Economic Geology, v. 74, p. 462-468.

Davis, J.B. and Kirkland, D.W. 1970. Native sulfur deposition in the Castile Formation, Culberson County, Texas: Economic Geology, v. 65, p. 107-121.

de Ronde, C.E.J., Hannington, M.D., Stoffers, P., Wright, I.C., Ditchburn, R.G., Reyes, A.G., Baker, E.T., Massoth, G.J., Lupton, J.E., Walker, S.L., Greene, R.R., Soong, C.W.R., Ishibashi, J., Lebon, G.T., Bray, C.J., and Resing, J.A., 2005, Evolution of a submarine magmatic-hydrothermal system: Brothers Volcano, Southern Kermadec Arc, New Zealand: Economic Geology, v. 100, p. 1097-1133.

de Ronde, C.E.J. and Blattner, P. 1988. Hydrothermal alteration, stable isotopes, and fluid inclusions of the Golden Cross epithermal gold-silver deposit, Waihi, New Zealand: Economic Geology, v. 83, p. 895-917.

Deer, W.A., Howie, R.A., and Zussman, J., 1992, An introduction to the rock-forming minerals: Harlow, United Kingdom, Longman Scientific Technical, 696 p.

Douville, E., Bienvenu, P., Charlou, J.L., Donval, J.P., Fouquet, Y., Appriou, P., and Gamo, T., 1999, Yttrium and rare earth elements in fluids from various deep-sea hydrothermal systems: Geochimica et Cosmochimica Acta, v. 63, p. 627-643.

Duncan, A.R. and Pantin, H.M., 1969, Evidence of submarine geothermal activity in the Bay of Plenty, New Zealand: Journal of Marine and Freshwater Research, v. 3, p. 602-606.

Ehrlich, G.G. and Schoen, R., 1967, Possible role of sulfur-oxidizing bacteria in surficial acid alteration near hot springs: United States Geological Survey Professional Paper 575-C

Einaudi, M.T., Hedenquist, J.W., and Inan, E.E., 2003, Sulfidation state of fluids in active and extinct hydrothermal systems; transitions from porphyry to epithermal environments, *in* Simmons, S.F., and Graham, I., eds., *in* Geothermal, and ore-forming fluids; rulers and witnesses of processes within the earth, Society of Economic Geologists Special Publication, v. 10, p. 285-313.

Ewart, A., Taylor, S.R., and Capp, A.C., 1968, Geochemistry of the pantellerites of Mayor Island, New Zealand: Contributions to Mineralogy and Petrology, v. 17, p. 116-140.

Faure, G., 1998. Principles and applications of geochemistry, 2nd edition: New Jersey, Prentice Hall, 600 p.

Faure, G. and Mensing, T.M., 2005, Isotopes; principles and applications, 3rd edition: New Jersey, John Wiley & Sons, 897 p.

Fedo, C.M., Nesbitt, H.W., and Young, G.M., 1995, Unraveling the effects of potassium metasomatism in sedimentary rocks and paleosols, with implications for paleoweathering conditions and provenance: Geology, v. 23, p. 921-924.

Feely, H.W. and Kulp, J.L., 1957, Origin of Gulf Coast salt-dome sulphur deposits: Bulletin of the American Association of Petroleum Geologists, v. 41, p. 1802-1853.

Finlow-Bates, T. and Stumpfl, E.F, 1981, The behaviour of so-called immobile elements in hydrothermally altered rocks associated with volcanogenic submarine-exhalative ore deposits: Mineralium Deposita, v. 16, p. 319-328.

Fisher, R.V. and Schmincke, H., 1984, Pyroclastic rocks: Federal Republic of Germany (DEU), Springer-Verlag, 472 p.

Gifkins, C.C., Herrmann, W., and Large, R.R., 2005, Altered volcanic rocks. A guide to description and interpretation: University of Tasmania, Centre for Ore Deposit Research, 275 p.

Gifkins, C.C., Allen, R., and McPhie, J., 2000, Textural characteristics of diagenetic and hydrothermal alteration in glassy volcanic rocks; examples from the Mount Read Volcanics, Tasmania: Volcanic environments and massive sulfide deposits; program and abstracts; international conference and field meeting, Centre for Ore Deposit and Exploration Studies (CODES) Special Publication, v. 3, p. 67-68.

Gifkins, C.C. and Allen, R.L., 2001, Textural and chemical characteristics of diagenetic and hydrothermal alteration in glassy volcanic rocks; examples from the Mount Read volcanics, Tasmania: Economic Geologists, v.96, p. 973-1002.

Giggenbach, W.F., 1995, Variations in the chemical and isotopic composition of fluids discharged from the Taupo Volcanic Zone, New Zealand; Taupo Volcanic Zone, New Zealand: Journal of Volcanology and Geothermal Research, v.68, p. 89-116.

Giggenbach, W.F., 1992, Magma degassing and mineral deposition in hydrothermal systems along convergent plate boundaries, Economic Geology, v. 87, p. 1927-1944.

Giggenbach, W.F., Shinohara, H., Kusakabe, M., and Ohba, T., 2003, Formation of acid volcanic brines through interaction of magmatic gases, seawater, and rock within the white island volcanic-hydrothermal system, New Zealand; Volcanic, *in* Geothermal, and ore-forming fluids; rulers and witnesses of processes within the earth, Society of Economic Geologists Special Publication, v. 10, p. 19-40.

Giorgetti, G., Monecke, T., Kleeberg, R., and Hannington, M.D., 2006, Low-temperature hydrothermal alteration of silicic glass a the Pacmanus Hydrothermal Vent Field, Manus Basin, An XRD, SEM, and AEM-TEM study: Clays and Clay Minerals, v. 54, p. 240-251.

Glasby, G.P., 1971, Direct observation of columnar scattering associated with geothermal gas bubbling in the Bay of Plenty, New Zealand: New Zealand Journal of Marine and Freshwater Research, v. 5, p. 483-496.

Goetz, A.F.H., Rock, B.N., and Rowan, L.C., 1983, Remote sensing for exploration; an overview; an issue devoted to techniques and results of remote sensing, Economic Geology, v. 78, p. 573-590.

Grassineau, N.V., Mattey, D.P., and Lowry, D., 2001, Sulfur isotope analysis of sulfide and sulfate minerals by continuous flow-isotope ratio mass spectrometry: Analytical Chemistry, v. 73, p. 220-225.

Hannington, M.D., Peter, J.M., and Scott, S.D., 1986, Gold in sea-floor polymetallic sulfide deposits: Economic Geology, v.81, p. 1867-1883.

Hannington, M.D., Poulsen, K.H., Thompson, J.F.H., Sillitoe, R.H., 1999, Volcanogenic gold in the massive sulfide environment, *in* Barrie, C.T., and Hannington, M.D., eds., Volcanic-associated massive sulfide deposits; processes and examples in modern and ancient settings: Reviews in Economic Geology, v.8, p. 325-356.

Hannington, M.D., de Ronde, C.E.J., and Petersen, S., 2005, Sea floor tectonics and submarine hydrothermal systems: Economic Geology 100th Anniversary Volume, p. 111-141.

Hauff, P. 2005. Applied Reflectance Spectroscopy Instruction Manual, v. 4.1: Colorado, Spectral International Inc.

Hayba, D.O., Bethke, P.M., Heald, P., and Foley, N.K., 1985, Geologic, mineralogic, and geochemical characteristics of volcanic-hosted epithermal precious-metal deposits; geology and geochemistry of epithermal systems, Reviews in Economic Geology, v.2, p. 129-167.

Heald, P., Foley, N.K., and Hayba, D.O., 1987, Comparative anatomy of volcanic-hosted epithermal deposits; acid-sulfate and adularia-sericite types: Economic Geology: v. 82, p. 1-26.

Hedenquist, J.W., Simmons, S.F., Giggenbach, W.F., and Eldridge, C.S., 1993, White Island, New Zealand, volcanic-hydrothermal system represents the geochemical environment of high-sulfidation cu and au ore deposition: Geology, v. 21, p. 731-734.

Hedenquist, J.W., and Lowenstern, J.B., 1994, The role of magmas in the formation of hydrothermal ore deposits: Nature, v. 370, p. 517-527.

Hedenquist, J.W., Arribas, A., Jr., and Reynolds, T.J, 1998, Evolution of an intrusion-centered hydrothermal system; Far Southeast-Lepanto porphyry and epithermal Cu-Au deposits, Philippines: Economic Geology, v. 93, p. 373-404.

Hedenquist, J.W., Arribas R, A., and Gonzalez-Urien, E., 2000, Exploration for epithermal gold deposits: Gold in 2000, Reviews in Economic Geology, v. 13, p. 245-277.

Herzig, P.M., Hannington, M.D., and Arribas, A. Jr., 1998, Sulfur isotopic composition of hydrothermal precipitates from the Lau back-arc; implications for magmatic contributions to seafloor hydrothermal systems: Mineralium Deposita, v. 33, p. 226-237.

Holland, H.D., 1965, Some applications of thermochemical data to problems of ore deposits; Part 2, Mineral assemblages and the composition of ore forming fluids: Economic Geology, v. 60, p. 1101-1166.

Huggett, J.M. and Cuadros, J., 2005, Low-temperature illitization of smectite in the late Eocene and early Oligocene of the Isle of Wight, Hampshire basin, U.K: American Mineralogist, v. 90, p. 1192-1202.

Huston, D.L., Kamprad, J., and Brauhart, C., 1999, Definition of high-temperature alteration zones with PIMA; an example from the Panorama VHMS district, central Pilbara Craton: AGSO Research Newsletter, v. 30, p. 10-12.

Irvine, T.N. and Baragar, W.R.A., 1971, A guide to the chemical classification of the common volcanic rocks: Canadian Journal of Earth Sciences, v. 8, p. 523-548.

Ishikawa, Y., Sawaguchi, T., and Iwaya S., Horiuchi, M., 1976, Delineation of prospecting targets for Kuroko deposits based on modes of volcanism of underlying dacite and alteration haloes: Mining Geology, v. 26, p. 105-117.

Jones, G.E., Feely, H.W., Kulp, J.L., and Starkey, R.L., 1956, Biological origin of native sulfur in salt domes of Texas and Louisiana: Science, v. 123. p. 1124-1125.

Jones, S., Herrmann, W., and Gemmell, J.B., 2005, Short wavelength infrared spectral characteristics of the HW horizon; implications for exploration in the Myra Falls volcanic-hosted massive sulfide camp, Vancouver Island, British Columbia, Canada: Economic Geology, v. 100, p. 273-294.

Kaplan, I.R. and Rittenberg, S.C., 1962, Fractionation of isotopes in relation to the problem of elemental sulphur transport by microorganisms: Nature, v.194, p. 1098-1099.

Kaplan, I.R. and Rafter, T.A., 1958, Fractionation of stable isotopes of sulfur by thiobacilli: Science, v. 127, p. 517-518.

Kester, D.R. 1975. Dissolved gases other than CO (sub 2), *in* Riley J.P., and Skirrow, G., eds., Chemical Oceanography Volume 1: New York, Acad. Press. p. 498-556

Large, R.R., Gemmell, J.B., and Paulick, H., 2001, The alteration box plot; a simple approach to understanding the relationship between alteration mineralogy and lithogeochemistry associated with volcanic-hosted massive sulfide deposits: Economic Geology, v. 96, p. 957-971.

Le Bas, M.J., Le Maitre, R.W., Streckeisen, A., and Zanettin, B.A., 1986, Chemical classification of volcanic rocks based on the total alkali-silica diagram: Journal of Petrology, v. 27, p. 745-750.

Lindgren, W, 1922, A suggestion for the terminology of certain mineral deposits, Economic Geology: v.17, p. 292-294.

MacLean, W.H., 1990, Mass change calculations in altered rock series: Mineralium Deposita, v. 25, p. 44-49.

MacLean, W.H. and Barrett, T.J., 1993, Lithogeochemical techniques using immobile elements; deep exploration using lithogeochemistry: Journal of Geochemical Exploration, v. 48, p. 109-133.

Marumo, K. and Hattori, K.H., 1999, Seafloor hydrothermal clay alteration at Jade in the back-arc Okinawa Trough; mineralogy, geochemistry and isotope characteristics: Geochimica et Cosmochimica Acta, v. 63, p. 2785-2804.

McDonough, W.F. and Sun, S.S., 1995, The composition of the earth; chemical evolution of the mantle: Chemical Geology, v. 120, p. 223-253.

McLennan, S.M., 1989, Rare earth elements in sedimentary rocks; influence of provenance and sedimentary processes; geochemistry and mineralogy of rare earth elements: Reviews in Mineralogy, v. 21, p. 169-200.

McLennan, S.M., Hemming, S., McDaniel, D.K., and Hanson, G.N., 1993, Geochemical approaches to sedimentation, provenance, and tectonics, *in* Johnsson, M.J. and Basu, A.,

eds., Processes Controlling the Composition of Clastic Sediments: Geological Society of America Special Paper, v. 284, p. 21-40.

McLennan, S.M., Taylor, S.R., McCulloch, M.T., and Maynard, J.B., 1990, Geochemical and Nd-Sr isotopic composition of deep-sea turbidites; crustal evolution and plate tectonic associations: Geochimica et Cosmochimica Acta, v. 54, p. 2015-2050.

McLennan, S.M., Bock, B., Hemming, R., Hurowitz, J.A., Lev, S.M., and McDaniel, D.K. 2003. The role of provenance and sedimentary processes in the geochemistry of sedimentary rocks, *in* Lentz, D.R., ed., Geochemistry of Sediments and Sedimentary Rocks: Evolutionary Considerations to Mineral Deposit-Forming Environments: St. John's, Newfoundland, Geological Association of Canada, pp. 7-38.

Moore, D.M. and Reynolds, R.C., Jr. 1989. X-ray diffraction and the identification and analysis of clay minerals: New York; Oxford University Press, 332p.

Mortimer, N. and Parkinson, D, 1996, Hikurangi plateau; a Cretaceous large igneous province in the Southwest Pacific Ocean: Journal of Geophysical Research, v.101, p. 687-696.

Mosser, J.L., Mosser, A.G., and Brock, T.D., 1973, Bacterial origin of sulfuric acid in geothermal habitats: Science, v. 179, p. 1323-1324.

Munha, J. and Kerrich, R., 1980, Sea water basalt interaction in spilites from the Iberian pyrite belt: Contributions to Mineralogy and Petrology, v. 73, p. 191-200.

Naden, J., Kilias, S.P., and Darbyshire, D.P.F., 2005, Active geothermal systems with entrained seawater as modern analogs for transitional volcanic-hosted massive sulfide and

continental magmato-hydrothermal mineralization; the example of Milos Island, Greece: Geology, v.33, p.541-544.

Nesbitt, H.W., 2003, Petrogenesis of siliciclastic sediments and sedimentary rocks. *in* Lentz D.R., ed., Geochemistry of Sediments and Sedimentary Rocks: Evolutionary Considerations to Mineral Deposit-Forming Environments: St. John's, Newfoundland, Geological Association of Canada, p. 39-52.

Norris, R.J. and Cooper, A.F., 1995, Origin of small-scale segmentation and transpressional thrusting along the Alpine Fault, New Zealand: Geological Society of America Bulletin, v. 107, p. 231-240.

Ohmoto, H. and Rye, R.O., 1979, Isotopes of sulfur and carbon. *in* Barnes, H.J., ed., Geochemistry of hydrothermal ore deposits: New York, John Wiley & Sons, p. 509-567

Ohmoto, H. and Lasaga, A.C., 1982, Kinetics of reactions between aqueous sulfates and sulfides in hydrothermal systems: Geochimica et Cosmochimica Acta, v. 46, p. 1727-1745.

Pantin, H.M. and Wright, I.C., 1994, Submarine hydrothermal activity within the offshore Taupo Volcanic Zone, Bay of Plenty continental shelf, New Zealand: Continental Shelf Research, v.14, p. 1411-1438.

Paulick, H. and Bach, W., 2006, Phyllosilicate alteration mineral assemblages in the active subsea-floor PACMANUS hydrothermal system, Papua New Guinea, ODP leg 193: Economic Geology, v.101, p. 633-650.

Peter, J.M. and Shanks, W.C.,III., 1992, Sulfur, carbon, and oxygen isotope variations in submarine hydrothermal deposits of Guaymas Basin, Gulf of California, USA: Geochimica et Cosmochimica Acta, v. 56, p. 2025-2040.

Pillans, B. and Wright, I., 1992, Late quaternary tephrostratigraphy from the southern Gavre Trough-Bay of Plenty, northeast New Zealand: New Zealand Journal of Geology and Geophysics, v. 35, p. 129-143.

Rafter, T.A., Hulston, J.R., and Kaplan, I.R., 1960, Sulphur isotopic variations in nature; Part 7, Sulphur isotopic measurements on sulphur and sulphates in New Zealand geothermal and volcanic areas: New Zealand Journal of Science, v.3, p. 209-218.

Rees, C.E., Jenkins, W.J., and Monster, J. 1978. The sulphur isotopic composition of ocean water sulphate, Geochimica et Cosmochimica Acta, 42: 377-382.

Rickwood, P.C., 1989, Boundary lines within petrologic diagrams which use oxides of major and minor elements: Lithos, v. 22, p. 247-263.

Rimstidt, J.D. and Barnes, H.L., 1980, The kinetics of silica-water reactions: Geochimica et Cosmochimica Acta, v. 44, p. 1683-1700.

Rimstidt, J.D. 1997. Gangue mineral transport and deposition, *in* Barnes, H.L, ed., Geochemistry of hydrothermal ore deposits: New York, John Wiley & Sons, p. 487-516.

Robertson, J., 1999, Morphology and mineralogy of shallow submarine hydrothermal vents of the Calypso Geothermal Field, Bay of Plenty, New Zealand: the Australasian Institute of Mining and Metallurgy, New Zealand branch 32nd annual conference, v. 32, p. 41-50.

Rowan, L.C., Hook, S.J., Abrams, M.J., and Mars, J.C., 2003, Mapping hydrothermally altered rocks at Cuprite, Nevada, using the advanced spaceborne thermal emission and reflection radiometer (ASTER), a new satellite-imaging system, Economic Geology, v. 98, p. 1019-1027.

Rye, R.O., Bethke, P.M., and Wasserman, M.D., 1992, The stable isotope geochemistry of acid sulfate alteration, Economic Geology, v. 87, p. 225-262.

Sakai, H., Des Marais, D.J., Ueda, A., and Moore, J.G., 1984, Concentrations and isotope ratios of carbon, nitrogen and sulfur in ocean-floor basalts: Geochimica et Cosmochimica Acta, v. 48, p. 2433-2441.

Sakai, H., 1957, Fractionation of sulphur isotopes in nature: Geochimica et Cosmochimica Acta, v.12, p. 150-169.

Schneider, A., 1970, The sulfur isotope composition of basaltic rocks: Contributions to Mineralogy and Petrology, v. 25, p. 95-124.

Schoen, R., 1969, Rate of sulfuric acid formation in Yellowstone National Park: Geological Society of America Bulletin, v. 80, p. 643-649.

Schoen, R. and Rye, R.O., 1970, Sulfur isotope distribution in solfataras, Yellowstone National Park: Science, v. 170, p. 1082-1084.

Schoen, R., White, D.E., and Hemley, J.J., 1974, Argillization by descending acid at Steamboat Springs, Nevada: Clays and Clay Minerals, v. 22, p. 1-22.

Shanks, W.C.,III, Bohlke, J.K., and Seal, R.R.,II., 1995, Stable isotopes in mid-ocean ridge hydrothermal systems; interactions between fluids, minerals, and organisms; seafloor hydrothermal systems; physical, chemical, biological, and geological interactions: Geophysical Monograph, v. 91, p. 194-221.

Sillitoe, R.H., 1993, Epithermal models; genetic types, geometrical controls and shallow features; mineral deposit modeling: Geological Association of Canada Special Paper, v. 40, p. 403-417.

Sillitoe, R.H. and Hedenquist, J.W., 2003, Linkages between volcanotectonic settings, ore-fluid compositions, and epithermal precious metal deposits, *in* Simmons, S.F. and Graham, I., eds., Volcanic, geothermal, and ore-forming fluids; rulers and witnesses of processes within the earth, Society of Economic Geologist Special Publication, v.10, p. 315-343.

Sillitoe, R.H., Hannington, M.D., and Thompson, J.F.H., 1996, High sulfidation deposits in the volcanogenic massive sulfide environment: Economic Geology, v. 91, p. 204-212.

Simmons, S.F, 1991, Hydrologic implications of alteration and fluid inclusion studies in the Fresnillo District, Mexico; evidence for a brine reservoir and a descending water table during the formation of hydrothermal Ag-Pb-Zn orebodies: Economic Geology, v. 86, p. 1579-1601.

Simmons, S.F. and Browne, P.R.L. 2000. Hydrothermal minerals and precious metals in the Broadlands-Ohaaki geothermal system: Implications for understanding low-sulfidation epithermal environments: Economic Geology, v. 95, p. 971-999.

Simmons, S.F., White, N.C., and John, D.A., 2005, Geological characteristics of epithermal precious and base metal deposits: Economic Geology 100th Anniversary Volume, p. 455-522

Smith, V. and Shane, P., 2002, Geochemical characteristics of the widespread Tahuna Tephra, New Zealand: Journal of Geology and Geophysics, v. 45, p. 103-107.

Smitheringale, W.G. and Jensen, M.L., 1963, Sulfur isotopic composition of the Triassic igneous rocks of eastern United States: Geochimica et Cosmochimica Acta, v. 27, p. 1183-1207.

Steiner, A. and Rafter, T.A., 1966, Sulfur isotopes in pyrite, pyrrhotite, alunite and anhydrite from steam wells in the Taupo Volcanic Zone, New Zealand: Economic Geology, v. 61, p. 1115-1129.

Steven, T.A. and Ratte, J.C., 1960, Geology and ore deposits of the Summitville District, San Juan Mountains, Colorado: United States Geological Survey Professional Paper 343, p. 70

Stoffers, P., Hannington, M., Wright, I., Herzig, P., de Ronde, C., Arpe, T., Battershill, C., Botz, R., Britten, K., Browne, P., Cheminee, J.L., Fricke, H.W., Garbe-Schoenberg, D., Hekinian, R., Hissman, K., Huber, R., Robertson, J., Schauer, J., Schmitt, M., Scholten, J., Schwarz-Schampera, U., Smith, I., and *Sonne* Cruise SO-135, Shipboard Scientific Party, International (III), 1999, Elemental mercury at submarine hydrothermal vents in the bay of Plenty, Taupo Volcanic Zone, New Zealand: Geology, v. 27, p. 931-934.

Stoffers, P. and Wright, I., 1999, Cruise report *SONNE* 135, Havre Trough-Taupo Volcanic Zone; Tectonic, magmatic and hydrothermal processes; Suva, Fiji - Wellington, New Zealand, 9 September 1998-15 October 1998: Berichte-Reports, Institut für Geowissenschaften, Universität Kiel, Nr. 1, 77 p.

Stoffregen, R.E., 1987, Genesis of acid-sulfate alteration and Au-Cu-Ag mineralization at Summitville, Colorado: Economic Geology, v. 82, p. 1575-1591.

Stolz, A.J., Varne, R., Davies, G.R., Wheller, G.E., and Foden, J.D., 1990, Magma source components in an arc-continent collision zone; the Flores-Lembata Sector, Sunda Arc, Indonesia: Contributions to Mineralogy and Petrology, v.105, p. 585-601.

Sutton, A.N., Blake, S., and Wilson, C.J.N., 1995, An outline geochemistry of rhyolite eruptives from Taupo Volcanic Centre, New Zealand; Taupo Volcanic Zone, New Zealand: Journal of Volcanology and Geothermal Research, v.68, p. 153-175.

Swayze, G.A., 2004, Chapter 7: Using reflectance spectroscopy to evaluate minerals of environmental concern, *in* King P.L. and Ramsey, M.S. and Swayze, G.A., eds., Infrared Spectroscopy in Geochemistry, Exploration Geochemistry, and Remote Sensing, Short Course Series Volume 33: Mineralogical Association of Canada, Canada, pp. 181-196.

Swinden, H.S., Jenner, G.A., and Szybinski, Z.A., 1997, Magmatic and tectonic evolution of the Cambrian-Ordovician Laurentian margin of Iapetus; geochemical and isotopic constraints from the Notre Dame Subzone, Newfoundland; the nature of magmatism in the Appalachian Orogen: Geological Society of America Memoir, v. 191, p. 337-365.

Thompson, A.J.B., Hauff, P.L., and Robitaille, J.A., 1999, Alteration mapping in exploration; application of short-wave infrared (SWIR) spectroscopy, Society of Economic Geologists Newsletter, v.39, p. 1-27.

Ueda, A. and Sakai, H., 1984, Sulfur isotope study of quaternary volcanic rocks from the Japanese islands arc: Geochimica et Cosmochimica Acta, v. 48, p. 1837-1848.

van Ruitenbeek, F.J.A., Cudahy, T., Hale, M., and van der Meer,Freek D., 2005, Tracing fluid pathways in fossil hydrothermal systems with near-infrared spectroscopy: Geology, v. 33, p. 597-600.

Wallace, A.R., 2003, Geology of the Ivanhoe Hg-Au district, northern Nevada; influence of Miocene volcanism, lakes, and active faulting on epithermal mineralization; Gold deposits in northern Nevada; Part 1, Regional studies and epithermal deposits: Economic Geology, v. 98, p. 409-424.

Wallace, L.M., McCaffrey, R., Beavan, J., and Ellis, S., 2005, Rapid microplate rotations and backarc rifting at the transition between collision and subduction: Geology, v. 33, p. 857-860.

Wallace, L.M., Beavan, J., McCaffrey, R., and Darby, D., 2004, Subduction zone coupling and tectonic block rotations in the North Island, New Zealand: Journal of Geophysical Research, v. 109, p. 21.

Weissberg, B.G., 1969, Gold-silver ore-grade precipitates from New Zealand thermal waters, Economic Geology, v. 64, p. 95-108.

Weissberg, B.G., Browne, P.R.L., and Seward, T.M., 1979, Ore metals in active geothermal systems, *in* Barnes, H.J., ed., Geochemistry of hydrothermal ore deposits: New York, John Wiley & Sons, p. 738-780.

White, N.C. and Hedenquist, J.W., 1995, Epithermal gold deposits: Styles, characteristics and exploration: Society of Economic Geologists Newsletter, v. 23, p.1-13.

White, N.C., Wood, D.G., and Lee, M.C., 1989, Epithermal sinters of Paleozoic age in North Queensland, Australia: Geology, v. 17, p. 718-722.

White, N.C. and Hedenquist, J.W., 1990, Epithermal environments and styles of mineralization; variations and their causes, and guidelines for exploration; epithermal gold mineralization of the circum-pacific; geology, geochemistry, origin and exploration; II: Journal of Geochemical Exploration, v. 36, p. 445-474.

Whitford, D.J., Korsch, M.J., Porritt, P.M., and Craven, S.J., 1988, Rare-earth element mobility around the volcanogenic polymetallic massive sulfide deposit at Que River, Tasmania, Australia: Chemical Geology, v. 68, p.105-119.

Winchester, J.A. and Floyd, P.A., 1977, Geochemical discrimination of different magma series and their differentiation products using immobile elements: Chemical Geology, v. 20, p. 325-343.

Wood, R. and Davy, B., 1994, The Hikurangi Plateau: Marine Geology, v. 118, p. 153-173.

Woodhead, J.D., Harmon, R.S., and Fraser, D.G. 1987. O, S, Sr, and Pb isotope variations in volcanic rocks from the northern Mariana Islands; implications for crustal recycling in intra-oceanic arcs: Earth and Planetary Science Letters, v. 83, p. 39-52.

Wright, I.C., 1990, Late quaternary faulting of the offshore Whakatane Graben, Taupo Volcanic Zone, New Zealand: New Zealand Journal of Geology and Geophysics, v. 33, p. 245-256.

Wright, I.C., 1992, Shallow structure and active tectonism of an offshore continental back-arc spreading system: the Taupo Volcanic Zone, New Zealand: Marine Geology, v. 103, p. 287-309.

Yan, Y., Tillick, D.A., Peacor, D.R., and Simmons, S.F., 2001, Genesis of dioctahedral phylosilicates during hydrothermal alteration of volcanic rocks: II. The Broadlands-Ohaaki hydrothermal system, New Zealand: Clays and Clay Minerals, v. 49, p. 141-155.

Yang, K., Browne, P.R.L., Huntington, J.F., and Walshe, J.L., 2001, Characterising the hydrothermal alteration of the Broadlands-Ohaaki geothermal system, New Zealand, using short-wave infrared spectroscopy: Journal of Volcanology and Geothermal Research, v. 106, p. 53-65.

Young, G.M. and Nesbitt, H.W., 1998, Processes controlling the distribution of Ti and Al in weathering profiles, siliciclastic sediments and sedimentary rocks: Journal of Sedimentary Research, v. 68, p. 448-455.